

Design of transition metal-based nanostructured electrocatalysts

Dissertation

zur Erlangung des akademischen Grades

Doktor der Naturwissenschaften

im Promotionsfach Chemie

am Fachbereich Chemie, Pharmazie,
Geographie und Geowissenschaften
der Johannes Gutenberg-Universität Mainz

vorgelegt von

Yupeng Zhao

geboren in Shandong

Mainz, 2024

Dekanin: [REDACTED]
Erster Berichterstatter: [REDACTED]
Zweite Berichterstatter: [REDACTED]

Tag der mündlichen Prüfung:

Die vorliegende Arbeit wurde in der Zeit von Oktober 2019 bis April 2024 am Department für Chemie der Johannes Gutenberg-Universität Mainz unter Betreuung von [REDACTED] angefertigt.

Hiermit versichere Ich, Yupeng Zhao, Matrikelnummer [REDACTED] dass ich meine Promotionsarbeit selbstständig verfasst und keine anderen als die angegebenen schriftlichen und elektronischen Quellen, sowie andere Hilfsmittel benutzt habe. Alle Ausführungen, die anderen Schriften wörtlich oder sinngemäß entnommen wurden, habe ich kenntlich gemacht.

(Ort, Datum)

(Unterschrift)

Kurzzusammenfassung

Traditionelle Energiequellen wie Kohle und Erdöl dominieren nach wie vor unsere Energielandschaft. Ihre Nutzung trägt jedoch erheblich zur Umweltverschmutzung, zu erhöhten Treibhausgasemissionen und zum unumkehrbaren Klimawandel bei. Um diesen drängenden Problemen entgegenzuwirken, ist die Entwicklung nachhaltiger Energieträger wie Wasserstoff (H_2) und Sauerstoff (O_2) von entscheidender Bedeutung, um die Verknappung fossiler Brennstoffe abzumildern. Vor diesem Hintergrund erweisen sich umweltfreundliche und erneuerbare Energieumwandlungs- und -speicherlösungen, einschließlich Wasserspaltung, Brennstoffzellen und Batterien, als vielversprechende Strategien zur Bewältigung unserer derzeitigen Energie- und Umweltprobleme. Im Mittelpunkt dieser Technologien stehen die Wasserstoffentwicklungsreaktion (HER), die Sauerstoffentwicklungsreaktion (OER) und die Sauerstoffreduktionsreaktion (ORR). Eine entscheidende Herausforderung bei diesen Technologien ist die Entwicklung kostengünstiger und effizienter Katalysatoren, die für Prozesse wie die wässrige Wasserspaltung und Metall-Luft-Batterien unerlässlich sind.

Diese Studie fasst die wesentlichen Parameter für die Bewertung der Leistung von Sauerstoff-Elektrokatalysatoren zusammen, gibt einen Überblick über die jüngsten Durchbrüche auf dem Gebiet der Sauerstoff-Elektrokatalysatoren und schlägt künftige Forschungsrichtungen vor. Darüber hinaus werden die Beiträge des Autors zu diesem Forschungsbereich hervorgehoben, die die Synthese, Charakterisierung und Bewertung der elektrochemischen Leistung von Sauerstoff-Elektrokatalysatoren umfassen.

In dieser Doktorarbeit stellen wir Richtlinien für die Entwicklung von Elektrokatalysatoren vor, die sich darauf konzentrieren, durch kontrollierte morphologische Anpassungen mehr aktive Stellen freizulegen und die katalytische Wirksamkeit durch Manipulation der elektronischen Struktur zu erhöhen. Konkret werden poröse ZIF-67-Polyeder als Vorstufen für verschiedene Behandlungen wie die Immobilisierung von Polyoxometallaten, Säureätzung, Karbonisierung oder Sulfidierung verwendet. Die resultierenden Verbundwerkstoffe behalten die poröse Architektur der ZIF-67-Polyeder bei und bieten mehr aktive Stellen für die Elektrokatalyse. Darüber hinaus werden ultradünne Pd-Metallene (Sub-Nanometer und gekrümmte Metall-Nanoblätter) hergestellt und mit Defekttechniken modifiziert, einschließlich der Einführung von Poren, konkaven Strukturen und MoO_x/WO_x -Dotierung. Charakterisierungstechniken wie Rasterelektronenmikroskopie (SEM), Rasterkraftmikroskopie (AFM), hochauflösende Transmissionselektronenmikroskopie (HR-TEM) und elementares Mapping wurden eingesetzt, um die Morphologie und die elementare Zusammensetzung zu untersuchen. Die Ergebnisse zeigen die poröse Struktur von Verbundwerkstoffen auf ZIF-67-Basis sowie ultradünne und defekte Merkmale von Pd-Metallen. Analytische Methoden wie Röntgenbeugung (XRD), Röntgenphotoelektronenspektroskopie (XPS), Röntgenabsorptionsspektroskopie (XAS), Fourier-Transform-Infrarotspektroskopie (FT-IR) und Raman-Spektroskopie wurden zur Analyse der Zusammensetzung und der elektronischen Strukturen eingesetzt. Die

Kurzzusammenfassung

elektrokatalytischen Aktivitäten und Langzeitstabilitätstests der entwickelten Katalysatoren wurden für verschiedene Reaktionen, insbesondere OER und ORR, gründlich bewertet. Im Anschluss an diese Bewertungen wird eine gründliche Bewertung der postkatalytischen chemischen und strukturellen Integrität durchgeführt, um die tatsächlichen aktiven Stellen für OER und ORR zu verstehen. Gleichzeitig wird eine eingehende Untersuchung der elektrochemisch aktiven Oberfläche und des Elektronentransferprozesses an der Grenzfläche durchgeführt, um unser Verständnis der beteiligten katalytischen Mechanismen zu vertiefen. Insgesamt zeigen diese Elektrokatalysatoren eine außergewöhnliche Leistung, die durch niedrige Überspannungen und eine bemerkenswerte Ausdauer von mehreren bis zu Dutzenden von Stunden gekennzeichnet ist. Diese überragende Leistung ist auf ihre inhärente Aktivität, die zahlreichen aktiven Stellen, die große Oberfläche und ihre fein abgestimmten elektronischen Strukturen zurückzuführen.

Abstract

Traditional energy sources, such as coal and petroleum, continue to dominate our energy landscape. However, their usage significantly contributes to environmental pollution, elevated greenhouse gas emissions, and irreversible climate change. To counter these pressing issues, it is vital to develop sustainable energy carriers, thereby reducing our reliance on rapidly diminishing fossil fuels. In this light, eco-friendly and renewable energy conversion and storage solutions, including water splitting, fuel cells, and batteries, emerge as promising strategies to address our current energy and environmental predicaments. Central to these technologies are the hydrogen evolution reaction (HER), oxygen evolution reaction (OER), and oxygen reduction reaction (ORR). A critical challenge in these technologies is the development of cost-effective, efficient and robust catalysts, essential for processes like aqueous water splitting and metal-air batteries.

This study summarizes the essential parameters for assessing the performance of oxygen electrocatalysts and reviews recent breakthroughs in the field of oxygen electrocatalysts and proposes prospective research trajectories. Based on these studies, the thesis summarizes the author's contributions to this area of study, which include the synthesis, characterization, and assessment of the electrochemical performance of OER/ORR electrocatalysts.

In this Ph.D. thesis, novel electrocatalysts are designed which focus on revealing more active sites through controlled morphological adjustments and boosting catalytic efficiency *via* electronic structure manipulation. Specifically, porous ZIF-67 polyhedrons are utilized as precursors for various treatments such as polyoxometalates immobilization, acid etching, carbonization, or sulfidation. The resulting composites retain the porous architecture of ZIF-67 polyhedrons, offering increased active sites for electrocatalysis. Moreover, ultra-thin Pd metallene (sub-nanometer and curved metal nanosheets) are fabricated and modified with defect engineering techniques, including the introduction of pores, concave structures, and MoO_x/WO_x doping. Characterization techniques such as scanning electron microscopy (SEM), atomic force microscopy (AFM), high-resolution transmission electron microscopy (HR-TEM), and elemental mapping were employed to study the morphology and elemental composition. The results reveal the porous structure of ZIF-67 based composites, and ultrathin and defective feature of Pd metallene. X-ray diffraction (XRD), X-ray photoelectron spectroscopy (XPS), X-ray absorption spectroscopy (XAS), Fourier transform infrared spectroscopy (FT-IR), and Raman spectroscopy were used to analyze compositions and electronic structures. Electrocatalytic activities and long-term stability tests of the catalysts were evaluated for various reactions, notably the OER and ORR. Post-catalytic chemical and structural integrity was studied to understand the real active sites for OER and ORR. In-depth investigations into the electrochemically active surface area and the interfacial electron transfer processes were undertaken to deepen our understanding of the catalytic mechanisms involved. In sum, these electrocatalysts exhibit exceptional performance, characterized by low overpotentials and remarkable endurance. This superior performance is attributed to their inherent activity, abundance of active sites, extensive surface area, and their finely tuned electronic structures.

Table of Contents

Kurzzusammenfassung	I
Abstract	III
List of abbreviations and units	VII
1 Introduction	1
1.1 Electrochemical oxygen evolution/reduction reaction	1
1.1.1 Significance of electrochemical oxygen evolution/reduction in energy conversion and storage	1
1.1.2 Electrochemical oxygen evolution reaction	3
1.1.3 Electrochemical oxygen reduction reaction	5
1.2 Performance analysis of the electrochemical oxygen evolution/reduction	7
1.2.1 Rotating-ring disk electrode technique	8
1.2.2 Current density and overpotential	9
1.2.3 Tafel slope	9
1.2.4 Electrochemically active surface area	10
1.2.5 Electron transfer number and Faradaic efficiency	11
1.2.6 Electrochemical impedance spectroscopy	12
1.2.7 Stability	14
1.2.8 d-band center	14
1.3 Noble-metal-based catalysts for electrochemical oxygen evolution/reduction reactions 15	15
1.3.1 IrO ₂ and RuO ₂ based catalysts for OER	15
1.3.2 Pt and Pd based catalysts for ORR	19
1.4 Noble-metal-free catalysts for electrochemical oxygen evolution/reduction reactions .	24
1.4.1 Noble metal free based electrocatalysts for OER	24
1.4.2 Noble metal free electrocatalysts for ORR	32
2 Objectives of work	39
3 Results and discussion	41
3.1 Polyoxometalate-assisted synthesis of amorphous zeolitic imidazolate for efficient electrocatalytic oxygen evolution	45
3.2 POM@ZIF derived mixed metal oxide catalysts for sustained electrocatalytic oxygen evolution	51
3.3 In situ formation of robust nanostructured Cobalt oxyhydroxide / Cobalt oxide oxygen evolution reaction electrocatalysts	57
3.4 Atomically Engineered WO_x/MoO_x-Modified Defect-Rich Pd Metallene for Enhanced Alkaline Oxygen Reduction Electrocatalysis	75

3.5	Hydrogenation catalysis by hydrogen spillover on platinum-functionalized heterogeneous boronic acid-polyoxometalates.....	93
4	Summary and outlook	101
5	References.....	105
6	Appendix	113
6.1	Supporting information: Polyoxometalate-assisted synthesis of amorphous zeolitic imidazolate for efficient electrocatalytic oxygen evolution	113
6.2	Supporting information: POM@ZIF Derived Mixed Metal Oxide Catalysts for Sustained Electrocatalytic Oxygen Evolution.....	125
6.3	Supporting information: In situ formation of robust nanostructured Cobalt oxyhydroxide / Cobalt oxide oxygen evolution reaction electrocatalysts	137
6.4	Supporting information: Atomically Engineered WO _x /MoO _x -Modified Defect-Rich Pd Metallene for Enhanced Alkaline Oxygen Reduction Electrocatalysis	147
6.5	Supporting information: Hydrogenation Catalysis by Hydrogen Spillover on Platinum-Functionalized Heterogeneous Boronic Acid-Polyoxometalates	172
7	Acknowledgements	227
8	Curriculum Vitae	229

List of abbreviations and units

In addition to the standard notations, the following abbreviations were used:

Abbreviations

GHG	Greenhouse Gas
PEM	Proton Exchange Membrane
HER	Hydrogen Evolution Reaction
OER	Oxygen Evolution Reaction
FCs	Fuel Cells
AFCs	Alkaline Fuel Cells
PAFCs	Phosphoric Acid Fuel Cells
MCFCs	Molten Carbonate Fuel Cells
SOFCs	Solid Oxide Fuel Cells
SPFCs	Solid Polymer Fuel Cells
PEMFCs	Proton Exchange Membrane Fuel Cells
ORR	Oxygen Reduction Reaction
AEM	Adsorbate Evolving Mechanism
LOM	Lattice-Oxygen Participation Mechanism
ER	Eley-Rideal
LH	Langmuir–Hinshelwood
PBC	$\text{Pr}_{0.5}\text{Ba}_{0.5}\text{CoO}_{3-\delta}$
BSCF	$\text{Ba}_{0.5}\text{Sr}_{0.5}\text{Co}_{0.8}\text{Fe}_{0.2}\text{O}_{3-\delta}$
ΔE_o	Oxygen Adsorption Energy
ECSA	Electrochemically Active Surface Area
FE	Faradaic Efficiency
RRDE	Rotating-Ring Disk Electrode
RHE	Reversible Hydrogen Electrode
η	Overpotential
ΔE_o	Oxygen Adsorption Energy
j	Current Density
LSV	Linear Sweep Voltammetry
CVs	Cyclic Voltammograms
C_{dl}	Double-Layer Capacitance
C_s	Specific Capacitance
K-L	Koutecky–Levich
EIS	Electrochemical Impedance Spectroscopy
AC	Alternating Current
DC	Direct Current
CA	Chronoamperometry
CP	Chronopotentiometry
ADT	Accelerated Durability Test
XPS	X-Ray Photoelectron Spectroscopy
XAS	X-Ray Absorption Spectroscopy
AFM	Atomic force microscopy
RDS	Rate-Determining Step

List of abbreviations and units

1D	1 Dimensional
DFT	Density Functional Theory
LDH	Layered Double Hydroxide
SA	Specific Activity
MA	Mass Activity
MOFs	Metal-Organic Frameworks
PtM	Pt Alloying Transition Metal
POM	Polyoxometalate
ATR-FTIR	Attenuated Total Reflectance Fourier Transform Infrared Spectroscopy
pXRD	Powder X-Ray Diffraction
TEM	Transmission Electron Microscopy
EDX	Energy-Dispersive X-Ray Spectroscopy

Units:

A	Ampere
mA	Milliampere
μ A	Microampere
V	Volt
mV	Millivolt
Ω	Ohm
e	Electron
eV	Electron Volt
<i>I</i>	Current
<i>j</i>	Current Density
<i>t</i>	Time
ν	Scan Rate
<i>E</i>	Potential
M	Molar
mM	Millimolar
L	Liter
mL	Milliliter
m	Meter
mm	Millimeter
μ m	Micrometer
nm	Nanometer
Å	Ångström
kg	Kilogram
g	Gram
mg	Milligram
μ g	Microgram
°C	Degree Celsius
s	Second
min	Minute
h	Hour
rpm	Revolutions per minute
J	Joule

List of abbreviations and units

W	Watt
mW	Milliwatt
°	Degree
%	Percent

1 Introduction

1.1 Electrochemical oxygen evolution/reduction reaction

1.1.1 Significance of electrochemical oxygen evolution/reduction in energy conversion and storage

From the mid-18th century until today, the annual global emissions of carbon dioxide (CO₂) increased from 10 million tons each year to 34 billion tons each year,^[1] which caused many climate and environmental problems, such as global warming,^[2] melting glaciers,^[3] etc. In response, an increasing number of countries are announcing carbon net-zero targets.^[4,5] Especially, the German Federal Government set a target to achieve a 65% reduction in greenhouse gas (GHG) emissions by 2030 compared to the base year 1990 and net-zero greenhouse gas emissions by 2045.^[6,7] Similarly, China, the European Union, the United States, and Japan also plan to reduce their carbon emissions and meet the goal of reaching the 2050 net zero emissions target.^[8] In 2018, 89% of global CO₂ emissions came from fossil fuels and industry.^[9] On this basis, the utilization of clean, sustainable, and inexhaustible substitutes for traditional fossil fuel energy is far more significant. Various energy sources, such as wind power, solar power, bioenergy, geothermal, tidal energy, etc., are widely used as substantial carbon-free feedstocks to generate electricity.^[10] However, these feedstocks are more intermittent and weather- or season-independent.^[11] Consequently, various energy storage methods are proposed, such as thermal energy storage in molten salt, hydrogen energy storage, battery energy storage, capacitors, and supercapacitors.^[12]

Hydrogen energy storage appeals to more attention among all the methods due to its high gravimetric energy density, uninterrupted power supply, environmental friendliness, and adaptability. As shown in Fig.1, the electricity generated by different sustainable energy sources can be applied to a proton exchange membrane (PEM) electrolyzer, where the electrical energy is converted to chemical energy. The solution to achieve the energy conversion is electrochemical water splitting ($2\text{H}_2\text{O} \xrightarrow{\text{Energy}} 2\text{H}_2 + \text{O}_2$), which was first reported in 1789 by Troostwijk and Deiman.^[13] It includes two half-reactions: the hydrogen evolution reaction (HER) on the cathode and the oxygen evolution reaction (OER) on the anode.

1. Introduction

Currently, electrodes and catalysts with low-cost and long-term durability for HER have been studied widely and well-developed^[14,15] However, the application at the industrial scale is still limited by anodic OER, which involves a complex proton-coupled 4-electron transfer, showing sluggish kinetics. As a result, a higher external voltage and more energy are needed to drive electrochemical water splitting. Developing highly active, low-cost, and robust anode electrodes or catalysts therefore is critically important in electrochemical water splitting. Additionally, the transport section accounts for around 20% of global CO₂ emissions. In particular, passenger vehicles, including private cars and buses, contribute 9% of global CO₂ emissions.^[16] To reduce CO₂ emissions from vehicles, fuel cells (FCs) are widely studied and developed because of their eco-friendliness and high energy density. The first successful fuel cell (FC) based on hydrogen and oxygen was developed by Francis Bacon in 1932.^[17] Afterward, a wide range of FCs was developed, such as alkaline fuel cells (AFCs), phosphoric acid fuel cells (PAFCs), molten carbonate fuel cells (MCFCs), solid oxide fuel cells (SOFCs), solid polymer fuel cells (SPFCs), and proton exchange membrane fuel cells (PEMFCs). Although FCs have been studied for decades, several significant challenges exist before they can be widely applied in commercial practice. Especially, the development of FCs is significantly hampered by the sluggish oxygen redox kinetics on the cathode, where oxygen reduction reaction (ORR) occurs. Besides, noble metal-based catalysts are commonly used on cathodes, which also hinders the technological application of FCs. Thus, developing effective and inexpensive electrocatalysts with long-term catalytic stability is required for FC commercialization and CO₂ emission reduction.

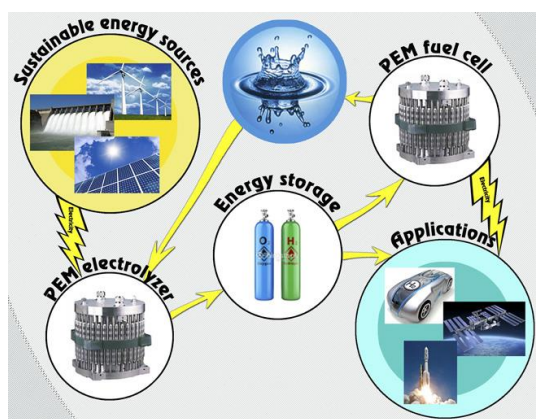


Fig. 1. Schematic of applications of proton exchange membrane (PEM) electrolyzer and PEMFCs coupled with sustainable energy sources. Reproduced with permission^[18].

Copyright 2016, the authors.

1.1.2 Electrochemical oxygen evolution reaction

Proton-coupled four-electron transfer is involved in the OER process, resulting in sluggish kinetics. A better understanding of the catalytic reaction mechanisms is needed to develop optimal electrocatalysts for OER. Traditionally, the most common understanding of reaction control is the binding strength of oxygen or oxygenated intermediates, which follows the Sabatier principle. Namely, optimal catalysis occurs when the binding energy (ΔG) between the catalyst and reactant is neither too strong nor too weak.^[19] This concept is based on the notion that if the ΔG is too weak, it is difficult for the catalyst surface to bind to the reactant, whereas if the ΔG is too strong, the product will fail to dissociate and lower the activity.^[19]^[20] On this basis, depending on whether the lattice oxygens participate in the reaction, two possible reaction mechanisms have been proposed: adsorbate evolving mechanism (AEM) and lattice-oxygen participation mechanism (LOM) (Fig.2).

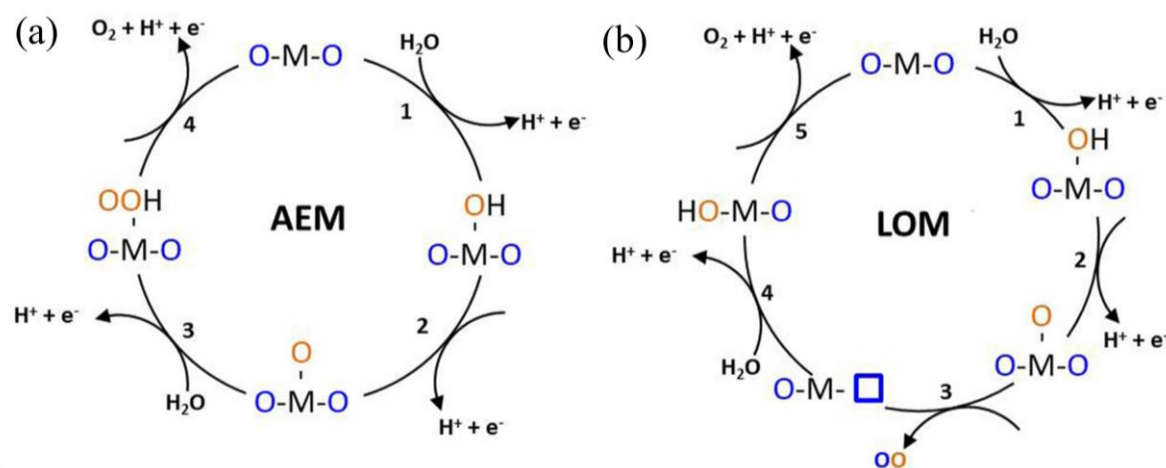


Fig.2 (a) Conventional AEM mechanism. (b) LOM mechanism. M represents the active sites. The oxygen in blue and orange represents the oxygen atoms in H_2O and metal oxides respectively. Reproduced with permission.^[21] Copyright 2023, the authors.

(I) Adsorbate evolving mechanism

AEM is the conventional OER mechanism and the most used to describe OER for an acid or alkaline environment. Depending on the concerned active sites during the process of O_2 formation, two different reaction pathways have been proposed. One is Eley-Rideal (ER) (in heterogeneous system) or water nucleophilic attack (WNA) (in homogeneous system) type AEM concerning a single metal cation active site (*), where OH^- (in alkaline) or H_2O (in acidic) is oxidized to OH^* , O^* , and OOH^* , as shown in Table 1 and Fig. 3a. Another OER mechanism

1. Introduction

is Langmuir–Hinshelwood (LH) (in heterogeneous system) or the interaction of two metal-oxo entities (I2M) (in homogeneous system) type AEM concerning two adjacent metal cation active sites, where two O* intermediates are integrated into O₂, rather than being oxidized to OOH*. The ER-type mechanism has been investigated in Ru-based catalysts, while the LH-type mechanism has been reported for Co-based catalysts.^[20,22] Both ER-type and LH-type pathways assume proton-coupled electron transfer and the formation of O*/OOH* intermediates. The binding energy between the catalyst surface and oxygen intermediates determines the reaction speed and required overpotential, especially in the formation process of OOH* from OH*, which requires the highest overpotential.^[23] Modulation of the binding strength of intermediates on the catalyst surface plays an important role in optimizing its reaction activity.

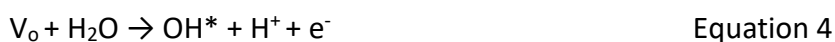
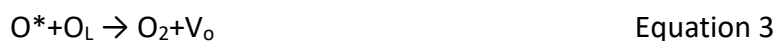
Table 1: OER pathways in acidic and alkaline conditions

Electrolyte	OER pathways	
Acidic condition $2\text{H}_2\text{O} \rightarrow \text{O}_2 + 4\text{H}^+ + 4\text{e}^-$	Single active sites	$\text{H}_2\text{O} + * \rightarrow \text{OH}^* + \text{H}^+ + \text{e}^-$ $\text{OH}^* \rightarrow \text{O}^* + \text{H}^+ + \text{e}^-$ $\text{O}^* + \text{H}_2\text{O} \rightarrow \text{OOH}^* + \text{H}^+ + \text{e}^-$ $\text{OOH}^* \rightarrow \text{O}_2^* + \text{H}^+ + \text{e}^-$ $\text{O}_2^* \rightarrow \text{O}_2 + *$
	Two adjacent active sites	$\text{H}_2\text{O} + * \rightarrow \text{OH}^* + \text{H}^+ + \text{e}^-$ $\text{OH}^* \rightarrow \text{O}^* + \text{H}^+ + \text{e}^-$ $2\text{O}^* \rightarrow 2^* + \text{O}_2$
Alkaline condition $2\text{H}_2\text{O} \rightarrow 4\text{H}^+ + \text{O}_2 + 4\text{e}^-$	Single active sites	$\text{OH}^- + * \rightarrow \text{OH}^* + \text{e}^-$ $\text{OH}^* + \text{OH}^- \rightarrow \text{O}^* + \text{H}_2\text{O} + \text{e}^-$ $\text{O}^* + \text{OH}^- \rightarrow \text{OOH}^* + \text{e}^-$ $\text{OOH}^* + \text{OH}^- \rightarrow \text{O}_2^* + \text{H}_2\text{O} + \text{e}^-$ $\text{O}_2^* \rightarrow \text{O}_2 + *$
	Two adjacent active sites	$\text{OH}^- + * \rightarrow \text{OH}^* + \text{e}^-$ $\text{OH}^* + \text{OH}^- \rightarrow \text{O}^* + \text{H}_2\text{O} + \text{e}^-$ $2\text{O}^* \rightarrow 2^* + \text{O}_2$

In the table, * represents the active site.

(II) Lattice-oxygen participation mechanism (LOM)

Recently, experimental findings showed that some perovskites such as $\text{Pr}_{0.5}\text{Ba}_{0.5}\text{CoO}_{3-\delta}$ (PBC) and $\text{Ba}_{0.5}\text{Sr}_{0.5}\text{Co}_{0.8}\text{Fe}_{0.2}\text{O}_{3-\delta}$ (BSCF) present more active properties for OER, rather than the poor activity for OER as calculated based on AEM.^[24,25] So LOM was proposed to better explain this phenomenon. In the LOM pathway, lattice O^{2-} anions of catalysts directly participate in oxygen evolution and the formation of oxygen molecules, as shown in Fig. 2b. In a typical LOM, the first two steps concerning the formation of *O are the same as those in AEM. Then, the formed *O couples with the lattice O^{2-} to release an oxygen molecule, Meanwhile, an oxygen vacancy V_O is left in the lattice. In the end, the vacancy will be refilled by the migration of OH^- from the dissociation of water. The acidic LOM can be concluded as follows:



Because the formation of OOH* from O* is not involved in LOM, the barrier in the formation of OOH* from O* is broken, and a lower overpotential compared to AEM can be achieved. LOM gives a better explanation for the excellent catalytic properties of PBC and BSCF. In addition, LOM still includes the formation of O* , so the Sabatier principle can be applied as well.

1.1.3 Electrochemical oxygen reduction reaction

The oxygen reduction reaction is the reverse reaction of the oxygen evolution reaction and plays an important role in fuel cells and metal-air batteries. In an acid condition, the two main final products, H_2O (Fig. 3 and eq. 6 and 7) and H_2O_2 (Fig. 3 and eq. 8) are generated by a direct four-electron pathway, and an indirect two-electron pathway, respectively.^[26] Notably, the 2-electron transfer process is preferred in industrial H_2O_2 production while the 4-electron transfer pathway is more desired in FCs and other energy conversion technologies, and their

1. Introduction

mechanisms are more complicated. So, we will focus more on the 4-electron transfers in this thesis.

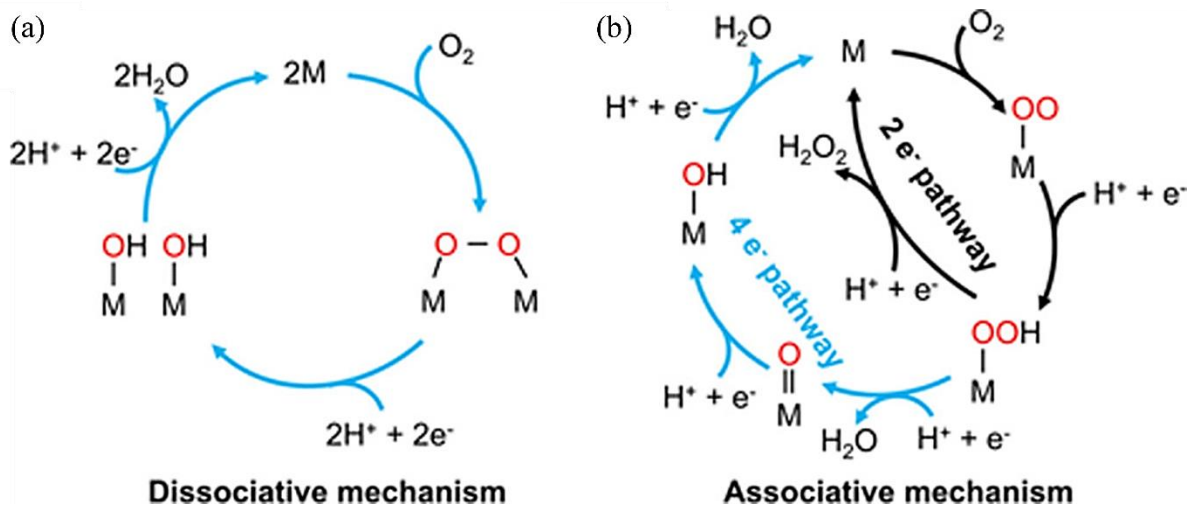
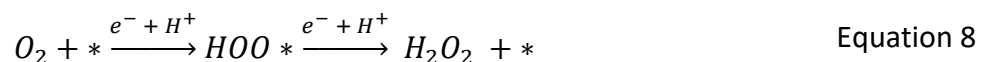
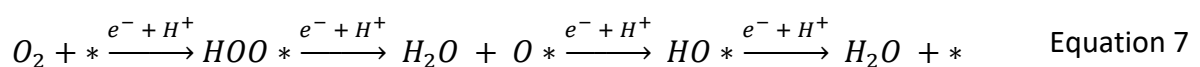
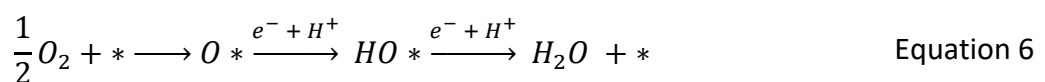


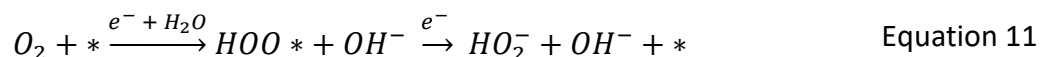
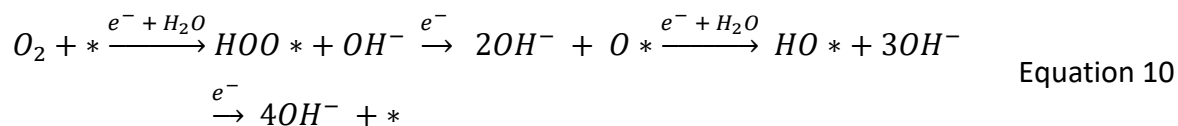
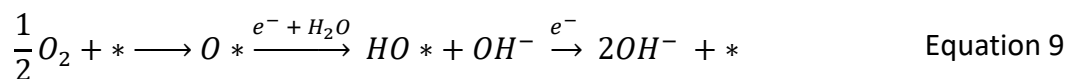
Fig. 3 ORR catalytic cycle following dissociative (a) and associative mechanisms (b).

Reproduced with permission. ^[27] Copyright 2022, American Chemical Society.

Generally, the 4-electron transfer process can follow either a dissociative or an associative pathway, depending on the oxygen adsorption mode (an O_2 molecule adsorbed by two adjacent active sites or by a single active site), and the binding strength of oxygen to the active sites.^[26,28] For the dissociative mechanism, the oxygen molecule is adsorbed by two adjacent active sites, followed by the dissociation of the bridging oxygen configuration. Then the two oxygen atoms ($2O^*$) are coupled with a proton to form an intermediate (HO^*), which is further reduced to H_2O (eq. 6). Typically, this dissociative pathway occurs on the surface of noble-metal-based catalysts attributable to the strong σ bonding interactions with O_2 . In contrast, the associative pathway starts with one proton-coupled electron transfer and the formation of a HOO^* intermediate. Next, HOO^* intermediate can be converted into H_2O_2 in a two-electron transfer pathway or undergoes two further proton-coupled electron transfer process to generate H_2O .^[28] The reaction can be summarized as follows:



Under alkaline conditions, the products would be OH^- in 4-electron transfer and HO_2^- in 2-electron transfer pathway. The reaction can be summarized as follows:



The oxygen-containing intermediates, like $\text{O} *$ and $\text{HO} *$, are involved in both the dissociative and associative mechanism. Similar to the OER mechanism, it is reasonable to regard oxygen adsorption energy (ΔE_o) as a descriptor for ORR activities. According to the Sabatier principle, the optimal catalyst for ORR should bind oxygen neither too strongly nor too weakly.^[29,30] Specifically, the oxygen adsorption (the formation of $\text{O}_2 *$ in associative mechanism) or the dissociation of O-O bound to generate $\text{O} *$ (dissociative mechanism) will be hindered in case of too weak interaction and in another case of too strong interaction, which results in difficult removal of intermediates ($\text{O} *$ and $\text{HO} *$).

1.2 Performance analysis of the electrochemical oxygen

evolution/reduction

Numerous catalysts and electrodes have been synthesized to gain satisfying electrochemical performance. To comprehensively evaluate the catalytic activities of the catalysts or electrodes, a standard measurement protocol is of fundamental importance, i.e., onset potential, current density (j), Tafel slope, electrochemical surface area (ECSA), and Faradaic efficiency (FE).

1.2.1 Rotating-ring disk electrode technique

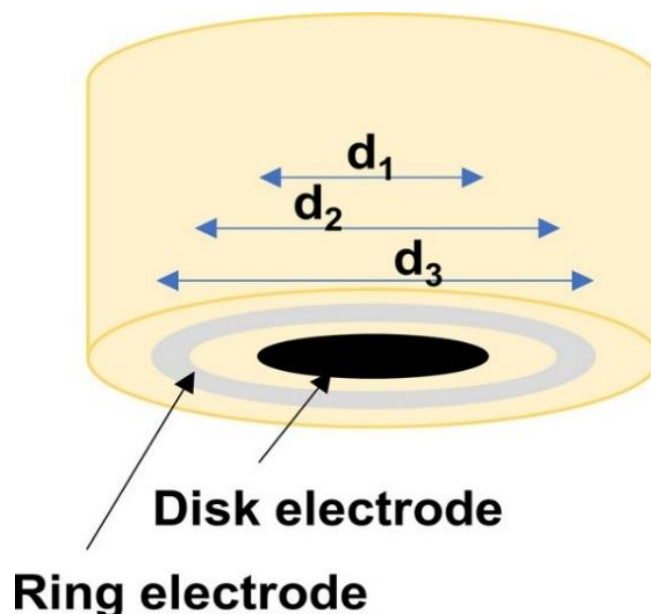


Fig. 4 Schematic representation of the RRDE. Reproduced with permission. ^[27] Copyright 2022, American Chemical Society.

To effectively perform electrochemical measurement and gain the insight of reaction kinetics and mechanism, rotating-ring disk electrode (RRDE) and rotating disk electrode (RDE) are widely used as the powerful setup to assess the electrochemical behavior in both OER and ORR. A standard RRDE consists of a conductive disk electrode (made of glassy carbon, Pt, Au, etc.) and a concentric ring electrode (made of Pt, Au, glassy carbon, etc.), as shown in Fig. 4. The desired potentials on ring and disk can be applied individually. Notably, only disk electrode exists in RDE setup. In both RDE and RRDE, the rotating speed of the electrode can be controlled by the configuration, leading to well-defined laminar flow profiles across the electrode surface that enables quantitative analysis of reaction kinetic rate constant without interference from mass transport. For example, the kinetic current can be gained after voltametric measurements using an RDE with a certain rotating speed. We will explain this point in detail in 1.2.5. Moreover, in the RRDE setup, when the electrode rotates, the product formed at the disk electrode is transported to the ring electrode, where it can be converted to another species by applying a second potential. For this reason, RRDEs are operated using bipotentiostats where individual potential can be set for the disk electrode and the ring

electrode. Based on this approach, the electron transfer number and faradaic efficiency can be effectively measured with the assistance of RRDE. We will explain this point in detail in 1.2.

1.2.2 Current density and overpotential

The thermodynamic redox potential for O_2/OH^- or O_2/H_2O at 1 atm and 298 K is 1.23 V - 0.0591 pH vs. reversible hydrogen electrode (RHE). In practice, OER requires a higher potential, while ORR requires a lower potential due to the existence of energetic and kinetic barriers.^[31,32] The required additional potential is known as overpotential (η). In OER, overpotentials at different current densities (j_{10}, j_{50}, j_{100}) are commonly used to compare the catalytic performance of different catalysts, which can be acquired by linear sweep voltammetry (LSV). A lower η is preferred as it indicates less energy is required to achieve higher current density and faster reaction kinetics. Note that, the current density (j) is also normalized to the geometric surface area of the electrode, or, more rarely, to the ECSA.

1.2.3 Tafel slope

Tafel slope describes the relationship between the j and η , which originates from the classic Butler - Volmer equation (eq. 12, cathodic polarization) below:

$$j = j_0 \left[\exp \left(\frac{\alpha z F}{RT} \eta \right) - \exp \left(- \frac{(1-\alpha) z F}{RT} \eta \right) \right] \quad \text{Equation 12}$$

Where j is the electrode current density ($A \cdot m^{-2}$), j_0 is exchange current density ($A \cdot m^{-2}$), α is so-called transfer coefficient, z is the number of electrons involved in the electrode reaction, η is overpotential (V), F is the Faraday constant, R is universal gas constant, and T is absolute temperature (K). The reaction j is controlled by forward and backward sub-reactions. When in strong polarization region, where η is very high and meets $\exp \left(\frac{\alpha z F}{RT} \eta \right) \gg \exp \left(- \frac{(1-\alpha) z F}{RT} \eta \right)$, the backward reaction is negligible, and the first term dominates. Then the Butler - Volmer equation can be explained as Tafel equation:

$$\eta = - \frac{2.3RT}{\alpha z F} \text{Log } j_0 + \frac{2.3RT}{\alpha z F} \text{Log } j \quad \text{Equation 13}$$

The above equation can be simplified as:

$$\eta = a \log j + b \quad \text{Equation 14}$$

Where the constants of a and b represent $-\frac{2.3RT}{\alpha zF}$ and $\frac{2.3RT}{\alpha zF} \log j_0$ respectively. Meanwhile, b is known as Tafel slope, the value of which is an indicator of reaction kinetics. A smaller Tafel slope indicates a smaller overpotential is required to achieve the targeted current density. Tafel slope can be obtained by electrochemical impedance spectroscopy (EIS) data and voltammetry measurement. Notably, the contributions from catalysts and electrode are also included in voltammetry and the EIS gives purely charge transfer kinetics.

1.2.4 Electrochemically active surface area

In the heterogeneous electrochemical reaction system, ECSA plays an important role in normalizing the current density and revealing the real electrocatalytic activities. Specifically, ECSA refers to the area of the catalyst that is accessible to the electrolyte and works for charge transfer and/or storage. When the catalysts or electrodes contact with electrolyte, electrical double-layer capacitance (C_{dl}) appears at the interface between electrode and electrolyte. Meanwhile, the ECSA is proportional to C_{dl} , which in sequence can be measured by cyclic voltammograms (CVs) in non-Faradaic regions.^[33] The ECSAs exhibits more accurate information on active surface area compared to classic geometrical surface area.^[34] In detail, as shown in eq. 15 and 16, C_{dl} is related to non-Faradaic current and voltage scan rate. On this basis, C_{dl} can be measured via CVs in the redox-free potential range with different scan rates. Finally, the ECSAs can be obtained based on the C_{dl} and the specific capacitance (C_s). Notably, the C_s is related to the nature of the materials and reaction environment.

$$C_{dl} = \frac{dQ}{dE} = \frac{j dt}{dE} = j \frac{dt}{dE} = j \cdot v \quad \text{Equation 15}$$

$$ECSA = \frac{C_{dl}}{C_s} \quad \text{Equation 16}$$

Where Q is the electrical charge, E is the potential, t is time, v is potential scan rate, C_s is specific capacitance of the catalyst, j is the current density. Amongst, j is positive and negative in case of charging (positive scan, j_p) and discharging (negative scan, j_n) process which are

supposed to share same absolute value in an ideal faradaic region. In practical, the half current density difference ($j_p - j_n$) is adopted to calculate C_{dl} .

1.2.5 Electron transfer number and Faradaic efficiency

For multi-electron transfer reactions, various products would be generated with different electron transfer numbers. Specifically, in cases of OER and ORR, possible two-electron and four-electron pathways can occur simultaneously. It is vital to calculate the electron transfer number to have a deeper understanding of reaction pathway. Conventionally, two experimental methods are widely used to determine electron transfer number: RRDE method and the Koutecky–Levich (KL, eq.17-19) method, where j_k is the catalytic current density without the loss caused by mass transfer, j is the apparent current density (extracted from the LSV curve under different applied potentials) and j_L is the diffusion-limited current density (the highest current density under relatively negative potentials). According to eq.18, j_k is determined by electron transfer number (n), the faradic constant (F), the diffusion coefficient of O_2 (D_0), the kinetic viscosity of the solution (C_0), and the RDE rotation speed (ν). However, in practice, KL method shows poor accuracy to determine n , as the KL plots are often not linear and the calculated n_{KL} sometimes exceed theoretical limits.^[35] The electron transfer number calculated with assistance of RRDE technique follows the equation (eq. 20). In detail, a chronoamperometry (CA) of the disk electrode is recorded at a constant ring potential (1.5 V vs. RHE), which allows possible HO_2^- intermediate being oxidized. Meanwhile, a suitable rotation rate (mostly at 1600 rpm) and scan rate are adopted in the O_2 saturated condition to prevent mass transfer limitations. Similarly, the H_2O_2 ratio can be calculated by eq.21.

$$\frac{1}{j} = \frac{1}{j_K} + \frac{1}{j_L} = \frac{1}{B\omega^{1/2}} + \frac{1}{j_L} \quad \text{Equation 17}$$

$$B = 0.62nFC_0D_0^{2/3}\nu^{-1/6} \quad \text{Equation 18}$$

$$j_K = nFkC_0 \quad \text{Equation 19}$$

$$n = \frac{4I_d}{I_d + I_r/N} \quad \text{Equation 20}$$

$$\% (HO_2^-) = \frac{2I_r/N}{I_d + I_r/N} \quad \text{Equation 21}$$

Where n is the electron transfer number, I_d and I_r are the current on disk and Pt ring, respectively, N is the collection efficiency.

Faradaic efficiency (FE) is another parameter to determine utilization efficiency of electrons supplied from external circuit. Specifically, it describes the overall selectivity of an electrochemical process, defined as the ratio of the amount of product formed (in moles) to the amount of product that can be produced by the total charge passed, expressed as a fraction or percentage.^[36] In the case of OER, O_2 production can be detected by gas chromatography, Clark electrode or optical fluorescence oxygen sensing probe. Additionally, FE can also be measured with the assistance of an RRDE setup. Generally, a relatively small constant current is applied on the disk electrode, and a potential at 0.4 V vs. RHE is applied on the ring electrode to reduce generated O_2 from the disk in an Ar/ N_2 condition. Notably, the current applied on the disk should be at an appropriate value ($\sim 1 \text{ mA}\cdot\text{cm}^{-2}$) to ensure a suitable O_2 generation, which can be sufficiently transferred to the ring electrode and simultaneously to avoid local saturation and bubble formation at the disk electrode. On this basis, FE can be calculated as follows,

$$FE = \frac{I_r}{NI_d} \quad \text{Equation 22}$$

1.2.6 Electrochemical impedance spectroscopy

In a typical electrochemical reaction system, charge transfer, mass transfer from the bulk electrolyte to the catalyst surface, and the resistance of the electrolyte result in the impedance. To have a better understanding of the above-mentioned features, scientists interpreted them into the equivalent electrical circuits, including resistances, capacitors, or constant phase elements which are connected in parallel or series. Similar with the normal electrical circuit, the impedance follows Ohm's law as well. Practically, a small amplitude alternating current (AC) signal excitation is applied when the electrochemical cell is in equilibrium (open circuit state) or under a stable direct current (DC) polarization condition. Notably, in the EIS measurement, the response signal must be caused by the input excitation

signal. Meanwhile, input and output signals meet a linear relationship (Ohm's law). In addition, the excitation does not cause changes in the internal structure of the system, and the system can return to its original state when the disturbance stops. The impedance expression can be presented by Nyquist Plot and Bode Plot. In the Nyquist Plot, the real part (Z_{re}) and imaginary part (Z_{im}) are plotted on the X-axis and Y-axis respectively. In this case, each point is an impedance value at the respective frequency. In contrast, two separate logarithmic plots exist in the Bode plot: magnitude vs. frequency and phase vs. frequency, which are commonly used in the engineering community.^[37]

We take charge-transfer and diffusion processes controlled electrochemical reaction as an example, the equivalent circuit is shown in Fig. 5.

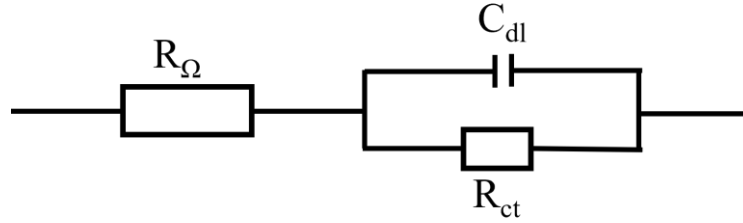


Fig. 5 Equivalent circuit of charge-transfer and diffusion processes controlled electrochemical reaction.^[38] R_{Ω} , R_{ct} , and C_{dl} , represent the solution resistance, charge transfer resistance, and double layer capacitance, respectively.

Meanwhile, the impedance can be described by the eq. 23-25. When ω is high enough, $\omega^{-1/2}$ is negligible, charge-transfer is the reaction rate determining step and Nyquist Plot is a semi-circle and the diameter is charge-transfer resistance (R_{ct}) (eq. 26). In the case of the small ω (eq. 27), Nyquist Plot is a straight line with the slope of 1. It indicates the reaction rate is determined by a mass diffusion process. On this basis, we can get more information on charge transfer and mass transfer with the assistance of EIS measurement.

$$Z = R_{\Omega} + \frac{1}{j\omega C_d + \frac{1}{R_{ct} + \sigma\omega^{-1/2}(1-j)}} \quad \text{Equation 23}$$

$$Z_{Re} = R_{\Omega} + \frac{R_{ct} + \sigma\omega^{-1/2}}{(\sigma\omega^{1/2}C_d + 1)^2 + \omega^2 C_d^2 (R_{ct} + \sigma\omega^{-1/2})^2} \quad \text{Equation 24}$$

$$Z_{Im} = R_{\Omega} + \frac{\omega C_d (R_{ct} + \sigma \omega^{-1/2})^2 + \sigma \omega^{-1/2} (\sigma \omega^{1/2} C_d + 1)}{(\sigma \omega^{1/2} C_d + 1)^2 + \omega^2 C_d^2 (R_{ct} + \sigma \omega^{-1/2})^2} \quad \text{Equation 25}$$

$$Z = R_{\Omega} + \frac{1}{j\omega C_d + \frac{1}{R_{ct}}} \quad \text{Equation 26}$$

$$Z_{Im} = Z_{Re} - R_{\Omega} - R_{ct} + 2\sigma^2 C_d \quad \text{Equation 27}$$

1.2.7 Stability

Apart from the electroactivity of the catalyst, stability is another significant parameter to be considered for industrial applications. The stability can be tested by CA, chronopotentiometry (CP), and accelerated durability test (ADT). Specifically, CA and CP work at a fixed potential or current for a long time, while recording the obtained current or required potential. LSV before and after CA and CP can also be studied to compare the electrical activity changes. ADT is carried out at an accelerated scan rate in a short period compared to CA and CP. Normally, CV cycling is performed at a suitable potential range (1.2-1.8 V vs. RHE for OER; 1.1-0.3 V vs. RHE for ORR) at a scan rate of 0.1 V/s for thousands of cycles. As a result, the LSV curves pre- and post-ADT can be compared and a durable catalyst is supposed to show nearly identical performance.

1.2.8 d-band center

d-band center is one of the most successful descriptors in heterogeneous and electrocatalysis, which was proposed by Norskov in 1995.^[39] Briefly, Norskov found that the adsorption energy was highly linearly correlated with the energy center of the valence d-band density of states (d-band center). The energy level of the d-band center determines the ease of filling the antibonding energy band with electrons and thus the stability and strength of the adsorption bonding. On this basis, the calculation of a catalyst can be used to predict the catalytic properties. In practice, d-band center theory successfully predicted the outstanding catalytic activities, like Pt₃Ni for ORR and MoS₂ for HER. Besides, it gives the instructions for the catalyst design as well, including coordination number modulation to increase d-band center value, which will be discussed in detail in the following chapter.

1.3 Noble-metal-based catalysts for electrochemical oxygen evolution/reduction reactions

Developing efficient low-cost, and highly durable catalysts for OER and ORR plays a vital role in oxygen energy transfer and storage. However, the state-of-the-art catalysts are still noble metal based, like the IrO_2 and RuO_2 for OER, and Pt and Pd for ORR. These noble metals or noble metal oxides are regarded as the benchmark catalysts, which are usually compared with the newly synthesized catalysts. At the same time, noble metal catalysts play an important role in understanding the reaction mechanism. Additionally, many researchers are also putting more effort into new noble metal-based catalysts with reduced metal usage, e.g., alloys. The target is not only to develop more active catalysts but also to better understand the reaction mechanism and provide the guidelines for the next-generation noble metal-free catalysts design.

1.3.1 IrO_2 and RuO_2 based catalysts for OER

IrO_2 and RuO_2 are the benchmark catalysts in OER and investigated deeply to gain an insight of OER mechanisms. Casalongue et al. found that the oxidation state of Ir undergoes a change from 4+ to 5+ with the assistance of in-situ X-ray photoelectron spectroscopy (XPS, Fig. 6a).^[40] Especially, the oxidation process is dominant on the surface of the catalyst. Based on the observed experimental evidence, they proposed an OOH^- mediated deprotonation mechanism. Additionally, Pfeifer et al. found that Ir^{3+} intermediates formed during OER, which are confirmed experimentally by application of synchrotron based XPS and X-ray absorption spectroscopies (XAS).^[41] Based on this finding, they proposed iridium vacancy model, which concerned O^- formation during the OER reaction, as shown in Fig.6b. Moreover, Kasian et. al proposed three different dissolution mechanisms depending on the potential applied on anode (Fig. 6c), including direct dissolution of Ir metal (blue arrow), the transition from Ir^{5+} to Ir^{3+} (green arrow), and formation of IrO_3 at high potentials (red arrow).^[42] These reaction pathways can be summarized by forementioned AEM, which are not involved the lattice oxygen in the catalysts. Not only AEM, but also LOM are verified by IrO_2 . The isotope labelling method was used to detect lattice oxygen participation during OER by Simon Geiger and his colleagues.^[43] They labelled Ir^{18}O_2 and Ir^{18}O_x films, which were polarized galvanostatically in the H_2^{16}O -based electrolyte. The produced O_2 species with mass-to-charge ratios of 32

1. Introduction

($^{16}\text{O}^{16}\text{O}$), 34 ($^{16}\text{O}^{18}\text{O}$) and 36 ($^{18}\text{O}^{18}\text{O}$) were measured. They found the active lattice oxygen in amorphous iridium oxide can participate in the OER and boost catalytic activities.

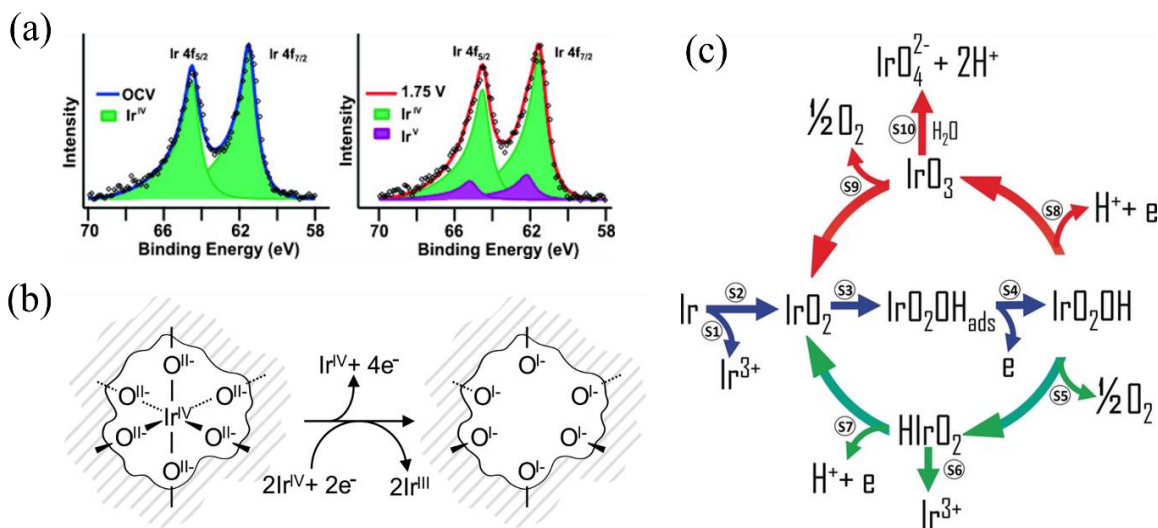


Fig. 6 (a) Curve-fitted Ir 4f XPS spectra of Iridium (+4) oxide nanoparticles under open circuit conditions (left) and under oxygen evolution conditions (right), the green and purple components correspond to Ir⁴⁺ and Ir⁵⁺, respectively. Reproduced with permission.^[40] Copyright 2014, WILEY-VCH Verlag GmbH & Co. KGaA, Weinheim. (b) Oxidation state transition of Ir from +4 to +3. Reproduced with permission.^[41] Copyright 2016 Royal Society of Chemistry (c) Three possible pathways of Ir dissolution during the OER. Reproduced with permission. Copyright 2018, The Authors. Published by Wiley-VCH Verlag GmbH & Co. KGaA.

Apart from the OER mechanism understanding, researchers are also putting more focus on minimizing the usage of noble metals by composition and structure optimization. Based on the understanding of OER reaction mechanism, rationally introducing heteroatom into noble metal systems can improve catalytic activities because of the modification of the electronic structure and synergistic effect.^[44] The heteroatoms are normally transition metals which can help with reducing the usage of noble metals as well. For example, Yahui Wang et. al successfully doped Ce into IrO₂ nanoparticles, which modified the electronic structure of IrO₂ and decreased the energy barrier of the transition from *O to *OOH, which is rate-determining step (RDS) in OER.^[45] The catalyst they synthesized achieved very low overpotential ($\eta_{10} = 24 \text{ mV}$) at $10 \text{ mA}\cdot\text{cm}^{-2}$, while 380 mV is needed for IrO₂. Meanwhile, the

Ir normalized mass activity also indicates the Ce doping can largely reduce the usage of Ir. In addition to single metal doping, poly metals doping is also applied for IrO₂ based OER electrocatalysts. In this regard, Zaman et. al successfully co-doped Co and Ni into IrO₂ and atomically substituted 50% usage of Ir.^[46] Furthermore, the Ni-Co co-doped IrO₂ shows lower overpotential than the individually doping cobalt and nickel catalysts. Based on this observation, many other heteroatoms have been adopted to substitute noble metals, including Cu,^[47] F,^[48] B,^[49] and Nb.^[49]

Additionally, morphology modification is adopted as well by researchers to expose more active sites with less noble metal usage. Noble metal-based materials from 1 dimensional (1D) to 3D are widely investigated. 1D noble metal-based materials are referred to the single noble metal atom containing materials. Ru and Ir single atoms are successfully immobilized into different substrates. Gu group has synthesized Ir single atoms modified NiO^[50] and amorphous CoO^[51] catalysts, in which the weight ratios of Ir are only 18% and 14.8% respectively. Meanwhile, the catalysts exhibit very high catalytic activities. The density functional theory (DFT) calculations reveal that the immobilized Ir single atoms can not only work as the active sites, but also modulate the electronic structure of neighbor metal atoms (Ni and Co), which further increase adsorption free energies of OH⁻ and intermediates (*OH and *O) and leads to the dramatically improved OER activity. Similarly, other noble metal single atoms, like Ru, Pt, and Au, are synthesized with different substrate, including metal alloys,^[52] carbon,^[53,54] metal carbides,^[55] metal oxides,^[56] and layered double hydroxides (LDH)^[57]. All the noble metal single atoms show improved catalytic activities. However, the number of single atoms is limited by the number of defects, which are used to fix the single atoms. Besides, during the long-term catalytic process, the atomically dispersed single atoms tend to aggregate and form the clusters, resulting in the degradation of the catalytic performance, especially in a high loading of single atoms. Because of this phenomenon, Rational design single atoms-based catalysts without single atoms aggregation is considered as the current research challenge.

The design of 2D noble metal-based materials is another option to achieve its cost-effectiveness. The idea is using surfactants to control the growth direction of the crystalline and form ultra-thin materials. On this basis, a certain facet of the crystalline can be tuned. For example, the (001) planes for Ru^[58] nanosheet and (111) and (200) planes for Ir^[59] can be prepared. The DFT calculations indicate these facets are more active toward reducing the

1. Introduction

energy barriers of the RDS in OER process, which can explain the greatly improved catalytic properties compared to pristine RuO₂ and IrO₂. Meanwhile, the electronic structures of noble metal nanosheets can be tuned by some defect-inducing method and other metal doping methods^[60]. Compared to the single atom catalysts, 2D noble metal-based materials are more stable as fewer aggregation is observed during OER. The bottleneck of the design of this kind of material is the choice of suitable surfactants. Some surfactants would be adhesive to the synthesized nanosheets, as the result, the active sites would be blocked and decrease the usage efficiency of noble metals. Recently, the metal carbonyl assisted synthesized method appeared, which allows slow CO emission.^[61] Meanwhile, CO can help control the crystalline expand dimension. This method is mainly used in the design of ORR catalyst, which will be discussed in the following part.

Finally, 3D noble metal-based materials are very popular in cost-effective noble metal-based catalysts design. The guideline is to synthesize porous, core-shell, or hollow structured nanoparticles with a small size to increase the surface area and expose more active sites. Compared to 1D single atoms, 3D nanoparticles can provide higher surface area and more active sites, which can also be deposited on a proper substrate. Meanwhile, the synthesis method is more facile compared to 1D and 2D. In a typical hollow structure synthesis method, the precursor noble metal-based nanoparticles are firstly synthesized and then are etched by acid to gain the porous structure. For example, Shaojun Guo group has prepared a class of IrM (M = Co, Ni, CoNi) multi-metallic porous hollow nanocrystals by using a Lewis acid.^[62] The noble metal containing metal organic frameworks (MOFs) are usually used as the precursor, which go through further pyrolysis or other treatment to gain small size of nanoparticles or porous structures heritage from the pristine MOF. For example, Wenrui Li et. al. prepared the IrO_x clusters supported on porous CeO₂ by the calcination of Ir containing MOF. The catalyst possesses micropores centered at approximately 1.2 nm as well as mesopores around 3.4 nm, which potentially provided more active sites for OER.

In conclusion, all the catalyst designs (from 1D to 3D) show both advantages and disadvantages. More efforts are still needed to develop more effective, stable, and cost-effective catalysts. The research focuses could vary from the improvement of the stability of the of 1D single atoms catalysts to decreasing the noble metals usage in 3D catalysts.

1.3.2 Pt and Pd based catalysts for ORR

Furthermore, Pt and Pd also show high catalytic activities towards ORR compared to other metals due to their appropriate binding energy between the bulk metals surface and O/OH adsorbates, as shown in Fig.7.^[63] To this end, many efforts have been put on the development of Pt and Pd based ORR catalysts. It is same with other noble metals catalyst, the target is to reduce the usage the Pd and Pt, and at the same time, improve their activities. In the case of pure Pt and Pd catalysts, surface facet, shape, and size engineering play an important role in improving their catalytic activities. Various Pt/Pd catalysts with different structures and surface facets have been widely prepared. Notably, the ORR catalytic performance of different Pt facets varies in different electrolytes. For example, in a catalytic solution containing coordinating anions (such as H₂SO₄ solution), ORR activity follows the order Pt (111) < Pt (100), as the strong adsorption of anions (SO₄²⁻) deactivate the Pt (111) surface dramatically and decrease the catalytic reactivity. However, in the presence of weakly coordinating anions such as ClO₄ and OH⁻, ORR activity follows the order Pt (100) << Pt (110) ≈ Pt (111).^[64] This means Pt-based catalyst with a cubic crystal with (100) facet in dominant would be more active for ORR in H₂SO₄ and those with an octahedral (or tetrahedral, or icosahedral) structure with (111) and (110) facets in dominant would be ideal catalysts for ORR in HClO₄ and KOH solutions.

In the following discussion, we mainly focus on the Pt (111), as HClO₄ and KOH solutions are the most widely used electrolytes in the ORR electrocatalysis. Meanwhile, it was found that the ORR activities were highly dependent on dense surface steps, edges, and kinks on high-index facets of bulk nanoparticles.^[65] The guidelines for the development of more active pure Pt catalysts are to design a stepped surface with high index facets instead of a smooth (111) surface. On this basis, defect engineering is applied to introduce surface steps, edges, kinks, and low-coordinated atoms. For example, defect rich porous Pd nanosheets were synthesized recently.^[66] The materials possess abundant highly active sites because of the existence of abundant pore structures and strain effect, which further contribute to the tunable electronic structure. At the same time, Guo and co-workers prepared different types of defects on Pd nanosheets.^[67] Compared to edge and pore defects, concave surface defects have shown the highest ORR activity, due to the increased coordination number at the metal sites, and moderately downshifted d-band center.

1. Introduction

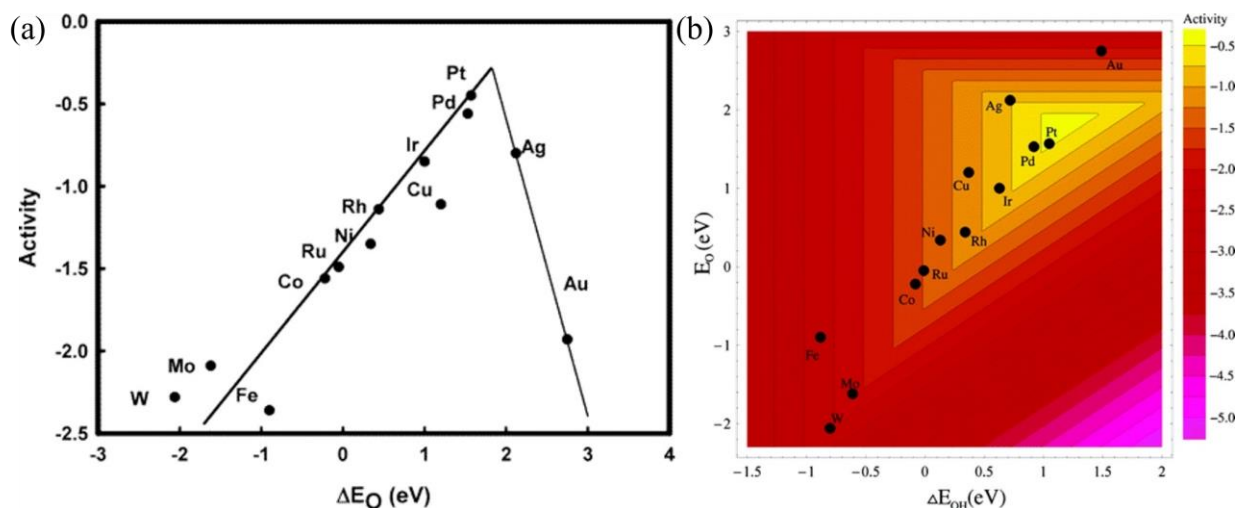


Fig. 7 Trends in oxygen reduction activity plotted as a function of the O atom binding energy (a), and both the O and OH binding energy (b). Reproduced with permission.^[63] Copyright 2004, American Chemical Society.

Apart from facet control, size control of the nanoparticles is also important for the catalytic performance improvement. However, the Pt particle size effect on ORR is still not well understood and a focus of current research. Shoemaker and coworkers prepared Pt nanoparticles with different sizes (from 1 to 5 nm) and tested their specific activities (SA) and mass activities (MA).^[68] They found that the SA increased sharply by around 4-fold as the particles grow from 1.3 nm to 2.2 nm and then slowly as particle size further increased. However, the MA reached the maximum (by 2-fold) as the particles grew from 1.3 nm to 2.2 nm and then decreased as particle size further increased (Fig. 8a). Similarly, Chorkendorff and colleagues also observed the same results with the Pt particle size from 2 to around 11 nm. The maximum of MA was located at 3 nm.^[69] The explanation given by Shoemaker and colleagues is that with the particle size decreasing from 5 to 1 nm, the number of (111) and (100) terrace sites decreased rapidly, and low coordination number edges dominated the surfaces, which results in the overly strong binding between Pt surfaces and O_2 . Note that alternative explanations have also been put forward: some researchers argued that the SA did not depend on the particle size, even in the range of 1 to 5 nm. As shown in Fig. 8b, Nesselberger et al. found that carbon supported Pt particles with different sizes (from 1 to 5 nm) showed comparable SA. At same time, MA increased linearly with increasing Pt nanoparticles dispersion.^[70] They proposed the catalytic activities are related to the interparticle distance. The decreased interparticle distance leads to the overlap of the electric

double layers between neighboring particles, resulting in a potential drop within the compact layer and leading to weaker adsorption energy on Pt surfaces, which is referred to as a proximity effect. Additionally, when the size of Pt nanoparticles is below 1 nm, some interesting trend occurs. It was found that Pt₁₂ showed higher activity by a factor of 10 compared with 2.5 nm Pt/C. However, if one Pt atom was added into Pt₁₂, which changed to Pt₁₃, the catalytic activities decreased by a factor of 2. Pt₁₇ and Pt₁₉ are more active than Pt₁₃ again. That is because Pt₁₃ possesses icosahedral structure, which shows much higher binding energy, resulting the poor activity. But with more Pt atom being added on icosahedral core, edge structure appeared and improved the catalytic activities of Pt₁₇ and Pt₁₉.^[71]

Different opinions and ideas were proposed based on recently discovered interesting and amazing phenomena. However, the relationship between the ORR activity and the shape/size of nanoparticles is not well established. Moreover, Angelopoulos et al. used voltametric Bi and Ge oxidation method to quantify the amount of charge associated with (111) terraces and (100) terraces, and further observed the relationship between electrocatalytic reactivities and amount of exposed different facets. with the assistance of Bi and Ge specific adsorption technique, Angelopoulos et al. proposed the predominant active sites on Pt nanoparticles were (110) and (311) rather (111) terrace atoms, which were historically recognized as main active sites for ORR.^[72] More efforts need to be made to fully understand the size and shape effects on ORR.

1. Introduction

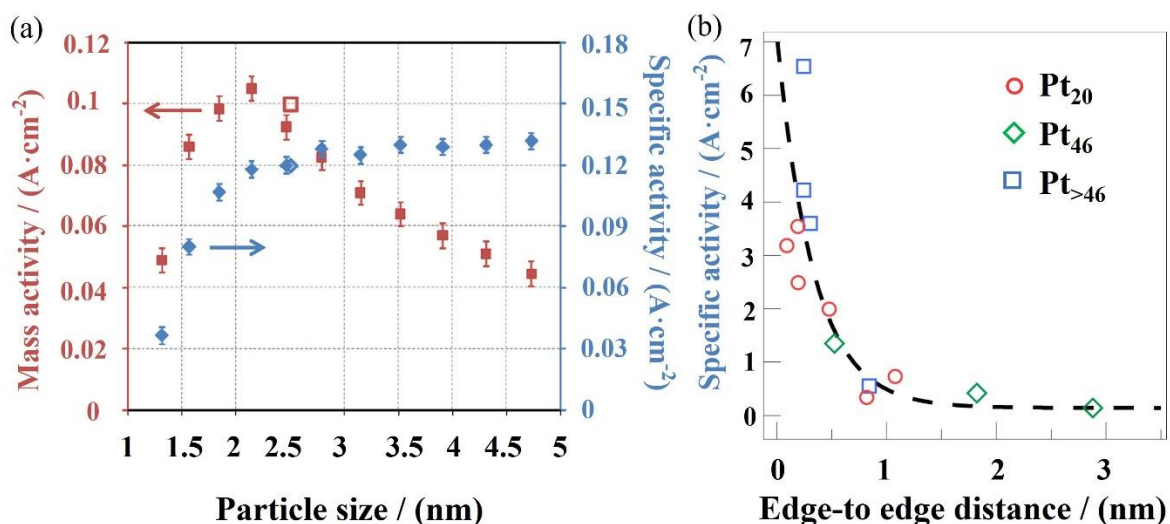


Fig. 8 a) MAs and SAs of Pt/C for oxygen reduction reaction at 0.93 V with different particle sizes, b) SAs of the ORR determined at 0.85 V RHE in rotating disk electrode measurements of Pt nanoclusters deposited onto a glassy carbon electrode. Reproduced with permission.^[68,70] Copyright 2011, American Chemical Society. Copyright 2013, Springer Nature Limited.

Aside from tuning the size and surface facets of nanoparticles, Pt and Pd alloying with transition metals can effectively enhance the ORR activities and stabilities. In the case of Pt, various Pt alloying transition metals (PtM) have been widely investigated and reported, including Co,^[73–76] Ni,^[75–77] Fe,^[76,78,79] Cu,^[75,77] Ag,^[77,80] Au,^[77,80] Pd,^[78,80] Cr,^[81] Mo,^[82] Mn,^[83] V^[76] etc. Amongst all the transition metals, Co, Ni, and Fe exhibit superior properties and have led to more intensive studies. Stamenkovic et al. combined simulations with experiments and established the electrocatalytic trends on Pt₃M.^[76] The trend followed the order of Pt < Pt₃Ti < Pt₃V < Pt₃Ni < Pt₃Fe ≈ Pt₃Co. However, the Pt alloys have been observed to decrease as a function of voltage cycling in PEMFC operation conditions.^[84,85] Han et al. pointed out that the stability of Pt alloys are related to the dissolution potentials of the alloying elements. As shown in Fig. 9c, PtCo and PtFe alloys possess very low dissolution potentials and are easier to dissolve during the catalytic reaction. As a result, the alloys surface would become pure Pt due to the dissolution of Co and Fe, resulting in the degradation of properties. Meanwhile, Vojislav R. Stamenkovic et al. also designed a Pt-skin and -skeleton structure by thermal annealing at around 1000 K.^[76] During the thermal annealing process, Pt atoms segregated to the surface and doped transition metal atoms moved to the sublayers, leading the formation

of Pt-skin. The catalytic activities of bulk Pt, Pt-skeleton, and Pt-skin surfaces followed the order of Pt < Pt-skeleton < Pt-skin. Meanwhile, the annealed Pt-skin surface was very stable under electrochemical environment. Similarly, transition metal doping Pd nanosheet also exhibited higher catalytic properties than the pure Pd nanosheet. For example, Shaoda Huang et al. and Mingchuan Luo et al. have prepared Fe and Mo dopant respectively, both of which exhibited improved catalytic properties.^[86,87] Not only the binary Pt alloys, ternary and quaternary Pt Alloys have also been synthesized and evaluated by different groups. Because of the synergetic effects in different transition metals and Pt, the catalytic activities and stabilities could be further improved on base of binary Pt alloys.^[88,89] Meanwhile, apart from the thermal annealing, other methods to improve the stability of Pt/Pd are under development as well, such as nonmetallic elements (C,^[90] H,^[91] and B^[92]) doping.

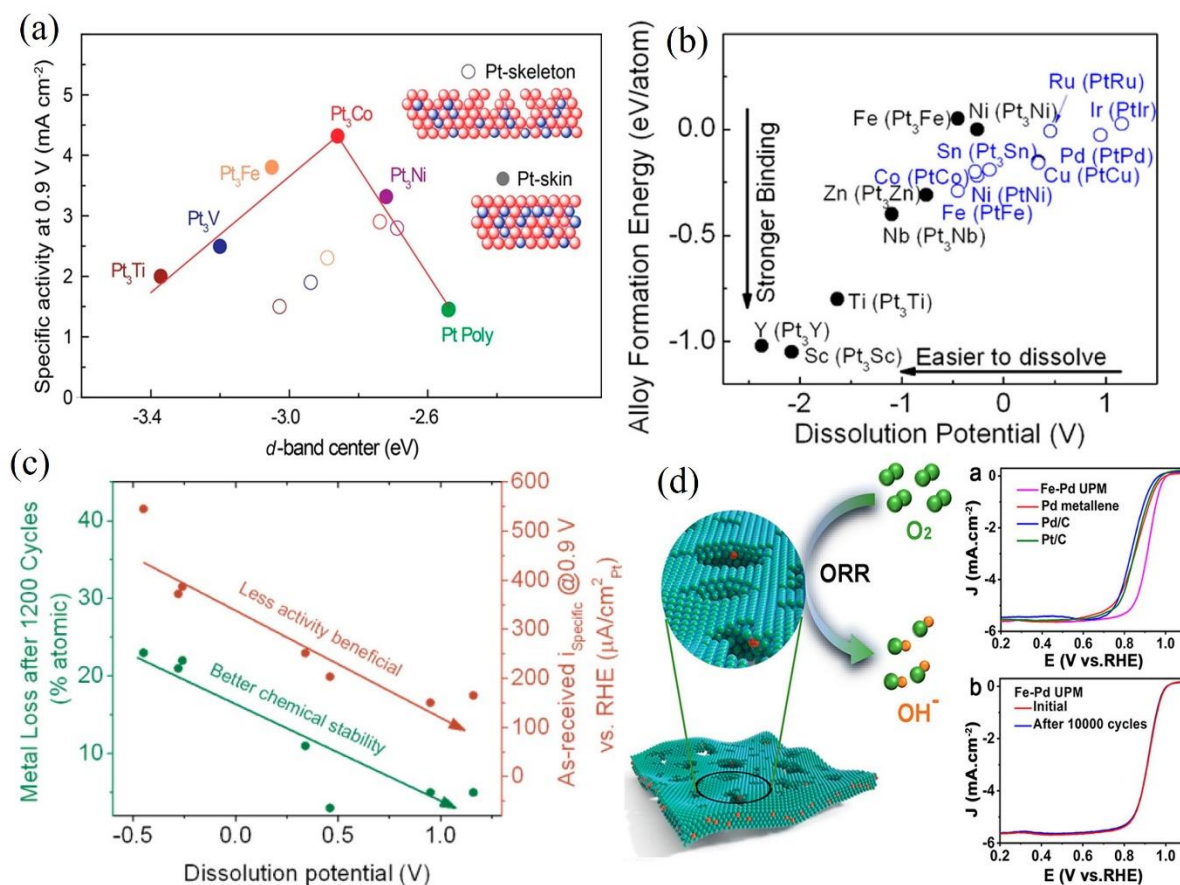


Fig. 9 (a) Relationships between experimentally acquired SA of Pt₃M surfaces versus the d-band center location for the Pt-skin and Pt-skeleton surfaces. Reprinted with permission.^[76] Copyright 2007, Springer Nature Limited. (b) Thermodynamic dissolution potential (V_{dissolve}) versus Pt alloy formation energy (E_{alloy}) of different Pt-alloyed transition metals. Reprinted

1. Introduction

with permission.^[93] Copyright 2015, American Chemical Society (c) Transition metal dopant loss after 1.2k cycles (green) and the SA of Pt alloy catalysts (red). Here the metal dopant loss was defined as the dopant composition change from (b). Reprinted with permission.^[93] Copyright 2015, American Chemical Society. (d) Sublayer Fe dopant in porous Pd nanosheet with enhanced catalytic activities and stability. Reprinted with permission.^[93] Copyright © 2022, American Chemical Society.

1.4 Noble-metal-free catalysts for electrochemical oxygen evolution/reduction reactions

Noble metals exhibit excellent electrocatalytic properties, but their application is still limited by the rarity and high cost. In this context, tremendous efforts have been devoted to exploring noble-metal-free substitutions with comparable electrocatalytic properties and durability that lead to significant advances in electrocatalytic OER and ORR.

1.4.1 Noble metal free based electrocatalysts for OER

Metal hydroxides/oxyhydroxides

Transition metal hydroxides and oxyhydroxides are the most widely investigated because of their high-performance OER electrocatalytic activities, especially for Ni,^[94,95] Fe,^[96] and Co^[96,97] based compounds. In 1983, D. E. Hall initially found that α -Ni(OH)₂ exhibited OER electrocatalytic activity.^[95] Inspired by this finding, other metal (Fe, Co, and et al.) hydroxides were shown to be active for electrocatalytic OER. In addition, the catalytic mechanism was revealed in recent years with the assistance of advanced measurement techniques. As described by Bode et al., two distinct redox transformations occur during the potential cycling across the Ni(2+)/(3+,4+) redox potential: the reduction/oxidation cycle between α -Ni(OH)₂ and γ -NiOOH (α and γ); and between β -Ni(OH)₂ and β -NiOOH, as shown in Fig. 10a.^[98,99] The oxidation process of α -Ni(OH)₂ to γ -NiOOH occurs at lower potential than the transformation from β -Ni(OH)₂ to β -NiOOH. However, β -NiOOH is unstable and could change to γ -NiOOH, especially at high pH values. Meanwhile, overcharging would take place if the potential is increased above the charging potential of β -Ni(OH)₂ to β -NiOOH, leading to the transformation of β -NiOOH to γ -NiOOH as well.^[98] Jianwen Huang et al. observed the phase transformation by Raman measurement and found that there was a reversible phase

transition between α -Ni(OH)₂ and γ -NiOOH prior to OER, revealing γ -NiOOH acts as the real activity contributor for OER (Fig. 10b).^[100] At the same time, researchers also found that some heteroatom doping can effectively improve electrocatalytic performance.^[98,101] The typical cases are NiFe-layered double (oxy)hydroxide (NiFe-LDH). The NiFe-LDH compounds can be expressed with the formula: $[\text{Ni}_{1-x}^{2+}\text{Fe}_x^{3+}(\text{OH})_2]^{x+}(\text{A}^{n-})_{x/n}\cdot\gamma\text{H}_2\text{O}$, where x is the molar ratio of Fe that is incorporated, A is the anion, n is the charge of the anions, and γ is the amount of water that is intercalated. The crystal structure is same as in the mineral hydrotalcite, as shown in Fig. 10c. However, the role of Fe in the system is still under debate. Many efforts have been devoted to developing a mechanistic picture of OER. Friebel et al. prepared Ni_{1-x}Fe_xOOH with different Fe content.^[102] The result indicates that the appropriate addition of Fe (25%) to NiOOH led to 500-fold higher OER current density (at 0.3 V vs. RHE) compared to pure Ni and Fe oxyhydroxide films and more than 175 mV decrease in overpotential, as shown in Fig. 10d. With the assistance of in-situ X-ray absorption spectroscopy (XAS) and high energy resolution fluorescence detection (HERFD), they found that Fe³⁺ in Ni_{1-x}Fe_xOOH occupies octahedral sites with extraordinary short Fe-O bond distances by replacing Ni and sharing the edges with surrounding [NiO₆] octahedra, which further led to optimal adsorption energies of OER intermediates and low overpotentials at Fe sites. It means the real active sites are doped Fe atoms. They also proposed a higher Fe loading resulted in the nucleation of a γ -FeOOH phase, which possess longer Fe-O bond distance and higher overpotential for OER. In addition, Chen et al. reported that the formation of Fe⁴⁺ in NiFe-LDH during the OER process was directly observed by operando Mössbauer spectroscopy. Up to 21% of the total Fe³⁺ atoms were oxidized to Fe⁴⁺, which further worked as active sites in water oxidation. Meanwhile, they proposed that the oxidized Fe⁴⁺ species generated at an edge, a corner, or a related “defect” site could be much more active kinetically and lead to rapid water oxidation. Up to now, other different mechanisms are kept being proposed based on the experiment and advanced characterization techniques and deeper understanding on NiFe-LDH would be acquired.

1. Introduction

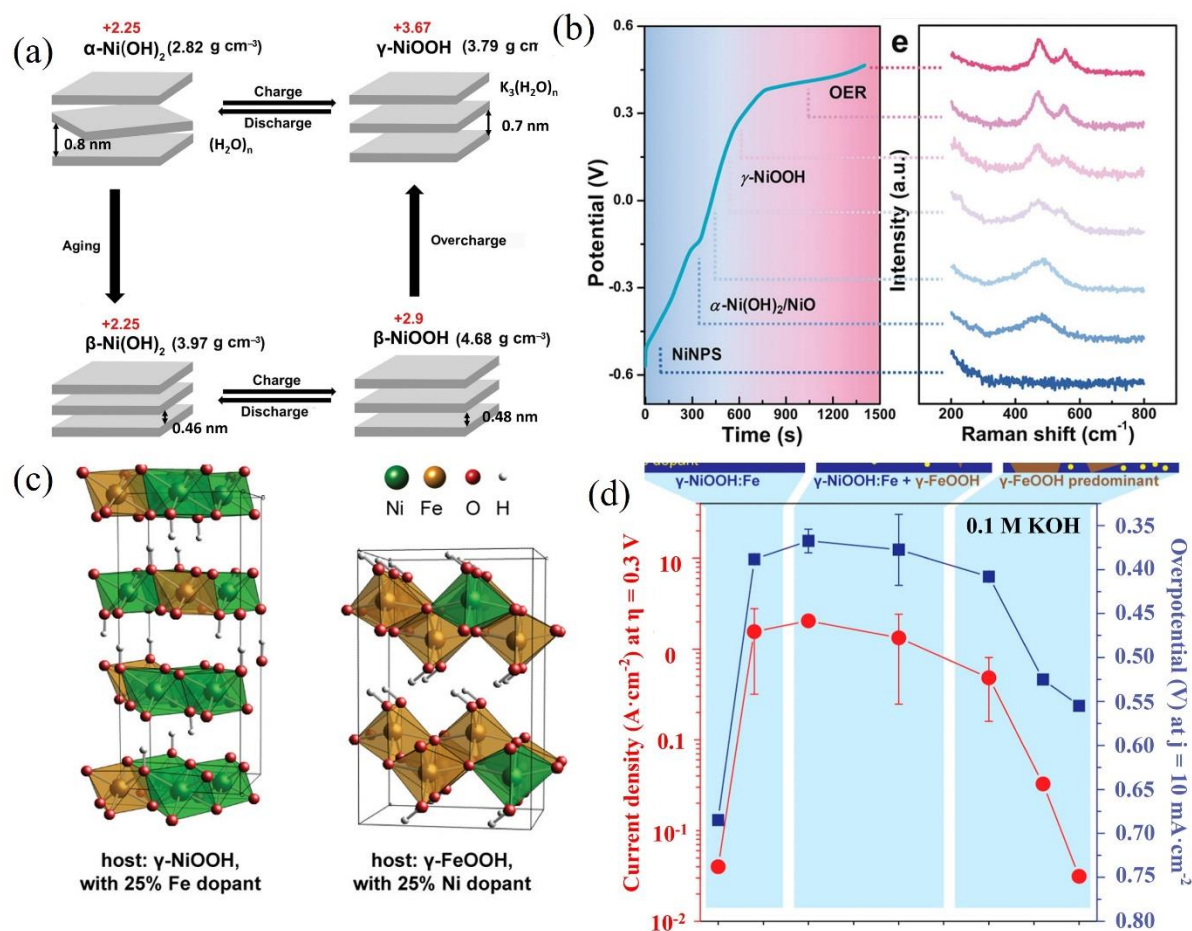


Fig. 10 (a) Charge-cischarge cyclic diagram of crystalline structure transition of Ni(OH)₂/NiOOH proposed by Bode. Reprinted with permission.^[98] Copyright 2013, Royal Society of Chemistry (b) Surface reconstruction analyses by in situ Raman spectra achieved during the chronopotentiometry measurement, Reprinted with permission.^[100] Copyright 2019 Wiley-VCH Verlag GmbH & Co. KGaA, Weinheim (c) Examples of unit cells for Fe-substituted γ-NiOOH and Ni-substituted γ-FeOOH model structures, and (d) measured OER activity of mixed Ni–Fe catalysts as a function of Fe content in 0.1 M KOH. Reprinted with permission.^[102] Copyright 2015, American Chemical Society.

Transition metal oxides

Metal oxides attracted wide attention because of their outstanding catalytic activities and superior stabilities, especially the first-row late transition metal, including Fe, Co and Ni. Amongst all of them, Co₃O₄ is one of the most promising candidates and became the research focus since the beginning of last century, due to their activity and durability in alkaline electrolytes. Co₃O₄ possesses the typical spinel structure, where Co²⁺ (Co_{Td}²⁺) and Co³⁺ (Co_{Oh}³⁺)

cations occupy the tetrahedral and octahedral sites respectively. The catalytic abilities of $\text{Co}_{\text{Td}}^{2+}$ and $\text{Co}_{\text{Oh}}^{3+}$ was tested by many researchers to determine the real active sites.^[103–105] Kim et al. prepared spinel-type ZnCo_2O_4 and Co_3O_4 thin film which were used as OER catalyst. Notably, in ZnCo_2O_4 , Zn^{2+} took the place of $\text{Co}_{\text{Td}}^{2+}$ in the tetrahedral sites. By comparing the catalytic properties of ZnCo_2O_4 and Co_3O_4 in both 1 M KOH (pH 13.8) and 0.1 M phosphate buffer solution (pH 7), they concluded that $\text{Co}_{\text{Td}}^{2+}$ is not catalytically critical for OER, as comparable performance and stability were acquired. However, similar ion replacement method was adopted by Wang et al. to determine the roles of $\text{Co}_{\text{Td}}^{2+}$ and $\text{Co}_{\text{Oh}}^{3+}$ played during OER process.^[104] They used inactive Zn^{2+} and Al^{3+} to replace $\text{Co}_{\text{Td}}^{2+}$ and $\text{Co}_{\text{Oh}}^{3+}$ and found that $\text{Co}_{\text{Td}}^{2+}$ was responsible for the formation of CoOOH , which further acted as the active site for OER. To some degree, ion replacement can bring some uncertainties to the active sites analysis, even Zn^{2+} and Al^{3+} are treated as inert. The introduced “inert ion” may modulate the electronic structures in the system and make themselves or originally inactive part active. On this basis, Bergmann et al. used advanced XAS to directly observe the local structure change during the OER process.^[103] They found the structurally reversible evolution of crystalline Co_3O_4 electrocatalysts: a sub-nanometer shell of the Co_3O_4 is transformed into an X-ray amorphous $\text{CoO}_x(\text{OH})_y$. The formed $\text{CoO}_x(\text{OH})_y$ was recognized as the active site. In addition, apart from the mechanism research, the modification of Co_3O_4 was also investigated by many groups as well. The guideline is mainly engineering electronic structure and morphology. For example, Lei Xu et al. demonstrated Co_3O_4 nanosheets with oxygen vacancies can effectively improve the catalytic activities: the SA is 10 times higher than that of pristine Co_3O_4 at 1.6 V.^[106] Similarly, Bao et al. prepared NiCo_2O_4 ultrathin nanosheets rich in oxygen vacancies and analyzed the origins of the catalytic performance. With the assistance of DFT calculations, they concluded that the ultrathin thickness and presence of oxygen vacancies led to decrease the water adsorption energy and the increase of active sites. Researchers also put much effort on nickel oxides and iron oxides and gained deeper understanding of their catalytic mechanisms and high-performance catalysts.

Apart from the spinel structured metal oxides, perovskites type of metal oxides has been widely studied as well and as treated as remarkable catalyst materials because of their highly tunable elemental compositions, unique electronic structures, and robustness in alkaline solutions. Perovskites type of metal oxides have the general formula of ABO_3 , in which A

1. Introduction

represents alkaline, alkaline-earth or rare-earth cations, and B represents transition or p-block metals. The typical ABO_3 perovskite structure is shown in Fig. 11a. In 1984, Bockris et al. first reported the OER performance of $LaMO_3$ ($M =$ transition metals) and used the 3d electron number of bulk transition metal ions as the activity descriptor.^[107] Afterwards, other perovskites oxides with high catalytic performance were found and the related reaction mechanisms and activity descriptors were proposed. Man et al. studied several perovskites based on density-functional theory (DFT) and found that the catalytic activities follow the following order: $SrCoO_3 > LaNiO_3 > SrNiO_3 > SrFeO_3 > LaCoO_3 > LaFeO_3 > LaMnO_3$,^[108] which were experimentally proved by other researchers.^[24,107–110] They proposed that $\Delta G_{O^*} - \Delta G_{HO^*}$ can be used as the descriptor to evaluate and predict the OER catalytic activities (Fig. 11b). At the same time, Shao-Horn et al. prepared a series of heteroatom substituted perovskites ($A_{1-x}A'_xB_yB'_{1-y}O_3$, where A or A' is a rare-earth or alkaline-earth metal, and B or B' is a transition metal) and observed their OER catalytic activities.^[24] The resultant perovskite oxides exhibit a volcano shape as a function of the e_g filling of surface B-site cations, as shown in Fig. 11c. They proposed the e_g -filling descriptor, which is different from the 3d electrons (both e_g and t_{2g} electrons) of B-site cations. As predicted by the e_g activity descriptor, BCSF exhibited the highest OER activities with at least an order of magnitude higher than that of IrO_2 in alkaline media, because its e_g electron number is 1.2, which is very close to the volcano plot peak. In 2013, Grimaud et al. proposed O p-band center could be a descriptor of OER catalytic activities by observation the catalytic properties of double perovskites ($Ln_{0.5}Ba_{0.5}CoO_{3-\delta}$ ($Ln=Pr, Sm, Gd,$ and Ho)). They found that moving the O p-band center closer to the Fermi level can improve OER activities, but moving computed O p-band center too close to the Fermi level decreases oxide stability during OER. The explanation is if the p-band center is closer to the Fermi level, oxygen vacancies are generated and M-O covalency is increased, resulting in higher activities. While if the O p band center is too close to the Fermi level, rapid amorphization in the near surface occurs, which decreases the catalytic activities. Benefit from these OER catalytic descriptors for perovskite oxides, numerous critical advances have been made in the design and synthesis of advance perovskite-type OER catalysts in recent years. However, because of the complex structure of perovskite oxides, a single catalytic descriptor is not commonly applicable when predicting and describing its OER performance. At the same time, developing more active perovskite oxides is also important as understanding the reaction mechanism. The specific routes used to prepare new perovskites with high performance include

composition engineering, crystal facet control, morphology control, defect engineering, and hybridization. However, compared with the commercial OER electrocatalysts, the as-reported perovskite-oxide catalyst family is still far away from the wide-spread application. More progress is required, and more theoretical and experimental investigations are needed in this field.

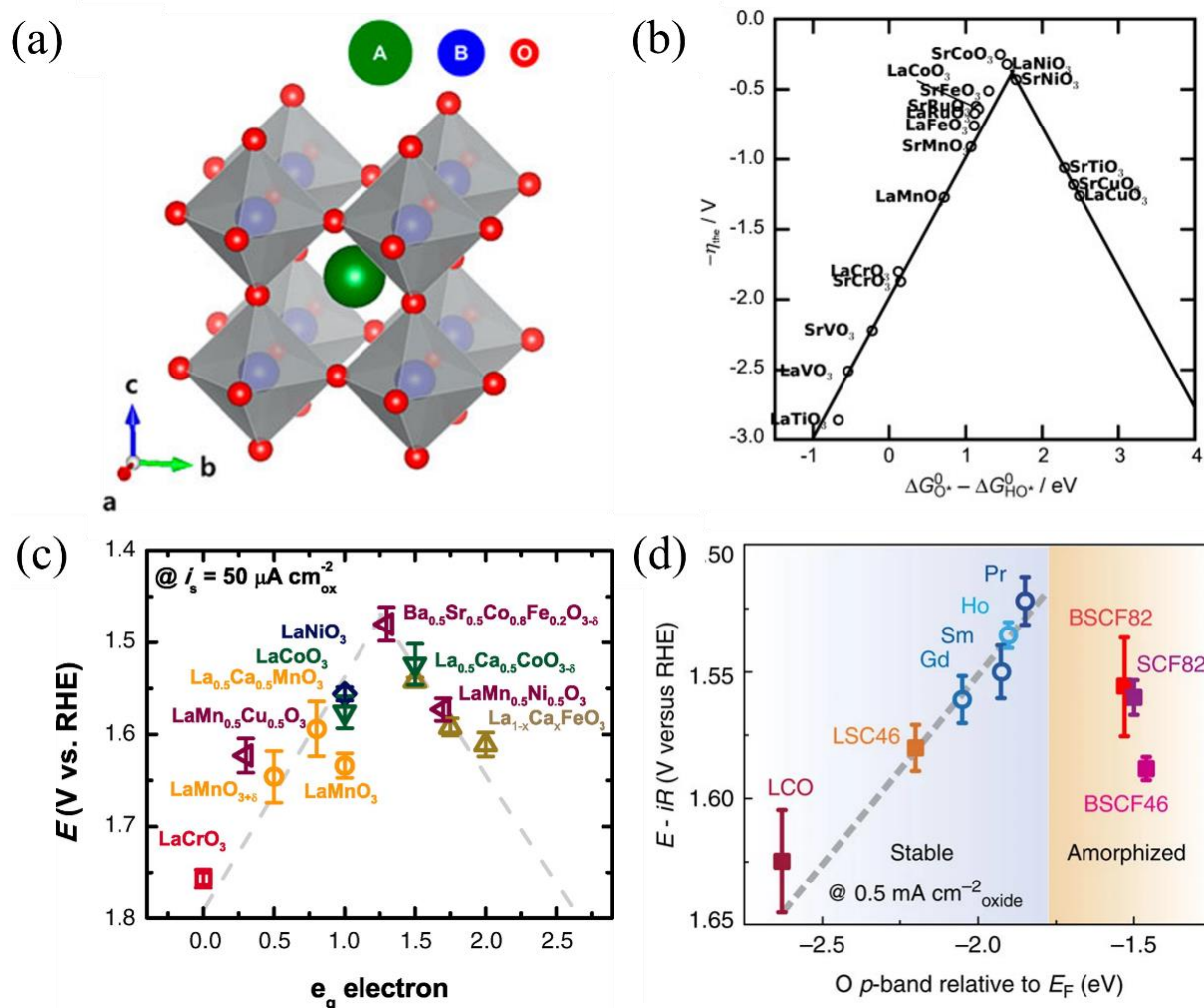


Fig. 11 (a) Scheme of typical ABO₃ perovskite structure. Reprinted with permission.^[111] Copyright 2022 Kim, Oh, Park, Kim, Lee and Lim. (b) Activity trends towards oxygen evolution plotted for perovskites. The negative theoretical overpotential was plotted against the standard free energy of the $\Delta G_{O^*} - \Delta G_{HO^*}$ step. Reprinted with permission.^[112] Copyright 2011 WILEY-VCH Verlag GmbH & Co. KGaA, Weinheim. (c) The relation between the OER catalytic activity, defined by the overpotentials at $50 \mu A \cdot cm^{-2}_{ox}$ of OER current, and the occupancy of the e_g -symmetry electron of the transition metal (B in ABO₃). Reprinted with permission.^[24] Copyright 2011, American Association for the Advancement of Science. (d) The iR -corrected

1. Introduction

potential of OER at $0.5 \text{ mA} \cdot \text{cm}^{-2}_{\text{oxide}}$ versus the O p-band center relative to Fermi level (eV) of $(\text{Ln}_{0.5}\text{Ba}_{0.5})\text{CoO}_{3-\delta}$ with Ln=Pr, Sm, Gd and Ho, for LaCoO_3 (LCO), $\text{La}_{0.4}\text{Sr}_{0.6}\text{CoO}_{3-\delta}$ (LSC46), $\text{Ba}_{0.5}\text{Sr}_{0.5}\text{Co}_{0.8}\text{Fe}_{0.2}\text{O}_{3-\delta}$ (BSCF82), $\text{Ba}_{0.5}\text{Sr}_{0.5}\text{Co}_{0.4}\text{Fe}_{0.6}\text{O}_{3-\delta}$ (BSCF46) and $\text{SrCo}_{0.8}\text{Fe}_{0.2}\text{O}_{3-\delta}$ (SCF82). Reprinted with permission.^[109] Copyright 2013, Springer Nature Limited.

In addition, polyoxometalates (POMs) and their derivatives are also promising electrocatalysts for OER due to their chemically diverse, structurally well-defined nanoscale (~1-5 nm) and high number of redox-active metals per molecular unit. More specifically, POMs are assembled by the connection of $\{\text{MO}_x\}$ polyhedra where M is an early d-block element in a high oxidation state, usually $\text{V}^{\text{IV,V}}$, $\text{Mo}^{\text{V,VI}}$, or $\text{W}^{\text{V,VI}}$. The most well-established prototypes are the so-called Keggin anion $[\text{XM}_{12}\text{O}_{40}]^{n-}$ (X = e.g. B, Si, P; M = Mo, W) or Wells-Dawson anion $[\text{X}_2\text{M}_{18}\text{O}_{62}]^{m-}$ (X = S, P; M = Mo, W). In 2004, Howells et al. first reported that di-Ru-substituted POM $[\text{Ru}_2\text{Zn}_2(\text{H}_2\text{O})_2(\text{ZnW}_9\text{O}_{34})_2]^{14-}$ showed OER electrocatalytic properties.^[113] This finding inspired other researchers to develop POM molecules as water oxidation catalysts. In 2010, Yin et al. synthesized $[\text{Co}_4(\text{H}_2\text{O})_2(\text{PW}_9\text{O}_{34})_2]^{10-}$ ($\text{Co}_4\text{-POM}$) molecules which showed high OER catalytic activity. In the following discussion of “the real catalyst”, Finke and Stracke deeply investigated the true active sites in $\text{Co}_4\text{-POM}$ during OER process.^[114,115] They found that the dominant catalysts were heterogeneous CoO_x , which formed from the decomposition of $\text{Co}_4\text{-POM}$ at pH 8.0. Furthermore, Goberna-Ferrón et al. reported another molecule POM catalyst: $[\text{Co}_9(\text{H}_2\text{O})_6(\text{OH})_3(\text{HPO}_4)_2(\text{PW}_9\text{O}_{34})_3]^{16-}$ (Co_9).^[116] They performed experiments with an excess chelating agent for free aqueous Co^{2+} ions. As a result, they could observe the catalytic performance of Co_9 without the formation of a Co_x film on the electrode. The result indicated Co_9 could act as the true homogeneous water oxidation electrocatalyst and maintain constant reaction rates and efficiencies without any significant apparition of fatigue for several days. However, their application was still limited by its poor conductivity. To solve this problem, they also synthesized the heterogeneous catalyst: $\text{Cs}_{15}\text{K}[\text{Co}_9(\text{H}_2\text{O})_6(\text{OH})_3(\text{HPO}_4)_2(\text{PW}_9\text{O}_{34})_3]$ mixed with carbon paste, which exhibited higher activities at a wide range of pH values.^[117] Other conductive substrates were used as well to increase the conductivities of catalysts. For example, Luo et al. deposited a robust Dexter-Silverton POM OER electrocatalyst $[\text{Co}_{6.8}\text{Ni}_{1.2}\text{W}_{12}\text{O}_{42}(\text{OH})_4(\text{H}_2\text{O})_8]$ on a conductive 3D nickel foam substrate. The as-synthesized catalyst showed superior catalytic properties, long-term stability, and high Faradaic efficiency. Additionally, other conductive substrates, like carbon nanotubes^[118,119] and graphene,^[120]

showed good electrocatalytic properties as the conductive substrates to facilitate the multi-electrons transfer required for OER.

Other noble metal free OER electrocatalysts

Apart from above mentioned metal hydroxides, metal oxyhydroxides, and metal oxides, other transition metal-based catalysts also drew a lot attention and were widely studied. Some of them showed superior electrocatalytic properties, including metal phosphides, sulfides, nitrides, selenides, and carbides.

Metal sulfides, phosphides, and selenides have been widely developed towards catalytic water splitting, especially for HER. Traditionally, metal sulfides and phosphides are considered unsuitable for OER, as sulfides and phosphides tend to be oxidized at higher potential. However, S, and P atoms located near the metal atoms, can result in increased 3d–2p repulsion between the metal d-band center and the coordinated oxygen's p-band centers, which would deactivate the catalysts by coordination of the hydroxide ligand.^[121] Some researchers devoted much effort to revealing the role of S, Se, and P atoms during catalysis process and the true catalytically active species. In 2016, Mabayoje et al. investigated the activity of electrodeposited nickel sulfide (NiS).^[122] The results indicated amorphous thin films of nickel oxide (NiO_x) formed in potential range where water is oxidized to oxygen. The original NiS acted as pre-catalyst. Similarly, Ryu et al. prepared CoP nanoparticles, which transformed into cobalt-oxo/hydroxo molecular during catalysis.^[123]

Several metal nitrides intrinsically possess metallic characteristics and good electrical conductivity, which offers possibility for OER. For example, Xu et al. synthesized metallic Ni₃N nanosheets with disordered structure, which gave improved OER activity compared with bulk Ni₃N and NiO nanosheets.^[124] They also investigated the real active sites in their catalyst, and they proposed the in-situ formed NiOOH/Ni₃N on the surface is the real active sites, based on the observation of a Ni²⁺ to Ni³⁺ oxidation peak at around 1.4 V vs RHE. A similar theory was proposed by Yu et al. based on the XPS measurement on the catalyst (Fe₃N/Fe₄N).^[125] They proposed that the iron oxide film formed on the surface of Fe₃N/Fe₄N is the real active site and the inner Fe_xN cores acted as highly conductive support to provide reliable electron transfer to the surface-active sites. The guidelines of metal nitrides design are always focusing

1. Introduction

on the in-situ transformed metal oxides/hydroxides film on the surface of the catalysts, which can act as active sites.

In conclusion, metal phosphides, sulfides, nitrides, selenides, and carbides attracted much attention because of their superior catalytic properties, while most of them are pre-catalysts and transformed to metal oxides/hydroxides in the process of OER. Compared to bulk metal oxides/hydroxides, the in-situ grown metal oxides/hydroxides possess thin 2D structures and expose more active sites. Meanwhile, their metal nitride substrates are good conductors, which can help overcome relatively low electrical conductivity restrictions of metal oxides/hydroxides and accelerate electron transfer efficiency.

1.4.2 Noble metal free electrocatalysts for ORR

In the past decades, great progress has been made on noble metal free catalysts investigation. Some catalysts even possess comparable catalytic properties to Pt and Pd catalyst. In this section, we will mainly focus on some advanced ORR electrocatalysts, including Metal (M)-N-C catalysts, single atom catalysts, metal oxides, and metal chalcogenides.

M-N-C catalysts

Amongst all ORR electrocatalysts, catalysts of the M-N-C family are the most promising candidates. M-N-C represents the metal cluster or metal atoms deposited on nitrogen-rich carbon (metal-nitrogen-carbon composite). Tracking back to 1964, Jasinski et al. reported that Co phthalocyanine (CoPc) exhibited ORR catalytic properties.^[126] After that, tremendous efforts were made to develop new catalysts. The strategies are mainly focusing on increasing the intrinsic activity by size control and composition modulation, as well as morphology modulation to expose more active sites. Dehui et al. successfully immobilized iron nanoparticles into carbon nanotubes. The prepared catalyst showed enhanced catalytic activities and stability. Carbon nanotubes can protect Fe nanoparticles from acid corrosion. In the following investigation, researchers found that Fe-N_x/C catalysts derived by high-temperature calcination are the desirable carbon-based ORR electrocatalysts. However, this type of ORR electrocatalysts lacks sufficient activity in acidic environment and the active site of this structure is still undetermined. In 2016, Jiang et al. synthesized highly active Fe-N-C ORR catalyst containing Fe-N_x coordination sites and Fe/Fe₃C nanocrystals (Fe@C-FeNC) to

investigate the real active sites and catalytic mechanism.^[127] At same time, they also prepared reference catalysts without Fe nanoparticles by acid etching. The results showed that Fe nanoparticles or Fe-N_x themselves did not achieve high activity, and the synergism between Fe nanoparticles and Fe-N_x played an important role in the catalysis. Meanwhile, the catalytic activities are related to the content of Fe-N_x. The employed DFT calculation indicated the interaction between metallic Fe and Fe-N₄ coordination structure favored the adsorption of oxygen molecules, leading to superior catalytic properties. The synergistic effect between Co-N_x active sites and metallic Co nanoparticles is also observed by Sidi Wang et al..^[128] Different opinions on the real active sites exist all the time. Zitolo et al. synthesized Fe-N-C materials quasi-free of crystallographic iron structures after argon or ammonia pyrolysis.^[129] According to the EXAFS and Mössbauer spectroscopy measurement, 97.1% - 97.5% of Fe atoms exist as mononuclear iron centers in FeN_xC_y. Also, similar catalysts with Fe nanoparticles or crystalline Fe₂N were prepared as contrast catalysts. The better catalytic properties of FeN_xC_y indicates Fe based particles in catalysts were inactive. However, their application was limited by low loading of active Fe sites, which was less than 0.5%. In 2016, a new Zn evaporation assisted strategy was adopted by Yin et al., who successfully synthesized atomically dispersed Co-N_x single site catalysts with high metal loading over 4 wt%.^[130] Owing to its high metal loading, the obtained Co-N_x single sites exhibit excellent ORR performance with a half-wave potential (0.88 V vs. RHE) that is more positive than commercial Pt/C (0.81 V vs. RHE). Yuanjun Chen et al. prepared single-atom Fe/N-doped porous carbon catalyst (ISA Fe/CN) with the similar synthetic method and found ISA Fe/CN showed excellent ORR performance with a half-wave potential ($E_{1/2}$) of 0.9V vs. RHE and high kinetic current density of 37.83 mA·cm⁻² at 0.85 V vs. RHE, which outperformed commercial Pt/C.^[131] They also investigated the origins of the enhanced properties by using DFT calculation. The computation results indicated electrons were more easily transferred from a single Fe atom to the adsorbed *OH intermediates, thus significantly facilitating ORR.

In conclusion, M-N-C catalysts have made a lot of impressive progress and some of them exhibited comparable electrocatalytic ORR performance. However, many efforts are still needed, especially on 1) a deeper understanding of the real active site. 2) improving the concentration of metal loading on the carbon substrates, especially for single atom family catalysts, 3) understanding the reaction mechanism and the role of metals in the catalysts.

1. Introduction

Metal oxide ORR catalysts

Metal oxide family catalysts are also active toward ORR and numerous efforts have been devoted to developing efficient and robust catalysts. Amongst all metal oxides, spinel type and perovskite type metal oxides exhibit promising ORR performance and have attracted widespread attention from researchers. In 2015, Gaungping Wu et al. successfully prepared $\text{Co}^{\text{II}}\text{Fe}^{\text{III}}\text{Co}^{\text{III}}\text{O}_4$ which exhibited more positive onset potential (0.98 V vs. RHE) and halfwave potential (0.866 V vs. RHE) than commercial Pt/C and the normal spinel Co_3O_4 .^[132] DFT calculations showed that the higher catalytic activity of the $\text{Co}^{\text{II}}\text{Fe}^{\text{III}}\text{Co}^{\text{III}}\text{O}_4$ originates from the dissimilarity effect of Fe and Co atoms at the octahedral site, which modulates the oxygen adsorption energy and elongates the bond between metal and the adsorbed oxygen compared to the normal spinel Co_3O_4 , shown in Fig. 12a, b. This heteroatom doping method can effectively modulate the electronic structure of the catalyst to generate high performance catalysts. In addition, introducing abundant oxygen vacancies into spinel type metal oxides can effectively enhance electrocatalytic activities. For example, Li et al. successfully synthesized ultrafine Co_3O_4 nanoparticles with abundant oxygen vacancies, which showed impressive ORR activities (Fig. 12c).

Similarly, composite modulation and oxygen vacancy are also helpful in improving the ORR electrocatalytic properties of perovskite type metal oxides. As mentioned in the previous part, perovskite oxides have the general formula of ABO_3 . Both A and B sites can be substituted by other elements. As an example, Hammouche et al. investigated perovskite-type oxides $\text{La}_{1-x}\text{Ca}_x\text{CoO}_3$ (with $0 \leq x \leq 0.6$).^[133] Its catalytic activity reached a maximum when x equaled 0.4. Suntivich compared the ORR activities of a series of B site substituted perovskite type metal oxides.^[134] They found that their ORR activities of all the prepared oxides exhibited a volcano shape as a function of the e_g -filling of B ions, as shown in Fig. 12d. Meanwhile, when e_g -filling has a value of ~ 1 , the catalytic activities reach a maximum. They proposed transition-metal e_g -filling and covalency could be a descriptor for ORR activities and provide guidelines for developing highly active non-precious-metal-containing oxide catalysts for ORR. Guided by oxygen vacancy engineering, Zhu et al. synthesized $\text{La}_{0.95}\text{FeO}_{3-\delta}$ with a large amount of O vacancies that lead to high catalytic activities.^[135]

1. Introduction

Other noble metal free based electrocatalysts

Apart from the metal oxides described above, carbon-based metal cluster or single metal atom catalysts, some metal nitrides, carbides, phosphides, and chalcogenides also exhibit ORR electrocatalytic abilities. Amongst all of them, metal nitrides have been long investigated as promising ORR electrocatalysts because of their higher conductivity and better stability than metal oxides, and their stability can be enhanced by heterometal doping.^[137] In one example, Tian et al. synthesized a binary transition metal nitride ($\text{Ti}_{0.95}\text{Ni}_{0.05}\text{N}$), which showed almost comparable ORR activities to that of commercial Pt/C in alkaline electrolyte. Also, its catalytic performance in acid electrolyte was far better than that of TiN. It was proposed that Ni doping enhanced the electron transfer from Ti atom to absorbed oxygen molecules. Meanwhile, as the Ti binds O atoms strongly, whereas Ni binds O weakly, the doping of Ni can reduce the Ti-O strength, contributing to high ORR activity. In another example, Luo et al. proposed that doping method can enrich d electrons of metal and facilitated the dissociation of adsorbed O_2 .^[138] By Co doping method, they prepared $\text{V}_{0.95}\text{Co}_{0.05}\text{N}$ and found its ORR catalytic properties were largely enhanced, as shown in Fig 13a. They explained that the activity resulted from enriched d electrons in V via Co atoms doping and facilitated O_2 dissociation. With more in-depth understanding of the composition-structure-activity relationship in metal nitride, more advanced metal nitrides catalysts were synthesized. Dong et al. synthesized Ti and Co binary metal nitride mounted on nitrogen doped reduced graphene oxide, which exhibited superior ORR activities with a half-wave potential (0.90 V vs. RHE) ~ 30 mV more positive than that of commercial Pt/C catalyst.^[139]

Recently, metal carbide has gained wide attention because of their unique electronic interaction between the metal carbide nanoparticles and carbon substrate. In this regard, Hai et al. prepared nitrogen-enriched core-shell structured Fe/Fe₃C-C nanorods, which exhibited significantly improved activities and advanced kinetics for ORR in neutral phosphate buffer solution (pH = 7.0) compared with the commercial Pt/C catalysts (Pt 10%).^[140] The real active sites were investigated by Hu et al., who proposed encapsulated Fe₃C can effectively activate the surrounding graphitic layers, which acted as the main active sites for ORR.^[141] Based on this finding, Xiao et al. prepared more active catalysts by increasing of the contact between the Fe₃C and graphitic layer.^[142] Yang et al. investigated the real active sites and catalytic mechanism by DFT calculation in case of Fe₃C and Co nanoparticles encapsulated hierarchical

structure of N-doped carbon which exhibited better ORR electroactivity than commercial Pt/C catalyst.^[143] As shown in calculated reaction pathway of ORR on C-N6 (pyridinic-N, schematic illustration in Fig. 13b) site, NC, and Fe₃C-Co/NC (Fig. 13 c), the rate-determining step is OOH formation. The π bonds between N-C and C-C were weakened by combining with Fe₃C-Co, which makes the OOH* bond to C-N₆ stronger, leading to facilitated *OOH formation.

In addition, metal sulfide and phosphides are also considered relevant ORR electrocatalysts. For example, CoP, FeP, and Co₉S₈ were experimentally found active toward ORR.^[144,145] The heteroatom doping, morphology modulation, and defect strategies can be applied on them to get moderate electronic structures for more favorable ORR.

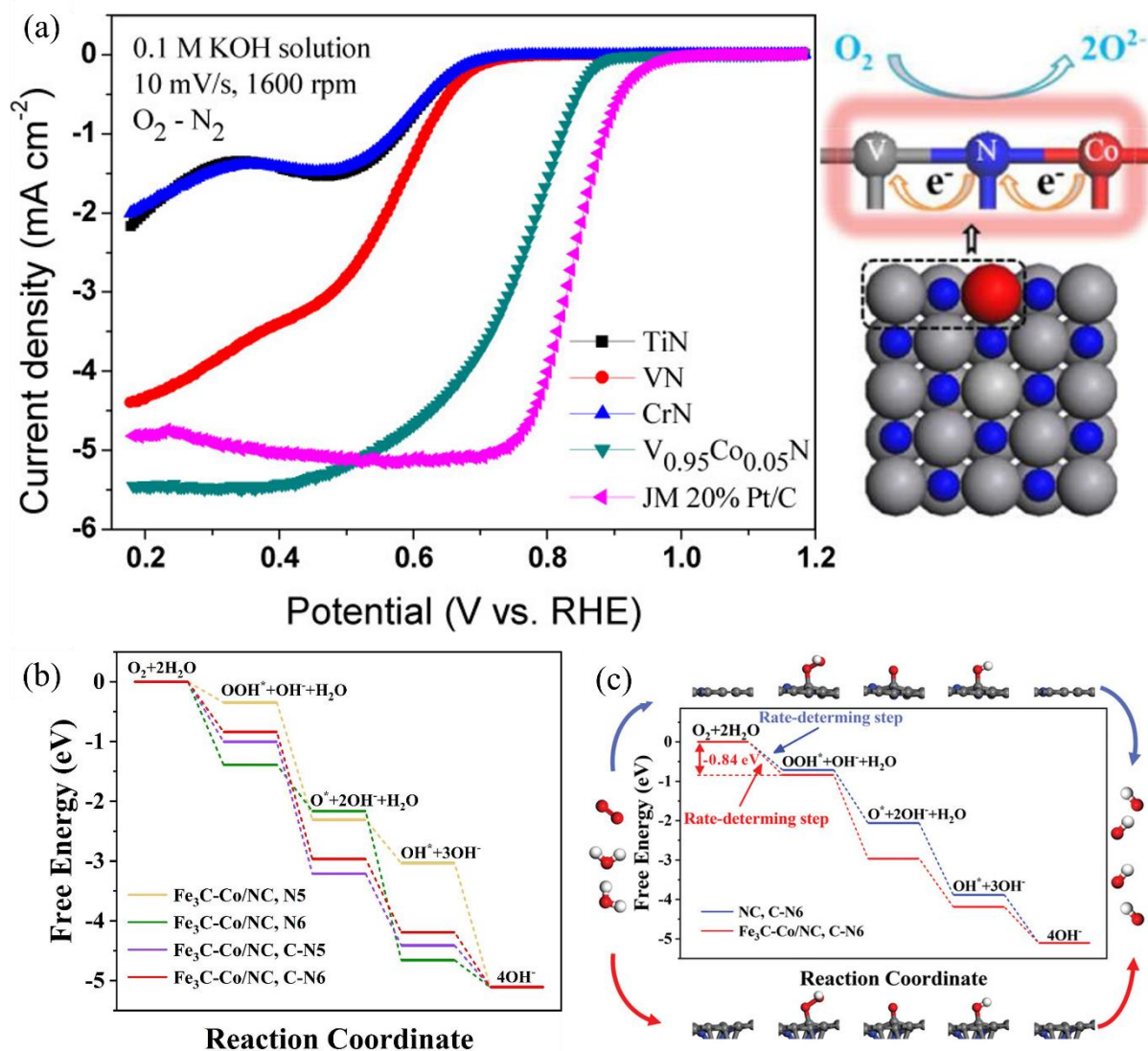


Fig. 13 (a) Left: Linear sweep voltammetry curves of VN, TiN, CrN, JM 20% Pt/C, and V_{0.95}M_{0.05}N, calculated by subtracting N₂-saturated solution from O₂-saturated solution at a

1. Introduction

rotation speed of 1600 rpm in 0.1 M KOH solution; Right: simple schematic top view of the (200) surface of Co doped VN and the route of d electron enrichment by Co doping.

Reprinted with permission.^[138] Copyright 2016, American Chemical Society. (b) Relative energy diagram for ORR on N5 (pyrrolic-N), N6 (pyridinic-N), C-N5 (C atom adjacent to the pyrrolic-N) and C-N6 sites on Fe₃C-Co/NC. (c) Top: Relative energy diagram for ORR on C-N6 sites on Fe₃C-Co/NC and NC; Bottom: Schematic presentation of the bond length around C-N6 sites on Fe₃C-Co/NC and on NC. Reprinted with permission. Copyright 2019 WILEY-VCH Verlag GmbH & Co. KGaA, Weinheim

In conclusion, much impressive progress has been made in the past investigation on noble metal free-based catalyst. But there is still a long way to go to employ them in industrial application. The noble metal-based catalysts must meet the following requirements: (i) The catalysts should possess comparable or even better ORR electrocatalytic activities as/than that of commercial Pt/C. (ii) The catalysts can be easily synthesized at a large scale. (iii) The catalysts should be robust enough and work for a long period (more than 1000h) without obvious degradation. To this end, a lot of efforts are required, including reaction mechanisms investigation and new materials design.^[143]

2 Objectives of work

OER and ORR are crucial electrochemical reactions and play an important role in energy conversion and storage systems, such as water electrolysis and metal air batteries. However, these technologies are limited by the electrocatalytic activities of catalysts. The main objective of this work is to design effective and stable catalysts and understand the origins of the intrinsic activities.

The effort to achieve this goal can be categorized into three parts.

- The synthesis of ORR/OER catalysts by composition and morphology control and evaluation of their electrocatalytic properties.
- Understanding the real active sites for OER/ORR based on the observation of chemical and morphological conversion before and after catalysis.
- Tuning the electronic structure of catalysts by defect engineering and understanding the impact on electrocatalytic properties.

Objective 1 of this study is to synthesize OER/ORR catalysts that are not only highly active but also robust, achieved through meticulous control of composition and morphology. For this purpose, ZIF-67 polyhedrons with their inherent porous structure are chosen as precursors. These are morphologically refined through acid-etching to create a hollow structure. Concurrently, the composition is adjusted via a metal ion exchange process, leveraging the ease with which cobalt ions in the framework nodes can be substituted by other metal ions. The final metal oxides and sulfide-based OER catalysts are obtained through a low-temperature annealing and sulfidation process. In parallel, the focus for ORR catalyst development is on Pd metallene. The electrocatalytic activities of the resulting catalysts are studied under technologically relevant conditions in aqueous alkaline electrolytes.

Objective 2 of this research is to decipher the true active sites in OER/ORR catalysts throughout the catalytic process. This involves a comprehensive investigation of the composition, morphology, and electrocatalytic performance both before and after catalysis.

2. Objectives of work

Such analysis is anticipated to shed light on the actual active sites, thereby offering valuable guidance for the future synthesis of OER/ORR catalysts.

Objective 3 centers on the development of ORR catalysts. Pd inherently exhibits a strong binding affinity to oxygen atoms, which hinders the favorable generation of intermediates (*OH and *OOH) and their subsequent conversion to H₂O. This results in comparatively lower oxygen reduction activity. To address this, defect engineering will be applied to Pd metallene. This technique is designed to adjust the electronic structure and modulate the binding energy of Pd metallene to O₂, thereby enhancing its efficiency in the oxygen reduction reaction.

3 Results and discussion

Section 3.1, 3.2, and 3.5 in this dissertation summarize results which have been published in peer-reviewed journals. Section 3.3 and 3.4 have been deposited on the preprint server ChemRxiv. These articles are reprinted in the following with permission of the respective publishers.

In section 3.1, titled “Polyoxometalate-assisted synthesis of amorphous zeolitic imidazolate for efficient electrocatalytic oxygen evolution”, Ni-modified Keggin-type POM ($[\text{PNi}(\text{H}_2\text{O})\text{W}_{11}\text{O}_{39}]^{5-}$) was successfully deposited in ZIF-67 by a facile one-pot method. The material was characterized by ATR-FTIR, pXRD, HR-TEM combined with EDX. The electrocatalytic activities were tested by a standard three-electrode electrochemical setup. The results show the improved electrocatalytic OER performance of POM functionalized composite. Meanwhile, we also found a certain degradation of the material during long-term stability test and the formation of Co_2O_3 , which acted as real active site for OER after POM decomposition.

Based on the results of section 3.1, we converted the POM-doped ZIF-67 into a stable oxygen evolution electrocatalyst by chemical etching, cation exchange, and thermal annealing steps, as described in section 3.2, titled “POM@ZIF Derived Mixed Metal Oxide Catalysts for Sustained Electrocatalytic Oxygen Evolution”. After optimization, carbon-supported amorphous metal oxides were obtained, as shown by XPS, HR-TEM, EDX and Raman spectroscopy, amongst others. The resulting composite exhibited structural and compositional advantages which lead to low overpotential (306 mV at $j = 10 \text{ mA}\cdot\text{cm}^{-2}$) and long-term stability. Post catalytic analysis shows the formation of crystalline Fe_2O_3 , which was determined by SAED and EDX. Additionally, Co^{2+} was oxidized to Co^{3+} , which is the favored Co oxidation state for OER catalysis.

In section 3.3, titled “In situ formation of robust nanostructured Cobalt oxyhydroxide / Cobalt oxide oxygen evolution reaction electrocatalysts”, we have developed mixed metal sulfide precursors (such as CoMo_2S_4 and FeS_2) using a straightforward synthesis method. Our investigation focuses on how the metal sulfide precursors are transformed *in situ* to yield

3. Results and discussion

highly stable composite OER catalysts, comprising γ -CoOOH nanofibers and Co_2O_3 nanoparticles. These entities serve as the actual active sites for OER electrocatalysis, contributing to both high activity and enhanced stability. Furthermore, the study underscores the importance of the presence of crystalline mixed metal sulfide precursors. This is crucial for the simultaneous in situ formation of both stable and active Co_2O_3 nanoparticles and γ -CoOOH nanofibers. The research highlights that utilizing these earth-abundant minerals could provide an economically and chemically feasible pathway for the scalable development of catalysts.

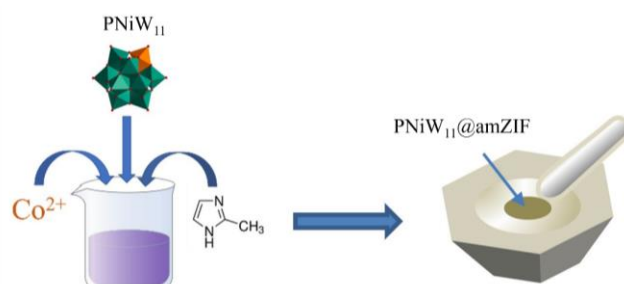
In Section 3.4, titled "Atomically Modified WO_x/MoO_x Enriched Defect-Rich Pd Metallene for Enhanced Alkaline Oxygen Reduction Electrocatalysis," we report the synthesis of a defect-rich Pd metallene via an accessible wet chemical method. Characterization studies have shown that this Pd metallene is characterized by a variety of atomic-scale defects, including pores, concave surfaces, and atomically integrated WO_x and MoO_x (denoted as D-PdWMo M). These specific defects effectively modify the electronic structure of the material, thereby significantly enhancing its catalytic activity for the ORR. The D-PdWMo M exhibits exceptional ORR performance, evidenced by a high half-wave potential of 0.927 V versus RHE and a mass activity of $1.3 \text{ A}\cdot\text{mgPd}^{-1}$ at 0.9 V versus RHE. These metrics notably exceed those of commercial Pt/C and Pd/C catalysts by 6.5 and 3.9 times, respectively. Furthermore, when integrated into a custom-built Zn-air battery with an extremely low D-PdWMo M loading of $26 \mu\text{gPd}\cdot\text{cm}^{-2}$, it achieves an impressive specific capacity of $809 \text{ mAh}\cdot\text{gZn}^{-1}$ and demonstrates excellent discharge potential stability, underscoring its practical applicability. This research offers novel insights into tailoring the electronic structure at the active sites, paving the way for the development of highly efficient electrocatalysts for ORR applications.

In section 3.5, titled "Hydrogenation Catalysis by Hydrogen Spillover on Platinum-Functionalized Heterogeneous Boronic Acid-Polyoxometalates," shows the activation of H_2 by polyoxometalate (POM)-based heterogeneous compounds, which are functionalized with Platinum particles. This activation is achieved through a synergy between a hydrogen spillover mechanism and electron-proton transfer facilitated by the POM. This dynamic interaction enables the selective catalytic reduction of olefins and nitroarenes, exhibiting a high tolerance for various functional groups. We report on a series of polyoxotungstates, each covalently functionalized with boronic acids. In their solid state, these compounds are interconnected through non-covalent forces, including π - π stacking and hydrogen bonding. The resultant

heterogeneous nanoparticles form stable colloidal dispersions in acetonitrile and can be further surface functionalized with platinum nanoparticles via in situ photoreduction. These newly developed materials demonstrate outstanding catalytic efficiency in the hydrogenation of olefins and nitrobenzene derivatives under mild conditions (1 bar H₂ and room temperature), showcasing their potential for practical applications in selective catalytic reduction processes.

3.1 Polyoxometalate-assisted synthesis of amorphous zeolitic imidazolate for efficient electrocatalytic oxygen evolution

Yupeng Zhao, Dandan Gao, Johannes Biskupek, Ute Kaiser, Rongji Liu, Carsten Streb



This publication reports on the synthesis and characterization of Ni modified Keggin-type POM ($[\text{PNi}(\text{H}_2\text{O})\text{W}_{11}\text{O}_{39}]^{5-}$ (=PNiW₁₁))-functionalized amorphous ZIFs (PNiW₁₁@amZIF), which shows high performance for OER with low overpotential (375 mV at 10 mA·cm⁻²), high faradaic efficiency (96 %), and a low Tafel slope of 69 mV·dec⁻¹.

Author Contributions:

Yupeng Zhao: Methodology, Data curation, Investigation, Writing original draft.

Dandan Gao: Investigation, Data curation, Writing original draft.

Johannes Biskupek: Investigation, Data curation, Writing original draft.

Ute Kaiser: Data curation, Writing original draft.

Rongji Liu: Conceptualization, Supervision, Data curation, Methodology, Writing original draft.

Carsten Streb: Project administration, Funding acquisition, Conceptualization, Supervision, Data curation, Methodology, Writing original draft.

Supporting Information can be found at pp 113.

“Y. Zhao, D. Gao, J. Biskupek, U. Kaiser, R. Liu, C. Streb, Results Chem **2022**, 4, 100568.”

Reprinted with permission, © 2022 The Authors. Published by Elsevier B.V.



Contents lists available at ScienceDirect

Results in Chemistry

journal homepage: www.sciencedirect.com/journal/results-in-chemistry

Polyoxometalate-assisted synthesis of amorphous zeolitic imidazolate for efficient electrocatalytic oxygen evolution

Yupeng Zhao^{a,b}, Dandan Gao^{a,b}, Johannes Biskupek^c, Ute Kaiser^c, Rongji Liu^{a,b,d,*}, Carsten Streb^{a,b,d,*}

^a Institute of Inorganic Chemistry I, Ulm University, Albert-Einstein-Allee 11, 89081 Ulm, Germany

^b Department of Chemistry, Johannes Gutenberg University Mainz, Duesbergweg 10-14, 55131 Mainz, Germany

^c Central Facility of Electron Microscopy, Ulm University, Albert-Einstein-Allee 11, 89081 Ulm, Germany

^d Helmholtz Institute Ulm, Helmholtzstr. 11, 89081 Ulm, Germany

ARTICLE INFO

Keywords:

Polyoxometalate
Electrocatalysis
Water-splitting
Oxygen evolution reaction
Composite

ABSTRACT

The development of earth-abundant element-based highly active and efficient catalysts for the oxygen evolution reaction (OER) is crucial for sustainable energy conversion technologies. In this work, we successfully used the Ni-modified Keggin-type polyoxometalate ([PNi(H₂O)W₁₁O₃₉]⁵⁻) as a precursor to chemically modify the zeolitic imidazolate framework ZIF 67 via a facile one-pot method. The resulting composite catalyst shows promising electrocatalytic OER performance in a 1 M aqueous KOH solution with high faradaic efficiency. Higher reactivity is observed compared with several reference composites. This synthetic approach could provide access to designing a new class of highly reactive catalysts for targeted reactions.

Introduction

The electrochemical oxygen evolution reaction (OER) from water is one of the most challenging chemical reactions for clean energy conversion and storage [1,2]. In the past decades, enormous efforts have been devoted to developing efficient and inexpensive water oxidation catalysts (WOCs) [3,4]. Specifically, polyoxometalates (POMs) have gained wide-spread attention and become one of the most promising classes of molecular WOCs [5,6]. POMs are polyanionic metal oxide clusters with based on earth-abundant high-valent transition metals (e. g., Mo, W, and V), and are capable of reversible storing multiple electrons [7,8]. The catalytic properties of POMs can be tuned via the introduction of transition metals (e.g., Fe, Co, and Ni) [9]. However, POMs are normally chemically unstable in alkaline media, where the OER is thermodynamically favored [6]. Also, the specific surface area of non-modified POM solids is low, which limits their catalytic performance [10]. One of the solutions to overcome these drawbacks is to embed POMs into porous substrates, like carbon nanotubes [7], metal foams [1,11], and MOFs [12]. Zeolitic imidazolate frameworks (ZIFs), formed by coordination reactions between imidazolate-derived ligands and metal ions, are also good candidates as substrates for POMs [3,12]. However, highly crystalline ZIFs can cause problems, as most of the

active sites are confined within the framework pores, so that mass transfer and gas bubble blockage can limit reactivity [13]. Recently, amorphization of ZIFs was proposed as an efficient method to solve the above-mentioned issues, as amorphous ZIFs (amZIFs) possess a high number of reactive defect sites, leading to improved OER performance [14]. In previous reports, amZIFs were synthesized via thermal conversion [15], ball-milling [16], scanning-electron beam exposure [16], and imidazolate assisted amorphization [14].

Herein, a facile one-pot strategy has been developed to fabricate Ni-modified Keggin-type POM ([PNi(H₂O)W₁₁O₃₉]⁵⁻ (=PNIW₁₁))-functionalized amZIFs (PNIW₁₁@amZIF) (Fig. 1). The resulting composite is highly OER active, so that the synthetic approach opens new pathways for designing amorphous ZIFs doped with POMs to achieve highly efficient catalytic properties.

Results and discussion

The composite (PNIW₁₁@amZIF) was prepared via a facile one-pot method. Briefly, during the standard synthesis of ZIF 67 in methanol solution, an aqueous PNIW₁₁ solution was introduced, which led to the formation of amZIF with a homogenous dispersion of POMs. As references, we used pure crystalline ZIF 67 and we prepared a reference

* Corresponding authors at: Department of Chemistry, Johannes Gutenberg University Mainz, Duesbergweg 10-14, 55131 Mainz, Germany.

E-mail addresses: Rongji.liu@uni-mainz.de (R. Liu), Carsten.streb@uni-mainz.de (C. Streb).

<https://doi.org/10.1016/j.rechem.2022.100568>

Received 5 August 2022; Accepted 9 October 2022

Available online 13 October 2022

2211-7156/© 2022 The Authors. Published by Elsevier B.V. This is an open access article under the CC BY-NC-ND license (<http://creativecommons.org/licenses/by-nc-nd/4.0/>).

composite using non-Ni-modified POMs ($[\text{PW}_{12}\text{O}_{40}]^{3-}$), resulting in $\text{PW}_{12}@amZIF}$ (Fig. S1). The immobilization of POM anions into amZIFs is observed by attenuated total reflection Fourier transform infrared spectroscopy (ATR-FTIR), transmission electron microscopy (TEM) combined with energy-dispersive X-ray spectroscopy (EDX). As shown in Fig. 2a, in cases of $\text{PNiW}_{11}@amZIF}$ and $\text{PW}_{12}@amZIF}$, prominent peaks (red dots) at 1055, 953, 884, and 805 cm^{-1} are assigned to $\nu_{(P-O)}$, $\nu_{(W-O)}$, corner-sharing $\nu_{(W-O-W)}$, and edge-sharing $\nu_{(W-O-W)}$, respectively [17–19], which also supports the presence of POM anions. Peaks corresponding to amZIF were not prominent due to the high POM loading. Signals in the range of 600–1500 cm^{-1} are attributed to the characteristic stretching and bending modes of the imidazole ring and the peak at 1579 cm^{-1} is attributed to the stretching mode of C=N in 2-methylimidazole [20,21]. The appearance of Ni and W detected by STEM-EDX mapping in $\text{PNiW}_{11}@amZIF}$ is assigned to the presence of PNiW_{11} anions (Fig. S2), which also supported the deposition of POMs into amZIF. Note that the reference composite $\text{PW}_{12}@amZIF}$ shows similar features but does not show any signals associated with nickel.

The powder X-ray diffraction (pXRD) patterns of the as-prepared composites are shown in Fig. 2b. No distinct peaks are observed for $\text{PW}_{12}@amZIF}$ and $\text{PNiW}_{11}@amZIF}$, highlighting the amorphous structure of the two composites. This was supported by high-resolution TEM (HRTEM) and selected area electron diffraction (SAED) (Fig. 3e, i), which indicated no observable lattice fringes or distinct electron diffraction peaks by detecting only amorphous material. Thus, introducing the aqueous POM solution to the standard ZIF 67 reaction mixture results in the formation of amorphous composites.

TEM images together with electron diffraction patterns and SEM images (Fig. 3) indicate that POM encapsulation significantly affects the morphologies of $\text{PW}_{12}@amZIF}$ and $\text{PNiW}_{11}@amZIF}$. In the case of pure ZIF 67 (Fig. 3a), the regular polyhedral particles with large dimensions (ca. 1 μm) are observed. However, in the case of $\text{PW}_{12}@amZIF}$, original polyhedral motifs are preserved, but the edges become rounded. Meanwhile, the particle diameters are reduced to ca. 100 nm. A completely different scenario is observed in $\text{PNiW}_{11}@amZIF$. The polyhedral structure disappears, with the dimensions of irregular-shaped particles ranging from ~50 to ~200 nm, which is much smaller than the crystalline ZIF 67. Both $\text{PW}_{12}@amZIF}$ and $\text{PNiW}_{11}@amZIF}$ show significant aggregation with aggregate diameters of ca. 10 μm . We also note a major morphological difference between $\text{PW}_{12}@amZIF}$ and $\text{PNiW}_{11}@amZIF}$. The $\text{PW}_{12}@amZIF}$ aggregates are composed of rounded nanoparticles, while in $\text{PNiW}_{11}@amZIF}$, the aggregates mainly consist of nanorods and nanosheets. Although the POM clusters are not directly imaged by HRTEM, local EDX mappings (Fig. S2) shows a homogeneous distribution of the expected metal elements in both $\text{PW}_{12}@amZIF}$ and $\text{PNiW}_{11}@amZIF}$. However, HRTEM clearly indicates that the POM does not aggregate into larger nanoscale structures. The elemental oxidation states of $\text{PNiW}_{11}@amZIF}$ were

detected via X-ray photoelectron spectroscopy (XPS) as well. The survey XPS spectrum (Fig. S3) shows the presence of O, W, Ni, C, and Co, which agrees with the integration of POM into ZIF. Besides, we also find that the main valence of W is W^{5+} , indicating the reduction of W^{6+} . Meanwhile, Co^{2+} is partially oxidized to Co^{3+} . The results indicate the occurrence of electrons transfer between the ZIF and POM during the material synthesis, and suggests that structural rearrangement of the POM might be possible.

Next, the electrochemical catalytic activities of the catalysts were investigated in alkaline solution (1 M aqueous KOH, pH = 13.7) with a standard three-electrode electrochemical setup, in which Hg/HgO worked as reference electrode and platinum foil worked as the counter electrode. The catalysts were drop-casted on the disk of a rotating ring-disk electrode (RRDE) composed of a glassy carbon disk and Pt ring (RRDE). All applied potentials were converted to reversible hydrogen electrode potentials (RHE, details in SI). The OER electrocatalytic performance of the catalysts was assessed via linear sweep voltammetry (LSV) at a scan rate of 5 $\text{mV}\cdot\text{s}^{-1}$. The results indicate that $\text{PNiW}_{11}@amZIF}$ possesses the best catalytic ability toward OER with an overpotential of $\eta = 375$ mV at the current density of $j = 10$ $\text{mA}\cdot\text{cm}^{-2}$ (Fig. 4a, Table S1). In contrast, significantly higher overpotentials are observed for $\text{PW}_{12}@amZIF}$ (423 mV) and crystalline ZIF 67 (468 mV) respectively. The catalyst also shows superior catalytic properties compared to reported POM@ZIF based catalysts (Table S2). The results reveal that the deposition of POM precursors in amZIF improves electrocatalytic properties. Also, the use of Ni-containing POM precursors results in more active OER catalysts compared to the use of non-modified PW_{12} . Tafel plot analysis (η versus $\log(j)$) (Fig. 4b, Fig. S4) was applied to assess the OER kinetics. $\text{PNiW}_{11}@amZIF}$ shows the lowest Tafel slope of 69 $\text{mV}\cdot\text{dec}^{-1}$ which indicates this catalyst possesses faster reaction kinetics than $\text{PW}_{12}@amZIF}$ (86 $\text{mV}\cdot\text{dec}^{-1}$) and crystalline ZIF 67 (105 $\text{mV}\cdot\text{dec}^{-1}$). This suggests that OER is kinetically favored in $\text{PNiW}_{11}@amZIF}$ compared with $\text{PW}_{12}@amZIF}$ and ZIF 67. To gain deeper insights into the reaction mechanism, we used RRDE analysis. A potential of 1.5 V was applied on the Pt ring electrode to oxidize possibly formed partially oxidized species produced in case of two-electron transfer reaction, such as H_2O_2 (details in SI). An extremely low ring current (μA scale) was detected (Fig. S5), which indicates negligible peroxide intermediates formation and a desirable 4-electron pathway with an electron transfer number $n = 3.9$ for OER. The faradaic efficiency of $\text{PNiW}_{11}@amZIF}$ was also assessed through RRDE with the ring potential of 0.40 V to reduce the O_2 generated in the disk during OER (Fig. 4c). As a result, the ring current of ~23 μA (collection efficiency was determined to be 0.15), and disk current of ~160 μA are detected, which revealed a high faradaic efficiency of 96 % (detailed calculation see SI).

The double-layer capacitances (C_{dl}) of $\text{PNiW}_{11}@amZIF}$ and $\text{PW}_{12}@amZIF}$, which are proportional to the electrochemically active

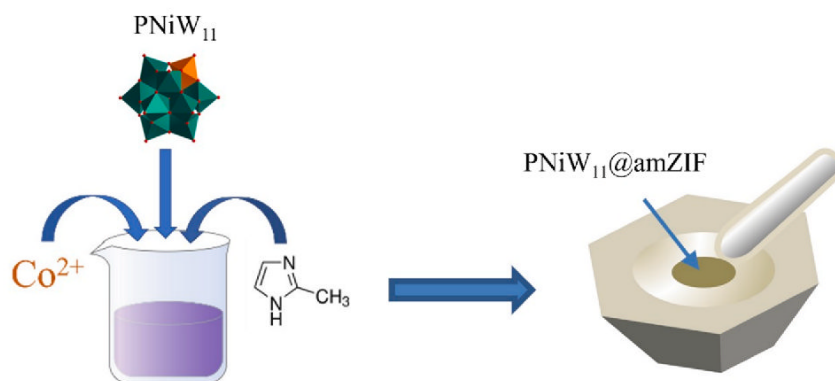


Fig. 1. Schematic materials design and fabrication approach (PNiW_{11} : $\text{K}_5\text{PNi}(\text{H}_2\text{O})\text{W}_{11}\text{O}_{39}\cdot x\text{H}_2\text{O}$).

3. Results and discussion

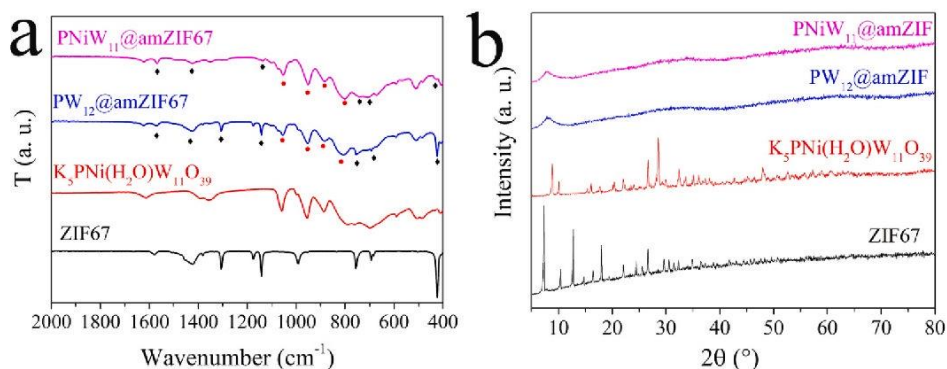


Fig. 2. (a) ATR-FTIR spectra and (b) pXRD of PNiW₁₁@amZIF, PW₁₂@amZIF, K₅PNi(H₂O)W₁₁O₃₉, and ZIF 67.

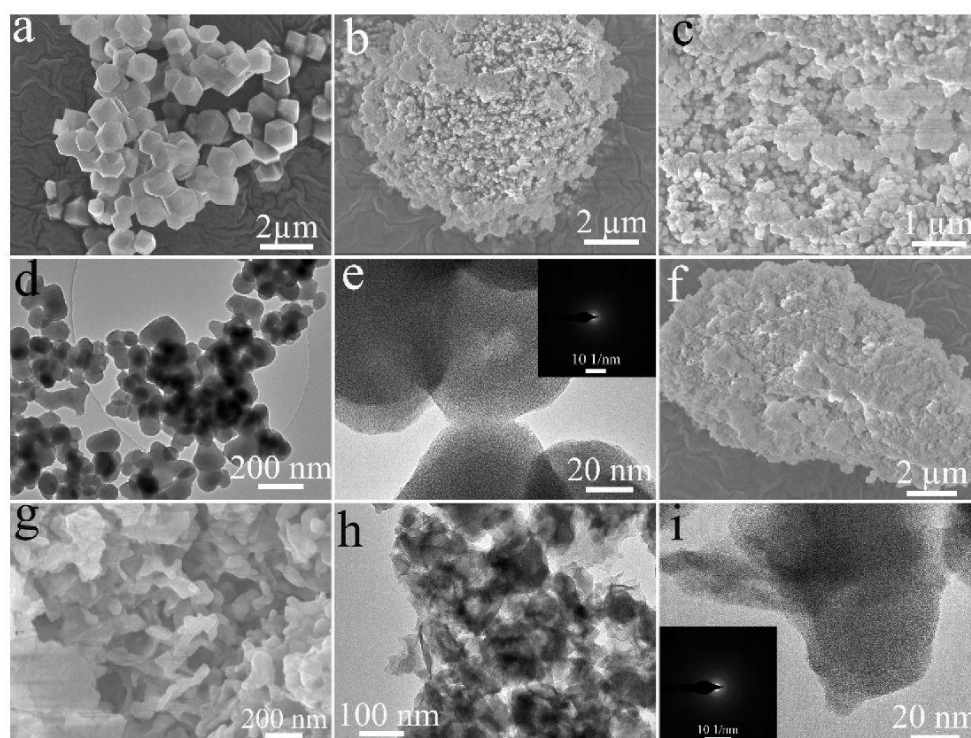


Fig. 3. Structural characterizations: SEM images of ZIF 67 (a), PW₁₂@amZIF (b, c), and PNiW₁₁@amZIF (f, g); TEM images of PW₁₂@amZIF (d) and PNiW₁₁@amZIF (h); HTREM images with corresponding selected area electron diffraction (insert) pattern of PW₁₂@amZIF (e) and PNiW₁₁@amZIF (i).

areas (ECSAs), were examined to gain a deeper understanding of the factors triggering the good catalytic performance in OER (Fig. 4d). Both PNiW₁₁@amZIF and PW₁₂@amZIF show higher C_{dl} than the crystalline ZIF 67, which indicates the deposition of POMs in amZIF increases number of accessible reactive sites and enhances electrocatalytic performance in OER. Also, the higher C_{dl} in PNiW₁₁@amZIF than PW₁₂@amZIF indicates the modification of Ni in POMs is beneficial to increasing the active sites and improve electrocatalytic properties as well. This observation is in line with the experimental electrocatalytic data described above, and with recent literature results [22,23]. Electrochemical impedance spectroscopy (EIS) (Fig. 4e) was tested to evaluate the charge transfer ability within the reaction systems. The results indicate that PNiW₁₁@amZIF possesses the lowest charge transfer resistance, which reveals a higher reaction rate than PW₁₂@amZIF and ZIF 67.

Next, the long-term stability of PNiW₁₁@amZIF was examined under a given operating condition (1 M aqueous KOH, $E = 1.63$ V) using chronoamperometry. Here, PNiW₁₁@amZIF was drop-cast on the carbon paper that is inactive to OER. As shown in Fig. 4f, the value of j decreases rapidly during the initial 2 h. Then the value of j reaches a stable state and 75 % of the original current density remains. During the OER, bubbles formed continuously. After 14 h of catalysis, the bubbles on the surface of carbon paper were removed (see the arrow in Fig. 4f) and j increased immediately, which indicates that the formation of bubbles hinders efficient OER. The chronoamperometric tests at higher potentials were performed as well. The results (Fig. S7) also indicate slight degradation of the catalyst over the course of the experiment. The post-catalysis material characterization was carried out to gain a deeper understanding of the material transition during catalysis. The chemical and morphological analysis was performed using post catalytic TEM/

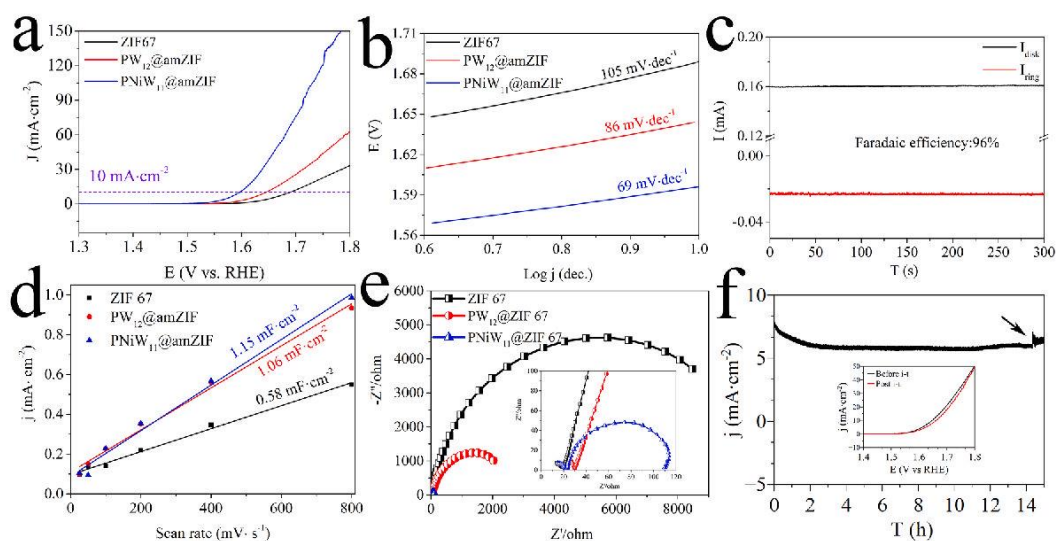


Fig. 4. a) IR-corrected OER polarization curves, b) Tafel plots, and c) Faradaic efficiency, d) C_{dl} and e) EIS for ZIF 67, $PW_{12}@amZIF$, and $PNiW_{11}@amZIF$; f) Stability of $PNiW_{11}@amZIF$.

EDX (Fig. S6). After catalysis, fiber-like crystalline structures formed in the materials, which were identified as Co_2O_3 by EDX and SAED. The elemental mapping revealed the aggregation of Co and O, while W and Ni are still uniformly dispersed on the amZIF after catalysis. We propose that the initial drop of j is based on the bubble formation and the chemical/morphological rearrangements occurring under OER operation. After the first 2 h of OER, the Co_2O_3 formed does not further change, and the catalyst reaches the final stable catalytic state.

In summary, we report a facile in-situ synthesis of POMs modified amZIF. The resulting composite shows high performance for OER with low overpotential (375 mV at 10 mA cm^{-2}), high faradaic efficiency (96%), and a Tafel slope of 69 mV dec^{-1} . The catalytic can keep high catalytic properties after long-term catalysis. We propose that the concept of this new material design allows us to prepare targeted amorphous ZIF with the modification of POMs to provide more active sites for catalysis.

CRediT authorship contribution statement

Yupeng Zhao: Methodology, Data curation, Investigation, Writing – original draft. **Dandan Gao:** Investigation, Data curation, Writing – original draft. **Johannes Biskupek:** Investigation, Data curation, Writing – original draft. **Ute Kaiser:** Data curation, Writing – original draft. **Rongji Liu:** Conceptualization, Supervision, Data curation, Methodology, Writing – original draft. **Carsten Streb:** Project administration, Funding acquisition, Conceptualization, Supervision, Data curation, Methodology, Writing – original draft.

Declaration of Competing Interest

The authors declare that they have no known competing financial interests or personal relationships that could have appeared to influence the work reported in this paper.

Data availability

Data will be made available on request.

Acknowledgments

The authors gratefully acknowledge financial support by the Deutsche Forschungsgemeinschaft DFG (Cluster of Excellence EXC2154,

POLIS, project number: 390874152 and TRR 234 Catalight, project number: 364549901). C.S. gratefully acknowledges financial support by Johannes Gutenberg University Mainz, the Rheinland-Pfalz Research Initiative SusInnoScience and the Gutenberg Research College.

Appendix A. Supplementary data

Supplementary data to this article can be found online at <https://doi.org/10.1016/j.rechem.2022.100568>.

References

- [1] W. Li, S. Watzel, H.A. El-Sayed, Y. Liang, G. Kieselich, A.S. Bandarenka, K. Rodewald, B. Rieger, R.A. Fischer, *J. Am. Chem. Soc.* 141 (2019) 5926–5933.
- [2] B. Rausch, M.D. Symes, G. Chisholm, L. Cronin, *Science* 214 (345) (1979) 1326–1330.
- [3] S. Mukhopadhyay, J. Debgupta, C. Singh, A. Kar, S.K. Das, S. Mukhopadhyay, D.R. J. Debgupta, C. Singh, A. Kar, R.S.K. Das, *Angew. Chem.* 130 (2018) 1936–1941.
- [4] B. Y. Xia, Y. Yan, N. Li, H. bin Wu, X. W. D. Lou, X. Wang, *Nature Energy* 2016 1:1 2016, 1, 1–8.
- [5] M. Blasco-Ahicart, J. Soriano-Lopez, J. J. Carbo, J. M. Poblart, J. R. Galan-Mascaros, *Nature Chemistry* 2017 10:1 2017, 10, 24–30.
- [6] W. Luo, J. Un Hu, H. Diao, B. Schwarz, C. Streb, Y.-F. Song, W. Luo, J. Hu, H. Diao, B. Schwarz, C. Streb, *Angew. Chem. Int. Ed.* 56 (2017) 4941–4944.
- [7] J. Hu, Y. Ji, W. Chen, C. Streb, Y.-F. Song, *Energy Environ. Sci.* 9 (2016) 1095.
- [8] J.W. Jordan, G.A. Lowe, R.L. McSweeney, C.T. Stoppello, R.W. Lodge, S. T. Skowron, J. Biskupek, G.A. Rance, U. Kaiser, D.A. Walsh, G.N. Newton, A. N. Khllobystov, *Adv. Mater.* 31 (2019) 1904182.
- [9] A. Patel, N. Narkhede, S. Singh, S. Pathan, <https://doi.org/10.1080/01614940.2016.1171606> 2016, 58, 337–370.
- [10] S.B. Ingavale, I. Patil, H. Parse, D.C. Sesu, P. Marbaniang, N. Ramgiri, B. Kakade, A. Swami, *Int. J. Hydrogen Energy* 44 (2019) 24922–24933.
- [11] D. Gao, R. Liu, J. Biskupek, U. Kaiser, Y.F. Song, C. Streb, *Angew. Chem. Int. Ed.* 58 (2019) 4644–4648.
- [12] G. Paille, M. Gomez-Mingot, C. Roch-Marchal, M. Haouas, Y. Benseghir, T. Pino, M. H. Ha-Thi, G. Landrot, P. Mialane, M. Fontecave, A. Dolbecq, C. Mellot-Draznicks, *ACS Appl. Mater. Interfaces* 11 (2019) 47837–47845.
- [13] J. Li, W. Huang, M. Wang, S. Xi, J. Meng, K. Zhao, J. Jin, W. Xu, Z. Wang, X. Liu, Q. Chen, L. Xu, X. Liao, Y. Jiang, K.A. Owusu, B. Jiang, C. Chen, D. Fan, L. Zhou, L. Mai, *ACS Energy Lett.* 4 (2019) 285–292.
- [14] C. Liu, J. Wang, J. Wan, Y. Cheng, R. Huang, C. Zhang, W. Hu, G. Wei, C. Yu, *Angew. Chem.* 132 (2020) 3659–3666.
- [15] T.D. Bennett, D.A. Keen, J.-C. Tan, E.R. Barney, A.L. Goodwin, A.K. Cheetham, *Angew. Chem.* 123 (2011) 3123–3127.
- [16] S. Cao, T.D. Bennett, D.A. Keen, A.L. Goodwin, A.K. Cheetham, *Chem. Commun.* 48 (2012) 7805–7807.
- [17] S. Rana, S. Mallick, L. Mohapatra, G.B.B. Varadwaj, K.M. Parida, *Catal. Today* 198 (2012) 52–58.
- [18] L.R. Pizzio, M.N. Blanco, *Mater. Lett.* 61 (2007) 719–724.

3. Results and discussion

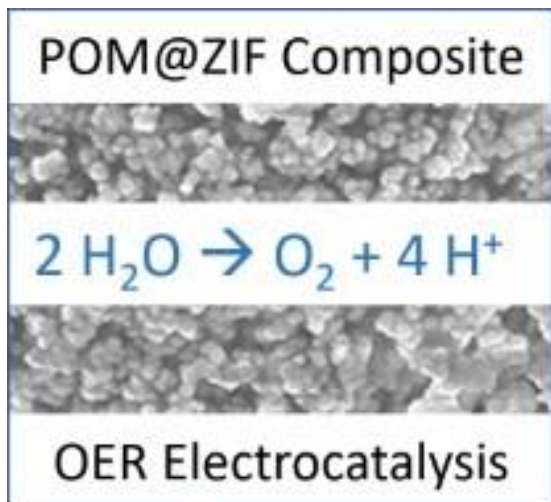
Y. Zhao et al.

Results in Chemistry 4 (2022) 100568

- [19] X. Sun, J. Dong, Z. Li, H. Liu, X. Jing, Y. Chi, C. Hu, Dalton Trans. 48 (2019) 5285–5291.
- [20] A. Khan, M. Ali, A. Ilyas, P. Naik, I.F.J. Vankelecom, M.A. Gilani, M.R. Bilal, Z. Sajjad, A.L. Khan, Sep. Purif. Technol. 206 (2018) 50–58.
- [21] A. Zanon, S. Chaemchuen, B. Mousavi, F. Verpoort, J. CO2 Util. 20 (2017) 282–291.
- [22] V.K. Abdelkader-Fernández, D.M. Fernandes, S.S. Balula, L. Cunha-Silva, C. Freire, J. Mater. Chem. A 8 (2020) 13509–13521.
- [23] V.K. Abdelkader-Fernández, D.M. Fernandes, S.S. Balula, L. Cunha-Silva, C. Freire, ACS Appl. Energy Mater. 3 (2020) 2925–2934.

3.2 POM@ZIF derived mixed metal oxide catalysts for sustained electrocatalytic oxygen evolution

Yupeng Zhao, Dandan Gao, Si Liu, Johannes Biskupek, Ute Kaiser, Rongji Liu, Carsten Streb



This publication demonstrated how polyoxometalate (POM)-doped ZIF-67 can be converted into a stable oxygen evolution electrocatalyst by chemical etching, cation exchange, and thermal annealing steps. The resulting composite shows structural and compositional advantages which lead to low overpotential (306 mV at $j=10 \text{ mA} \cdot \text{cm}^{-2}$) and long-term stability under harsh OER conditions (1.0 M aqueous KOH).

Author Contributions:

Yupeng Zhao: Conceptualization, Methodology, Data curation, Investigation, Writing original draft.

Dandan Gao: Investigation, Data curation, Writing original draft.

Si Liu: Methodology, Data curation, Writing original draft.

Johannes Biskupek: Investigation, Data curation, Writing original draft.

Ute Kaiser: Data curation, Writing original draft.

Rongji Liu: Conceptualization, Supervision, Data curation, Methodology, Writing original draft.

Carsten Streb: Project administration, Funding acquisition, Conceptualization, Supervision, Data curation, Methodology, Writing original draft.

Supporting Information can be found at pp 125.

“Y. Zhao, D. Gao, S. Liu, J. Biskupek, U. Kaiser, R. Liu, C. Streb, *Chemistry – A European Journal* **2023**, 29, e202203220” Reprinted with permission, © 2022 The Authors. *Chemistry - A European Journal* published by Wiley-VCH GmbH



POM@ZIF Derived Mixed Metal Oxide Catalysts for Sustained Electrocatalytic Oxygen Evolution

Yupeng Zhao,^[a, b] Dandan Gao,^[a, b] Si Liu,^[b] Johannes Biskupek,^[c] Ute Kaiser,^[c]
Rongji Liu,^{*[a, b, d]} and Carsten Streb^{*[a, b, d]}

Abstract: The design of efficient and stable oxygen evolution reaction (OER) catalysts based on noble-metal-free materials is crucial for energy conversion and storage. In this work, it was demonstrated how polyoxometalate (POM)-doped ZIF-67 can be converted into a stable oxygen evolution electrocatalyst by chemical etching, cation exchange, and thermal annealing steps. Characterization by X-ray photoelectron

spectroscopy, transmission electron microscopy, energy-dispersive X-ray spectroscopy and Raman spectroscopy indicate that POM-doped ZIF-67 derived carbon-supported metal oxides were synthesized. The resulting composite shows structural and compositional advantages which lead to low overpotential (306 mV at $j=10 \text{ mA}\cdot\text{cm}^{-2}$) and long-term stability under harsh OER conditions (1.0 M aqueous KOH).

Introduction

Electrochemical splitting of water into oxygen and hydrogen is one of the most promising large-scale solutions for converting and storing electrical energy.^[1–4] Technological implementation and scale-up of this process is hindered, particularly as the oxygen evolution reaction (OER) is demanding, as it involves the proton-coupled transfer of four electrons, operates under harsh oxidative conditions, and often shows slow reaction kinetics.^[5–7] Developing effective oxygen evolution catalysts (OECs) is therefore crucial to improve conversion efficiency from intermittent electrical to storable chemical energy. While early studies have focused on understanding the performance of RuO₂ and IrO₂ electrocatalysts,^[8,9] recent research has centered

on developing robust catalysts based on earth-abundant metals.^[5,7,10–13] Recently, composites based on zeolitic imidazolate frameworks (ZIFs) and polyoxometalates (POMs) have gained widespread attention as promising OER catalysts.^[4,14–16] Specifically, ZIF-67 shows ordered porosity and high specific surface area,^[17] making it ideal for the doping with POMs which can introduce reversible multi-electron redox behaviors.^[4] In addition, ZIF-67 is constructed around OER-active Co²⁺ metal nodes. Based on these concepts, a large number of studies have explored the depositing of POMs into ZIFs pores to access OER-active materials. For example, [H₆CoW₁₂O₄₀]₂@ZIF-8 shows stable OER properties at neutral pH,^[10] also, TBA-SiW₁₁CoO₃₅@ZIF-67 exhibits enhanced OER activities compared with pristine ZIF-67,^[17] and similarly, OER activity of TBA-SiW₉Co₃@ZIF-67 is increased when compared with that of the non-modified ZIF-67.^[18] Despite this progress, there are still major challenges in the field of POM@ZIF-derived OER catalysts. One challenge is that in native ZIFs, most active sites (i.e. metal nodes and embedded POMs) are confined in the inside of the framework,^[19] making access by the water substrate and release of the gaseous O₂ product difficult, resulting in often limited performance.^[20] Also, both POMs and ZIFs are poor electrical conductors, so that electrocatalytic performance is limited due to high internal resistance.^[11] Finally, POMs are unstable in alkaline solutions and most POMs spontaneously degrade at pH > 8. Similarly, ZIFs are prone to degradation under electrochemical conditions in alkaline media. This can result in the conversion of Co²⁺ from ZIF-67 to α -Co(OH)₂ and β -Co(OH)₂, followed by the formation of their corresponding oxidized forms (CoOOH),^[21,22] while the original frameworks collapse and lose their porosity.^[23,24] As these chemical and structural changes generally lead to low catalytic activity, various conversion routes have been developed to access more robust, more active POM@ZIF derived composites, leading to metal oxides,^[25] metal sulfides,^[26] metal carbides,^[27] and metal phosphides.^[28,29] Often, these composites combine increased

[a] Y. Zhao, Dr. D. Gao, Dr. R. Liu, Prof. Dr. C. Streb
Department of Chemistry
Johannes Gutenberg University Mainz
Duesbergweg 10–14, 55131 Mainz (Germany)
E-mail: rongji.liu@uni-mainz.de
carsten.streb@uni-mainz.de
Homepage: <https://www.strebgroupp.net/>

[b] Y. Zhao, Dr. D. Gao, Dr. S. Liu, Dr. R. Liu, Prof. Dr. C. Streb
Institute of Inorganic Chemistry I
Ulm University
Albert-Einstein-Allee 11, 89081 Ulm (Germany)

[c] Dr. J. Biskupek, Prof. Dr. U. Kaiser
Central Facility of Electron Microscopy for Materials Science
Ulm University
Albert-Einstein-Allee 11, 89081 Ulm (Germany)

[d] Dr. R. Liu, Prof. Dr. C. Streb
Helmholtz-Institute Ulm
Electrochemical Energy Conversion
Helmholtzstrasse 11, 89081 Ulm (Germany)

Supporting information for this article is available on the WWW under <https://doi.org/10.1002/chem.202203220>

© 2022 The Authors. Chemistry – A European Journal published by Wiley-VCH GmbH. This is an open access article under the terms of the Creative Commons Attribution Non-Commercial License, which permits use, distribution and reproduction in any medium, provided the original work is properly cited and is not used for commercial purposes.

electrical conductivity with chemical and mechanical stability, making them interesting new OER catalysts.

Here, we report a facile chemical route to convert POM-doped ZIF-67, giving access to a noble metal-free OER catalyst using a combination of acid etching followed by cation-exchange and thermal annealing. The route enables conversion of the original $[\text{H}_3\text{PW}_{12}\text{O}_{40}]$ -doped amorphous ZIF-67 ($\text{PW}_{12}@amZIF$) into carbon-supported metal oxide composites. The catalyst shows excellent OER performance in 1 M aqueous KOH electrolyte with sustained electrochemical activity. This work presents a facile approach to produce high performance electrocatalyst composite for OER in alkaline media.

Results and Discussion

The synthesis process, using a weak acid-assisted etching and subsequent ion exchange and thermal annealing is presented in Figure 1. Briefly, amorphous POM doped ZIF-67 ($\text{PW}_{12}@amZIF$) was prepared via a facile in situ method (details in the Supporting Information). To improve porosity and pore accessibility, the native $\text{PW}_{12}@amZIF$ was etched with tannic acid.^[20] Next, Ni^{2+} and Fe^{3+} were introduced into the system by a cation exchange process. The final product was obtained after annealing at 300 °C in air for 3 h, and labelled **Catalyst 1**. For synthetic details, see the Supporting Information. To understand the synergistic effect of the presence of multiple metal reaction sites, catalysts without W, Fe, and Ni were also prepared for as reference materials, and labelled **Catalyst 2**

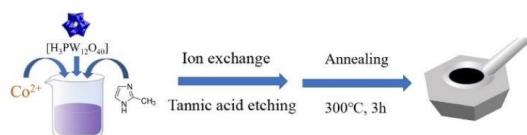


Figure 1. schematic materials design and fabrication approach.

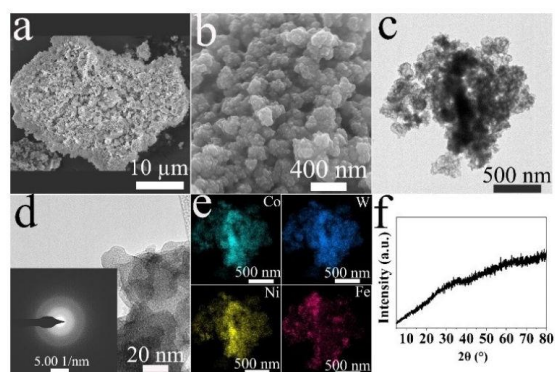


Figure 2. Structural and compositional analysis of Catalyst 1: (a and b) SEM images at low and high magnification. (c and d) TEM and HRTEM images with insert of SAED pattern. (e) STEM-EDX elemental mappings (f) pXRD pattern.

(without W), **Catalyst 3** (without Fe), and **Catalyst 4** (without Ni), respectively.

Scanning electron microscopy (SEM), aberration-corrected high-resolution transmission electron microscopy (HRTEM), and scanning transmission electron microscopy (STEM) were employed to examine the morphology of **Catalyst 1** and its precursor $\text{PW}_{12}@amZIF$. The resulting HRTEM image (Figure 2c) reveals that **Catalyst 1** possesses a hollow structure that does not exist in the pristine $\text{PW}_{12}@amZIF$. We assign the formation of these hollow structures to the tannic acid etching, as similar properties have been reported previously in tannic acid-etched materials.^[20] Also, the particle size of **Catalyst 1** (Figure 2a, b) is larger than $\text{PW}_{12}@amZIF$ (Figure S1a, b), suggesting that aggregation occurred during the cation-exchange and thermal annealing, resulting in low specific surface area. For **Catalyst 1**, no obvious lattice fringes are observed in HRTEM (Figure 2d) and the corresponding selected area electron diffraction (SAED) pattern (Figure 2d insert) only shows an obvious halo, which indicates their amorphous structure^[30] and is in agreement with the powder X-ray diffraction (pXRD) data (Figure 2f). Energy-dispersive X-ray spectroscopy (EDX)-STEM elemental mappings (Figure 2e) verify the presence of homogeneously dispersed W, Co, Ni, and Fe within the catalyst. This indicates that the Ni and Fe ion exchange into the material was successful and led to a homogeneous distribution of these metal ions. To gain more composition information of **Catalyst 1**, inductively coupled plasma optical emission spectroscopy (ICP-OES, Table S1) was employed as well and gave an approximate atomic ratio of 1:1.1:2:0.2 (Ni/W/Co/Fe).

The elemental oxidation states of **Catalyst 1** were studied by X-ray photoelectron spectroscopy (XPS). The survey XPS spectrum (Figure 3a) indicates the presence of O, C, W, Co, Ni, and Fe. The deconvoluted high-resolution W 4f XPS spectrum (Figure 3b) suggests the presence of W^{6+} in **Catalyst 1** (35.34 eV for $\text{W } 4f_{7/2}$ and 37.51 eV for $\text{W } 4f_{5/2}$).^[31] XPS analysis also suggests that both, Ni (Figure 3c) and Fe (Figure 3d) are present in oxidation state +3 (856.07 eV for $\text{Ni } 2p_{3/2}$ and 873.37 eV for $\text{Ni } 2p_{1/2}$; 711 eV for $\text{Fe } 2p_{3/2}$ and 724 eV for $\text{Fe } 2p_{1/2}$). In contrast, XPS analysis for cobalt (Figure 3e), suggest mixed

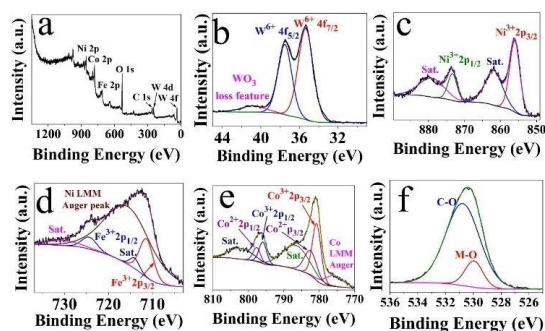


Figure 3. XPS spectra of Catalyst 1: (a) overview spectrum, (b-f) deconvoluted high-resolution spectra of W 4f (b), Ni 2p (c), Fe 2p (d), Co 2p (e), and (f) O 1s.

Co^{2+/3+} oxidation states as indicated by the characteristic signals at 780.7 eV (2p_{3/2} for Co³⁺) and 782.4 eV (2p_{3/2} for Co²⁺).^[32] The molar ratio of Co³⁺: Co²⁺ is approx. 1.6: 1. The deconvoluted XPS spectrum for O 1s (Figure 3f) indicates two distinct signals assigned to metal oxide and carbon oxygen species. The presence of metal oxide species is further indicated by characteristic signals in the Raman spectrum of **Catalyst 1** (Figure S2). Further, Raman spectroscopy also showed two intense signals at 1313 cm⁻¹ and 1586 cm⁻¹, corresponding to the D and G bands of the carbon matrix.^[33,34] The obtained results indicate that the organic imidazole ligands of the ZIF have been converted into carbonaceous compounds after thermal annealing, which act as heterogeneous support for the metal oxides formed.

Next, we investigated the electrochemical activity of **Catalyst 1** in alkaline aqueous solution (1 M aqueous KOH, pH = 13.7) with a standard three-electrode electrochemical setup, in which Hg/HgO was used as reference electrode and platinum foil as the counter electrode. The catalysts were drop-cast on a glassy carbon rotating disk electrode (RDE) which was used as working electrode. All potentials were converted to reversible hydrogen electrode potentials (RHE, see details in Supporting Information). The OER electrocatalytic performance was assessed by linear sweep voltammetry (LSV) at a scan rate of 5 mV·s⁻¹. **Catalyst 1** shows the best performance for OER with an overpotential of $\eta = 306$ mV at the current density of $j = 10$ mA·cm⁻² (Figure 4a, b). In contrast, **Catalyst 2**, **Catalyst 3**, and **Catalyst 4** show significantly higher overpotentials at the current density of $j = 10$ mA·cm⁻². Tafel plot analysis (η versus log(j)) was used to assess the OER kinetics (Figure 4c). Amongst the materials compared, **Catalyst 1** shows the lowest Tafel slope (54 mV·dec⁻¹), while the reference samples show slightly higher Tafel slopes, suggesting that OER is kinetically favored in **Catalyst 1** compared with the reference samples.

To gain deeper insights into the reaction mechanism of **Catalyst 1**, rotating ring-disk electrode (RRDE) voltammetry was used. While the OER reaction was performed at the disk electrode, the Pt ring electrode (at $E = 1.5$ V) was used to oxidize

and detect any partially oxidized intermediates formed, such as H₂O₂ (see details in Supporting Information). Under the given conditions, only a very low ring current (μ A scale) was detected, which indicates that peroxide intermediate formation is negligible, so that **Catalyst 1** favors the preferred 4-electron OER pathway (Figure S3). The faradaic efficiency of **Catalyst 1** was also assessed using RRDE voltammetry. Here, the ring potential was set to $E = 0.40$ V, so that any oxygen formed by OER on the disk electrode is reductively detected at the ring electrode (Figure 4d). Based on the observed ring current (~ 21 μ A, current collection efficiency: 0.15) and disk current (~ 147 μ A), we were able to calculate an OER faradaic efficiency of 94.3% for **Catalyst 1** (detailed calculation in the Supporting Information).

The double-layer capacitance (C_{dl}), which is proportional to the electrochemically active surface area (ECSA), and electrochemical impedance spectroscopy (EIS) were used to gain a deeper understanding of the electrocatalytic performance. The resulting C_{dl} indicates **Catalyst 1** exhibited comparable ECSAs with other reference catalysts **2**, **3** and **4** (Figure S4 and Figure 4e). In contrast, EIS analysis indicates that **Catalyst 1** features the lowest charge transfer resistance (R_{ct}) among the catalysts studied, which leads to efficient interfacial electron transfer (Figure S5). Thus, the high OER performance of **Catalyst 1** is due to low internal charge transfer resistance as well as high intrinsic reactivity of the catalyst.

Next, we examined the long-term stability of **Catalyst 1** under a given operating condition (1 M KOH, $\eta = 340$ mV) using chronoamperometry. In this case, the catalyst was dropped on carbon paper which is chemically stable under OER conditions. As shown in Figure 4f, the value of j increases by 29.3% during the initial first hour. Then it reaches a maximum and drops slightly (ca. 3%) over the following 14 h. We suggest that the initial increase of j is due to chemical and morphological changes of the catalyst, which was studied by post-catalytic STEM-EDX analyses (Figure S6). The elemental mapping reveals that Co, Ni, and O are still distributed homogeneously and that there are no crystalline Co and Ni-based composites present. However, for W and Fe, aggregation is observed and some sheet-like crystalline structures are formed. These are identified as Fe₂O₃ by SAED (lattice spacing) and EDX (elemental ratio between Fe and O). Based on earlier reports, this formation could contribute to the catalytic activity of the catalyst.^[35] Also, post-catalytic XPS analysis of **Catalyst 1** indicates that the Co²⁺ ions are oxidized to more OER-active Co³⁺ species during the catalytic process (Figure S7).^[22] These factors contribute to the observed behavior during the chronoamperometric analysis.

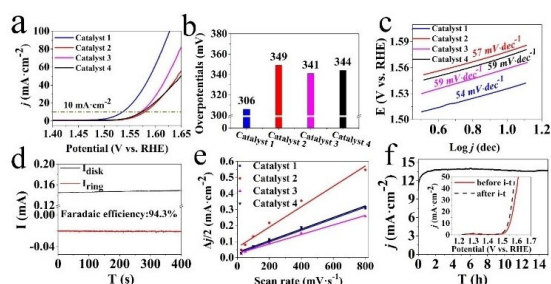


Figure 4. Electrochemical OER performance of **Catalyst 1** and reference catalysts in 1 M aqueous KOH: a) IR-corrected OER polarization curves, b) Overpotentials at $j = 10$ mA·cm⁻², c) Tafel plot, d) RRDE analysis to determine faradaic efficiency for **Catalyst 1**, e) Half of the capacitive current density ($\Delta j/2$) at 0.87 V vs. RHE as a function of the scan rates and f) Chronoamperometry curves at $\eta = 340$ mV (insert: LSV polarization curves comparison before and after 15 h stability test).

Conclusion

A facile design route for the synthesis of noble-metal-free OER catalysts was reported. Structural and compositional synergisms lead to enhanced electrocatalytic OER performance with low overpotential (306 mV at $j = 10$ mA·cm⁻²), high faradaic efficiency (94.3%), and a Tafel slope of 54 mV·dec⁻¹. The catalyst shows long-term robustness and offers a new path for the

scalable design of OER electrocatalysts based on earth-abundant components.

Experimental Section

Synthesis PW₁₂@amZIF: In a typical synthesis, aqueous [H₃PW₁₂O₄₀] \cdot xH₂O solution (0.07 mmol in 10 mL) was added to Co(NO₃)₂ \cdot 6H₂O (0.546 g, 1.8 mmol) methanol solution (25 mL) and kept under magnetic stirring for 0.5 h. Afterward, 2-methylimidazole (0.616 g, 7.5 mmol) methanol solution (25 mL) was added. This reaction was stirred for another 2.5 h. The final, solid product was collected by centrifugation, washed with methanol, and dried at 70 °C overnight.

Acid etching: PW₁₂@amZIF: 150 mg of PW₁₂@amZIF was dispersed in 5 ml of ethanol by sonication for 20 min. The dispersion was added into ethanol/ DI water (10 mL: 15 mL) solution containing 75 mg of tannic acid. The solution was stirred for 10 minutes. Finally, the material was collected via centrifugation, washing with ethanol, and drying at 70 °C overnight.

Metal ions exchange: 50 mg of acid etched material was dispersed in 10 ml of ethanol. Then 24 ml of DI water containing 2.5 mM NiCl₂ and 0.25 mM FeCl₃ were added dropwise. Finally, the solution was stirred at room temperature for 3 h and the material was collected via centrifugation, washing with ethanol, and drying at 70 °C overnight.

Annealing process: The as-prepared material was annealed in air at 300 °C for 3 h with a heating rate of 5 °C \cdot min⁻¹ and natural cool-down to room temperature

Acknowledgements

The authors gratefully acknowledge financial support by the Deutsche Forschungsgemeinschaft DFG (Cluster of Excellence EXC2154, POLiS, project number: 390874152 and TRR 234 Catalight, project number: 364549901 and project no 389183496). R.L. gratefully acknowledges financial support by the Alexander von Humboldt Foundation. R.L., D.G. and C.S. gratefully acknowledge financial support by Johannes Gutenberg University Mainz, the Rheinland-Pfalz Research Initiative SusInnoScience and the Gutenberg Research College. Open Access funding enabled and organized by Projekt DEAL.

Conflict of Interest

The authors declare no conflict of interest.

Data Availability Statement

The data that support the findings of this study are available from the corresponding author upon reasonable request.

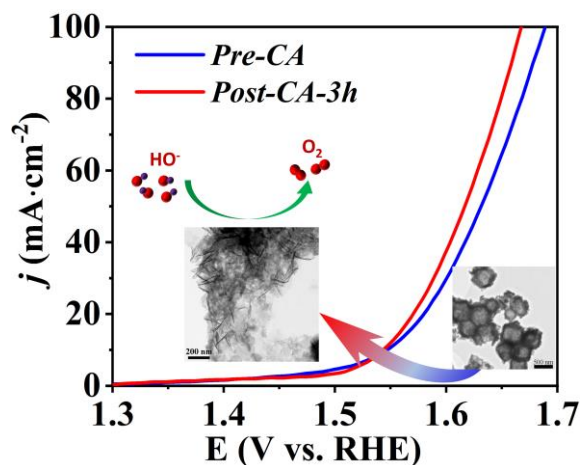
Keywords: composites \cdot electrocatalysis \cdot metal oxides \cdot oxygen evolution reactions \cdot polyoxometalates

- [1] H. Wen, S. Zhang, T. Yu, Z. Yi, R. Guo, *Nanoscale* **2021**, *13*, 12058–12087.
- [2] T. Reier, M. Oezaslan, P. Strasser, *ACS Catal.* **2012**, *2*, 1765–1772.
- [3] S. Yang, J. Y. Zhu, X. N. Chen, M. J. Huang, S. H. Cai, J. Y. Han, J. Sen Li, *Appl. Catal. B* **2022**, *304*, 120914.
- [4] W. Luo, J. Hu, H. Diao, B. Schwarz, C. Streb, Y. F. Song, *Angew. Chem. Int. Ed.* **2017**, *56*, 4941–4944; *Angew. Chem.* **2017**, *129*, 5023–5026.
- [5] W. Li, S. Watzel, H. A. El-Sayed, Y. Liang, G. Kieslich, A. S. Bandarenka, K. Rodewald, B. Rieger, R. A. Fischer, *J. Am. Chem. Soc.* **2019**, *141*, 5926–5933.
- [6] H. Lv, Y. v. Geletii, C. Zhao, J. W. Vickers, G. Zhu, Z. Luo, J. Song, T. Lian, D. G. Musaev, C. L. Hill, *Chem. Soc. Rev.* **2012**, *41*, 7572–7589.
- [7] B. Rausch, M. D. Symes, G. Chisholm, L. Cronin, *Science* **2014**, *345*, 1326–1330.
- [8] R. Samanta, P. Panda, R. Mishra, S. Barman, *Energy Fuels* **2022**, *36*, 1015–1026.
- [9] Y. Lee, J. Suntivich, K. J. May, E. E. Perry, Y. Shao-Horn, *J. Phys. Chem. Lett.* **2012**, *3*, 399–404.
- [10] S. Mukhopadhyay, J. Debgupta, C. Singh, A. Kar, S. K. Das, *Angew. Chem. Int. Ed.* **2018**, *57*, 1918–1923; *Angew. Chem.* **2018**, *130*, 1936–1941.
- [11] B. Y. Xia, Y. Yan, N. Li, H. bin Wu, X. W. D. Lou, X. Wang, *Nat. Energy* **2016**, *1*, 1–8.
- [12] X. F. Lu, Y. Fang, D. Luan, X. W. D. Lou, *Nano Lett.* **2021**, *21*, 1555–1565.
- [13] Y. Liu, D. Zhou, T. Deng, G. He, A. Chen, X. Sun, Y. Yang, P. Miao, *ChemSusChem* **2021**, *14*, 5359–5383.
- [14] M. Blasco-Ahicart, J. Soriano-Lopez, J. J. Carbo, J. M. Poblet, J. R. Galan-Mascaros, *Nat. Chem.* **2018**, *10*, 24–30.
- [15] J. Li, S. Gadipelli, *Chem. Eur. J.* **2020**, *26*, 14167–14172.
- [16] S. L. Zhang, B. Y. Guan, X. F. Lu, S. Xi, Y. Du, X. W. Lou, *Adv. Mater.* **2020**, *32*, 2002235.
- [17] V. K. Abdelkader-Fernández, D. M. Fernandes, S. S. Balula, L. Cunha-Silva, C. Freire, *J. Mater. Chem. A* **2020**, *8*, 13509–13521.
- [18] G. Paille, M. Gomez-Mingot, C. Roch-Marchal, M. Haouas, Y. Benseghir, T. Pino, M. H. Ha-Thi, G. Landrot, P. Mialane, M. Fontecave, A. Dolbecq, C. Mellot-Draznieks, *ACS Appl. Mater. Interfaces* **2019**, *11*, 47837–47845.
- [19] J. Li, W. Huang, M. Wang, S. Xi, J. Meng, K. Zhao, J. Jin, W. Xu, Z. Wang, X. Liu, Q. Chen, L. Xu, X. Liao, Y. Jiang, K. A. Owusu, B. Jiang, C. Chen, D. Fan, L. Zhou, L. Mai, *ACS Energy Lett.* **2019**, *4*, 285–292.
- [20] C. Wang, J. Zhang, Z. Zhang, G. Ren, D. Cai, *RSC Adv.* **2020**, *10*, 38906–38911.
- [21] X. Cai, F. Peng, X. Luo, X. Ye, J. Zhou, X. Lang, M. Shi, *ChemSusChem* **2021**, *14*, 3163–3173.
- [22] W. Zheng, M. Liu, L. Y. S. Lee, *ACS Catal.* **2020**, *10*, 81–92.
- [23] X. Cai, F. Peng, X. Luo, X. Ye, J. Zhou, X. Lang, M. Shi, *ChemSusChem* **2021**, *14*, 3163–3173.
- [24] W. Zheng, M. Liu, L. Y. S. Lee, *ACS Catal.* **2020**, *10*, 81–92.
- [25] Z. Kou, W. Zang, Y. Ma, Z. Pan, S. Mu, X. Gao, B. Tang, M. Xiong, X. Zhao, A. K. Cheetham, L. Zheng, J. Wang, *Nano Energy* **2020**, *67*, 104288.
- [26] Y. J. Tang, Y. Wang, X. L. Wang, S. L. Li, W. Huang, L. Z. Dong, C. H. Liu, Y. F. Li, Y. Q. Lan, *Adv. Energy Mater.* **2016**, *6*, 1–7.
- [27] J. Q. Chi, X. Shang, S. S. Lu, B. Dong, Z. Z. Liu, K. L. Yan, W. K. Gao, Y. M. Chai, C. G. Liu, *Carbon NY* **2017**, *124*, 555–564.
- [28] J. Sen Li, S. Zhang, J. Q. Sha, H. Wang, M. Z. Liu, L. X. Kong, G. D. Liu, *ACS Appl. Mater. Interfaces* **2018**, *10*, 17140–17146.
- [29] J. Sen Li, S. Zhang, J. Q. Sha, H. Wang, M. Z. Liu, L. X. Kong, G. D. Liu, *ACS Appl. Mater. Interfaces* **2018**, *10*, 17140–17146.
- [30] X. Zhou, L. Yu, X.-Y. Yu, X. Wen, D. Lou, X. Zhou, L. Yu, X. W. Lou, X. Y. Yu, *Adv. Energy Mater.* **2016**, *6*, 1601177.
- [31] D. Gao, R. Liu, J. Biskupek, U. Kaiser, Y.-F. Song, C. Streb, *Angew. Chem. Int. Ed.* **2019**, *58*, 4644–4648; *Angew. Chem.* **2019**, *131*, 4692–4696.
- [32] L. F. Gu, J. J. Chen, T. Zhou, X. F. Lu, G. R. Li, *Nanoscale* **2020**, *12*, 11201–11208.
- [33] S. Wang, Y. Wang, S. Lin Zhang, S.-Q. Zang, X. Wen Lou, S. Wang, Y. Wang, S. L. Zhang, X. W. Lou, S. Zang, *Adv. Mater.* **2019**, *31*, 1903404.
- [34] H. Zhang, W. Zhou, F. Lu, T. Chen, X. Wen, D. Lou, H. Zhang, X. F. Lu, D. X. W. Lou, W. Zhou, T. Chen, *Adv. Energy Mater.* **2020**, *10*, 2000882.
- [35] D. R. Kauffman, X. Deng, D. C. Sorescu, T. D. Nguyen-Phan, C. Wang, C. M. Marin, E. Stavitski, I. Waluyo, A. Hunt, *ACS Catal.* **2019**, 5375–5382.

Manuscript received: October 14, 2022
Accepted manuscript online: December 2, 2022
Version of record online: February 1, 2023

3.3 In situ formation of robust nanostructured Cobalt oxyhydroxide / Cobalt oxide oxygen evolution reaction electrocatalysts

Yupeng Zhao, Dandan Gao, Johannes Biskupek, Ute Kaiser, Rongji Liu, Carsten Streb



This publication demonstrated how mixed metal sulfide precursors are converted in-situ to the highly stable γ -CoOOH nanofibers and Co_2O_3 nanoparticles. Mechanistic studies reveal that the presence of crystalline mix metal sulfide precursors is critical for the simultaneous in-situ formation of stable and active Co_2O_3 nanoparticles and γ -CoOOH nanofibers, highlighting that use of these earth-abundant minerals might offer an economically and chemically viable route for scalable catalyst development.

Author Contributions:

Yupeng Zhao: Conceptualization, Methodology, Data curation, Investigation, Writing original draft.

Dandan Gao: Investigation, Data curation, Writing original draft.

Johannes Biskupek: Investigation, Data curation, Writing original draft.

Ute Kaiser: Data curation, Writing original draft.

Rongji Liu: Conceptualization, Supervision, Data curation, Methodology, Writing original draft.

Carsten Streb: Project administration, Funding acquisition, Conceptualization, Supervision, Data curation, Methodology, Writing original draft.

Supporting Information can be found at pp 137.

“Y. Zhao, D. Gao, J. Biskupek, U. Kaiser, R. Liu, C. Streb, Y. Zhao, D. Gao, R. Liu, C. Streb, S. Liu, J. Biskupek, U. Kaiser, 2024, DOI: 10.26434/CHEMRXIV-2024-J9ML0.”

In situ formation of robust nanostructured Cobalt oxyhydroxide / Cobalt oxide oxygen evolution reaction electrocatalysts

Yupeng Zhao,^[a,b] Dandan Gao,^[a,b] Johannes Biskupek,^[c] Ute Kaiser,^[c] Rongji Liu*,^[a,b,d] Carsten Streb*^[a,b,d]

-
- [a] Y. Zhao, Dr. D. Gao, Dr. R. Liu, Prof. Dr. C. Streb
Department of Chemistry
Johannes Gutenberg University Mainz
Duesbergweg 10-14, 55131 Mainz, Germany
E-mail: rongji.liu@uni-mainz.de; carsten.streb@uni-mainz.de
- [b] Y. Zhao, Dr. D. Gao, Dr. S. Liu, Dr. R. Liu, Prof. Dr. C. Streb
Institute of Inorganic Chemistry I
Ulm University
Albert-Einstein-Allee 11, 89081 Ulm, Germany
- [c] Dr. J. Biskupek, Prof. Dr. U. Kaiser
Central Facility of Electron Microscopy for Materials Science
Ulm University
Albert-Einstein-Allee 11, 89081 Ulm, Germany
- [d] Dr. R. Liu, Prof. Dr. C. Streb
Helmholtz-Institute Ulm, Electrochemical Energy Conversion
Helmholtzstr. 11, 89081 Ulm, Germany

Supporting information for this article is given via a link at the end of the document.

Abstract

The design of efficient and stable oxygen evolution reaction (OER) catalysts-based earth-abundant metal precursors is crucial for large-scale energy conversion and storage. To-date, many catalyst materials are limited by poor stability in harsh oxidative conditions. Thus, much research is targeted at developing materials that can operate under demanding OER conditions. One promising approach is the *in-situ* formation of catalysts which are inherently stable under the oxidizing, alkaline conditions often used in OER studies. Here, we report how mixed metal sulfide precursors (i.e. CoMo_2S_4 and FeS_2) which give the low overpotentials (307 mV at $j = 10 \text{ mA}\cdot\text{cm}^{-2}$) at the beginning of catalysis, are converted *in-situ* to give a highly stable composite OER catalyst under alkaline OER conditions (1 M aqueous KOH solution, pH = 13.8). Mechanistic studies reveal that under operation, the precursor materials are converted to $\gamma\text{-CoOOH}$ nanofibers and Co_2O_3 nanoparticles, both well-known prototype OER catalysts. The report demonstrates that the presence of crystalline mix metal sulfide precursors is critical for the simultaneous *in-situ* formation of the active catalysts, highlighting that use of these earth-abundant minerals might offer an economically and chemically viable route for scalable catalyst development.

Introduction

Electrocatalytic splitting of water into hydrogen and oxygen plays a crucial role in converting and storing electrical energy.^[1–3] However, specifically the anodic oxygen evolution reaction (OER) is severely hindered by a challenging proton-coupled four-electron transfer, together with operation at harsh oxidative conditions under highly alkaline or highly acidic conditions.^[4,5] Thus, the reaction often shows slow kinetics and is considered the bottleneck of electrochemical water splitting.^[6] Developing efficient and stable oxygen evolution catalysts (OECs) therefore is critical to enable large-scale conversion of electricity from intermittent sources, e.g. wind or solar energy. Early studies were primarily focused on noble-metal oxide catalysts, such as RuO₂ and IrO₂,^[7–10] but high cost, scarcity, and poor long-term stability limit their large-scale deployment.^[11] Thus, recent research has been centered on developing efficient catalysts based on economically viable earth-abundant metals to enable scale-up and industrial use.^[12,13]

One challenge in OER catalyst design is the stable electrical wiring of the reactive site to electrically conductive support, e.g. high surface-area carbon. One facile route to this end is the use of zeolitic imidazolate frameworks (ZIFs) as precursors, which combine tunable composition, facile incorporation of metals, and easy thermal conversion to conductive carbon matrices.^[14,15] Of specific interest is the cobalt-containing ZIF-67 which can easily be synthesized at large scale and features tunable chemical composition and reproducible particle morphology.^[16] Various methods have been developed to convert ZIF-67 into the corresponding carbon-anchored metal oxide,^[17,18] metal phosphide,^[19] metal carbide,^[20] and metal sulfide.^[21] For example, Li et. al. synthesized a ZIF-67 derived Co₃O₄@Z67-N700@CeO₂, which exhibited a low overpotential ($\eta = 350$ mV) at a current density (j) of 10 mA·cm⁻².^[18] Similarly, highly-dispersed Co₃O₄/N-doped porous carbons were synthesized by calcination of ZIF-67/COF, which also featured good catalytic activities ($\eta = 330$ mV at $j = 10$

$\text{mA}\cdot\text{cm}^{-2}$, a Tafel slope of $79\text{ mV}\cdot\text{dec}^{-1}$).^[17] Additionally, Wang et. al. also prepared a cobalt sulfide electrocatalyst ($\text{h-Co}_x\text{S}_y$) which exhibited outstanding electrocatalytic OER performance. Despite this progress, many challenges still exist. One major issue is that many ZIF-67-derived composites are unstable under harsh oxidative and / or alkaline conditions. This is specifically challenging for ZIF-67-derived metal sulfides which can be oxidized to sulfur-oxygen compounds (e.g., sulfite or sulfate) under typical OER conditions. Often, this conversion occurs during operation and results in catalyst degradation and loss of reactivity.^[22]

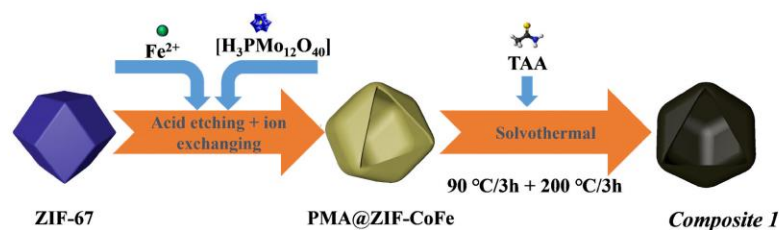
Here, we build on these studies and propose the use of ZIF-67-based metal sulfide as catalyst precursors which are converted into highly stable and highly active metal oxide/oxyhydroxide phases under oxidative, alkaline OER conditions. This conversion and activation route could provide a facile path in catalyst design to enable the self-selection of the most stable catalysts formed under the relevant catalytic conditions, resulting in high stability and high catalytic performance.

Here, we exemplify this approach by developing mixed metal sulfide catalyst precursors (i.e., CoMo_2S_4 and FeS_2) using a facile synthetic route. We show that under OER conditions, the metal sulfides convert into Co_2O_3 nanoparticles and $\gamma\text{-CoOOH}$ nanofibers, which act as high-performance active sites in the following OER catalysis.

Results and Discussion

Briefly, pristine ZIF-67 polyhedrons were prepared based on a modified literature route.^[23,24] The samples were subsequently treated with the etching agent / Mo-precursor $[\text{H}_3\text{PMo}_{12}\text{O}_{40}] \cdot x\text{H}_2\text{O}$ (phosphomolybdic acid, PMA) and the Fe-precursor $\text{FeCl}_2 \cdot 4\text{H}_2\text{O}$ in ethanol solution, resulting in the formation of PMA@ZIF-CoFe (Scheme 1, for details, see SI). After that, the original purple ZIF-67 became brown because of the partial replacement of the Co ions in ZIF-67 by Fe ions and the introduction of $[\text{PMo}_{12}\text{O}_{40}]^{3-}$ (Fig. S1a), as shown by Fourier transform infrared spectroscopy (FT-IR, see SI, Fig. S1b).^[24,25] Subsequently,

PMA@ZIF-CoFe was converted to the metal sulfide-based precursor (hereafter referred to as *Composite 1*) by a solvothermal reaction with thioacetamide (TAA) at ethanol (90°C for 3 h, followed by 200°C for 3 h). To explore the temperature effect on the catalyst, *Composite 2* was prepared by a similar synthetic route, where the solvothermal reaction was carried out at 90°C for 6 h.



Scheme 1. Schematic illustration of the preparation of *Composite 1*

Powder X-ray diffraction (pXRD) and FT-IR spectroscopy were used to examine the composition of *Composite 1* and *Composite 2*. As shown in Fig. 1a, the pXRD data shows the presence of crystalline FeS₂ and CoMo₂S₄ in *Composite 1*. The presence of these metal sulfides is further supported by the FT-IR spectrum of *Composite 1* (Fig. 1b) which indicates the presence of S=S, and metal (M)-S bonds.^[26–29] In comparison, the pXRD and FT-IR data of *Composite 2* (SI, Fig. S2) indicate the presence of amorphous metal sulfides. Notably, the presence of S-O bonds was also indicated by FT-IR spectroscopy, which suggests partial (surface) oxidation of the metal sulfides.^[23,30] This highlights that the elevated solvothermal temperature (200 °C for 3 h) is required to access crystalline metal sulfide phases as observed in *Composite 1*. Aberration-corrected high-resolution transmission electron microscopy (HRTEM), scanning electron microscopy (SEM), and scanning transmission electron microscopy (STEM) together with energy dispersive X-ray spectroscopy (EDX) were employed to examine the structure and morphologic structure of *Composite 1* and *Composite 2*. As shown in Fig. 1c and Fig S4a, *Composite 1* exhibits hollow polyhedral structures with an average diameter of around 800 nm, which is slightly smaller than that in the pristine ZIF-

3. Results and discussion

67 (Fig. S3a). We assign this size reduction to the acid etching process, as similar changes have been observed previously.^[31] The surface of the polyhedral shows some roughening which is not present in the pristine ZIF-67. The same morphological feature can be seen in the case of *Composite 2* as well (Fig. S3b, c) and is also assigned to the etching procedure. For *Composite 1*, the HRTEM image (Fig. 1d, f) indicates the presence of nanocrystalline regions (blue circles) on the particle surface and particle edges. The nanocrystals are identified as FeS₂ (JCPDS 42-1340) and CoMo₂S₄ (JCPDS 24-0332) by the corresponding selective area electron diffraction (SAED) analysis (Fig. 1e). The HRTEM image (Fig. 1f) of *Composite 1* shows lattice and fringes with interplanar spacing of 0.26 nm and 0.19 nm, corresponding to the ($\bar{4}04$) plane of CoMo₂S₄ and (220) plane of FeS₂. However, no obvious nanocrystals can be observed in HRTEM images (Fig. S3d) of *Composite 2*, and the broad diffraction rings rather than thin ones or single reflections in the corresponding SAED (Fig. S3d insert) indicates its amorphous feature. The results agree with the powder XRD measurement. In addition, STEM-energy-dispersive X-ray spectroscopy (EDX) elemental mappings verify the presence of homogeneously dispersed Co, Fe, Mo, and S within *Composite 1* (Fig. S4b) and *Composite 2* (Fig. S3f). All these results indicate that the synthesized PMA@ZIF-CoFe was successfully converted to metal sulfides (i.e. CoMo₂S₄ and FeS₂) and led to a homogeneous distribution of these metal ions. In addition, the atomic ratio of Co, Fe, Mo, and S (2.63:1:1.4:6.5) in *Composite 1* was determined by inductively coupled plasma optical emission spectroscopy (ICP-OES). The result indicates that in addition to the formation of crystalline CoMo₂S₄ and FeS₂, some amorphous cobalt sulfide might be present in *Composite 1*.

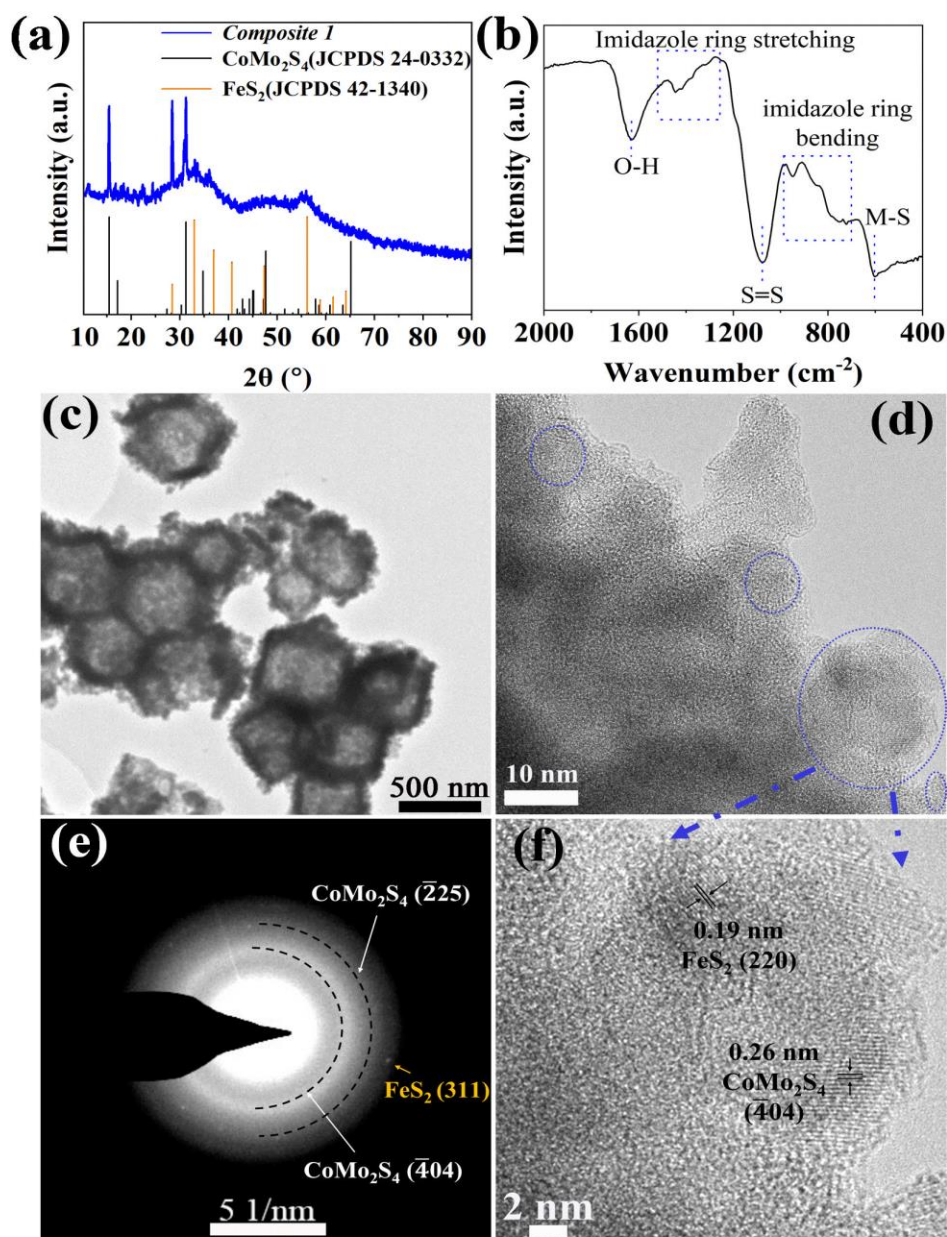


Figure 1. (a) pXRD pattern, (b) FT-IR spectrum, (c)TEM, and (d, f) HTREM images with (e) corresponding selected area electron diffraction pattern of *Composite 1*.

3. Results and discussion

The elemental composition and oxidation states in *Composite 1* and *Composite 2* were studied by X-ray photoelectron spectroscopy (XPS). The survey XPS spectra indicate the presence of Co, Fe, Mo, and S, in both *Composite 1* (Fig. S5a) and *Composite 2* (Fig. S5b). The deconvoluted high-resolution Fe 2p XPS spectra in *Composite 1* (Fig. 2a) and *Composite 2* (Fig. S5c) show characteristic peaks at ~ 712 eV, which are indicative of Fe²⁺ species.^[32] Satellite features (~ 786 eV) in the deconvoluted Co 2p XPS spectra for *Composite 1* (Fig. 2b) and *Composite 2* (Fig. S5d) suggest the presence of Co²⁺. This is further supported by peaks at ~ 781.5 eV which are characteristic of Co²⁺ 2p_{3/2} in both *Composite 1* and *Composite 2*.^[33] It should be noted that a strong and sharp signal appeared at 779 eV in the Co 2p_{3/2} spectrum of *Composite 1* which can be assigned to Co-S interactions. Given that the binding energies of Co are close to metallic Co, this observation aligns with recently reported data on CoMo₂S₄ catalysts.^[34–36] The metal-like properties of Co in CoMo₂S₄ may facilitate electron delocalization, thereby enhancing conductivity. In contrast, for *Composite 2*, the Co 2p_{3/2} spectrum shows a signal at 780.4 eV which is assigned to Co³⁺ (Fig. S5c). As for Mo 3d XPS spectrum of *Composite 1* (Fig. 2c), the main binding energies located at 229 eV (Mo 3d_{5/2}) and 232.2 eV (Mo 3d_{3/2}) for Mo⁴⁺, belonging to the Mo-S bond.^[34] In addition, the peaks at 232.5 eV and 235.6 eV are assigned to Mo⁶⁺. We assign it to the partial oxidation of metal sulfides. The predominant valence state of Mo⁴⁺ in CoMo₂S₄ provides additional confirmation of the metallic properties exhibited by Co within the CoMo₂S₄ structure. Notably, the S 2s signal also appeared at the same region of Mo 3d and was deconvoluted into three peaks at 233.9 eV, 226.4 eV, and 226 eV, corresponding to the three chemical states of the S species bonding with O (SO₄²⁻), Mo, and Co ions.^[35] However, only Mo⁶⁺ is observed in *Composite 2* (SI, Fig. S5e). This is expected, as CoMo₂S₄ is only formed at an elevated reaction temperature (200°C for *Composite 1*), while *Composite 2* is not exposed to this temperature.^[23] The deconvoluted XPS spectrum for S 2p (Fig. 2d) indicates the existence of metal sulfides in *Composite 1* (161.7 eV for S²⁻ 2p_{3/2} and 162.8 eV for S₂²⁻ 2p_{3/2}).^[37] Similarly, signals for S²⁻ 2p_{3/2} and S₂²⁻ 2p_{3/2} were

observed in *Composite 2*. It is worth noting that the XPS results of previously reported binding energies of Co 2p_{3/2} (778.9 eV), Mo 3d_{5/2} (228.7 eV), and S 2p_{3/2} (161.9 eV) in CoMo₂S₄ are in line with our observations, providing further support for the presence of CoMo₂S₄.^[36] Also, the signals belonging to SO₄²⁻ were also observed at 168.7 eV (2p_{3/2}) and 169.9 eV (2p_{1/2}), which also indicates the partial oxidation of the metal sulfides.^[38]

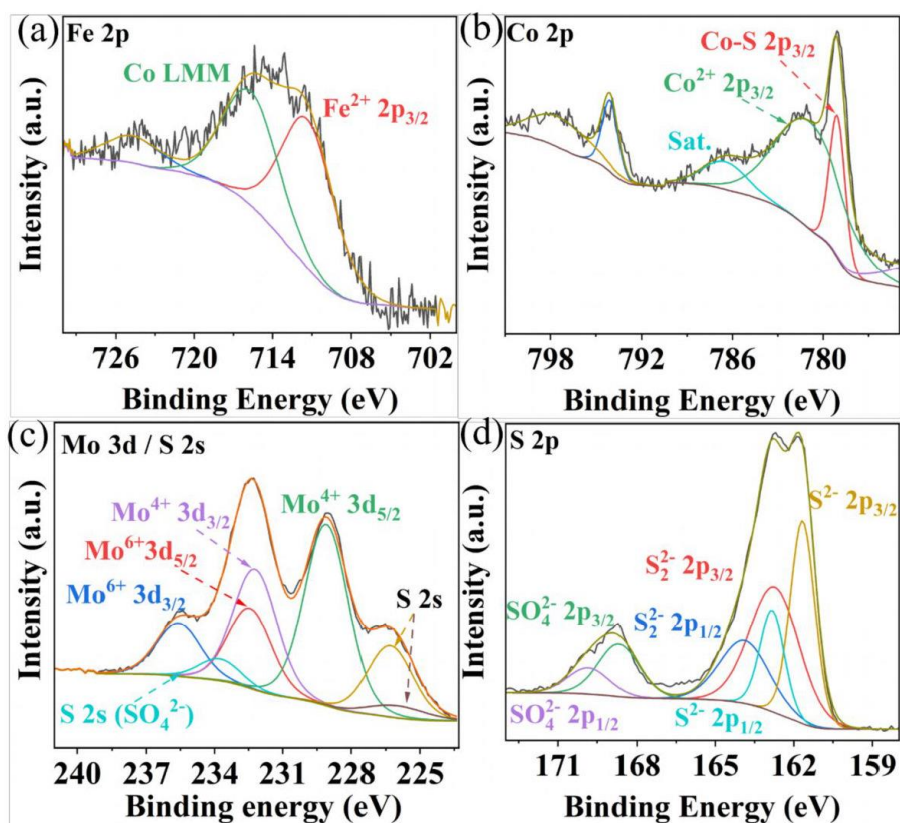


Figure 2. Deconvoluted high-resolution XPS spectra of Fe 2p (a), Co 2p (b), Mo 3d (c), and S 2p (d) of *Composite 1*.

Next, we studied the in-situ conversion of *Composite 1* into the real active OER catalyst under oxidative electrochemical conditions. To this end, we studied the changes of *Composite 1* in

3. Results and discussion

alkaline aqueous solution (1.0 M aqueous KOH) using a conventional three-electrode electrochemical setup. The catalyst was deposited on glassy carbon rotating disk electrode (RDE) working electrodes as follows: catalyst inks were prepared by sonicating a dispersion of the respective catalyst, 5 wt% Nafion solution, deionized (DI) water, and ethanol (for details, see SI). Subsequently, the respective ink was drop-cast onto the glassy carbon RDE working electrode. A Hg/HgO electrode was used as reference electrode, while a graphite rod was used as counter electrode. All potentials in this study have been converted to reversible hydrogen electrode potentials (RHE, see details in the SI). To assess synergistic effects of multiple metal reaction sites on OER, reference catalysts were prepared for comparison, labeled as *Composite 3* (without Mo), *Composite 4* (without Fe), and *Composite 5* (without Fe and Mo), (see SI for synthetic and analytical details).

Linear sweep voltammetry (LSV) at a scan rate of 5 mV/s was conducted to evaluate the OER electrocatalytic performance. As illustrated in Figure 3a, b, *Composite 1* showed the lowest overpotential of $\eta = 307$ mV at a current density of $j = 10 \text{ mA}\cdot\text{cm}^{-2}$ (Fig. 3a, b). *Composite 2* exhibited a slightly higher overpotential ($\eta = 315$ mV). However, in the absence of Mo (*Composite 3*), Fe (*Composite 4*), or both Mo and Fe (*Composite 5*), significantly higher overpotentials at the same current density were observed (Fig. 3a). Furthermore, Tafel slopes (η versus $\log(j)$) of $74 \text{ mV}\cdot\text{dec}^{-1}$ and $82 \text{ mV}\cdot\text{dec}^{-1}$ were obtained for *Composite 1* and *Composite 2* (Fig. S6a), while the other composites exhibited higher Tafel slopes. The significantly enhanced catalytic properties and OER kinetics of *Composite 1* and *Composite 2* underscore the vital role played by the concurrent presence of both Fe and Mo in the mixed metal sulfide-based catalysts.

Rotating ring-disk electrode (RRDE) voltammetry was employed to gain a deeper understanding of the OER reaction mechanism of *Composite 1*. To this end, an LSV measurement between 1.3 V and 1.7 V was performed on the disk electrode, where the OER

reaction takes place, while the Pt ring electrode (set at a fixed potential of 1.5 V) was used to detect any partially oxidized intermediates formed during OER, such as H₂O₂ (for analytical details see SI). Under the given conditions, a negligible ring current was detected, and the electron transfer number was calculated to be close to 4, indicating that H₂O₂ intermediates were scarcely generated, confirming a desirable 4-electron pathway for OER (SI, Fig. S6b, c). In addition, the faradaic efficiency (FE) was measured using RRDE voltammetry at potentials of 0.4 V (ring) and 1.5 V (disk) at a rotation rate of 1600 rpm, so that oxygen generated on the disk surface could be reductively collected at the ring electrode (current collection efficiency: 15.7%). Based on the detected ring current (~28 μA) and disk current (~185 μA), a FE of 96.2% was calculated for **Composite 1** (Fig. 3c, also refer to SI for detailed calculations).

Next, electrochemical impedance spectroscopy (EIS) was used to better understand the origins of the electrocatalytic performance. The results (SI, Fig. S7) indicate that **Composite 1** features the lowest charge-transfer resistance ($R_{ct} = 9 \Omega$) among the catalyst samples studied, suggesting efficient interfacial electron transfer. Also, the double-layer capacitance (C_{dl}), proportional to the electrochemically active surface area (ECSA), was determined to compare the amount of reactive sites in the composites. As shown in Fig. S8, all composites tested show comparable ECSAs. Therefore, we conclude that the superior OER performance of **Composite 1** is attributed to its low internal electron transfer resistance as well as intrinsic reactivity of the reactive sites.

3. Results and discussion

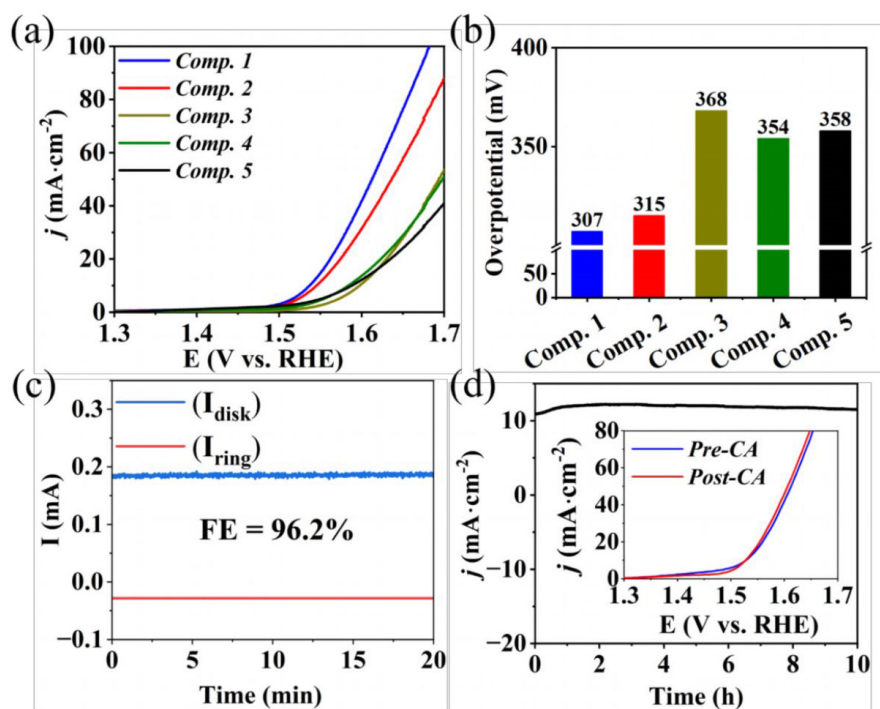


Figure 3. Electrocatalytic OER performance of *Composite 1*, *Composite 2*, and reference composites in 1 M aqueous KOH: a) iR-corrected OER polarization curves, b) Overpotentials at $j = 10 \text{ mA}\cdot\text{cm}^{-2}$, c) RRDE analysis to determine faradaic efficiency, and d) Chronoamperometry curves at $\eta = 330 \text{ mV}$ without iR compensation (insert: LSV polarization curves comparison before and after 10 h stability test) of *Composite 1*.

Subsequently, chronoamperometry (CA) measurements were utilized to evaluate the stability and study the morphological and compositional changes of *Composite 1* at 1.56 V vs. RHE in 1 M aqueous KOH. As illustrated in Fig 3d, the current density j remained essentially unchanged with only a minor increase in the initial phase (0-3 h), and a marginal decrease in the second phase (3-10 h) of CA. This finding is supported by LSV analysis before and after CA, which are essentially identical (Fig. 3d and SI, Fig. S9).

To explore our hypothesis of structural conversion of the metal sulfide precursors under OER conditions, a morphological and chemical investigation was carried out after the stability test

using AC-HRTEM and XPS. As shown in Fig. 4a, after 3 h of electrocatalysis, the hollow structure of *Composite 1* was converted into a mixture of 2-dimensional nanoplates and 1D nanofibers, which formed on the particle surface and particle edges (Fig. 4b, c and SI, Fig. S10a). These nanofibers were identified as γ -CoOOH, based on a 0.44 nm interplanar spacing in the HRTEM image (Fig. 4c) and the matching SAED pattern (SI, Fig. S10b, match with γ -CoOOH JCPDS 14-0673). Elemental mapping by STEM-EDX further confirmed the presence of Co and O (SI Fig. S11). Based on these findings, the improved catalytic activities were attributed to the formation of γ -CoOOH, a recognized active OER catalyst.^[1,39,40] This result aligns with the XPS measurement (SI, Fig. S12), which revealed the absence of Co^{2+} and the presence of Co^{3+} , as no satellite features (≈ 786 eV) for Co^{2+} were found. Also, XPS analysis indicated the absence of Mo and Fe signals, suggesting that the FeS_2 and CoMo_2S_4 are dissolved and leak into the electrolyte under operation. In addition, $\text{S}^{2-}/\text{S}_2^{2-}$ was oxidized to SO_4^{2-} , which is indicated by S 2p XPS data in Fig. S12. Moreover, after 10 h of electrocatalysis, nanoparticles (indicated by a white box in Fig. 4f and SI, Fig. S10d), were observed and identified as Co_2O_3 based on the corresponding SAED pattern (SI, Fig. S10e, JCPDS 02-0770). In addition, aggregation of γ -CoOOH nanofibers was observed after 10 h of electrocatalysis, as shown in Fig 4b, 4e, and Fig. S13. The average length of γ -CoOOH nanofibers increased from ~ 40 nm to ~ 110 nm after 3 and 10 h OER catalysis. This aggregation of γ -CoOOH nanofibers might be linked to the marginal loss of catalytic reactivity observed during the 10 h CA experiments (Fig. 3f). As a comparison, we also investigated structural and chemical changes of *Composite 2*. Notably, *Composite 2* exhibited poorer stability compared to *Composite 1* (SI, Fig. S14). *Composite 2* showed a CA behavior similar to *Composite 1*, featuring an initial slight current density increase followed by a subsequent drop in current density. Notably, the loss of reactivity was more pronounced than observed for *Composite 1*. Morphological and chemical investigations on *Composite 2* were carried out after the stability test to explore the origins of the stability difference between *Composite 1* and *Composite 2*. As shown in the SI, Fig.S13 -

3. Results and discussion

S17, similar morphological and chemical changes were observed after catalysis in *Composite 2* compared to *Composite 1*, including the formation of γ -CoOOH nanofibers and Co_2O_3 nanoparticles. However, there were fewer crystalline nanofibers and nanoparticles observed in *Composite 2* after electrocatalysis for 10 hours compared to *Composite 1*. Consequently, the lower number of γ -CoOOH nanofibers and Co_2O_3 nanoparticles provided fewer active sites for OER, resulting in its poorer stability. Thus, we propose that the crystalline metal sulfides could effectively prevent Co leakage during OER and facilitate the oxidation of Co^{2+} to Co^{3+} and the formation of Co_2O_3 and γ -CoOOH, contributing to high stability. In contrast, amorphous metal sulfides might show higher solubility or faster degradation than the crystalline systems, resulting in faster degradation and leaching.^[41,42]

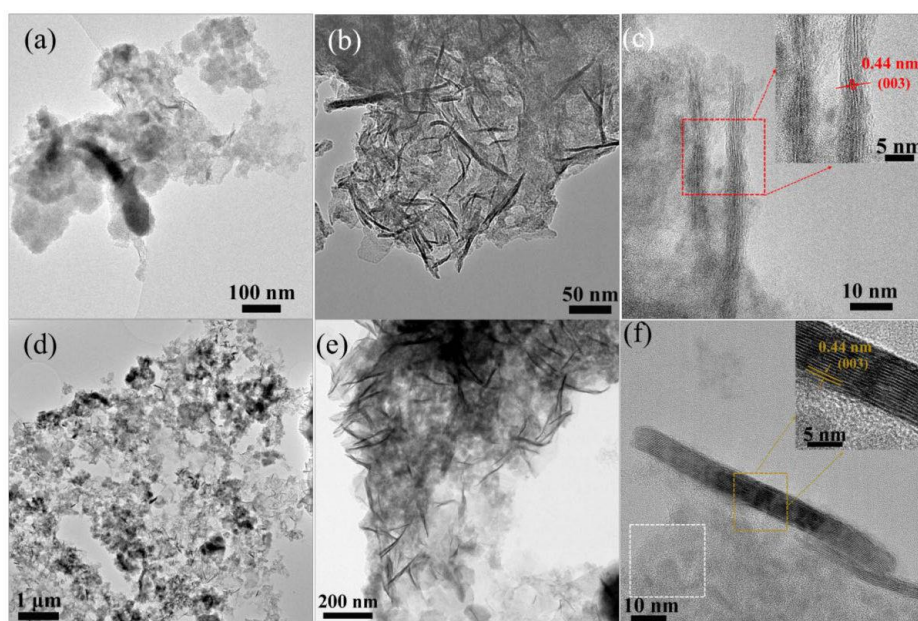


Fig. 4 TEM and HRTEM images of *Composite 1* after electrocatalysis for 3 h (a-c) and 10 h (d-f)

Conclusion

In summary, we report the *in situ* conversion of a CoMo₂S₄/FeS₂ composite heterojunction was prepared by a facile synthetic method. The synergistic effects of its structural and compositional characteristics contribute to the remarkable electrocatalytic performance, displaying a low overpotential (307 mV at $j = 10 \text{ mA}\cdot\text{cm}^{-2}$). As the electrocatalysis progresses, the crystalline metal sulfides are converted *in situ* into Co₂O₃ nanoparticles and γ -CoOOH nanofibers. These species act as the true active sites in OER electrocatalysis, resulting in high activity and high stability. We also observed the aggregation of γ -CoOOH nanofibers during prolonged electrocatalysis results in a slight degradation of its electrocatalytic properties. This synthetic approach and structural/compositional evolution hold significant promise for pre-catalyst design and stability enhancement in metal sulfide-based catalysts, providing insights into the genuine active sites for metal sulfide-based OER electrocatalysts.

Acknowledgments

The authors gratefully acknowledge financial support by the Deutsche Forschungsgemeinschaft DFG (Cluster of Excellence EXC2154, POLiS, project number: 390874152 and TRR 234 Catalight, project number: 364549901 and project no 389183496). R.L. gratefully acknowledges financial support by the Alexander von Humboldt Foundation. D.G. acknowledges the Deutsche Forschungsgemeinschaft (DFG) for a Walter Benjamin Fellowship (project no. 510966757). R.L., D.G., and C.S. gratefully acknowledge financial support by Johannes Gutenberg University Mainz, the Top-Level Research Initiative SusInnoScience and the Gutenberg Research College. Dr. Shuai Chen is acknowledged for XRD characterization support.

Reference

- [1] Z. P. Ifkovits, J. M. Evans, M. C. Meier, K. M. Papadantonakis, N. S. Lewis, *Energy Environ Sci* **2021**, *14*, 4740–4759.

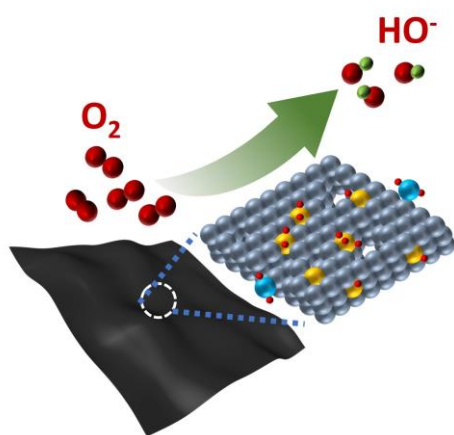
3. Results and discussion

- [2] X. Zou, Y. Zhang, *Chem Soc Rev* **2015**, *44*, 5148–5180.
- [3] B. Zhang, Y. Zheng, T. Ma, C. Yang, Y. Peng, Z. Zhou, M. Zhou, S. Li, Y. Wang, C. Cheng, *Advanced Materials* **2021**, *33*, 2006042.
- [4] J. Song, C. Wei, Z. F. Huang, C. Liu, L. Zeng, X. Wang, Z. J. Xu, *Chem Soc Rev* **2020**, *49*, 2196–2214.
- [5] L. Tian, X. Zhai, X. Wang, J. Li, Z. Li, *J Mater Chem A Mater* **2020**, *8*, 14400–14414.
- [6] N. T. Suen, S. F. Hung, Q. Quan, N. Zhang, Y. J. Xu, H. M. Chen, *Chem Soc Rev* **2017**, *46*, 337–365.
- [7] C. Spöri, J. T. H. Kwan, A. Bonakdarpour, D. P. Wilkinson, P. Strasser, *Angewandte Chemie International Edition* **2017**, *56*, 5994–6021.
- [8] H. Liu, X.-H. Zhang, Y.-X. Li, X. Li, C.-K. Dong, D.-Y. Wu, C.-C. Tang, S.-L. Chou, F. Fang, X.-W. Du, H. Liu, C. Dong, D. Wu, X. Du, X. Zhang, Y. Li, X. Li, C. Tang, S. Chou, F. Fang, *Adv Energy Mater* **2020**, *10*, 1902521.
- [9] J. Wang, L. Han, B. Huang, Q. Shao, H. L. Xin, X. Huang, *Nature Communications* **2019** *10*:1 **2019**, *10*, 1–11.
- [10] T. Reier, Z. Pawolek, S. Cherevko, M. Bruns, T. Jones, D. Teschner, S. Selve, A. Bergmann, H. N. Nong, R. Schlögl, K. J. J. Mayrhofer, P. Strasser, *J Am Chem Soc* **2015**, *137*, 13031–13040.
- [11] T. X. Nguyen, Y. H. Su, C. C. Lin, J. M. Ting, *Adv Funct Mater* **2021**, *31*, 2106229.
- [12] Z.-P. Wu, F. Lu, S.-Q. Zang, X. Wen, D. Lou, Z.-P. Wu, X. F. Lu, X. W. Lou, S.-Q. Zang, *Adv Funct Mater* **2020**, *30*, 1910274.
- [13] W. Xiong, H. Yin, T. Wu, H. Li, *Chemistry – A European Journal* **2023**, *29*, e202202872.
- [14] H. Wen, S. Zhang, T. Yu, Z. Yi, R. Guo, *Nanoscale* **2021**, *13*, 12058–12087.
- [15] Y. Wang, Y. Wang, L. Zhang, C. Sen Liu, H. Pang, *Inorg Chem Front* **2019**, *6*, 2514–2520.
- [16] C. Cui, X. Lai, R. Guo, E. Ren, W. Qin, L. Liu, M. Zhou, H. Xiao, *Electrochim Acta* **2021**, *393*, 139076.
- [17] G. lin Zhuang, Y. fen Gao, X. Zhou, X. yong Tao, J. min Luo, Y. jing Gao, Y. long Yan, P. yuan Gao, X. Zhong, J. guo Wang, *Chemical Engineering Journal* **2017**, *330*, 1255–1264.
- [18] X. Li, S. You, J. Du, Y. Dai, H. Chen, Z. Cai, N. Ren, J. Zou, *J Mater Chem A Mater* **2019**, *7*, 25853–25864.
- [19] B. Liu, S. Xue, S. Tan, D. Zhang, Z. Deng, H. Pan, W. Tu, R. Zhang, H. Zhang, Y. Wang, *Energy and Fuels* **2022**, *36*, 4532–4540.
- [20] Y. Li, Z. Yin, M. Cui, S. Chen, T. Ma, *Mater Today Energy* **2020**, *18*, 100565.
- [21] Z. Zhang, S. Li, X. Bu, Y. Dai, J. Wang, X. Bao, T. Wang, *New Journal of Chemistry* **2021**, *45*, 17313–17319.
- [22] M. Cui, C. Yang, B. Li, Q. Dong, M. Wu, S. Hwang, H. Xie, X. Wang, G. Wang, L. Hu, M. Cui, C. Yang, Q. Dong, M. Wu, H. Xie, X. Wang, L. Hu, B. Li, G. Wang, S. Hwang, *Adv Energy Mater* **2021**, *11*, 2002887.
- [23] Y. Guo, J. Tang, H. Qian, Z. Wang, Y. Yamauchi, *Chemistry of Materials* **2017**, *29*, 5566–5573.
- [24] X. Wang, L. Yu, Y. Guan, S. Song, X. Wen, D. Lou, X. Wang, L. Yu, B. Y. Guan, X. W. Lou, S. Song, *Advanced Materials* **2018**, *30*, 1801211.

- [25] S. Anantharaj, S. R. Ede, K. Sakthikumar, K. Karthick, S. Mishra, S. Kundu, *ACS Catal* **2016**, *6*, 8069–8097.
- [26] T. Abza, D. G. Dadi, F. G. Hone, T. C. Meharu, G. Tekle, E. B. Abebe, K. S. Ahmed, *Advances in Materials Science and Engineering* **2020**, *2020*, DOI 10.1155/2020/2628706.
- [27] W. Feng, L. Chen, M. Qin, X. Zhou, Q. Zhang, Y. Miao, K. Qiu, Y. Zhang, C. He, *Scientific Reports* **2015**, *5*, 1–13.
- [28] F. Sang, Z. Yin, W. Wang, E. Almatrafi, Y. Wang, B. Zhao, J. Gong, C. Zhou, C. Zhang, G. Zeng, B. Song, *J Clean Prod* **2022**, *378*, 134459.
- [29] Y. Sun, D. Lv, J. Zhou, X. Zhou, Z. Lou, S. A. Baig, X. Xu, *Chemosphere* **2017**, *185*, 452–461.
- [30] L. Yu, J. F. Yang, B. Y. Guan, Y. Lu, X. W. (David) Lou, *Angewandte Chemie* **2018**, *130*, 178–182.
- [31] Y. Zhao, D. Gao, J. Biskupek, U. Kaiser, R. Liu, C. Streb, *Results Chem* **2022**, *4*, 100568.
- [32] B. Fei, Z. Chen, J. Liu, H. Xu, X. Yan, H. Qing, M. Chen, R. Wu, B. Fei, Z. Chen, J. Liu, H. Xu, X. Yan, H. Qing, M. Chen, R. Wu, *Adv Energy Mater* **2020**, *10*, 2001963.
- [33] S. Dou, C.-L. Dong, Z. Hu, Y.-C. Huang, J. Chen, L. Tao, D. Yan, D. Chen, S. Shen, S. Chou, S. Wang, S. Dou, L. Tao, D. Yan, D. Chen, S. Wang, C. Dong, Y. Huang, J. Chen, Z. Hu, S. Chou, S. Shen, *Adv Funct Mater* **2017**, *27*, 1702546.
- [34] H. Cheng, Q. Liu, Y. Diao, L. Wei, J. Chen, F. Wang, H. Cheng, Q. Liu, Y. Diao, L. Wei, J. Chen, F. Wang, *Adv Funct Mater* **2021**, *31*, 2103732.
- [35] Y. Guo, J. Tang, J. Henzie, B. Jiang, W. Xia, T. Chen, Y. Bando, Y. M. Kang, M. S. A. Hossain, Y. Sugahara, Y. Yamauchi, *ACS Nano* **2020**, *14*, 4141–4152.
- [36] I. Alstrup, I. Chorkendorff, R. Candia, B. S. Clausen, H. Topsøe, *J Catal* **1982**, *77*, 397–409.
- [37] D. Ma, B. Hu, W. Wu, X. Liu, J. Zai, C. Shu, T. Tadesse Tsega, L. Chen, X. Qian, T. L. Liu, *Nature Communications* **2019**, *10*, 1–8.
- [38] A. M. De Jong, H. J. Borg, L. J. Van Ijzendoorn, V. G. F. M. Soudant, V. H. J. De Beer, J. A. R. Van Veen, J. W. Niemantsverdriet, *Sulfidation Mechanism of Molybdenum Catalysts Supported on a SiO₂/Si(100) Model Support Studied by Surface Spectroscopy*, **1993**.
- [39] D. Zhang, X. Kong, Y. Zhao, M. Jiang, X. Lei, *J Mater Chem A Mater* **2016**, *4*, 12833–12840.
- [40] B. Zhang, Y. Zheng, T. Ma, C. Yang, Y. Peng, Z. Zhou, M. Zhou, S. Li, Y. Wang, C. Cheng, *Advanced Materials* **2021**, *33*, DOI 10.1002/ADMA.202006042.
- [41] S. Anantharaj, S. Noda, S. Anantharaj, S. Noda, *Small* **2020**, *16*, 1905779.
- [42] S. Anantharaj, P. N. Reddy, S. Kundu, *Inorg Chem* **2017**, *56*, 1742–1756.

3.4 Atomically Engineered WO_x/MoO_x -Modified Defect-Rich Pd Metallene for Enhanced Alkaline Oxygen Reduction Electrocatalysis

Yupeng Zhao, Zhengfan Chen, Nana Ma, Weiyi Cheng, Kecheng Cao, Dong Zhang, Fan Feng, Dandan Gao, Rongji Liu*, Shujun Li*, Carsten Streb*



We report a defect-rich Pd metallene synthesized through a facile wet-chemical method. Characterization results reveal the presence of various types of atomic-scale defects, including pores, concave surfaces, and atomically doped WO_x and MoO_x , which finely tune the electronic structure, endowing it with excellent catalytic activity for the ORR. When incorporated into a homemade Zn-air battery with very low loading, it achieves a notable specific capacity and excellent discharge potential stability, highlighting its practical utility.

Author Contributions:

Yupeng Zhao: Conceptualization, Methodology, Data curation, Investigation, Writing original draft.

Zhengfan Chen: Investigation, Data curation, Writing original draft.

Nana Ma, Weiyi Cheng: Data curation, Writing original draft.

Kecheng Cao, Dong Zhang, Fan Feng, Dandan Gao: Investigation, Data curation, Writing original draft.

Rongji Liu, Shujun Li: Conceptualization, Supervision, Data curation, Methodology, Writing original draft.

Carsten Streb: Project administration, Funding acquisition, Conceptualization, Supervision, Data curation, Methodology, Writing original draft.

Supporting Information can be found at pp 147.

“Yupeng Zhao, Zhengfan Chen, Nana Ma, Weiyi Cheng, Kecheng Cao, Dong Zhang, Fan Feng, Dandan Gao, Rongji Liu, Shujun Li, Carsten Streb, Atomically WO_x/MoO_x modified defect-rich Pd metallene for Enhanced Alkaline Oxygen Reduction Electrocatalysis and Zn air batteries.” Submitted to ChemRxiv; DOI: 10.26434/chemrxiv-2024-fkr00.

Atomically Engineered WO_x/MoO_x-Modified Defect-Rich Pd Metallene for Enhanced Alkaline Oxygen Reduction Electrocatalysis

Yupeng Zhao,^[a,b] Zhengfan Chen,^[a,b] Nana Ma,^[c] Weiyi Cheng,^[c] Dong Zhang,^[d] Kecheng Cao,^[d] Fan Feng,^[a,b] Dandan Gao,^[a,b] Rongji Liu*,^[a,b,e] Shujun Li*,^[c] Carsten Streb*,^[a,b,e]

[a] Y. Zhao, Z. Chen, F. Feng, Dr. D. Gao, Dr. R. Liu, Prof. Dr. C. Streb
Department of Chemistry
Johannes Gutenberg University Mainz
Duesbergweg 10-14, 55131 Mainz, Germany
E-mail: rongji.liu@uni-mainz.de; carsten.streb@uni-mainz.de

[b] Y. Zhao, Z. Chen, F. Feng, Dr. D. Gao, Dr. R. Liu, Prof. Dr. C. Streb
Institute of Inorganic Chemistry I
Ulm University
Albert-Einstein-Allee 11, 89081 Ulm, Germany

[c] Dr. N. Ma, W. Cheng, Prof. Dr. S. Li
Henan Key Laboratory of Boron Chemistry and Advanced Materials,
School of Chemistry and Chemical Engineering,
Henan Normal University
Xinxiang, 453007 (China)
E-mail: llsj@htu.edu.cn

[d] Dong Zhang, Kecheng Cao,
School of Physical Science and Technology,
ShanghaiTech University,
Shanghai, 201210 China

[e] Dr. R. Liu, Prof. Dr. C. Streb
Helmholtz-Institute Ulm, Electrochemical Energy Conversion
Helmholtzstr. 11, 89081 Ulm, Germany

Supporting information for this article is given via a link at the end of the document.

Abstract

Defect engineering is a key chemical tool to modulate the electronic structure and reactivity of nanostructured catalysts. Here, we report how engineering defects in a palladium metallene nanostructure results in a highly active catalyst for the alkaline oxygen reduction reaction (ORR). A defect-rich WO_x and MoO_x modified Pd metallene (denoted as **D-Pd M**) was synthesized by a facile wet-chemical method. Detailed structural analyses reveal the presence of three distinct atomic-scale defects, that is pores, concave surfaces, and surface-anchored individual WO_x and MoO_x sites. The presence of this combination of defects results in excellent catalytic ORR activity with a half-wave potential of 0.93 V vs. RHE and a mass activity of 1.3 A·mg_{Pd}⁻¹ at 0.9 V vs. RHE, outperforming the commercial references Pt/C and Pd/C by factors of 6.5 and 3.9, respectively. The practical usage of the compound is demonstrated by integration into a custom-designed Zn-air battery. At notably low **D-Pd M** loading (26 μg_{Pd}·cm⁻²), the system achieves a high specific capacity (809 mAh·g_{Zn}⁻¹) together with excellent discharge potential stability. In sum, this study provides a blueprint for the targeted introduction of distinct

defect sites into metallene ORR catalysts, leading to materials with outstanding performance metrics.

Introduction

The oxygen reduction reaction (ORR) is one of the most important catalytic processes for energy conversion and storage technologies including fuel cells, metal-air batteries and electrochemical H₂O₂ production.^[1-3] The ORR is a challenging reaction, due to the high O₂ bond dissociation energy (498 KJ·mol⁻¹) and the sluggish kinetics of O₂-related proton-coupled multi-electron processes.^[2,4] These factors significantly impede the practical application of the ORR. To overcome these challenges, numerous electrocatalysts have been developed, including those based on platinum group metals (PGMs),^[5] noble metal-free materials,^[6,7] and even metal-free catalysts.^[8] Currently, both the intrinsic activity and the long-term stability of noble metal-free and metal-free catalysts are significantly inferior to those of PGM-based electrocatalysts.^[4]

Owing to their unique electronic structure and optimum oxygen molecule adsorption energy, electrocatalysts based on PGMs have received widespread attention and are still a focal point for advanced ORR catalyst development.^[9] However, challenges remain, particularly in the case of platinum-based catalysts. While these materials demonstrate excellent catalytic performance, they often suffer from poor long-term stability.^[10-12] Importantly, highly dispersed, Pt nanoparticles show a notable tendency to aggregate during catalysis, resulting in the formation of larger particles with reduced their reactivity.^[13] Furthermore, the high binding energy of Pt and Pd to oxygen molecules limits the generation and conversion of intermediates (such as *OH and *OOH) into H₂O/OH, indicating potential opportunities for enhancing the catalytic properties by modification in their electronic structure.^[14,15] Moreover, the substantial cost associated with Pt and Pd is major impediment to their broad industrial use.^[16] Thus, chemical strategies are urgently required which optimize electronic structure and reactivity of PGMs while at the same time making optimum use of all metal centers available in the catalyst.^[17-19]

These challenges have recently been targeted by the development of two-dimensional (2D) metal nanosheets, so-called metallenes, which have shown unique electronic structure and high reactivity and durability.^[20-22] Metallenes are metal or alloy materials featuring individual layers of atomic thickness.^[23,24] Metallenes offer optimum utilization of the individual metal atoms due to their high specific accessible surface area and abundance of low-coordinated reactive metal sites.^[25-27] A significant breakthrough in this realm was achieved by Guo and colleagues, who successfully synthesized PdMo bimetalene.^[28] The group discovered that strain and quantum effects within the ultrathin structure of the metallene leads to a downward

shift of the d-band center, thereby lowering the oxygen molecule binding energy and enhancing electrocatalytic performance. Moreover, the electronic structure can be further modulated by doping with Mo atoms. As a result, PdMo bimetallic exhibits a lower d-band center and superior ORR catalytic activity compared to pure Pd metallene. Building on this advancement, Jin and co-workers further demonstrated that the durability of PdMo bimetallic can be significantly improved by interstitial doping with carbon. This modification results in stabilization of the Mo sites within the bimetallic structure.^[29] In addition, defect engineering has proven to be a critical tool in the advancement of Pd metallene. Wang and colleagues successfully developed a defect rich Pd metallene characterized by abundant pores, which created a multitude of highly active sites. This innovation resulted in a significant enhancement in ORR activity.^[30] Concurrently, research by Guo and coworkers revealed that the concave surfaces on Pd metallene lead to a modest downward shift in the d-band center and allow fine-tuning of oxygen molecule binding energies. This structural modification contributes to improved ORR performance, showcasing the impact of the surface geometry on catalytic efficiency.^[31]

Here, we build on these pioneering studies and report a novel ultrathin Pd metallene doped with atomic WO_x/MoO_x (referred to as **D-Pd M**) featuring by a curved defect-rich structure. Key for the synthetic access to this new compound is the use of molecular metal oxides (polyoxometalates, POMs), here $[\text{H}_3\text{PMo}_{12}\text{O}_{40}] \times \text{H}_2\text{O}$ (=PMO₁₂), as reducing agent, and tungsten hexacarbonyl ($\text{W}(\text{CO})_6$) as a structure-directing agent. PMO₁₂ and $\text{W}(\text{CO})_6$ also acted as molecular precursors to deposit MoO_x and WO_x into the Pd metallene. The resulting **D-Pd M** showed excellent ORR activity, with a high half-wave potential ($E_{1/2} = 0.93$ V vs. RHE), high mass activity ($1.3 \text{ A} \cdot \text{mg}_{\text{Pd}}^{-1}$ at 0.9 V vs. RHE) and superior stability over 10,000 test cycles. Practical applicability of **D-Pd M** was demonstrated by integration into an operational Zn-air battery at ultra-low Pd loading ($26 \mu\text{g}_{\text{Pd}} \cdot \text{cm}^{-2}$), showing high specific capacity ($809 \text{ mAh} \cdot \text{g}_{\text{Zn}}^{-1}$), exceptional discharge performance and ultra-long cycling stability (continuous operation for 300 hours over 300 charge/discharge cycles).

Results and Discussion

Fig. 1 illustrates the synthetic procedure to access **D-Pd M**. Initially, a solution of PMO₁₂ in N,N-dimethylformamide (DMF) was irradiated with ultraviolet (UV) light ($\lambda_{\text{max}} = 254$ nm) to reduce the POM cluster. The solution undergoes a clear transition from its initial yellow to dark blue color, and a new broad peak at 760 nm appeared in the reduced solution (SI, Fig. S1), all of which suggests that the POM cluster was reduced to heteropoly blue.^[32,33] The solution

containing the reduced PMo_{12} was then combined with a DMF solution containing the metal precursors palladium (II) acetylacetonate ($\text{Pd}(\text{acac})_2$) and $\text{W}(\text{CO})_6$, resulting in reduction of Pd^{2+} to Pd (0) and formation of the palladene sheets.^[30] During the reaction, carbon monoxide was gradually released by thermal decomposition of $\text{W}(\text{CO})_6$. CO is known to strongly adsorb on Pd (111) facet, which in turn facilitates the anisotropic lateral growth and formation of 2D ultrathin metallene.^[23,31,34] For comparison, conventional Pd metallene (**Pd M**) was prepared using a modified literature method, (see Supporting Information),^[34] where citric acid was used as the reducing agent instead of PMo_{12} .

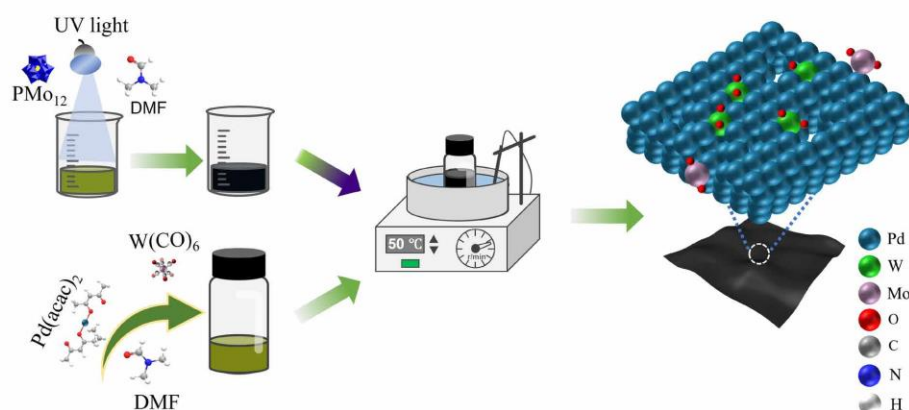


Figure 1. Schematic illustration for the fabrication of D-Pd M.

The morphology and structural properties of the as-synthesized **D-Pd M** and Pd M were characterized by transmission electron microscopy (TEM) and high-resolution transmission electron microscopy (HRTEM). As shown in **Fig. 2a**, **D-Pd M** exhibits an ultrathin 2D nanosheet structure with a lateral diameter of $\sim 1 \mu\text{m}$. In contrast, Pd M exhibits a hexagonal nanosheet structure with an average diameter of 70 nm (SI, **Fig. S2**). Selected area electron diffraction (SAED; SI, **Fig. S3**), confirms the presence of a face-centered cubic (fcc) structure, and atomic force microscopy (AFM) measurements (SI, **Fig. S4**) give an average thickness of approximately 0.9 nm, suggesting the presence of 3 to 5 Pd atom layers.^[28] TEM energy-dispersive X-ray spectroscopy (TEM-EDX; SI, **Fig. S5**) shows the homogenous distribution of Pd, W, and Mo throughout the metallene. The atomic ratio of Pd:W:Mo was determined by inductively coupled plasma optical emission spectroscopy (ICP-OES) to be 93.8 : 5.2 : 1. Detailed morphological analysis of the TEM data reveals curved surface with abundant defects, including pores and concave structures (SI, **Fig. S6**). The defects were further probed by HR-STEM. **Fig. 2b** shows the presence of pores (red circle, **area 1**) and concave areas (dark blue

3. Results and discussion

circle, **area 2**), also see **Fig. S7**.^[15] The brighter contrast observed in **Fig. 2b** is indicative of the lower thickness in these areas compared to their surroundings. Notably, in the higher magnification of **area 1 (Fig. 2c)**, step atoms at the inner edge can be observed. Meanwhile, in **Fig. 2d**, the clear atom distribution and brighter contrast indicate the presence of a concave structure.^[15] Numerous concave structures with various diameters, typically less than 10 nm, are observed in **Fig. 2e** (dark blue circles). We also use a false-color mode to illustrate the thickness contrast more clearly (SI, **Fig. S8 a-d**). Additionally, curved structures are also observed in HRTEM (green rectangles in **Fig. 2e**, and SI, **Fig. S8e**), which leads to lattice distortion. The fast Fourier transformation (FFT) pattern (SI, **Fig. S8f**) exhibits a sixfold symmetric fcc structure, implying that the metallene is stacked dominantly along the (111) facets.^[15] TEM analyses give a lattice spacing of 0.23 nm (**Fig. 2f**), which exceeds that of bulk Pd, suggesting the presence of intrinsic tensile strain due to its atomically thin structure. The results are consistent with powder X-ray diffraction (pXRD) analyses shown in **Fig. 2g**, where the peak at 39.4° is attributed to the (111) plane of the fcc structure of Pd metallene. Additionally, smaller peaks corresponding to the (200) plane at 46.7° and the (220) plane at 68.1° in **D-Pd M** compared to Pd M and Pd/C indicate the predominance of the (111)-exposed feature. Furthermore, the shifts to lower 2θ angles observed in **D-Pd M** compared to Pd M and Pd/C are attributed to strain effects and lattice distortions caused by the defect structure. Next, the oxidation states of **D-Pd M** were investigated by X-ray photoelectron spectroscopy (XPS). The deconvoluted spectrum of Pd 3d shows the distinct characteristic peaks centered at 335.4 eV and 340.7 eV, which are assigned to Pd (0) 3d_{5/2} and Pd (0) 3d_{3/2}, respectively (**Fig. 2h**). The small peaks at 336.7 eV and 342 eV are assigned to PdO, assigned to surface oxidation of Pd.^[25,26] The results indicate that **D-Pd M** is dominated by metallic Pd. The deconvoluted W 4f spectrum (**Fig. 2i**) shows the existence of W⁵⁺ species.^[35] In contrast, the oxidation state of Mo cannot be assigned reliably by XPS due the low concentration of Mo species in **D-Pd M**.

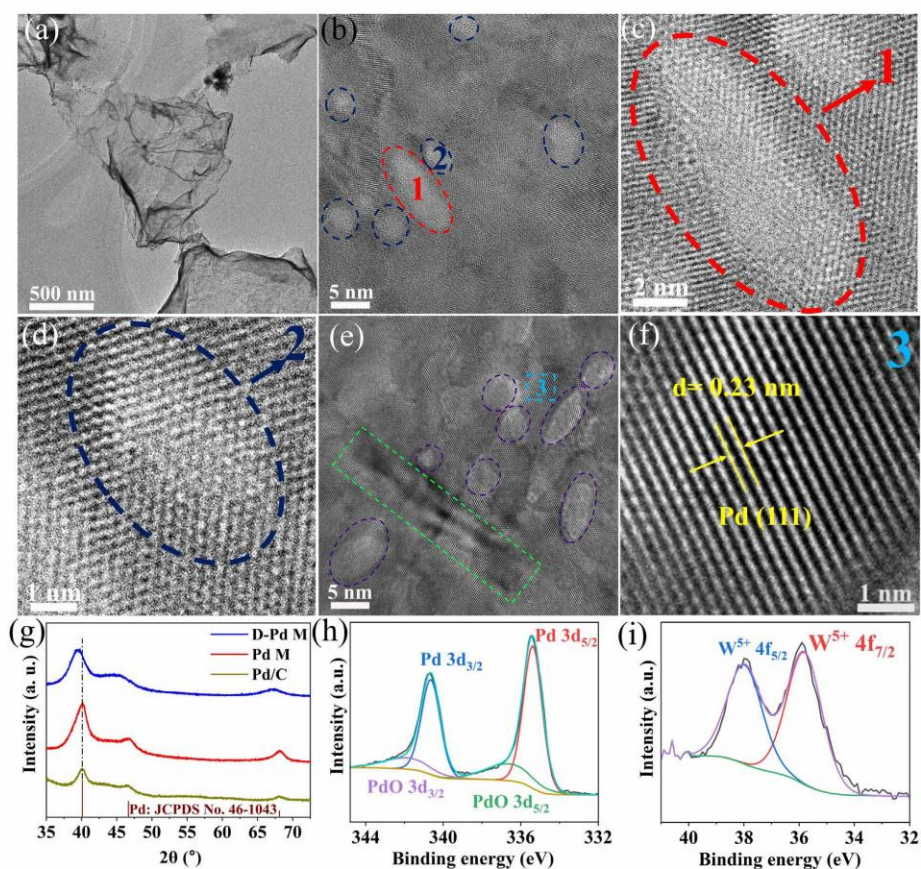


Figure 2. (a) TEM image and (b, e) HRTEM images of **D-Pd M**, with corresponding enlarged crystal details shown in (c, d, and f) for selected areas (area 1, area 2, and area 3, respectively). (g) XRD patterns of **D-Pd M**, Pd M, and Pd/C. (h) Deconvoluted XPS spectra of Pd 3d and (i) W 4f of **D-Pd M**.

X-ray absorption spectroscopy (XAS) characterization was performed to further investigate the chemical states and local coordination environments of **D-Pd M**. The normalized Pd K-edge X-ray absorption near-edge structure (XANES) spectrum (**Fig. 3a**) of **D-Pd M** is similar to the Pd foil reference, indicating its dominant metallic state,^[25,26] which coincides with the XPS result. Fourier transform extended X-ray absorption fine structures (FT-EXAFS) analysis was employed to investigate the local environment of the Pd atoms (**Fig. 3b**). The strong peak in the **D-Pd M** EXAFS spectra at 2.57 Å is assigned to the Pd-Pd pairs.^[28] The average coordination number (CN) of elements is proportional to the intensity of FT- $\chi(k)$ peak and the corresponding fitting results of Pd K-edge FT-EXAFS (SI, **Fig. S9** and **Table S1**) give an average CN of 10.7±1.0, which is lower than that in Pd foil (CN_{Pd foil} = 12), indicating the existence of

unsaturated Pd sites. This is in agreement with the proposed thin layered structure and the presence of multiple defects in the **D-Pd M**.^[31] The W species in **D-Pd M** was further investigated by analyzing its L₃-edge XANES and FT-EXAFS spectra. As shown in **Fig. 3c**, the white-line peak intensity is between WO₂ and WO₃, which gives an approximate oxidation state of +5.^[35,36] This finding is consistent with the results obtained from XPS analysis. In addition, the peaks in the FT-EXAFS spectrum (**Fig. 3d**) at 1.38 Å and 2.43 Å can be assigned W-O and W-Pd environments.^[36,37] The corresponding fitting results of W L₃-edge FT-EXAFS show the CN of W-Pd is 6.3±0.8. Based on these results, we propose that WO_x (x = 2.5) is doped on the surface of metallene. Additionally, W substitutes the position of Pd, as illustrated in **Fig. S12**.^[38] Notably, while W-W pairs are present in bulk WO₂ and WO₃, they are not observed in **D-Pd M** according to the FT-EXAFS spectrum and wavelet transform (WT) analysis (**Fig. 3g**), which can better resolve features in K-space and radial distance. The results indicate that atomic WO_x species are doped on the surface of the metallene. Furthermore, we also investigated the chemical states and local coordination environments of Mo in **D-Pd M** by employing MoO₂, MoO₃, and Mo foil as reference materials. In **Fig. 3e**, MoO₃ exhibits a distinct pre-edge feature at around 19,995 eV, which is not observed in MoO₂ and Mo foil. Additionally, a weak pre-edge is observed in **D-Pd M**, suggesting that the oxidation state of Mo in **D-Pd M** falls between that of MoO₂ and MoO₃.^[39] Furthermore, the near-edge structure XANES spectra also support this conclusion. The FT-EXAFS spectrum in **Fig. 3f** indicates the presence of Mo-O and Mo-Pd pairs, with no Mo-Mo species observed (**Fig. 3h**), suggesting atomic dispersion of MoO_x. The fitting results of Mo K-edge FT-EXAFS for Mo-Pd give a CN of 0.9±0.2, indicating that the MoO_x are located on the surface of the Pd sheets rather than being embedded in the Pd lattice, as illustrated in **Fig. S12**.^[39] More detailed peak assignments for FT-EXAFS of Pd, W, and Mo can be found in **Table S1**. The comparison of corresponding fitting results and the raw data can be found in **Fig. S9-11**.

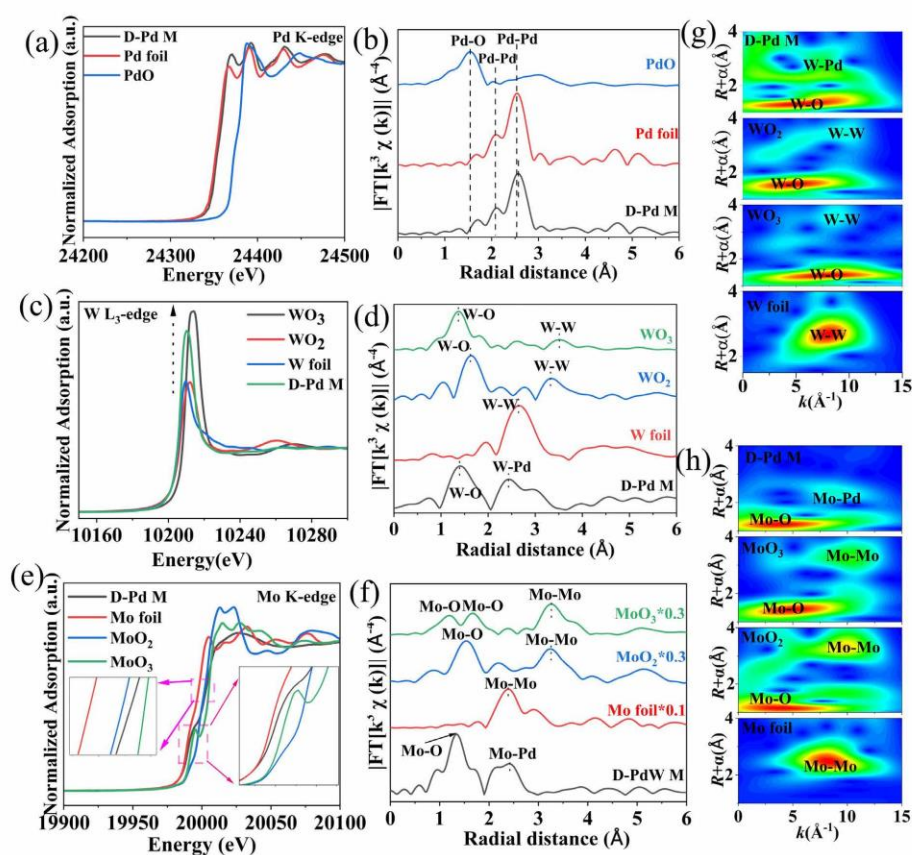


Figure 3. XAS characterizations of **D-Pd M**. Experimental XANES spectra (a, c, and e) and EXAFS spectra (b, d, and f) of Pd, W, and Mo, respectively. Wavelet transform profiles of W (g) and Mo (h).

In the next step, we evaluated the electrocatalytic performance of the **D-Pd M** for ORR in 0.1 M aqueous KOH using a typical three-electrode electrochemical setup. Here, the saturated calomel electrode (SCE) was used as the reference electrode, and a graphite rod was employed as the counter electrode. All potentials in this study have been converted to reversible hydrogen electrode potentials (RHE, see details in the SI). Prior to the measurement, freshly prepared **D-Pd M** and Pd M were deposited on a VULCAN® XC-72 carbon support (See details in SI). In addition, commercial 10% Pd/C and 20% Pt/C were also used as ORR catalyst references. The respective catalysts ink was drop-cast onto the glassy carbon rotating disk electrode (GC-RDE), which acted as the working electrode. The metal loading on the electrode for **D-Pd M/C** and Pd M/C was controlled to be $10 \mu\text{g} \cdot \text{cm}^{-2}$, while that of commercial Pd/C and Pt/C was controlled to be $15 \mu\text{g} \cdot \text{cm}^{-2}$ to reach the well-defined limiting current densities. The typical cyclic

voltammetry (CV) curves of all the catalysts were recorded in N₂-saturated 0.1 M KOH at a scan rate of 50 mV·s⁻¹. As shown in **Fig. 4a** and **Fig. S13**, the peak located at 0.74 V of **D-Pd M/C** is assigned to Pd oxide reduction.^[28] Notably, the reduction potential is a descriptor of the Pd-O binding energy. Compared to Pd/C (0.69 V) and Pd M/C (0.73 V), the peak of **D-Pd M/C** shifts positively, revealing its weaker oxygen affinity.^[27,40] Next, we determined the electrochemically active surface areas (ECSAs) of **D-Pd M/C** and reference catalysts by underpotentially deposited hydrogen (H_{upd}) method in 0.1M HClO₄ electrolyte (See method details in SI). The ECSA values are estimated to be 83.1 m²·g_{Pd}⁻¹ for **D-Pd M/C**, 75 m²·g_{Pd}⁻¹ for Pd M/C, 35.6 m²·g_{Pd}⁻¹ for Pd/C, and 66.7 m²·g_{Pd}⁻¹ for Pt/C, respectively (SI, Fig. S14). The increased active areas of **D-Pd M** can be attributed to its porous and curved structure. This structural characteristic ensures that more active sites are exposed to the electrolyte during the catalytic process.

The linear sweep voltammetry (LSV) curves of all the samples were determined in an O₂-saturated 0.1 M KOH electrolyte at a scan rate of 20 mV·s⁻¹ to assess their ORR performance. As shown in **Fig. 4b**, **D-Pd M/C** shows the most positive half-wave potential ($E_{1/2}$, 0.93 V) and onset potential (E_{onset} , 1.02 V), as compared with those of Pd M/C (0.87 V, 0.99 V), Pd/C (0.87 V, 1.02 V), and Pt/C (0.88 V, 1.01 V), revealing that **D-Pd M/C** exhibited the best catalytic performance for ORR among all the catalysts. The diffusion-limiting current density (j_L) of **D-Pd M/C** (5.7 mA·cm⁻²) is also higher than that of Pd M/C (5.4 mA·cm⁻²), Pd/C (5.5 mA·cm⁻²), and Pt/C (5.6 mA·cm⁻²). Such high limiting current density is a benefit to the high-power densities of Zn-air batteries. Besides, **D-Pd M/C** has the smallest Tafel slop value (**Fig. 4c**) of 42.6 mV·dec⁻¹, compared with that of Pd M/C (74 mV·dec⁻¹), Pd/C (93.7 mV·dec⁻¹), and Pt/C (63.5 mV·dec⁻¹), which indicates faster ORR reaction kinetics on the surface of **D-Pd M**. To further quantify the intrinsic ORR activity, kinetic currents were calculated for all catalysts using the Koutecký-Levich (K-L) equation (see details in SI). These were then normalized based on the metal mass loading of the catalysts and the ECSA to determine the MA and specific activity (SA). As shown in **Fig. S15**, **D-Pd M/C** achieves an MA of 1.3 A·mg_{Pd}⁻¹ at the generally chosen potential of 0.9 V, which is 3.3, 3.9, and 6.5 times higher than that of Pd M/C, commercial Pd/C, and commercial Pt/C. Additionally, **D-Pd M/C** delivers an MA of 5.2 A·mg_{Pd}⁻¹ at 0.85 V. This value is also apparently higher than that of Pd M/C (1.4 A·mg_{Pd}⁻¹), commercial Pd/C (0.88 A·mg_{Pd}⁻¹), and commercial Pt/C (0.88 A·mg_{Pt}⁻¹). Likewise, **D-Pd M/C** also has specific activities of 6.13 mA·cm⁻² and 1.5 mA·cm⁻² at 0.85 V and 0.9 V, respectively, which significantly outperform Pd M/C (1.86 mA·cm⁻², 0.52 mA·cm⁻²), commercial Pd/C (2.46 mA·cm⁻², 0.91 mA·cm⁻²), and commercial Pt/C (1.31 mA·cm⁻², 0.3 mA·cm⁻²). The excellent

ORR catalytic performance of **D-Pd M/C** can be attributed to the lower Pd-O binding energy, which facilitates the generation of intermediates (*OH and *OOH) and their transformation to H₂O. Furthermore, to understand the catalytic process of **D-Pd M**, rotating ring-disk electrode (RRDE) measurements were used to determine the electron transfer number (*n*) and hydrogen peroxide yield, see details in SI. As shown in **Fig. 4d** and **Fig. S16a**, the electron transfer number is > 3.9 between 0.3 V to 0.95 V, revealing a four-electron transfer-dominated pathway, which agrees well with the results obtained from the K-L plot at rotation rates between 625 rpm and 2025 rpm (SI, **Fig. S16b, c**). The H₂O₂ yield is only 0-1.6% within the potential range from 0.8 to 0.3 V. Pd M/C, Pd/C, and Pt/C exhibit similar results, indicating a consistent four-electron transfer process (SI, **Fig. S17**).

Apart from electrocatalytic activity, stability is another essential criterion for the comprehensive evaluation of the catalytic performance. Therefore, we employed accelerated durability (ADT) tests by CV cycling between 0.6 and 1.0 V at a scan rate of 200 mV·s⁻¹ in an O₂-saturated 0.1 M KOH electrolyte. As shown in **Fig. 4e**, after 5,000 and 10,000 cycles, the E_{1/2} of **D-Pd M/C** shows only negligible decay (4 mV and 6 mV, respectively). In contrast, an apparent negative shift was observed for Pd M/C (10 mV and 23 mV), commercial Pd/C (19 mV and 23 mV), and commercial Pt/C (25 mV and 38 mV), respectively (SI, **Fig. S18**). In addition, the MA of **D-Pd M/C** at 0.9 V has decreased by 10.4% and 19.2% after 5,000 and 10,000 cycles (**Fig. 3f**), which outperforms those of Pd M/C (18.7% and 41%), commercial Pd/C (36.6% and 44.6%), and commercial Pt/C (60.4% and 74.6%). The same scenario was also observed at 0.85 V vs. RHE in all the catalysts (SI, **Fig. S19**). Additionally, the morphology and structure of **D-Pd M** have no obvious degradation after 10,000 cycles, compared to the pristine sample. In comparison, the apparent aggregation of Pt nanoparticles was observed in Pt/C (SI, **Fig. S20**).

3. Results and discussion

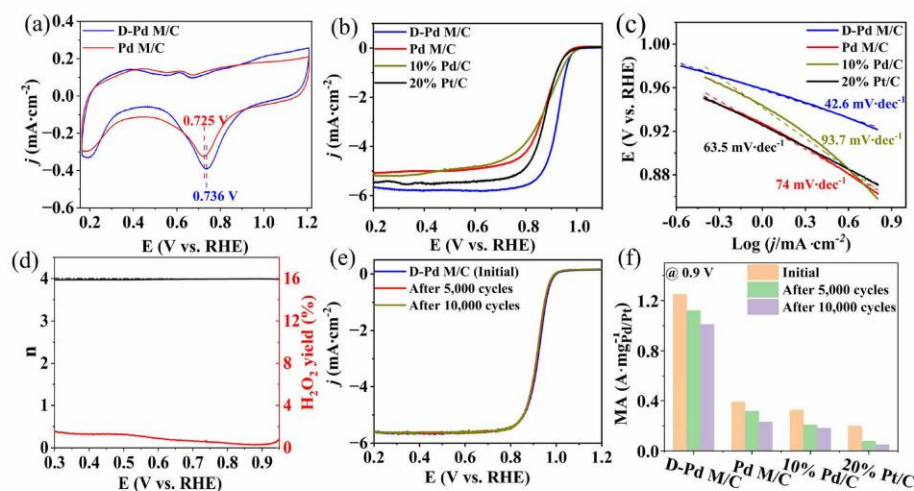


Figure 4. (a) CVs of **D-Pd M/C** and Pd M/C, (b) LSVs, and (c) Tafel slopes of **D-Pd M/C**, Pd M/C, Pd/C, and Pt/C, (d) electron transfer number and H₂O₂ yield of **D-Pd M**, (e) LSVs of **D-Pd M**, and (f) mass activities of **D-Pd M/C**, Pd M/C, Pd/C, and Pt/C at 0.9 V before and after 5,000 and 10,000 cycles.

Based on the previous report from Norskov, the binding energy between catalysts and O₂ is linearly correlated with the energy center of the valence *d*-band density of states (*d*-band center), making it one of the most successful descriptors of ORR activity.^[41] We therefore calculated the *d*-band centers of various defects in **D-Pd M** using density functional theory (DFT) to elucidate the reasons for the superior ORR activity of **D-Pd M**. We constructed a four-atom layer model for the **D-Pd M**, incorporating WO_x doping into the surface lattice of metallene and MoO_x attachment to the edge Pd atoms. The loading of W and Mo were set to 5% and 1%, respectively, to be in line with experimental results. As shown in **Fig. 5a**, the *d*-band centers of surface Pd atoms in different layer Pd sheets were calculated. A downward shift (~0.11 eV) in the *d*-band center of surface atoms is observed in the four-layer Pd sheet compared to the sixteen-layer Pd sheet, which results in less strongly bound O₂ on the surface Pd atoms.^[28] We note that the average spacing between the planes in four-layer Pd metallene is 3.2% greater than in a 16-layered nanosheet, indicating a higher level of tensile strain in the four-layer structure compared to multilayer Pd sheets. The electronic structures tuned by defects were also investigated. As illustrated in **Fig. 5b**, in a perfect four-layer Pd sheet, the *d*-band center of the surface atoms in the (111) plane is -1.67 eV. However, when subjected to concave defects and

pore defects, the sublayer layer atoms feature substantially lower d -band centers (-1.75 eV and -1.8 eV, respectively) compared to the surface atoms. This indicates a weaker binding ability to O_2 , thereby facilitating the formation and conversion of intermediates (*OH and *OOH) to H_2O/OH .^[14,15] The findings confirm that concave and pore defects serve as effective means to introduce highly active sites, thereby enhancing the catalytic properties for ORR. Moreover, embedding WO_x into the surface Pd lattice also leads to a downshift of the d -band center by 0.11 eV. The average d -band center of edge Pd atoms was calculated to be -1.59 eV, significantly higher than that of surface atoms. This discrepancy reveals the less favorable catalytic features for oxygen reduction reaction (ORR) exhibited by edge atoms. After attaching MoO_x to the edge Pd atoms, the d -band center of these atoms shifted downward to -1.69 eV, a value similar to the d -band center of surface atoms, indicating the improved catalytic properties. These computational results suggest that size effects, pore defects, concave defects, WO_x doping, and MoO_x modification can effectively enhance the ORR activity of **D-Pd M**.

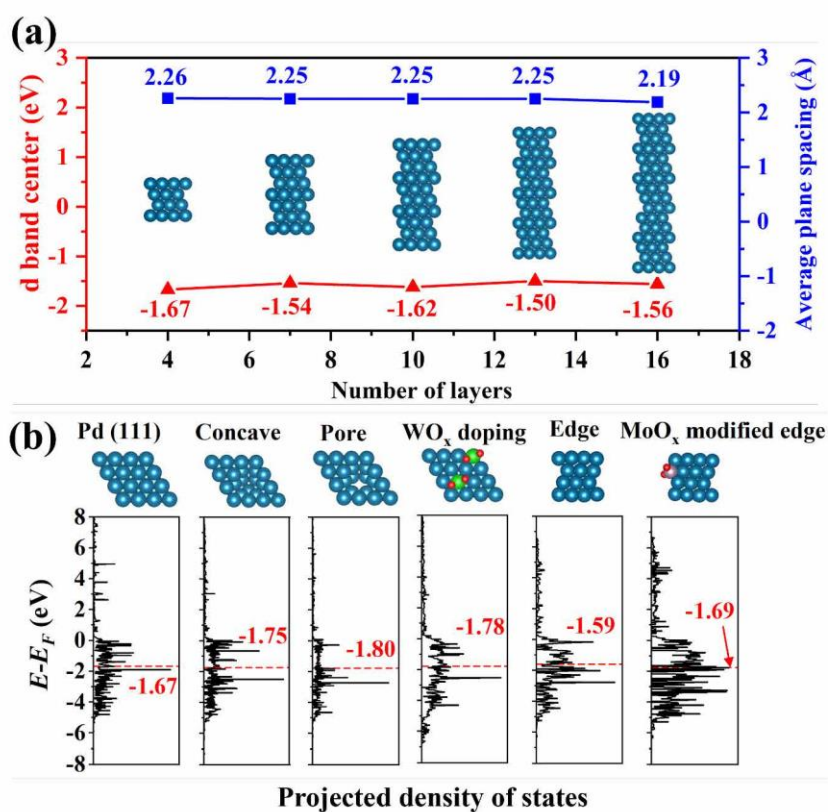


Figure 5. DFT calculations of *d*-band centers. (a) The *d*-band center of surface atoms and average plane spacings of Pd nanosheets with 4, 7, 10, 13, and 16 layers. The side view of atomic models is inserted. (b) From left to right, the *d* band centers of surface atoms in Pd (111), exposed sublayer atoms in concave defects, exposed sublayer atoms in pores defects, surface atoms in WO_x doping, edge atoms, and MoO_x modified edge atoms. The first four schematic illustrations are from the top view and the last two are from side view of atomic model. The navy, green, pink, and red balls represent Pd, W, Mo, and O, respectively.

Next, the practical utility of the **D-Pd M** catalyst was tested by integration into an aqueous custom-built Zn-air battery (SI, **Fig. S21**). Given the economic expense of Pd metal, we opted to test the system at an extremely low Pd loading at the cathode ($26 \mu\text{g}_{\text{Pd}}\cdot\text{cm}^{-2}$). The principal structure of the Zn-air battery is shown in **Fig. 6a**; briefly, the battery is based on a carbon paper-supported **D-Pd M/C** as the air cathode, a Zn plate as the anode, and 6 M aqueous KOH solution containing 0.2 M Zn(CH₃COO)₂ as the electrolyte. Initial tests show that the Zn-air battery achieves a high open-circuit potential (OCP) of 1.4 V (SI, **Fig. S21**). The specific capacities of the **D-Pd M/C**-battery at $15 \text{ mA}\cdot\text{cm}^{-2}$ is illustrated in **Fig. 6b**. For comparison, a reference Zn-air battery using commercial Pt/C coated carbon paper ($26 \mu\text{g}_{\text{Pt}}\cdot\text{cm}^{-2}$) as air cathode was tested under the same conditions. After normalizing for the weight loss of Zn, the **D-Pd M/C**-based battery exhibits a discharge specific capacity of $809 \text{ mAh}\cdot\text{g}_{\text{Zn}}^{-1}$, corresponding to an energy density of $982 \text{ Wh}\cdot\text{kg}_{\text{Zn}}^{-1}$, which outperforms the Pt/C-based battery ($785 \text{ mAh}\cdot\text{g}_{\text{Zn}}^{-1}$ and $890 \text{ Wh}\cdot\text{kg}_{\text{Zn}}^{-1}$). In addition, during the long-term discharge test, the potential of the **D-Pd M/C**-based cell remained remarkably stable and only a slight potential decrease of 0.05 V was observed. In contrast, a notable potential drop ($>0.2 \text{ V}$) was observed for the Pt/C-based battery. The stability of the **D-Pd M/C**-based battery is further shown by the discharge curves at various current densities (**Fig. 6c**). Also, the **D-Pd M/C**-based battery achieves a high power density ($55 \text{ mW}\cdot\text{cm}^{-2}$) compared with the Pt/C-based battery ($37 \text{ mW}\cdot\text{cm}^{-2}$), see **Fig. S22a**. The power density of the **D-Pd M/C**-based battery can be increased by at higher **D-Pd M** loadings, see **Fig. S22b**. To assess the cycling durability, the **D-Pd M/C**-based Zn-air battery was further tested at a charging and discharging rate of $15 \text{ mA}\cdot\text{cm}^{-2}$ for 60 minutes per cycle. As illustrated in **Fig. 6d**, **D-Pd M/C**-based battery exhibits a significantly longer cycling lifetime over 300 cycles ($\sim 300 \text{ h}$) with a small charge/discharge voltage gap. Initially, the charge/discharge voltage efficiency reached 80.1% with a potential gap of 0.33 V. During cycling, the voltage efficiency decreased slowly, while the discharging potential remained exceptionally stable throughout the measurement. The gradual increase in charging

potential resulted in a decrease in round-trip voltage efficiency, possibly attributed to imperfect oxygen evolution activity under conditions of very low palladium loading (SI, Fig. S22c).

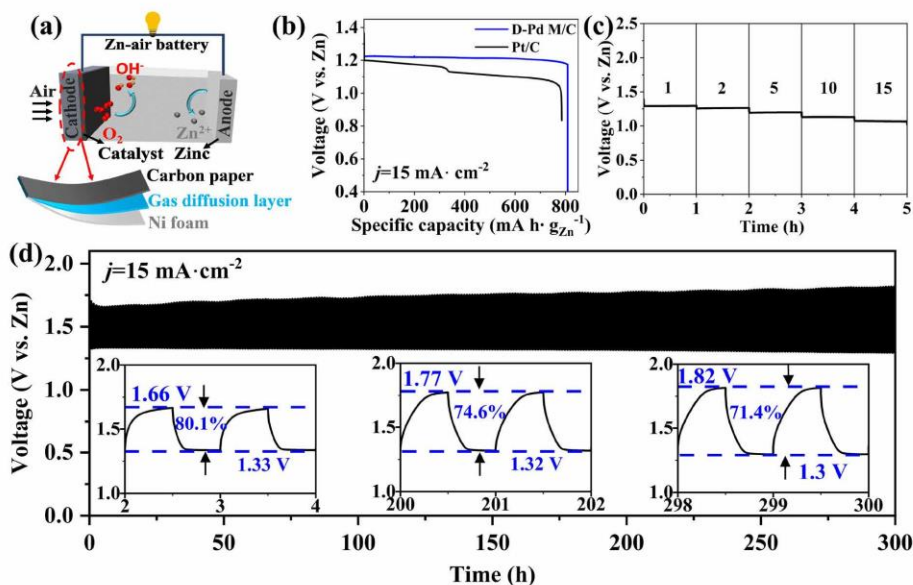


Figure 6. (a) Scheme of the aqueous Zn-air battery, (b) full discharge profile (voltage versus specific capacity of discharge) for a Zn-air battery using **D-Pd M/C** as the air cathode at a current density of 15 mA cm^{-2} , (c) the discharge curves of Zn-air batteries at current densities of 1, 2, 5, 10, and 15 mA cm^{-2} , and (d) the charge-discharge profiles of two Zn-air batteries worked at a current density of 15 mA cm^{-2} with each cycle lasting 60 min.

Conclusion

In summary, we have developed an efficient and robust ORR electrocatalyst by developing Pd-based defective metallene structures. The **D-Pd M** catalyst features an atomically thin few-layer palladium metal structure and contains various defects, including pores and concave structures. WO_x/MoO_x doping of the metallene surface was observed, resulting in a downward shift of the *d*-band center. The system showed high ORR activity with exceptionally high half-wave potential, high mass activity and superior durability. Theoretical computations and experimental data suggest that the excellent ORR reactivity can be attributed to a downshift of the *d*-band center due to the introduction of structural defects. The electrode was integrated as cathode in a Zn-air battery, resulting in excellent performance at very low Pd loadings. This

study offers valuable insights into achieving efficient ORR catalysts with reduced precious metal consumption, thereby contributing to sustainable energy conversion.

Acknowledgements

The authors gratefully acknowledge financial support by the Deutsche Forschungsgemeinschaft DFG (Cluster of Excellence EXC2154, POLiS, project number: 390874152 and TRR 234 CataLight, project no. 364549901 and project no. 389183496). R.L. gratefully acknowledges financial support by the Alexander von Humboldt Foundation. Shujun Li and Nana Ma gratefully acknowledge financial support by National Natural Science Foundation of China (22171073) and the Program for Innovation Talents in Universities of Henan Province (23HASTIT005). Kecheng Cao gratefully acknowledges financial support by XXXX. D.G. acknowledges the Deutsche Forschungsgemeinschaft (DFG) for a Walter Benjamin Fellowship (project no. 510966757). Financial support by the Carl Zeiss Foundation (Halocycles no P2021-10-007) is gratefully acknowledged by D.G. F. F. gratefully acknowledges the China Scholarship Council CSC for a PhD fellowship. R.L., D.G., and C.S. gratefully acknowledge financial support by Johannes Gutenberg University Mainz, the Top-Level Research Initiative SusInnoScience and the Gutenberg Research College.

Reference

- [1] S. Chu, A. Majumdar, *Nature* **2012** *488*:7411 **2012**, *488*, 294–303.
- [2] A. Han, X. Wang, K. Tang, Z. Zhang, C. Ye, K. Kong, H. Hu, L. Zheng, P. Jiang, C. Zhao, Q. Zhang, D. Wang, Y. Li, *Angewandte Chemie International Edition* **2021**, *60*, 19262–19271.
- [3] C. Lim, A. R. Fairhurst, B. J. Ransom, D. Haering, V. R. Stamenkovic, *ACS Catal* **2023**, *13*, 14874–14893.
- [4] Z. Ma, Z. P. Cano, A. Yu, Z. Chen, G. Jiang, X. Fu, L. Yang, T. Wu, Z. Bai, J. Lu, *Angewandte Chemie* **2020**, *132*, 18490–18504.
- [5] Z. Lyu, X.-G. Zhang, Y. Wang, K. Liu, C. Qiu, X. Liao, W. Yang, Z. Xie, S. Xie, *Angewandte Chemie* **2021**, *133*, 16229–16236.
- [6] Q. Yang, Y. Jia, F. Wei, L. Zhuang, D. Yang, J. Liu, X. Wang, S. Lin, P. Yuan, X. Yao, *Angewandte Chemie* **2020**, *132*, 6178–6183.

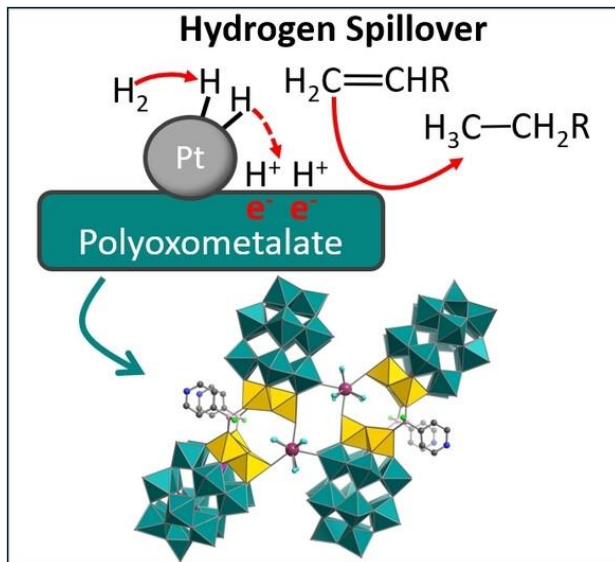
- [7] M. A. de Araújo, A. A. Koverga, A. M. P. Sakita, F. B. Ometto, L. G. da Trindade, E. A. Ticianelli, *ChemCatChem* **2023**, *15*, e202201594.
- [8] J. Zhang, L. iangti Qu, G. Shi, J. Liu, J. Chen, L. Dai, D. Zhang, J. Liu, L. Dai, L. Qu, G. Shi, J. Chen, *Angewandte Chemie* **2016**, *128*, 2270–2274.
- [9] Z. Zhao, C. Chen, Z. Liu, J. Huang, M. Wu, H. Liu, Y. Li, Y. Huang, *Advanced Materials* **2019**, *31*, 1808115.
- [10] K. J. Sawant, Z. Zeng, J. P. Greeley, *Angewandte Chemie* **2024**, *136*, e202312747.
- [11] E. Hornberger, V. Mastronardi, R. Brescia, P. P. Pompa, M. Klingenhof, F. Dionigi, M. Moglianetti, P. Strasser, *ACS Appl Energy Mater* **2021**, *4*, 9542–9552.
- [12] T. Đukić, L. Pavko, P. Jovanović, N. Maselj, M. Gatalo, N. Hodnik, *Chemical Communications* **2022**, *58*, 13832–13854.
- [13] D. Y. Chung, J. M. Yoo, Y. E. Sung, *Advanced Materials* **2018**, *30*, 1704123.
- [14] S. Huang, S. Lu, S. Gong, Q. Zhang, F. Duan, H. Zhu, H. Gu, W. Dong, M. Du, *ACS Nano* **2022**, *16*, 522–532.
- [15] F. Lin, F. Lv, Q. Zhang, H. Luo, K. Wang, J. Zhou, W. Zhang, W. Zhang, D. Wang, L. Gu, S. Guo, *Advanced Materials* **2022**, *34*, 2202084.
- [16] N. Zhang, Q. Shao, X. Xiao, X. Huang, *Adv Funct Mater* **2019**, *29*, 1808161.
- [17] L. Bu, N. Zhang, S. Guo, X. Zhang, J. Li, J. Yao, T. Wu, G. Lu, J. Y. Ma, D. Su, X. Huang, *Science (1979)* **2016**, *354*, 1410–1414.
- [18] X. Wang, Z. Li, Y. Qu, T. Yuan, W. Wang, Y. Wu, Y. Li, *Chem* **2019**, *5*, 1486–1511.
- [19] Y. Yang, W. Xiao, X. Feng, Y. Xiong, M. Gong, T. Shen, Y. Lu, H. D. Abruña, D. Wang, *ACS Nano* **2019**, *13*, 5968–5974.
- [20] L. Zhang, Z. Zhao, X. Fu, S. Zhu, Y. Min, Q. Xu, Q. Li, *ACS Appl Mater Interfaces* **2023**, *15*, 5198–5208.
- [21] Q. Yang, L. Shi, B. Yu, J. Xu, C. Wei, Y. Wang, H. Chen, *J Mater Chem A Mater* **2019**, *7*, 18846–18851.
- [22] B. R. Anne, S. Il Choi, *Curr Opin Electrochem* **2023**, *39*, 101303.
- [23] S. Huang, S. Lu, S. Gong, Q. Zhang, F. Duan, H. Zhu, H. Gu, W. Dong, M. Du, *ACS Nano* **2022**, *16*, 522–532.
- [24] M. Xie, S. Tang, B. Zhang, G. Yu, *Mater Horiz* **2023**, *10*, 407–431.
- [25] K. Chen, Z. Ma, X. Li, J. Kang, D. Ma, K. Chu, *Adv Funct Mater* **2023**, *33*, 2209890.
- [26] H. Wang, W. Wang, H. Yu, Q. Mao, Y. Xu, X. Li, Z. Wang, L. Wang, *Applied Catalysis B: Environment and Energy* **2022**, *307*, 121172.
- [27] J. Guo, L. Gao, X. Tan, Y. Yuan, J. Kim, Y. Wang, H. Wang, Y. J. Zeng, S. Il Choi, S. C. Smith, H. Huang, *Angewandte Chemie - International Edition* **2021**, *60*, DOI 10.1002/anie.202100307.

3. Results and discussion

- [28] M. Luo, Z. Zhao, Y. Zhang, Y. Sun, Y. Xing, F. Lv, Y. Yang, X. Zhang, S. Hwang, Y. Qin, J. Y. Ma, F. Lin, D. Su, G. Lu, S. Guo, *Nature* **2019** *574*:7776 **2019**, *574*, 81–85.
- [29] K. Zhang, Y. He, R. Guo, W. Wang, Q. Zhan, R. Li, T. He, C. Wu, M. Jin, *ACS Energy Lett* **2022**, *7*, DOI 10.1021/acsenergylett.2c01734.
- [30] H. Yu, T. Zhou, Z. Wang, Y. Xu, X. Li, L. Wang, H. Wang, *Angewandte Chemie International Edition* **2021**, *60*, 12027–12031.
- [31] W. Zhu, L. Zhang, P. Yang, C. Hu, Z. Luo, X. Chang, Z.-J. Zhao, J. Gong,] W Zhu,] L Zhang,] P Yang, C. Hu, Z. Luo, X. Chang, Z. Zhao, J. Gong, *Angewandte Chemie International Edition* **2018**, *57*, 11544–11548.
- [32] E. A. Nagul, I. D. McKelvie, P. Worsfold, S. D. Kolev, *Anal Chim Acta* **2015**, *890*, 60–82.
- [33] H. Zhou, Z. Ma, G. Yang, X. Jiang, S. Duan, Y. Wu, M. Wang, L. Ni, L. Feng, G. Diao, *Batter Supercaps* **2024**, e202300563.
- [34] Y. Li, Y. Yan, Y. Li, H. Zhang, D. Li, D. Yang, *CrystEngComm* **2015**, *17*, 1833–1838.
- [35] P. Castellero, V. Rico-Gavira, C. López-Santos, A. Barranco, V. Pérez-Dieste, C. Escudero, J. P. Espinós, A. R. González-Elipe, *Journal of Physical Chemistry C* **2017**, *121*, 15719–15727.
- [36] H. Wang, H. Zheng, L. Ling, Q. Fang, L. Jiao, L. Zheng, Y. Qin, Z. Luo, W. Gu, W. Song, C. Zhu, *ACS Nano* **2022**, *16*, 21266–21274.
- [37] K. Chen, F. Wang, X. Lu, Y. Li, K. Chu, *ACS Catal* **2023**, *13*, 9550–9557.
- [38] K. Chen, Z. Ma, X. Li, J. Kang, D. Ma, K. Chu, *Adv Funct Mater* **2023**, *33*, 2209890.
- [39] J. Wu, J. Fan, X. Zhao, Y. Wang, D. Wang, H. Liu, L. Gu, Q. Zhang, L. Zheng, D. J. Singh, X. Cui, W. Zheng, *Angewandte Chemie International Edition* **2022**, *61*, e202207512.
- [40] Y. Wang, D. Sun, M. Wang, Z. Feng, A. S. Hall, *Journal of Physical Chemistry C* **2020**, *124*, DOI 10.1021/acs.jpcc.9b11734.
- [41] B. Hammer, J. K. Nørskov, *Surf Sci* **1995**, *343*, 211–220.

3.5 Hydrogenation catalysis by hydrogen spillover on platinum-functionalized heterogeneous boronic acid-polyoxometalates

Shujun Li, Yubin Ma, Yue Zhao, Rongji Liu, Yupeng Zhao, Xusheng Dai, Nana Ma, Carsten Streb, Xuenian Chen



This work demonstrated how polyoxometalate (POM)-based heterogeneous compounds functionalized with Platinum particles activate H₂ by synergism between a hydrogen spillover mechanism and electron-proton transfer by the POM. This interplay facilitates the selective catalytic reduction of olefins and nitroarenes with high functional group tolerance. The resulting materials show excellent catalytic activity in hydrogenation of olefins and nitrobenzene derivatives under mild conditions.

Author Contributions:

Shujun Li: Conceptualization, Supervision, Methodology, Data curation, Investigation, Writing original draft.

Yubin Ma: Investigation, Data curation, Writing original draft.

Yue Zhao: Data curation, Investigation.

Rongji Liu, Yupeng Zhao: Data curation, Investigation,

Xusheng Dai: Investigation, Data curation, Writing original draft.

Nana Ma: Data curation, Writing original draft.

Carsten Streb: Conceptualization, Supervision, Methodology, Writing original draft.

Xuenian Chen: Conceptualization, Supervision.

Supporting Information can be found at pp 172.

“S. Li, Y. Ma, Y. Zhao, R. Liu, Y. Zhao, X. Dai, N. Ma, C. Streb, X. Chen, *Angewandte Chemie International Edition* 2023, 62, e202314999” Reprinted with permission, © 2023 The Authors. *Angewandte Chemie International Edition* published by Wiley-VCH GmbH



Polyoxometalates Hot Paper

 How to cite: *Angew. Chem. Int. Ed.* **2023**, *62*, e202314999
 doi.org/10.1002/anie.202314999

Hydrogenation Catalysis by Hydrogen Spillover on Platinum-Functionalized Heterogeneous Boronic Acid-Polyoxometalates

Shujun Li,* Yubin Ma, Yue Zhao, Rongji Liu, Yupeng Zhao, Xusheng Dai, Nana Ma, Carsten Streb,* and Xuenian Chen*

Abstract: The activation of molecular hydrogen is a key process in catalysis. Here, we demonstrate how polyoxometalate (POM)-based heterogeneous compounds functionalized with Platinum particles activate H₂ by synergism between a hydrogen spillover mechanism and electron-proton transfer by the POM. This interplay facilitates the selective catalytic reduction of olefins and nitroarenes with high functional group tolerance. A family of polyoxotungstates covalently functionalized with boronic acids is reported. In the solid-state, the compounds are held together by non-covalent interactions (π - π stacking and hydrogen bonding). The resulting heterogeneous nanoscale particles form stable colloidal dispersions in acetonitrile and can be surface-functionalized with platinum nanoparticles by in situ photoreduction. The resulting materials show excellent catalytic activity in hydrogenation of olefins and nitrobenzene derivatives under mild conditions (1 bar H₂ and room temperature).

Introduction

The self-assembly of supramolecular aggregates from molecular building blocks provides a powerful strategy towards novel, functional nanostructures.^[1-3] One particularly promising class of molecular components are molecular metal oxides, or polyoxometalates (POMs): POMs are anionic metal oxide clusters which bridge the gap between mononuclear metal oxo complexes and solid-state bulk metal oxides.^[4,5] POMs feature unique properties such as tuneable structure and charge, high redox activity and unique acid-base chemistry, which has led to their application in fields ranging from catalysis^[6,7] to bio-medicine.^[8] However, due to the high symmetry of many classical POMs, their controlled and predictable assembly into supramolecular aggregates is difficult to achieve.

One approach to this end is the use of organo-functionalized POMs (organoPOMs) where the metal oxo cluster shell has been covalently functionalized with organic moieties.^[9-11] Organo-functionalization provides control over the physical and electronic structure of the POMs, making them ideal building blocks for supramolecular assemblies.^[12-14] Thus organoPOMs have successfully been employed as molecular components in the assembly of functional supramolecular systems with unique functions.^[15]

Controlled aggregation of organoPOMs has been used to access a range of functional superstructures including vesicles, micelles, and hollow spheres, so-called blackberries.^[12,16-18] Also, organo-functionalization of POMs with metal coordination sites (e.g., pyridines) has been used for the design of nanostructured organoPOM aggregates.^[19-24] In one outstanding example, Izzet and colleagues described how Dawson-POMs can be covalently functionalized with terpyridine metal coordination sites. Binding of Fe²⁺ to these sites led to a hierarchical self-assembly, resulting in the formation of supramolecular triangles and nano-particles in the 6–10 nm range.^[24]

An alternative approach towards supramolecular organoPOM aggregation is the use of non-covalent interactions. This has been successfully used to link organoPOMs to a range of functional systems including macrocycles,^[25-27] biomolecules,^[28-30] and carbon nanotubes.^[31,32] This strategy offers a broad scope, as the component combinations are almost unlimited.

To-date, most organoPOMs are based on triol-, imido-, organophosphorus-, organosilicon-, or organotin-linkages.^[15,33] In contrast, the use of organoboronic acids as versatile and easily accessible organic linkage is still in its

[*] Prof. Dr. S. Li, M. Sc. Y. Ma, Dr. Y. Zhao, Dr. X. Dai, Dr. N. Ma, Prof. Dr. X. Chen
 Henan Key Laboratory of Boron Chemistry and Advanced Energy Materials, Key Laboratory of Green Chemical Media and Reactions, Ministry of Education, School of Chemistry and Chemical Engineering, Henan Normal University
 Xixiang, 453007 (China)
 E-mail: lisj@htu.edu.cn

Prof. Dr. S. Li, Dr. R. Liu, M. Sc. Y. Zhao, Prof. Dr. C. Streb
 Institute of Inorganic Chemistry I, Ulm University
 Albert-Einstein-Allee 11, 89081 Ulm (Germany)

Dr. R. Liu, M. Sc. Y. Zhao, Prof. Dr. C. Streb
 Department of Chemistry, Johannes Gutenberg University Mainz
 Duesbergweg 10–14, 55128 Mainz (Germany)
 E-mail: carsten.streb@uni-mainz.de

Prof. Dr. X. Chen
 Green Catalysis Center and College of Chemistry, Zhengzhou University
 Zhengzhou, 450001 (China)
 E-mail: xuenian_chen@zzu.edu.cn

© 2023 The Authors. Angewandte Chemie International Edition published by Wiley-VCH GmbH. This is an open access article under the terms of the Creative Commons Attribution License, which permits use, distribution and reproduction in any medium, provided the original work is properly cited.

infancy. Some of us have recently developed this field and demonstrated its use for designing supramolecular boronic acid-based organoPOM aggregates including several POM nanocapsules and a POM-boronic acid-polymer.^[34–36]

Here, we aimed at extending this synthetic approach to the design of boronic acid-based organoPOM assemblies. To this end we were inspired by earlier studies which showed that lanthanide ions are ideally suited to link POMs into larger aggregates.^[37–41]

Results and Discussion

In this work, four novel POM supramolecules (**Ln-POM**) were obtained by the reaction of 4-pyridinylboronic acid (4PyBA), Dawson anions $[P_2Nb_3W_{15}O_{62}]^{9-}$ ($=\{Nb_3W_{15}\}$) and the corresponding lanthanide ions in water. The resulting title compounds are virtually isostructural with the general formula of $H_{27}[(4PyB)_3O_2(OH)_3][Ln_2(H_2O)_{12}(P_2Nb_3W_{15}O_{62})_4(4PyBOH)_4] \cdot xH_2O$ (**Ln-POM**), ($Ln=La^{3+}$ for **La-POM**, Ce^{3+} for **Ce-POM**, Pr^{3+} for **Pr-POM**, and Eu^{3+} for **Eu-POM**). These compounds were fully characterized by single-crystal and powder X-ray diffraction, elemental analyses, FTIR spectroscopy and thermogravimetric analysis, see Supporting Information for details.

The title compounds are composed of two components: the first component is a tetramer formed from four $\{Nb_3W_{15}\}$ Dawson anions: two $\{Nb_3W_{15}\}$ units are covalently linked by two 4PyBA units. Each boronic acid features one terminal –OH group and two B–O–Nb bridges which link the $\{Nb_3W_{15}\}$ units (Figure 1a, and Supporting Information, Figure S1 and Table S2). The resulting POM dimers are then linked into tetramers by two Ln^{3+} cations which form Ln–O–W bonds between neighboring $\{Nb_3W_{15}\}$ clusters, resulting in the species $[Ln_2(H_2O)_{12}(P_2Nb_3W_{15}O_{62})_4(4PyBOH)_4]^{26-}$ ($Ln=La, Ce, Pr, Eu$), see Figure 1a. The second component is a T-shaped triboronate formed by condensation of three 4PyBAOH units, giving the species $[(4PyB)_3O_2(OH)_3]^-$, see Figure 1b. This species consists of three pyridine groups connected by a central $\{B_3O_2(OH)\}$ ring (Figure 1b). In the crystal lattice, both components form infinite 1D chains where the POM tetramer and triboronates are linked non-covalently by a combination of π – π stacking, hydrogen bonding and electrostatic interactions, see Figures 1c and 1d for structural details. Bond valence sum (BVS) calculations (see SI, Table S2) indicated that the terminal oxygen atoms of the tetramer-based boronic acid, as well as three oxygen atoms in the triboronates are singly protonated, i.e., –OH groups (see Figure 1a,b, green spheres). All oxygen ligands on the Ln^{3+} ions were identified by BVS as coordinated water molecules (Figure 1a, light-blue spheres).

In the following, we will use **Ce-POM** as model for all **Ln-POMs** reported here. As shown in Figure 1e, the POM tetramers and the triboronates interact with each other through π – π stacking between neighboring pyridine ligands (centroid-to-centroid distance ca. 3.6 Å – 3.7 Å) and hydrogen bonding interactions between the POM tetramer and the triboronate (observed by short N...O distances between

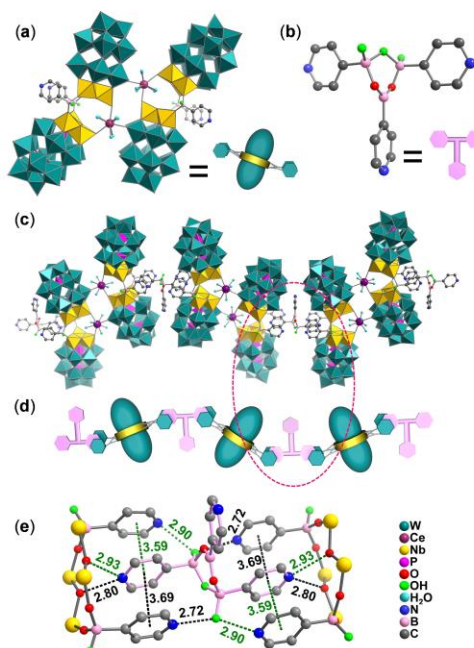


Figure 1. (a) Illustration of the tetrameric polyoxometalate anion $[\{Ce(H_2O)_6\}_2\{P_2Nb_3W_{15}O_{62}\}_4(4PyB(OH))_4]^{26-}$; (b) illustration of the T-shaped triboronate $[(4PyB)_3O_2(OH)_3]^-$; (c) illustration of the 1D supramolecular assembly of tetramers and triboronates; (d) simplified schematic diagram of the tetramer-triboronate assembly; (e) detailed illustration of the supramolecular interactions between the tetramer and triboronate components. All illustrations are based on single-crystal XRD data. H-atoms have been omitted for clarity.

2.7–2.9 Å). Note that these hydrogen-bonds involve the 3-pyridyl groups of the 4PyBA. These interactions might play a key role in forming the title compounds, as the use of the closely related 3-pyridyl boronic acid under similar conditions results in a strikingly different POM-organoboronic acid polymer.^[35]

When exploring the principal properties of **Ce-POM**, we noted that crystalline particles of **Ce-POM** can easily be dispersed in anhydrous acetonitrile using ultrasonication for ≈ 6 h followed by centrifugation to remove large particles. This process results in a colloidal suspension ($[\text{Ce-POM}] \approx 0.165$ mg/mL) which is stable under ambient conditions for more than one year and shows no indication of aggregation or precipitation. Scanning electron microscopy (SEM) of the isolated particles shows an average particle size of ≈ 45 nm, with a particle distribution range between ≈ 25 nm to 70 nm (Figures 2a,b). The colloids also show Tyndall scattering of red laser light ($\lambda = 650$ nm, Figure 2b, inset). Dynamic light scattering (DLS) and Small-angle X-ray scattering (SAXS) measurements verified that the particle size and distribution is retained in the dispersed

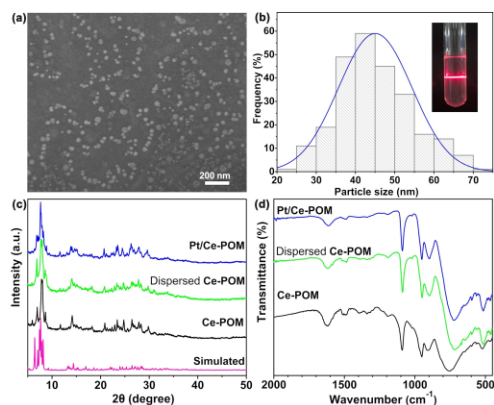


Figure 2. (a) SEM images and (b) particle size distribution of dispersed Ce-POM nanoparticles, (c) PXRD patterns and (d) IR spectra of Ce-POM, dispersed Ce-POM (recovered from acetonitrile) and Pt/Ce-POM.

phase and gave an average particle size of 61 nm and 46 nm respectively (Supporting Information, Figure S6 and S7). Powder X-ray diffraction (PXRD) and IR spectroscopy of the recovered Ce-POM particles (obtained by high-speed centrifugation from the colloidal suspension) indicate that the structure of Ce-POM is retained (Figures 2c,d).

We hypothesize that this facile dispersion of the compound might be related to the breaking of the weak intermolecular interactions in Ce-POM, similar to the top-down exfoliation used to access solid-state layered 2D materials.^[42,45] For experimental details on colloid preparation and characterization, see SI.

Recent ground-breaking studies have highlighted the importance of metal-substrate interactions in catalysis. In particular for hydrogen activation, it has been demonstrated that the interplay between noble-metal particles (e.g., Pt) and catalyst supports (e.g., metal oxides) can lead to a so-called hydrogen spillover.^[44,45] In hydrogen spillover, hydrogen atoms formed on the noble metal particle are transferred to the metal oxide support and can then be used for subsequent catalytic conversions. This phenomenon was first reported for Pt on WO₃,^[46] so we hypothesized that the concept can possibly be transferred to polyoxotungstate clusters as catalyst supports also. This idea is inspired by recent seminal reports, where hydrogen spillover involving noble-metal-functionalized POMs has been used: Yan and co-workers studied hydrogen spillover in the molecular POM-single-atom catalyst (POM-SAC)^[47] [PdPmO₁₁O₃₉]⁵⁻ and demonstrated high thermal reduction catalysis, e.g., for C=O and nitro group reduction.^[48] Yamaguchi, Suzuki and co-workers used mixed-valent {Ag^{IV}} clusters stabilized by polyoxotungstates to model processes related to hydrogen spillover.^[49,50] reaction of the species with H₂ led to the storage of electrons on the {Ag_n} clusters, while the protons were transferred to the polyoxotungstate shell. These studies

were focused on designing molecular models for H₂ activation, while to the best of our knowledge, POMs have thus far not been used as heterogeneous molecular metal oxide supports for noble-metal catalysts in hydrogen spillover.

Inspired by these studies, we have explored how the colloidal Ce-POM particles can be used as heterogeneous support for Pt catalyst particles. To this end, a suspension of Ce-POM was surface-modified with Pt by UV-photochemical reduction. To this end, a chloroplatinic acid solution containing Ce-POM colloidal particles in acetonitrile/ethanol was irradiated with UV-light, resulting in the formation of Pt/Ce-POM (for synthetic details see Supporting Information, Figure S11). Transmission electron microscopy (TEM) images show that crystalline Pt nanoparticles (Pt NPs, average size ≈ 3 nm) are uniformly dispersed on the surface of the larger Ce-POM particles (Figure 3a,b and Supporting Information, Figure S11). High-resolution TEM indicated lattice fringes (lattice spacing = 0.23 nm) which correspond to the (111) plane of metallic Pt. Note that due to the low Pt content, no diffraction peaks from Pt particles could be observed by PXRD analysis.

A striking first indication for a possible hydrogen spillover in Pt/Ce-POM was obtained when exposing the sample to gaseous H₂ (1 bar) at room temperature, which resulted in the instantaneous colour change from pale-yellow to deep blue (Supporting Information, Figure S14 and Supporting Video file). This is indicative of the formation of reduced, mixed-valent tungsten oxide-based systems, where the characteristic blue color is due to intervalence charge-transfer (IVTC) transitions between W^V and W^{VI} centers.^[51] Note that this tungsten reduction is reversible: when exposed to air, the sample returns to its original colour within approximately six minutes.

X-ray photoelectron spectroscopy (XPS) was used to gain in-depth understanding of the processes occurring during the reaction of Pt/Ce-POM with gaseous H₂. XPS of the native Pt/Ce-POM verifies that all W centers are present as W⁶⁺ (binding energies: 35.95 eV for W 4f_{7/2} and 38.05 eV for W 4f_{5/2}, Figure 4a), while the deconvoluted Pt spectrum indicates the presence of mixed-valent species, Pt⁰ (71.7 eV and 74.9 eV) and Pt²⁺ (73.44 eV and 76.60 eV) for Pt 4f_{7/2} and Pt 4f_{5/2} respectively (Figure 4b). These results suggest

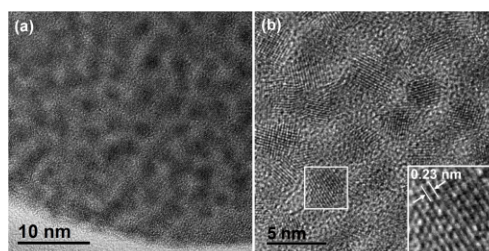


Figure 3. (a) and (b) TEM images of Pt NPs on Pt/Ce-POM at different magnifications. Inset: high-resolution TEM of the crystalline lattice observed.

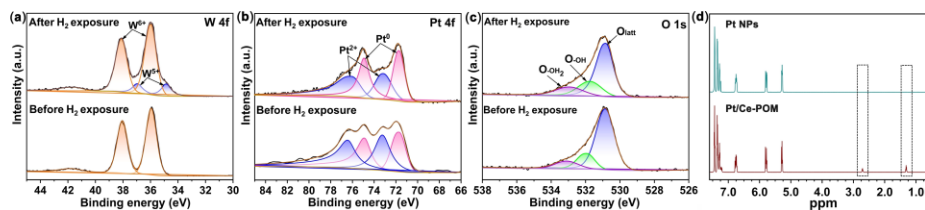


Figure 4. (a) - (c) deconvoluted XPS data for **Pt/Ce-POM** before and after exposure to H_2 : (a) W 4f, (b) Pt 4f, (c) O 1s. (d) 1H NMR spectra of the reaction of phenylethylene with **Pt/Ce-POM** and a **Pt NPs** reference after hydrogen spillover and replacing the residual H_2 with Argon.

that surface Pt centers in **Pt/Ce-POM** were partially oxidized when exposed to ambient atmosphere during sample preparation and handling. The positive shift of the binding energy (BE) of Pt in **Pt/Ce-POM** compared with bulk Pt metal (71.3 eV for Pt 4f_{7/2})^[52] is probably due to catalyst/support interactions between **Ce-POM** and Pt.^[53]

As shown in Figure 4 and Supporting Information, Table S3, reaction of **Pt/Ce-POM** with H_2 leads to a partial reduction of the W^{6+} centers to W^{5+} (characteristic BE: 34.86 eV and 36.90 eV). From XPS deconvolution, we can estimate the reduction degree to ≈ 15.9 atom-%. Comparison of the deconvoluted O 1s XPS data shows that upon H_2 exposure, the amount of protonated oxygen groups (i.e., $-OH$ and $-OH_2$) increases from 26.9 atom-% to 39.4 atom-% (Figure 4c and Supporting Information, Table S3). These data suggest that reaction of H_2 with **Pt/Ce-POM** leads to a hydrogen spillover where molecular H_2 is dissociated by Pt and retained as protons (stored by protonation of the POM) and electrons (stored as reduced W^{5+} atoms of the POM). Furthermore, after H_2 exposure, the amount of Pt^0 in **Pt/Ce-POM** increased, and the $Pt^0 : Pt^{2+}$ molar ratio changed from 1:1.2 to 1:0.89, indicating that part of the surface Pt^{2+} was reduced.

Based on this insight, and inspired by earlier works on Pt-on-tungsten oxide hydrogen spillover catalysts,^[45,46] we decided to investigate the catalytic performance of **Pt/Ce-POM** for selected model hydrogenations under mild conditions (1 bar H_2 , room temperature). Based on initial optimization reactions (details see Supporting Information, Table S4) we could show that **Pt/Ce-POM** efficiently catalyzes the hydrogenation of aliphatic and aromatic olefins to the corresponding alkanes. Full conversion is observed in most cases within 15 min reaction time at room temperature and 1 bar H_2 using 0.5 mol-% of **Pt/Ce-POM** (calculated based on Pt content, see Figure 5).

To gain further insights into the reaction mechanism, a set of control experiments was conducted using styrene as the model substrate (Table 1). In the absence of any catalyst, or when using the non-Pt-decorated **Ce-POM**, no phenylethylene can be detected (entry 1). When using commercial **Pt NPs** (entry 2) or a physical mixture of **Pt NPs** and **Ce-POM** (entry 3), only low conversion (<20%) is observed, which indicates that the two components in **Pt/Ce-POM** act in a synergistic fashion, as proposed by the hydrogen spillover mechanism. Both **Pt/Ce-POM** and **Pt/La-POM**

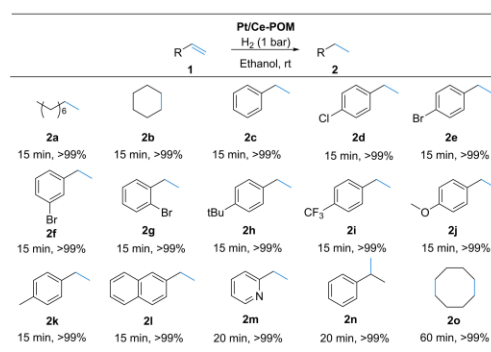


Figure 5. Hydrogenation of olefins to the corresponding alkanes catalyzed by **Pt/Ce-POM**. Reaction conditions: substrate (0.5 mmol), **Pt/Ce-POM** (0.5 mol% with respect to the substrate, based on Pt), EtOH (2 mL), r.t., H_2 (1 bar, H_2 balloon). Yields were determined by GC-MS.

Table 1: Control experiments for the styrene hydrogenation.^[a]

Entry	Catalyst	Yield [%] ^[b]
1	Ce-POM ^[c]	–
2	Pt NPs ^[d]	15.4
3	Pt NPs + Ce-POM ^[d]	19.6
4	Pt/La-POM	> 99
5	Pt/Ce-POM	> 99
6 ^[e]	Pt/Ce-POM or Pt NPs , no H_2	–

[a] Reaction conditions: styrene (0.5 mmol), catalyst (0.5 mol% based on Pt), ethanol (2 mL), reaction time: 15 min; [b] yields determined by GC-MS; [c] amount of **Ce-POM** identical to the amount of **Ce-POM** in the **Pt/Ce-POM** experiment, entry 5; [d] commercial **Pt NPs**, particle size 10 nm, [e] without H_2 .

show high catalytic efficiency with complete conversion, suggesting that the type of lanthanide ion present in the catalyst does not affect the catalytic performance (entries 4 and 5). Without H_2 , neither **Pt/Ce-POM** nor **Pt NPs** catalyze the conversion of styrene, which indicates that H_2 is essential as the reducing agent, i.e., proton and electron donor (entry 6).

To understand whether the **Ce-POM** is actively involved in the olefin hydrogenation reaction, the following 1H NMR

spectroscopic control experiments were performed. First, we performed the standard hydrogen spillover experiment for **Pt/Ce-POM** and **Pt NPs** (as reference). Upon reduction of the **Pt/Ce-POM**, the excess gaseous H_2 was removed by purging with Argon. Then, styrene was injected into the reaction vessel and the reaction was followed by 1H NMR, for experimental details see Supporting Information, Figure S16). As shown in Figure 4d, 1H NMR spectroscopy shows that styrene is only hydrogenated by **Pt/Ce-POM**, while no hydrogenation is observed for the **Pt NP** reference. This indicates that styrene reduction involves the **Ce-POM**, and suggests that the protons and electrons stored on the **Ce-POM** are used for olefin hydrogenation. Also, we note that the Pt particles are distributed uniformly across the external surface of the **Ce-POM**. This is expected to facilitate access to Pt-H species by the substrate to allow direct H transfer during the olefin hydrogenation.^[48]

Recycling experiments show that the hydrogenation performance of **Pt/Ce-POM** was retained over five runs (Supporting Information, Figure S17). Further, IR spectroscopy and PXRD of **Pt/Ce-POM** before and after the five catalytic runs confirm the stability of the material under the catalytic conditions employed (Supporting Information, Figure S18).

To investigate the scope of this process, we examined the catalytic activity of **Pt/Ce-POM** for the hydrogenation of nitrobenzene and carbonyl derivatives. As shown in the Supporting Information, Table S6, **Pt/Ce-POM** catalyzes the full conversion of most nitrobenzene derivatives studied to the corresponding amines within 30 min at room temperature and 1 bar H_2 . Note that **Pt/Ce-POM** does not catalyze carbonyl hydrogenation under the mild conditions used. As shown in the Supporting Information, Table S8, when various aldehydes or ketones were used as substrates, no hydrogenation products (i.e., alcohols) were detected in acetonitrile as solvent, and only very low amounts were observed in ethanol as solvent. We suggest that this selective hydrogenation behaviour is related to the differences in electron deficiency of the nitro- and carbonyl-compounds, which is expected to lead to different interactions between the substrate and **Pt/Ce-POM**.^[54] Also note that acetals were formed as side-products by reaction of the carbonyls with the ethanol solvent. We propose that this reaction was triggered by acid catalysis by **Pt/Ce-POM**.

Conclusion

In summary, a family of unprecedented boronic acid-POMs supramolecular assemblies are reported where weak intermolecular interactions facilitate the formation of stable colloidal suspensions. Loading of these aggregates with Pt particles results in high-performance hydrogenation catalysts which are considered to operate via a hydrogen spillover mechanism, see Figure 6. Initial mechanistic studies show that the title POMs play a key role as electron and proton reservoirs in the hydrogenation. The new concept presented in this study can trigger the development of new classes of technologically important catalysts, e.g., for the environ-

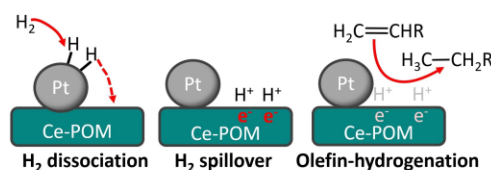


Figure 6. Schematic illustration of the proposed hydrogenation mechanism by **Pt/Ce-POM**.

mentally friendly production of fine-chemicals or pharmaceuticals. Future work will focus on mechanistic understanding of the structural and electronic linkage of Pt and **Ce-POM** particles as well as the atomic-level mechanism of hydrogen spillover to facilitate the observed hydrogenation reactivity.

Acknowledgements

This work was supported by the National Natural Science Foundation of China (22171073 and 22171246), the Program for Science & Technology Innovation Talents in Universities of Henan Province (23HASTIT005). C.S. gratefully acknowledges support by Johannes Gutenberg University Mainz, the Gutenberg Research College Mainz, the Rheinland-Pfalz Research Initiative through the Top-Level Research Area “SusInnoScience”, and the Deutsche Forschungsgemeinschaft DFG (TRR 234, CatalLight, project no: 364549901, project A4). This work contributes to the DFG SFB Initiative SFB 1633 “PCET”. Open Access funding enabled and organized by Projekt DEAL.

Conflict of Interest

The authors declare no conflict of interest.

Data Availability Statement

The data that support the findings of this study are available from the corresponding author upon reasonable request.

Keywords: Boronic Acid · Hydrogen Spillover · Polyoxometalate · Self-Assembly · Supramolecular

- [1] F. Freire, E. Quiñoá, R. Riguera, *Chem. Rev.* **2016**, *116*, 1242–1271.
- [2] K. Sato, M. P. Hendricks, L. C. Palmer, S. I. Stupp, *Chem. Soc. Rev.* **2018**, *47*, 7539–7551.
- [3] Q. Liu, X. Wang, *Angew. Chem. Int. Ed.* **2023**, *62*, e202217764.
- [4] M. T. Pope, A. Müller, *Angew. Chem. Int. Ed.* **1991**, *30*, 34–48.
- [5] L. Cronin, A. Müller, *Chem. Soc. Rev.* **2012**, *41*, 7333–7334.
- [6] I. A. Weinstock, R. E. Schreiber, R. Neumann, *Chem. Rev.* **2018**, *118*, 2680–2717.
- [7] S.-S. Wang, G.-Y. Yang, *Chem. Rev.* **2015**, *115*, 4893–4962.

- [8] F. de Azambuja, J. Moons, T. N. Parac-Vogt, *Acc. Chem. Res.* **2021**, *54*, 1673–1684.
- [9] A. Proust, B. Matt, R. Villanneau, G. Guillemot, P. Gouzerha, G. Izzet, *Chem. Soc. Rev.* **2012**, *41*, 7605–7622.
- [10] A. V. Anyushin, A. Kondinski, T. N. Parac-Vogt, *Chem. Soc. Rev.* **2020**, *49*, 382–432.
- [11] D. Pakulski, A. Gorczyński, D. Brykczynska, V. Montes-García, W. Czepa, I. Janica, M. Bielejewski, M. Kubicki, V. Patroniak, P. Samorí, A. Ciesielski, *Angew. Chem. Int. Ed.* **2023**, *62*, e202305239.
- [12] P. Yin, D. Li, T. Liu, *Chem. Soc. Rev.* **2012**, *41*, 7368–7383.
- [13] M. Stueckart, K. Y. Monakhov, *Chem. Sci.* **2019**, *10*, 4364–4376.
- [14] B. Li, L. Xuan, L. Wu, *Macromol. Rapid Commun.* **2022**, *43*, 2200019.
- [15] J. M. Cameron, G. Guillemot, T. Galambos, S. S. Amin, E. Hampson, K. Mall Haidaraly, G. N. Newton, G. Izzet, *Chem. Soc. Rev.* **2022**, *51*, 293–328.
- [16] S. Polarz, S. Landsmann, A. Klaiber, *Angew. Chem. Int. Ed.* **2014**, *53*, 946–954.
- [17] E. Hampson, J. M. Cameron, S. Amin, J. Kyo, J. A. Watts, H. Oshio, G. N. Newton, *Angew. Chem. Int. Ed.* **2019**, *58*, 18281–18285.
- [18] C. P. Pradeep, M. F. Misdrabi, F.-Y. Li, J. Zhang, L. Xu, D.-L. Long, T. Liu, L. Cronin, *Angew. Chem. Int. Ed.* **2009**, *48*, 8309–8313.
- [19] E. Hampson, J. M. Cameron, J. A. Watts, G. N. Newton, *Chem. Commun.* **2020**, *56*, 8237–8240.
- [20] J. Yan, H. Huang, S. Miao, Q. Zhang, Y. Yan, *Macromolecules* **2019**, *52*, 9545–9554.
- [21] C. Martin, K. Kastner, J. M. Cameron, E. Hampson, J. Alves Fernandes, E. K. Gibson, D. A. Walsh, V. Sans, G. N. Newton, *Angew. Chem. Int. Ed.* **2020**, *59*, 14331–14335.
- [22] X.-X. Li, Y.-X. Wang, R.-H. Wang, C.-Y. Cui, C.-B. Tian, G.-Y. Yang, *Angew. Chem. Int. Ed.* **2016**, *55*, 6462–6466.
- [23] Y. Zhu, P. Yin, F. Xiao, D. Li, E. Bitterlich, Z. Xiao, J. Zhang, J. Hao, T. Liu, Y. Wang, Y. Wei, *J. Am. Chem. Soc.* **2013**, *135*, 17155–17160.
- [24] G. Izzet, B. Abécassis, D. Brouri, M. Piot, B. Matt, S. A. Serapian, C. Bo, A. Proust, *J. Am. Chem. Soc.* **2016**, *138*, 5093–5099.
- [25] W. Guan, G. Wang, J. Ding, B. Li, L. Wu, *Chem. Commun.* **2019**, *55*, 10788–10791.
- [26] G. Izzet, M. Ménand, B. Matt, S. Renaudineau, L.-M. Chamoreau, M. Sollogoub, A. Proust, *Angew. Chem. Int. Ed.* **2012**, *51*, 487–490.
- [27] B. Zhang, L. Yue, Y. Wang, Y. Yang, L. Wu, *Chem. Commun.* **2014**, *50*, 10823–10826.
- [28] B. M. Čolović, M. Lacković, J. Lalatović, S. A. Mougharbel, U. Kortz, Z. D. Krstić, *Curr. Med. Chem.* **2020**, *27*, 362–379.
- [29] A. Blazevic, A. Rompel, *Coord. Chem. Rev.* **2016**, *307*, 42–64.
- [30] C. Molitor, A. Bijelic, A. Rompel, *Chem. Commun.* **2016**, *52*, 12286–12289.
- [31] D. Ma, L. Liang, W. Chen, H. Liu, Y.-F. Song, *Adv. Funct. Mater.* **2013**, *23*, 6100–6105.
- [32] C. Bosch-Navarro, B. Matt, G. Izzet, C. Romero-Nieto, K. Dirian, A. Raya, S. I. Molina, A. Proust, D. M. Guldi, C. Martí-Gastaldo, E. Coronado, *Chem. Sci.* **2014**, *5*, 4346–4354.
- [33] A. Dolbecq, E. Dumas, C. R. Mayer, P. Mialane, *Chem. Rev.* **2010**, *110*, 2680–2717.
- [34] S. Li, Y. Zhou, N. Ma, J. Zhang, Z. Zheng, C. Streb, X. Chen, *Angew. Chem. Int. Ed.* **2020**, *59*, 8537–8540.
- [35] S. Li, Y. Zhao, S. Knoll, R. Liu, G. Li, Q. Peng, P. Qiu, D. He, C. Streb, X. Chen, *Angew. Chem. Int. Ed.* **2021**, *60*, 16953–16957.
- [36] S. Li, Y. Zhao, H. Qi, Y. Zhou, S. Liu, X. Ma, J. Zhang, X. Chen, *Chem. Commun.* **2019**, *55*, 2525–2528.
- [37] M. Sadakane, M. H. Dickman, M. T. Pope, *Angew. Chem. Int. Ed.* **2000**, *39*, 2914–2916.
- [38] J. C. Liu, Q. Han, L. J. Chen, J. W. Zhao, C. Streb, Y. F. Song, *Angew. Chem. Int. Ed.* **2018**, *57*, 8416–8420.
- [39] F. Hussain, F. Conrad, G. R. Patzke, *Angew. Chem. Int. Ed.* **2009**, *48*, 9088–9091.
- [40] B. S. Bassil, M. H. Dickman, I. Römer, B. von der Kammer, U. Kortz, *Angew. Chem. Int. Ed.* **2007**, *46*, 6192–6195.
- [41] J.-C. Liu, J.-W. Zhao, C. Streb, Y.-F. Song, *Coord. Chem. Rev.* **2022**, *471*, 214734.
- [42] T.-H. Le, Y. Oh, H. Kim, H. Yoon, *Chem. Eur. J.* **2020**, *26*, 6360–6401.
- [43] V. Nicolosi, M. Chhowalla, M. G. Kanatzidis, M. S. Strano, J. N. Coleman, *Science* **2013**, *340*, 1226419.
- [44] W. Karim, C. Spreafico, A. Kleibert, J. Gobrecht, J. Vandevondele, Y. Ekinici, J. A. van Bokhoven, *Nature* **2017**, *541*, 7635.
- [45] R. Prins, *Chem. Rev.* **2012**, *112*, 2714–2738.
- [46] S. Khoobiar, *J. Phys. Chem.* **1964**, *68*, 411–412.
- [47] R. Liu, C. Streb, *Adv. Energy Mater.* **2021**, *11*, 2101120.
- [48] M. J. Hülsey, V. Fung, X. Hou, J. Wu, N. Yan, *Angew. Chem. Int. Ed.* **2022**, *61*, e202208237.
- [49] K. Yonesato, S. Yamazoe, D. Yokogawa, K. Yamaguchi, K. Suzuki, *Angew. Chem. Int. Ed.* **2021**, *60*, 16994–16998.
- [50] K. Yonesato, D. Yanai, S. Yamazoe, D. Yokogawa, T. Kikuchi, K. Yamaguchi, K. Suzuki, *Nat. Chem.* **2023**, *15*, 940.
- [51] C. Streb, *Dalton Trans.* **2012**, *41*, 1651–1659.
- [52] S. Hülfer, G. K. Wertheim, *Phys. Rev. B* **1975**, *11*, 678–683.
- [53] Y. Li, Y. Zhang, K. Qian, W. Huang, *ACS Catal.* **2022**, *12*, 1268–1287.
- [54] L. Zhang, M. Zhou, A. Wang, T. Zhang, *Chem. Rev.* **2020**, *120*, 683–733.

Manuscript received: October 6, 2023
 Accepted manuscript online: October 27, 2023
 Version of record online: November 13, 2023

4 Summary and outlook

The research on transition metal-based nanomaterials, covering their synthesis and application, is fundamental in the field of energy conversion and storage. This work introduces a cutting-edge synthetic methodology aimed at achieving superior electrocatalytic activity for both OER and ORR, achieved through precise morphological modulation and compositional control. The study includes thorough characterization of the materials' composition both before and after catalysis, leading to a detailed understanding of the synthesis mechanisms and the factors contributing to enhanced catalytic activities. The thesis encompasses several main projects, which are outlined and summarized in the document.

1) POM doped ZIFs and derived metal oxides

We explored the potential of POM (polyoxometalate) doped ZIF-67 composites as efficient OER catalysts, leveraging the ordered porosity and high specific surface area of ZIF-67 and the reversible multi-electron redox behaviors of POMs. A Ni-modified Keggin-type polyoxometalate ($[\text{PNi}(\text{H}_2\text{O})\text{W}_{11}\text{O}_{39}]^{5-}$) was used as a precursor for chemical modification of ZIF-67 through a simple one-pot method. Characterization results showed that $[\text{PNi}(\text{H}_2\text{O})\text{W}_{11}\text{O}_{39}]^{5-}$ was uniformly distributed within the pores of ZIF-67. Electrocatalytic tests for OER revealed enhanced activities compared to pure ZIF-67. However, post-catalysis analysis revealed the instability of the composite and the formation of Co_2O_3 , which caused some degradation in catalytic performance. To address this, further optimization was done through ion exchanging and thermal conversion, leading to the formation of mixed metal oxides. These oxides demonstrated structural and compositional benefits, resulting in low overpotential (306 mV at $j = 10 \text{ mA}\cdot\text{cm}^{-2}$) and improved long-term stability. This research presents a straightforward method for synthesizing high-performance electrocatalyst composites for OER in alkaline environments.

2) In situ formation of robust nanostructured Cobalt oxyhydroxide / Cobalt oxide oxygen evolution reaction electrocatalysts

Mixed metal sulfide precursors, based on ZIF-67, were synthesized through a combination of acid etching, ion exchange, and solvothermal treatment. Mechanistic studies revealed that

4. Summary and outlook

these precursor materials in-situ transformed into γ -CoOOH nanofibers and Co_2O_3 nanoparticles during the OER catalysis process, both recognized as established prototype OER catalysts. Crucially, the existence of crystalline mixed metal sulfide precursors is imperative for the concurrent in-situ development of stable and active Co_2O_3 nanoparticles and γ -CoOOH nanofibers. This innovative synthetic strategy, coupled with the observed structural and compositional evolution, shows significant potential for designing pre-catalysts. It also enhances the stability of metal sulfide-based catalysts and sheds light on the true active sites of these metal sulfide-based OER electrocatalysts.

3) Defect rich Pd metallene for ORR

A defect-rich Pd metallene (D-PdWMo M) was synthesized using a straightforward wet-chemical method. The characterization of D-PdWMo M revealed a variety of atomic-scale defects, including pores, concave surfaces, and atomic doping with tungsten and molybdenum oxides (WO_x and MoO_x). Density Functional Theory (DFT) calculations indicated that these defects resulted in a downward shift of the d-band center in Pd, which in turn led to a reduced binding energy with O_2 . As a result, D-PdWMo M demonstrated exceptional ORR activities, evidenced by a high half-wave potential (0.927 V vs. RHE) and a significant mass activity of $1.3 \text{ A}\cdot\text{mgPd}^{-1}$ at 0.9 V vs. RHE. Furthermore, when D-PdWMo M was employed in a Zn-air battery at an extremely low loading, it exhibited an impressive specific capacity of $809 \text{ mAh}\cdot\text{gZn}^{-1}$ and maintained excellent stability in discharge potential. This research offers new insights into adjusting the electronic structure of the active site, paving the way for the development of more efficient electrocatalysts for oxygen reduction reactions.

3) Platinum particle-functionalized POM-based compounds for hydrogenation of olefins and nitrobenzene derivatives.

A novel series of boronic acid-polyoxometalate (POM) supramolecular assemblies have been developed, where weak intermolecular interactions enable the formation of stable colloidal suspensions. By incorporating platinum (Pt) particles into these assemblies, they are transformed into highly efficient hydrogenation catalysts, believed to function through a hydrogen spillover mechanism. Preliminary mechanistic studies indicate that the POMs in question are crucial, acting as electron and proton reservoirs during the hydrogenation

process. This innovative concept opens the door for the creation of new categories of catalysts with significant technological importance, such as those used for the eco-friendly production of fine chemicals or pharmaceuticals. Future research will delve deeper into the mechanistic understanding of the structural and electronic connections between Pt and Ce-POM particles, as well as the atomic-level mechanism behind the hydrogen spillover that enables the observed hydrogenation reactivity.

Outlook: In the future, the rational design of novel transition metal-based nanomaterials can be achieved through meticulous control of composition and structure. There is an urgent need for new, facile, and efficient synthesis strategies, which will be a focal point in upcoming research endeavors. Furthermore, a deeper understanding of the synthesis and electrocatalytic mechanisms is essential to effectively guide the development of OER and ORR catalysts. Specifically, in the case of D-Pd M, although it exhibits superior discharge performance, its charging activity is hindered by relatively lower OER efficiency. Future efforts will be directed towards modifying D-Pd M/WMo to enhance its OER activity, thereby improving its overall electrocatalytic performance.

5 References

- [1] J. Macknick, *Carbon Manag* 2011, 2, 189–205.
- [2] P. A. Stott, J. A. Kettleborough, *Nature* 2002 416:6882 2002, 416, 723–726.
- [3] J. R. Laghari, *Nature* 2013 502:7473 2013, 502, 617–618.
- [4] O. Geden, *Nature Geoscience* 2016 9:5 2016, 9, 340–342.
- [5] J. Rogelj, M. Schaeffer, M. Meinshausen, R. Knutti, J. Alcamo, K. Riahi, W. Hare, *Environmental Research Letters* 2015, 10, 105007.
- [6] F. Ascione, N. Bianco, O. Böttcher, R. Kaltenbrunner, G. P. Vanoli, *Energy Build* 2016, 133, 688–710.
- [7] M. Neuwirth, T. Fleiter, P. Manz, R. Hofmann, *Energy Convers Manag* 2022, 252, 115052.
- [8] M. J. Nieto, *SSRN Electron. J.* 2022, 2022-170.
- [9] T. M. Gür, *Prog Energy Combust Sci* 2022, 89, 100965.
- [10] A. Rahman, O. Farrok, M. M. Haque, *Renewable and Sustainable Energy Reviews* 2022, 161, 112279.
- [11] S. M. Tatar, H. Akulker, H. Sildir, E. Aydin, *Int J Hydrogen Energy* 2022, 47, 27848–27865.
- [12] T. Bauer, C. Odenthal, A. Bonk, *Chemie Ingenieur Technik* 2021, 93, 534–546.
- [13] S. Trasatti, *Journal of Electroanalytical Chemistry* 1999, 476, 90–91.
- [14] R. Andaveh, G. B. Darband, M. Maleki, A. S. Rouhaghdam, *J Mater Chem A Mater* 2022, 10, 5147–5173.
- [15] M. Jin, X. Zhang, S. Niu, Q. Wang, R. Huang, R. Ling, J. Huang, R. Shi, A. Amini, C. Cheng, *ACS Nano* 2022, 16, 11577–11597.
- [16] Hannah Ritchie (October 6, 2020) - "Cars, planes, trains: where do CO₂ emissions from transport come from?" Published online at [OurWorldInData.org](https://ourworldindata.org/co2-emissions-from-transport). Retrieved from: '<https://ourworldindata.org/co2-emissions-from-transport>'.
- [17] M. Chandran, K. Palanisamy, D. Benson, S. Sundaram, *The Chemical Record* 2022, 22, e202100235.
- [18] J. Mo, Z. Kang, S. T. Retterer, D. A. Cullen, T. J. Toops, J. B. Green, M. M. Mench, F. Y. Zhang, *Sci. Adv.* 2016; 2: e1600690.
- [19] E. Fabbri, T. J. Schmidt, *ACS Catal* 2018, 8, 9765–9774.

5. References

- [20] C. Wang, Q. Zhang, B. Yan, B. You, J. Zheng, L. Feng, C. Zhang, S. Jiang, W. Chen, S. He, *Nano-Micro Letters* 2023 15:1 2023, 15, 1–41.
- [21] T. Reier, H. N. Nong, D. Teschner, R. Schlögl, P. Strasser, *Adv Energy Mater* 2017, 7, 1601275.
- [22] A. J. Medford, A. Vojvodic, J. S. Hummelshøj, J. Voss, F. Abild-Pedersen, F. Studt, T. Bligaard, A. Nilsson, J. K. Nørskov, *J Catal* 2015, 328, 36–42.
- [23] Z. Shi, X. Wang, J. Ge, C. Liu, W. Xing, *Nanoscale* 2020, 12, 13249–13275.
- [24] J. Suntivich, K. J. May, H. A. Gasteiger, J. B. Goodenough, Y. Shao-Horn, *Science* (1979) 2011, 334, 1383–1385.
- [25] Y. Hinuma, S. Mine, T. Toyao, K. I. Shimizu, *ACS Omega* 2022, 7, 18427–18433.
- [26] X. Wang, Z. Li, Y. Qu, T. Yuan, W. Wang, Y. Wu, Y. Li, *Chem* 2019, 5, 1486–1511.
- [27] Y. Zhao, D. P. Adiyeri Saseendran, C. Huang, C. A. Triana, W. R. Marks, H. Chen, H. Zhao, G. R. Patzke, *Chem. Rev.* 2023, 123, 9, 6257–6358.
- [28] A. Kulkarni, S. Siahrostami, A. Patel, J. K. Nørskov, *Chem Rev* 2018, 118, 2302–2312.
- [29] S. Guo, S. Zhang, S. Sun, *Angewandte Chemie International Edition* 2013, 52, 8526–8544.
- [30] Z. F. Huang, J. Wang, Y. Peng, C. Y. Jung, A. Fisher, X. Wang, *Adv Energy Mater* 2017, 7, 1700544.
- [31] F. Zhang, L. Yu, L. Wu, D. Luo, Z. Ren, *Trends Chem* 2021, 3, 485–498.
- [32] L. Yang, Z. Liu, S. Zhu, L. Feng, W. Xing, *Materials Today Physics* 2021, 16, 100292.
- [33] C. C. L. McCrory, S. Jung, J. C. Peters, T. F. Jaramillo, *J Am Chem Soc* 2013, 135, 16977–16987.
- [34] D. Voiry, M. Chhowalla, Y. Gogotsi, N. A. Kotov, Y. Li, R. M. Penner, R. E. Schaak, P. S. Weiss, *ACS Nano* 2018, 12, 9635–9638.
- [35] R. Zhou, Y. Zheng, M. Jaroniec, S. Z. Qiao, *ACS Catal* 2016, 6, 4720–4728.
- [36] P. A. Kempler, A. C. Nielander, *Nature Communications* 2023 14:1 2023, 14, 1–4.
- [37] H. S. Magar, R. Y. A. Hassan, A. Mulchandani, *Sensors (Basel)* 2021, 21(19), 6578.
- [38] A. C. Lazanas, M. I. Prodromidis, *ACS Measurement Science Au* 2023, 3, 162–193.
- [39] B. Hammer, J. K. Nørskov, *Surf Sci* 1995, 343, 211–220.
- [40] H. G. Sanchez Casalongue, M. Ling Ng, S. Kaya, D. Friebel, H. Ogasawara, A. Nilsson, H. G. Sanchez Casalongue, S. Kaya, D. Friebel, A. Nilsson, M. L. Ng, H. Ogasawara, *Angewandte Chemie International Edition* 2014, 53, 7169–7172.

- [41] V. Pfeifer, T. E. Jones, J. J. Velasco Vélez, C. Massué, M. T. Greiner, R. Arrigo, D. Teschner, F. Girgsdies, M. Scherzer, J. Allan, M. Hashagen, G. Weinberg, S. Piccinin, M. Hävecker, A. Knop-Gericke, R. Schlögl, *Physical Chemistry Chemical Physics* 2016, 18, 2292–2296.
- [42] O. Kasian, J. P. Grote, S. Geiger, S. Cherevko, K. J. J. Mayrhofer, *Angewandte Chemie International Edition* 2018, 57, 2488–2491.
- [43] S. Geiger, O. Kasian, M. Ledendecker, E. Pizzutilo, A. M. Mingers, W. T. Fu, O. Diaz-Morales, Z. Li, T. Oellers, L. Fruchter, A. Ludwig, K. J. J. Mayrhofer, M. T. M. Koper, S. Cherevko, *Nature Catalysis* 2018 1:7 2018, 1, 508–515.
- [44] Q. Shi, C. Zhu, D. Du, Y. Lin, *Chem Soc Rev* 2019, 48, 3181–3192.
- [45] Y. Wang, S. Hao, X. Liu, Q. Wang, Z. Su, L. Lei, X. Zhang, *ACS Appl Mater Interfaces* 2020, 12, 37006–37012.
- [46] W. Q. Zaman, Z. Wang, W. Sun, Z. Zhou, M. Tariq, L. Cao, X. Q. Gong, J. Yang, *ACS Energy Lett* 2017, 2, 2786–2793.
- [47] W. Sun, Y. Song, X. Q. Gong, L. M. Cao, J. Yang, *Chem Sci* 2015, 6, 4993–4999.
- [48] K. S. Kadakia, P. H. Jampani, O. I. Velikokhatnyi, M. K. Datta, S. K. Park, D. H. Hong, S. J. Chung, P. N. Kumta, *J Power Sources* 2014, 269, 855–865.
- [49] T. Wang, Y. Zeng, M. Xu, J. Zhang, S. Wu, S. Mu, J. Yu, *Langmuir* 2022, 38, 31, 9669–9677.
- [50] Q. Wang, X. Huang, Z. L. Zhao, M. Wang, B. Xiang, J. Li, Z. Feng, H. Xu, M. Gu, *J Am Chem Soc* 2020, 142, 7425–7433.
- [51] C. Cai, M. Wang, S. Han, Q. Wang, Q. Zhang, Y. Zhu, X. Yang, D. Wu, X. Zu, G. E. Sterbinsky, Z. Feng, M. Gu, *ACS Catal* 2021, 11, 123–130.
- [52] Y. Yao, S. Hu, W. Chen, Z. Q. Huang, W. Wei, T. Yao, R. Liu, K. Zang, X. Wang, G. Wu, W. Yuan, T. Yuan, B. Zhu, W. Liu, Z. Li, D. He, Z. Xue, Y. Wang, X. Zheng, J. Dong, C. R. Chang, Y. Chen, X. Hong, J. Luo, S. Wei, W. X. Li, P. Strasser, Y. Wu, Y. Li, *Nature Catalysis* 2019 2:4 2019, 2, 304–313.
- [53] L. Cao, Q. Luo, J. Chen, L. Wang, Y. Lin, H. Wang, X. Liu, X. Shen, W. Zhang, W. Liu, Z. Qi, Z. Jiang, J. Yang, T. Yao, *Nature Communications* 2019 10:1 2019, 10, 1–9.
- [54] C. Rong, X. Shen, Y. Wang, L. Thomsen, T. Zhao, Y. Li, X. Lu, R. Amal, C. Zhao, C. Rong, Y. Wang, T. Zhao, Y. Li, C. Zhao, X. Shen, X. Lu, R. Amal, *Advanced Materials* 2022, 34, 2110103.
- [55] X. Peng, S. Zhao, Y. Mi, L. Han, X. Liu, D. Qi, J. Sun, Y. Liu, H. Bao, L. Zhuo, H. L. Xin, J. Luo, X. Sun, *Small* 2020, 16, 2002888.
- [56] C. Zhao, Y. Tang, C. Yu, X. Tan, M. N. Banis, S. Li, G. Wan, H. Huang, L. Zhang, H. Yang, J. Li, X. Sun, J. Qiu, *Nano Today* 2020, 34, 100955.

5. References

- [57] J. Zhang, J. Liu, L. Xi, Y. Yu, N. Chen, S. Sun, W. Wang, K. M. Lange, B. Zhang, *J Am Chem Soc* 2018, 140, 3876–3879.
- [58] X. Kong, K. Xu, C. Zhang, J. Dai, S. Norooz Oliaee, L. Li, X. Zeng, C. Wu, Z. Peng, *ACS Catal* 2016, 6, 1487–1492.
- [59] L. Zu, X. Qian, S. Zhao, Q. Liang, Y. E. Chen, M. Liu, B. J. Su, K. H. Wu, L. Qu, L. Duan, H. Zhan, J. Y. Zhang, C. Li, W. Li, J. Y. Juang, J. Zhu, D. Li, A. Yu, D. Zhao, *J Am Chem Soc* 2022, 144, 2208–2217.
- [60] Z. L. Zhao, Q. Wang, X. Huang, Q. Feng, S. Gu, Z. Zhang, H. Xu, L. Zeng, M. Gu, H. Li, *Energy Environ Sci* 2020, 13, 5143–5151.
- [61] M. Xie, S. Tang, B. Zhang, G. Yu, *Mater Horiz* 2023, 10, 407–431.
- [62] J. Feng, F. Lv, W. Zhang, P. Li, K. Wang, C. Yang, B. Wang, Y. Yang, J. Zhou, F. Lin, G.-C. Wang, S. Guo, J. Feng, F. Lv, W. Zhang, P. Li, K. Wang, C. Yang, B. Wang, Y. Yang, J. Zhou, F. Lin, S. Guo, G. Wang, *Advanced Materials* 2017, 29, 1703798.
- [63] J. K. Nørskov, J. Rossmeisl, A. Logadottir, L. Lindqvist, J. R. Kitchin, T. Bligaard, H. Jónsson, *Journal of Physical Chemistry B* 2004, 108, 17886–17892.
- [64] S. Guo, S. Zhang, S. Sun, *Angewandte Chemie International Edition* 2013, 52, 8526–8544.
- [65] N. Hoshi, M. Nakamura, A. Hitotsuyanagi, *Electrochim Acta* 2013, 112, 899–904.
- [66] H. Yu, T. Zhou, Z. Wang, Y. Xu, X. Li, L. Wang, H. Wang, *Angewandte Chemie* 2021, 133, 12134–12138.
- [67] F. Lin, F. Lv, Q. Zhang, H. Luo, K. Wang, J. Zhou, W. Zhang, W. Zhang, D. Wang, L. Gu, S. Guo, *Advanced Materials* 2022, 34, 2202084.
- [68] M. Shao, A. Peles, K. Shoemaker, *Nano Lett* 2011, 11, 3714–3719.
- [69] F. J. Perez-Alonso, D. N. McCarthy, A. Nierhoff, P. Hernandez-Fernandez, C. Strebler, I. E. L. Stephens, J. H. Nielsen, I. Chorkendorff, *Angewandte Chemie International Edition* 2012, 51, 4641–4643.
- [70] M. Nesselberger, M. Roefzaad, R. Fayçal Hamou, P. Ulrich Biedermann, F. F. Schweinberger, S. Kunz, K. Schloegl, G. K. H. Wiberg, S. Ashton, U. Heiz, K. J. J. Mayrhofer, M. Arenz, *Nature Materials* 2013 12:10 2013, 12, 919–924.
- [71] T. Imaoka, H. Kitazawa, W. J. Chun, S. Omura, K. Albrecht, K. Yamamoto, *J Am Chem Soc* 2013, 135, 13089–13095.
- [72] S. St. John, A. P. Angelopoulos, *Electrochim Acta* 2013, 112, 258–268.
- [73] S. H. Liu, F. S. Zheng, J. R. Wu, *Appl Catal B* 2011, 108–109, 81–89.
- [74] B. A. Kakade, H. Wang, T. Tamaki, H. Ohashi, T. Yamaguchi, *RSC Adv* 2013, 3, 10487–10496.

- [75] K. Jayasayee, J. A. R. Van Veen, T. G. Manivasagam, S. Celebi, E. J. M. Hensen, F. A. de Bruijn, *Appl Catal B* 2012, 111–112, 515–526.
- [76] V. R. Stamenkovic, B. S. Mun, M. Arenz, K. J. J. Mayrhofer, C. A. Lucas, G. Wang, P. N. Ross, N. M. Markovic, *Nature Materials* 2007 6:3 2007, 6, 241–247.
- [77] V. E. Guterman, T. A. Lastovina, S. V. Belenov, N. Y. Tabachkova, V. G. Vlasenko, I. I. Khodos, E. N. Balakshina, *Journal of Solid State Electrochemistry* 2014, 18, 1307–1317.
- [78] L. B. Venaruso, R. H. Sato, P. A. Fiorito, G. Maia, *Journal of Physical Chemistry C* 2013, 117, 7540–7551.
- [79] S. Zhang, X. Zhang, G. Jiang, H. Zhu, S. Guo, D. Su, G. Lu, S. Sun, *J Am Chem Soc* 2014, 136, 7734–7739.
- [80] Y. T. Liang, S. P. Lin, C. W. Liu, S. R. Chung, T. Y. Chen, J. H. Wang, K. W. Wang, *Chemical Communications* 2015, 51, 6605–6608.
- [81] M. K. Jeon, Y. Zhang, P. J. McGinn, *Electrochim Acta* 2010, 55, 5318–5325.
- [82] A. Hassan, A. Carreras, J. Trincavelli, E. A. Ticianelli, *J Power Sources* 2014, 247, 712–720.
- [83] M. Ammam, E. B. Easton, *J Power Sources* 2013, 236, 311–320.
- [84] S. C. Ball, S. L. Hudson, B. R. Theobald, D. Thompsett, *ECS Trans* 2007, 11, 1267.
- [85] S. Chen, H. A. Gasteiger, K. Hayakawa, T. Tada, Y. Shao-Horn, *J Electrochem Soc* 2010, 157, A82.
- [86] S. Huang, S. Lu, S. Gong, Q. Zhang, F. Duan, H. Zhu, H. Gu, W. Dong, M. Du, *ACS Nano* 2022, 16, 522–532.
- [87] M. Luo, Z. Zhao, Y. Zhang, Y. Sun, Y. Xing, F. Lv, Y. Yang, X. Zhang, S. Hwang, Y. Qin, J. Y. Ma, F. Lin, D. Su, G. Lu, S. Guo, *Nature* 2019 574:7776 2019, 574, 81–85.
- [88] C. Wang, D. Li, M. Chi, J. Pearson, R. B. Rankin, J. Greeley, Z. Duan, G. Wang, D. Van Der Vliet, K. L. More, N. M. Markovic, V. R. Stamenkovic, *Journal of Physical Chemistry Letters* 2012, 3, 1668–1673.
- [89] P. Mani, R. Srivastava, P. Strasser, *J Power Sources* 2011, 196, 666–673.
- [90] K. Zhang, Y. He, R. Guo, W. Wang, Q. Zhan, R. Li, T. He, C. Wu, M. Jin, *ACS Energy Lett* 2022, 7, 3329–3336.
- [91] J. Wu, X. Cui, J. Fan, J. Zhao, Q. Zhang, G. Jia, Q. Wu, D. Zhang, C. Hou, S. Xu, D. Jiao, L. Gu, D. J. Singh, W. Zheng, *ACS Energy Lett* 2021, 6, 1912–1919.
- [92] L. Sun, H. Lv, Y. Wang, D. Xu, B. Liu, *Journal of Physical Chemistry Letters* 2020, 11, 6632–6639.
- [93] B. Han, C. E. Carlton, J. Suntivich, Z. Xu, Y. Shao-Horn, *Journal of Physical Chemistry C* 2015, 119, 3971–3978.

5. References

- [94] M. Gao, W. Sheng, Z. Zhuang, Q. Fang, S. Gu, J. Jiang, Y. Yan, *J Am Chem Soc* 2014, 136, 7077–7084.
- [95] D. E. Hall, *J Electrochem Soc* 1983, 130, 317–321.
- [96] X. Han, C. Yu, S. Zhou, C. Zhao, H. Huang, J. Yang, Z. Liu, J. Zhao, J. Qiu, X. Han, C. Yu, C. Zhao, H. Huang, J. Yang, Z. Liu, J. Qiu, S. Zhou, J. Zhao, *Adv Energy Mater* 2017, 7, 1602148.
- [97] F. Lyu, Y. Bai, Q. Wang, L. Wang, X. Zhang, Y. Yin, *Dalton Transactions* 2017, 46, 10545–10548.
- [98] M. Wehrens-Dijksma, P. H. L. Notten, *Electrochim Acta* 2006, 51, 3609–3621.
- [99] H. Bode, K. Dehmelt, J. Witte, *Electrochim Acta* 1966, 11, 1079–1087.
- [100] J. Huang, Y. Aoyao Li, Y. Zhang, G. Rao, C. Hunyang Wu, I. Hu, X. Wang, R. Lu, Y. Li, J. Xiong, *Angewandte Chemie* 2019, 131, 17619–17625.
- [101] D. A. Corrigan, *J Electrochem Soc* 1987, 134, 377–384.
- [102] D. Friebel, M. W. Louie, M. Bajdich, K. E. Sanwald, Y. Cai, A. M. Wise, M. J. Cheng, D. Sokaras, T. C. Weng, R. Alonso-Mori, R. C. Davis, J. R. Bargar, J. K. Nørskov, A. Nilsson, A. T. Bell, *J Am Chem Soc* 2015, 137, 1305–1313.
- [103] A. Bergmann, E. Martinez-Moreno, D. Teschner, P. Chernev, M. Gliech, J. F. De Araújo, T. Reier, H. Dau, P. Strasser, *Nature Communications* 2015 6:1 2015, 6, 1–9.
- [104] H. Y. Wang, S. F. Hung, H. Y. Chen, T. S. Chan, H. M. Chen, B. Liu, *J Am Chem Soc* 2016, 138, 36–39.
- [105] J. Y. C. Chen, L. Dang, H. Liang, W. Bi, J. B. Gerken, S. Jin, E. E. Alp, S. S. Stahl, *J Am Chem Soc* 2015, 137, 15090–15093.
- [106] L. Xu, Q. Jiang, Z. Xiao, X. Li, J. Huo, S. Wang, L. Dai, *Angewandte Chemie* 2016, 128, 5363–5367.
- [107] J. O. Bockris, T. Otagawa, *J Electrochem Soc* 1984, 131, 290–302.
- [108] I. C. Man, H. Y. Su, F. Calle-Vallejo, H. A. Hansen, J. I. Martínez, N. G. Inoglu, J. Kitchin, T. F. Jaramillo, J. K. Nørskov, J. Rossmeisl, *ChemCatChem* 2011, 3, 1159–1165.
- [109] A. Grimaud, K. J. May, C. E. Carlton, Y. L. Lee, M. Risch, W. T. Hong, J. Zhou, Y. Shao-Horn, *Nature Communications* 2013 4:1 2013, 4, 1–7.
- [110] Y. Matsumoto, E. Sato, *Mater Chem Phys* 1986, 14, 397–426.
- [111] D. Kim, L. S. Oh, J. H. Park, H. J. Kim, S. Lee, E. Lim, *Front Chem* 2022, 10, 1024865.
- [112] I. C. Man, H. Y. Su, F. Calle-Vallejo, H. A. Hansen, J. I. Martínez, N. G. Inoglu, J. Kitchin, T. F. Jaramillo, J. K. Nørskov, J. Rossmeisl, *ChemCatChem* 2011, 3, 1159–1165.
- [113] A. R. Howells, A. Sankarraj, C. Shannon, *J Am Chem Soc* 2004, 126, 12258–12259.

- [114] J. J. Stracke, R. G. Finke, *J Am Chem Soc* 2011, 133, 14872–14875.
- [115] J. J. Stracke, R. G. Finke, *ACS Catal* 2013, 3, 1209–1219.
- [116] S. Goberna-Ferrón, L. Vígara, J. Soriano-López, J. R. Galán-Mascarós, *Inorg Chem* 2012, 51, 11707–11715.
- [117] J. Soriano-López, S. Goberna-Ferrón, L. Vígara, J. J. Carbó, J. M. Poblet, J. R. Galán-Mascarós, *Inorg Chem* 2013, 52, 4753–4755.
- [118] F. M. Toma, A. Sartorel, M. Iurlo, M. Carraro, P. Parisse, C. MacCato, S. Rapino, B. R. Gonzalez, H. Amenitsch, T. Da Ros, L. Casalis, A. Goldoni, M. Marcaccio, G. Scorrano, G. Scoles, F. Paolucci, M. Prato, M. Bonchio, *Nat Chem* 2010, 2, 826–831.
- [119] G. Y. Lee, I. Kim, J. Lim, M. Y. Yang, D. S. Choi, Y. Gu, Y. Oh, S. H. Kang, Y. S. Nam, S. O. Kim, *J Mater Chem A Mater* 2017, 5, 1941–1947.
- [120] S. X. Guo, Y. Liu, C. Y. Lee, A. M. Bond, J. Zhang, Y. V. Geletii, C. L. Hill, *Energy Environ Sci* 2013, 6, 2654–2663.
- [121] S. Anantharaj, S. R. Ede, K. Sakthikumar, K. Karthick, S. Mishra, S. Kundu, *ACS Catal* 2016, 6, 8069–8097.
- [122] O. Mabayoje, A. Shoola, B. R. Wygant, and C. Buddie Mullins, *ACS Energy Lett.* 2016, 1, 1, 195–201
- [123] O. Mabayoje, A. Shoola, B. R. Wygant, C. B. Mullins, *ACS Energy Lett* 2016, 1, 195–201.
- [124] J. Ryu, N. Jung, J. H. Jang, H. J. Kim, S. J. Yoo, *ACS Catal* 2015, 5, 4066–4074.
- [125] K. Xu, P. Chen, X. Li, Y. Tong, H. Ding, X. Wu, W. Chu, Z. Peng, C. Wu, Y. Xie, *J Am Chem Soc* 2015, 137, 4119–4125.
- [126] F. Yu, H. Zhou, Z. Zhu, J. Sun, R. He, J. Bao, S. Chen, Z. Ren, *ACS Catal* 2017, 7, 2052–2057.
- [127] R. Jasinski, *Nature* 1964 201:4925 1964, 201, 1212–1213.
- [128] W. J. Jiang, L. Gu, L. Li, Y. Zhang, X. Zhang, L. J. Zhang, J. Q. Wang, J. S. Hu, Z. Wei, L. J. Wan, *J Am Chem Soc* 2016, 138, 3570–3578.
- [129] S. Wang, Q. He, C. Wang, H. Jiang, C. Wu, S. Chen, G. Zhang, L. Song, S. Wang, Q. He, C. Wang, H. Jiang, C. Wu, S. Chen, G. Zhang, L. Song, *Small* 2018, 14, 1800128.
- [130] A. Zitolo, V. Goellner, V. Armel, M. T. Sougrati, T. Mineva, L. Stievano, E. Fonda, F. Jaouen, *Nat Mater* 2015, 14, 937–942.
- [131] P. Yin, T. Yao, Y. Wu, L. Zheng, Y. Lin, W. Liu, H. Ju, J. Zhu, X. Hong, Z. Deng, G. Zhou, S. Wei, Y. Li, *Angewandte Chemie International Edition* 2016, 55, 10800–10805.
- [132] Y. Chen, S. Ji, Y. Wang, J. Dong, W. Chen, Z. Li, R. Shen, L. Zheng, Z. Zhuang, D. Wang, Y. Li, *Angewandte Chemie International Edition* 2017, 56, 6937–6941.

5. References

- [133] G. Wu, J. Wang, W. Ding, Y. Nie, L. Li, X. Qi, S. Chen, Z. Wei, *Angewandte Chemie International Edition* 2016, 55, 1340–1344.
- [134] A. Hammouche, A. Kahoul, D. U. Sauer, R. W. De Doncker, *J Power Sources* 2006, 153, 239–244.
- [135] J. Suntivich, H. A. Gasteiger, N. Yabuuchi, H. Nakanishi, J. B. Goodenough, Y. Shao-Horn, *Nat Chem* 2011, 3, 546–550.
- [136] Y. Zhu, W. Zhou, J. Yu, Y. Chen, M. Liu, Z. Shao, *Chemistry of Materials* 2016, 28, 1691–1697.
- [137] Z. Li, Y. Zhang, Y. Feng, C.-Q. Cheng, K.-W. Qiu, C.-K. Dong, H. Liu, W. Du, Z. Li, Y. Zhang, Y. Feng, C.-Q. Cheng, K.-W. Qiu, C.-K. Dong, H. X. Liu, -W Du, *Adv Funct Mater* 2019, 29, 1903444.
- [138] X. Tian, J. Luo, H. Nan, Z. Fu, J. Zeng, S. Liao, *J Mater Chem A Mater* 2015, 3, 16801–16809.
- [139] J. Luo, X. Tian, J. Zeng, Y. Li, H. Song, S. Liao, *ACS Catal* 2016, 6, 6165–6174.
- [140] Y. Dong, Y. Deng, J. Zeng, H. Song, S. Liao, *J Mater Chem A Mater* 2017, 5, 5829–5837.
- [141] Z. Wen, S. Ci, F. Zhang, X. Feng, S. Cui, S. Mao, S. Luo, Z. He, J. Chen, Z. H. Wen, S. M. Cui, S. Mao, J. H. Chen, S. Q. Ci, F. Zhang, Z. He, X. L. Feng, S. L. Luo, *Advanced Materials* 2012, 24, 1399–1404.
- [142] Y. Hu, J. O. Jensen, W. Zhang, L. N. Cleemann, W. Xing, N. J. Bjerrum, Q. Li, *Angewandte Chemie International Edition* 2014, 53, 3675–3679.
- [143] M. Xiao, J. Zhu, L. Feng, C. Liu, W. Xing, M. Xiao, J. Zhu, C. Liu, W. Xing, L. Feng, *Advanced Materials* 2015, 27, 2521–2527.
- [144] C. C. Yang, S. F. Zai, Y. T. Zhou, L. Du, Q. Jiang, *Adv Funct Mater* 2019, 29, 1901949.
- [145] S. Dou, L. Tao, J. Huo, S. Wang, L. Dai, *Energy Environ Sci* 2016, 9, 1320–1326.
- [146] K. P. Singh, E. J. Bae, J. S. Yu, *J Am Chem Soc* 2015, 137, 3165–3168.

6 Appendix

6.1 Supporting information: Polyoxometalate-assisted synthesis of amorphous zeolitic imidazolate for efficient electrocatalytic oxygen evolution

Supporting Information

for

Polyoxometalate-Assisted Synthesis of Amorphous Zeolitic Imidazolate for Efficient Electrocatalytic Oxygen Evolution

Yupeng Zhao,^{a,b} Dandan Gao,^{a,b} Johannes Biskupek,^c Ute Kaiser,^c Rongji Liu^{*,a,b,d}

Carsten Streb^{*,a,b,d}

^a Institute of Inorganic Chemistry I, Ulm University, Albert-Einstein-Allee 11, 89081
Ulm, Germany

^b Department of Chemistry, Johannes Gutenberg University Mainz, Duesbergweg 10-
14, 55131 Mainz, Germany, rongji.liu@uni-mainz.de; carsten.streb@uni-mainz.de

^c Central Facility of Electron Microscopy, Ulm University, Albert-Einstein-Allee 11,
89081 Ulm, Germany

^d Helmholtz Institute Ulm, Helmholtzstr. 11, 89081 Ulm, Germany

Table of Contents

1. Instrumental and experimental section
2. Synthetic section
3. Analytical section
4. Electrochemical studies

Instrumental and experimental section:

Powder X-ray diffraction (XRD): Rigaku XRD-6000 diffractometer using the following measurement parameter: 40 kV, 40 mA, Cu K α radiation ($\lambda = 0.154$ nm).

Scanning electron microscopy (SEM): Hitachi 5200. Samples were measured at 5 kV acceleration voltage.

(Scanning) transmission electron microscopy ((S)TEM) and energy-dispersive X-ray spectroscopy (EDX): Thermofisher Talos 200X STEM operated at 200 kV; acquisitions of TEM images with 4k by 4k CETA2 CMOS camera, acquisitions of scanning TEM images with a Fischione high angle annular darkfield (HAADF) detector, 4 quadrant silicon drift detector (Thermofisher SuperX) for EDX spectroscopy.

TEM sample preparation: The power samples were dispersed in ethanol and sonicated for few minutes. The solution subsequently was drop cast onto holey carbon grids.

Inductively coupled plasma atomic emission spectrometry (ICP-AES): Perkin Elmer Plasma 400 spectrometer. The POMs were dissolved in DI water.

Electrochemical measurements: CH Instruments CHI 710E workstation in a three-electrode setup (working electrode: a glassy carbon rotating disk electrode (RDE, disk surface area is 0.1256 cm²) and a rotating Pt ring-glassy carbon disk electrode (RRDE, carbon disk with the surface area of 0.1256 cm² surrounded by a Pt ring with a surface area of 0.1884 cm²), reference electrode: Hg/HgO electrode, counter electrode: platinum mesh) in 30 ml 1 M aqueous KOH electrolyte (pH 13.7).

Polarization curves: recorded by linear sweep voltammetry (LSV) with a scan rate of $5 \text{ mV}\cdot\text{s}^{-1}$. All potentials were converted to the reversible hydrogen electrode (RHE) according to the Nernst equation ($E_{\text{RHE}} = E_{\text{Hg/HgO}} + E_{\text{Hg/HgO}}^0 + 0.059 \text{ V} \times \text{pH}$).

Reaction pathway: The OER reaction pathway was studied by detecting the formation of HO_2^- with an RRDE electrode. In this case, the ring's current was recorded at a constant applied potential of 1.5 V to oxidize HO_2^- intermediates in Argon-saturated 1 M aqueous KOH solution. The disk's current was recorded with a potential scanning range from 1.2-1.8 V and a scanning rate of $5 \text{ mV}\cdot\text{s}^{-1}$. The average electron transfer number "n" was calculated with the following equation.

$$\text{Electron transfer number (n)} = (4 \times I_{\text{disk}}) / (I_{\text{disk}} + I_{\text{ring}}/N)$$

Faradaic efficiency: The faradaic efficiency test was performed by applying a constant potential (1.55 V) on the disk to drive OER and a constant potential (0.4 V) on the ring to reduce the O_2 produced by OER. The reaction system was pre-saturated by Argon. The faradaic efficiency (FE) was calculated with the following equation.

$$\text{FE} = I_{\text{ring}} / (I_{\text{disk}} \times N)$$

where I_{ring} and I_{disk} are the current of the ring and disk, respectively. N is the current collection efficiency (0.15 in this case) of the RRDE.

Fabrication of working electrodes: POMs@amZIF (5 mg) and Nafion solution (5 wt%, 20 μL) were dispersed in 980 μL of ethanol solution, followed by ultrasonication for 1 h. 7.54 μL of the catalyst dispersion was deposited on the surface of an RDE or RRDE electrode (loading density of $0.3 \text{ mg}\cdot\text{cm}^{-2}$) and dried naturally at room temperature.

Electrochemically Active Surface Area (ECSA): ECSAs for each material were estimated through the electrochemical double-layer (C_{dl}) capacitance of the catalytic surface using cyclic voltammograms (CVs) in a small potential range of 0.77–0.87 V. Before the CV data was collected, working electrodes were scanned for several potential cycles to stabilize the signals. There is a linear relationship between the current density (at 0.82 V) and scan rate, the slope is the C_{dl} .

Synthetic section

1. Chemicals and solvents:

Sodium tungstate dihydrate (Merck, CAS No. 10213-10-2), Disodiumhydrogenphosphate-7-hydrate (Acros Organics, CAS No. 7782-85-6), Nickel (II)-nitrate hexahydrate (Sigma-Aldrich, CAS No. 13478-00-7), Potassium chloride (Merck, CAS No. 7447-40-7), Cobalt dinitrate hexahydrate (Sigma-Aldrich, CAS No. 10026-22-9), 2-Methylimidazole (Sigma-Aldrich, CAS No. 693-98-1), Potassium hydroxide (Merck, CAS No. 1310-58-3), Hydrochloric acid (37%, Merck, CAS No. 7647-01-0), Phosphotungstic acid (Sigma-Aldrich, CAS No. 1343-93-7), Methanol (VWR, CAS No. 67-56-1).

2. Synthesis of $K_5[PNi(H_2O)W_{11}O_{39}]$:

$K_5[PNi(H_2O)W_{11}O_{39}]$ is a modification of the literature procedure.^{[1][2]} 9.1 mmol of Na_2HPO_4 , 100 mmol of $Na_2WO_4 \cdot 2H_2O$, and 12 mmol of $Ni(NO_3)_2 \cdot 6H_2O$ were dissolved in 200 mL of distilled water. The pH of the solution was adjusted to 4.8 with adding of concentrated HCl solution. Then the solution was heated to 90°C with stirring. After heating for 1 hour, excess KCl (approximate 60 g) was added with stirring. Then

the solution was cooled down and a large amount of precipitate appeared which was filtered off and recrystallized from hot water (60°C). The final solid product was dried at 70°C in an oven.

ICP-AES for $[\text{PNi}(\text{H}_2\text{O})\text{W}_{11}\text{O}_{39}]^{5-}$ in atomic ratio: P: Ni: W= 1: 0.99: 10.87

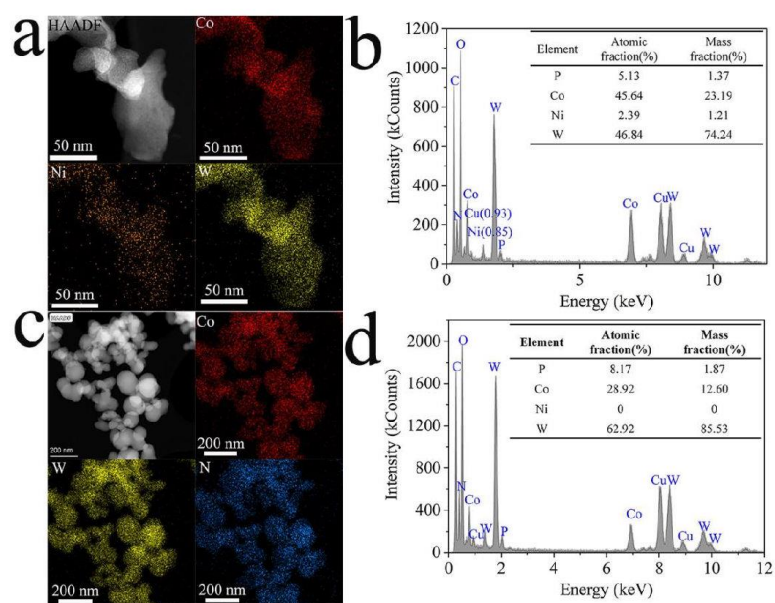
Synthesis of $\text{PNiW}_{11}@am\text{ZIF}$ and $\text{PW}_{12}@am\text{ZIF}$:

In a typical synthesis, aqueous $\text{K}_5\text{PNi}(\text{H}_2\text{O})\text{W}_{11}\text{O}_{39}$ solution (200 mg in 10 mL) was added to $\text{Co}(\text{NO}_3)_2 \cdot 6\text{H}_2\text{O}$ (0.546 g, 1.8 mmol) methanol solution (25 mL) and kept under magnetic stirring for 0.5 h. Afterward, 2-methylimidazole (0.616 g, 7.5 mmol) methanol solution (25 mL) was added. This reaction maintained stirring for a further 2.5 h. The final product was collected via centrifugation, washing with water and methanol, and drying at 70°C overnight. $\text{PW}_{12}@am\text{ZIF}$ was prepared by similar methods, but $\text{H}_3\text{PW}_{12}\text{O}_{40} \cdot x\text{H}_2\text{O}$ was used rather than $\text{K}_5\text{PNi}(\text{H}_2\text{O})\text{W}_{11}\text{O}_{39}$.

3. Synthesis of ZIF 67:

ZIF 67 was prepared through a similar procedure but no POMs aqueous solution was added to the systems.

Analytical section

Fig. S1. Images of $\text{PNiW}_{11}@amZIF$, $\text{PW}_{12}@amZIF$, and ZIF 67Fig. S2. Elemental dispersion of the a) $\text{PNiW}_{11}@amZIF$ and c) $\text{PW}_{12}@amZIF$; EDX elemental concentration of $\text{PNiW}_{11}@amZIF$ (b) and $\text{PW}_{12}@amZIF$ (d).

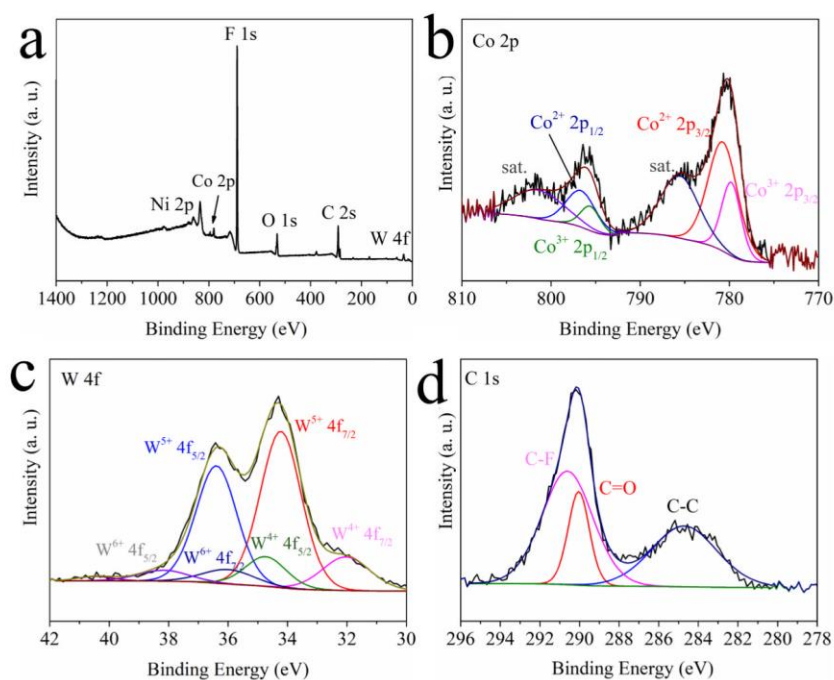


Fig. S3. XPS spectra of PNiW₁₁@amZIF: a) survey spectrum, (b-d) high-resolution spectra of Co 2p (b), W 4f (c), and C 1s (f).

Table S1 Main electrochemical data of PNiW₁₁@amZIF, PW₁₂@amZIF and ZIF 67

	η_{10}/mV	Tafel slop/ $\text{mV}\cdot\text{dec}^{-1}$	$C_{dl}/\text{mF}\cdot\text{cm}^{-2}$
PNiW ₁₁ @amZIF	375	69	1.15
PW ₁₂ @amZIF	423	86	1.06
ZIF 67	468	105	0.58

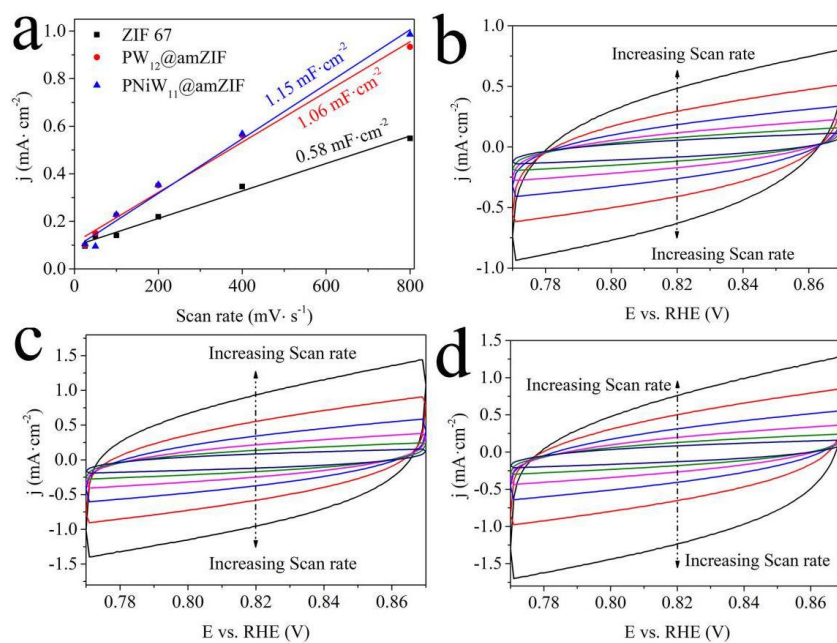


Fig. S4. a) Plots of the current density at 0.82 V vs. the scan rate and C_{dl} of catalysts (inset) and cyclic voltammograms of b) ZIF 67, c) $PW_{12}@amZIF @POM$, and d) $PNiW_{11}@amZIF$ performed in the non-Faradaic region of 0.77 to 0.87 V

with various scan rates.

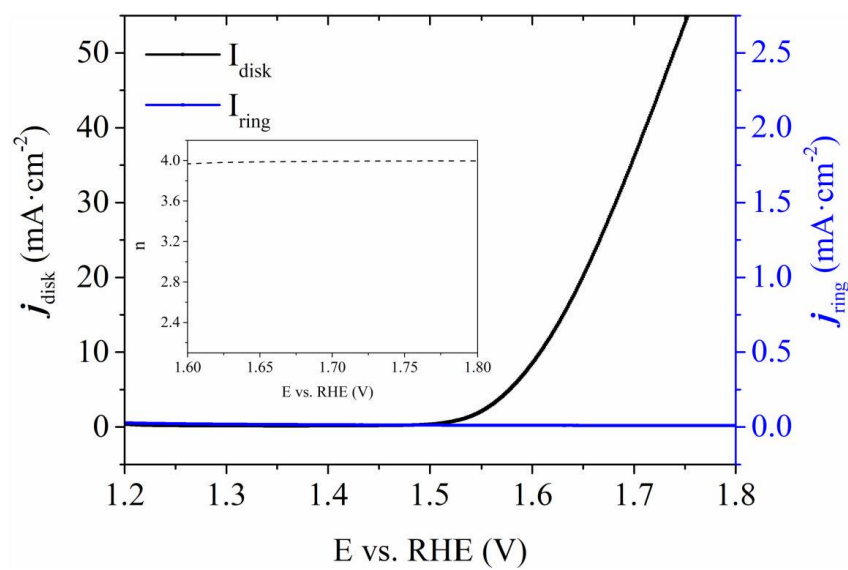


Fig. S5. Ring and disk current density of PNiW₁₁@amZIF on an RRDE (1600 rpm) in Argon saturated 1M KOH solution (ring potential 1.5 V) with corresponding electron transfer number (n) at different potential from 1.6 V to 1.8 V (vs. RHE) (inset).

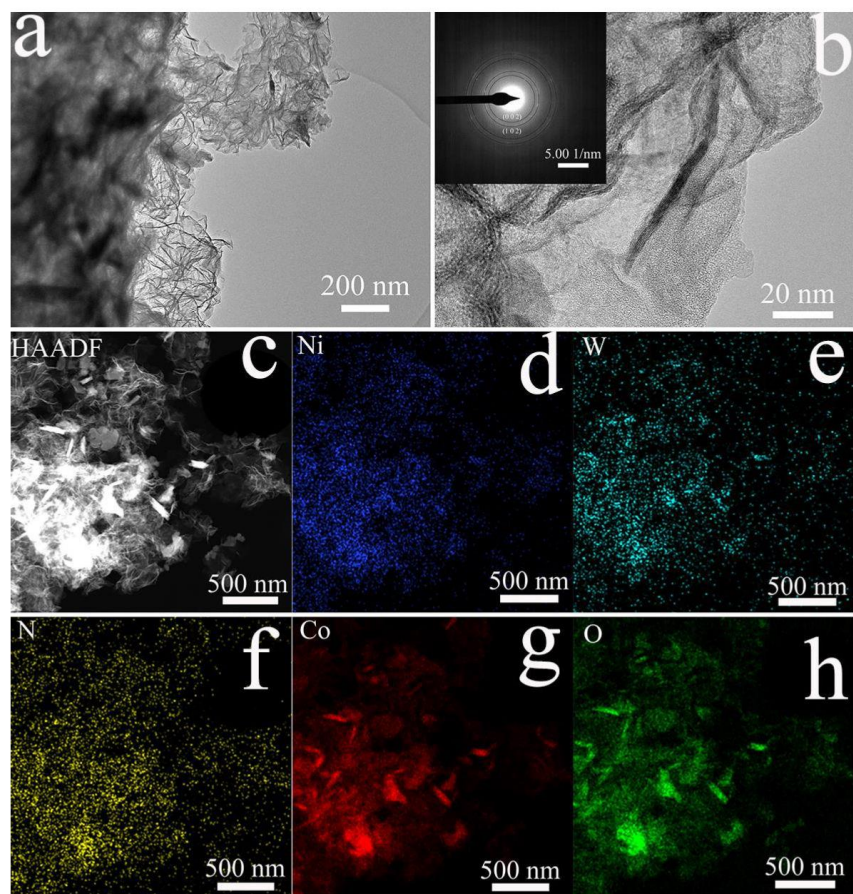


Fig. S6 Structural characterization of PNiW₁₁@amZIF post catalysis: TEM (a) and HRTEM (b) images with insert of electron diffraction pattern; HAADF (c) and EDX elemental mappings of Ni (d), W(e), N(f), Co (g), and O (h).

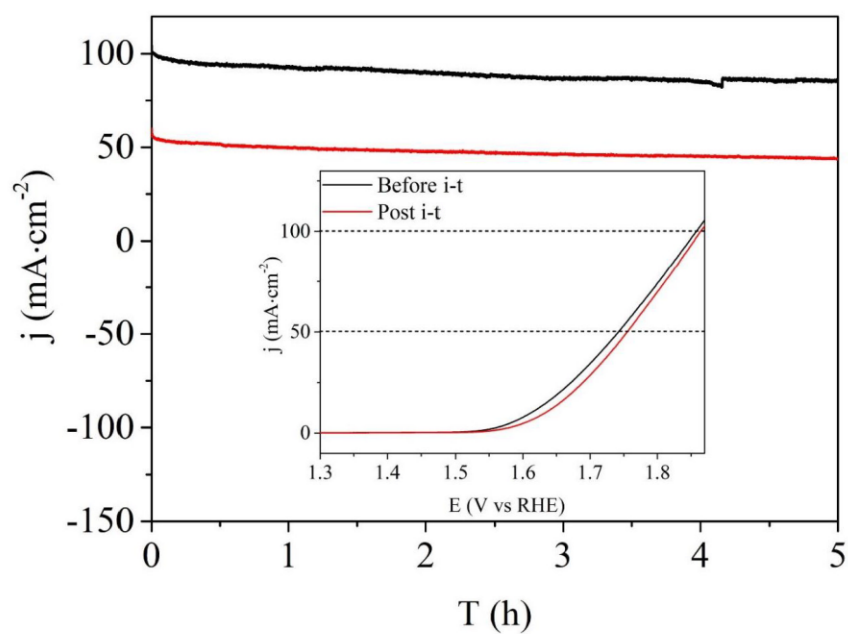


Fig. S7 Chronoamperometric test of PNiW₁₁@amZIF at 1.77 V and 1.86 V vs. RHE respectively

Table S2 Summary of various POM@MOF-based catalysts for OER

Catalysts	$j/\text{mA}\cdot\text{cm}^{-2}$	Electrolyte	η (mV)	ref
PNiW11@amZIF	10	1 M KOH	375	This work
SiW11Co@ZIF-67	10	1 M KOH	460	[1]
SiW11Co[h]@ZIF-67	10	1 M KOH	430	[1]
SiW9Co3@ZIF-67	10	1 M KOH	470	[1]
SiW9Co3[h]@ZIF-67	10	1 M KOH	420	[1]
ZIF-8@ZIF-67@POM	10	1 M KOH	490	[2]
[H6CoW12O40] @ZIF-8	1	0.1M Na2SO4	784.19	[3]
Co4(PW9)2@Co/Ni@C	10	1 M KOH	400	[4]
Co4(PW9)2@ N,S-Co@C	10	1 M KOH	410	[4]

- [1] V. K. Abdelkader-Fernández, D. M. Fernandes, S. S. Balula, L. Cunha-Silva, C. Freire, *J Mater Chem A Mater* **2020**, *8*, 13509–13521.
- [2] Y. Wang, Y. Wang, L. Zhang, C. sen Liu, H. Pang, *Inorg Chem Front* **2019**, *6*, 2514–2520.
- [3] S. Mukhopadhyay, J. Debgupta, C. Singh, A. Kar, S. K. Das, *Angewandte Chemie - International Edition* **2018**, *57*, 1918–1923.
- [4] V. K. Abdelkader-Fernández, D. M. Fernandes, L. Cunha-Silva, A. J. S. Fernandes, C. Freire, *Electrochim Acta* **2021**, *389*, 138719.

6.2 Supporting information: POM@ZIF Derived Mixed Metal Oxide Catalysts for Sustained Electrocatalytic Oxygen Evolution

**Chemistry–A European
Journal**

Supporting Information

**POM@ZIF Derived Mixed Metal Oxide Catalysts for
Sustained Electrocatalytic Oxygen Evolution**

Yupeng Zhao, Dandan Gao, Si Liu, Johannes Biskupek, Ute Kaiser, Rongji Liu,* and Carsten Streb*

Table of Contents

1. Instrumental and experimental section
2. Synthetic section
3. Analytical section
4. Electrochemical studies
5. References
6. Author Contributions

Instrumentation and experimental section:

Powder X-ray diffraction (XRD): Rigaku XRD-6000 diffractometer under the following conditions: 40 kV, 40 mA, CuK α radiation ($\lambda = 0.154$ nm).

Scanning electron microscopy (SEM): Hitachi 5200 SEM. Samples were measured at 10 kV acceleration voltage.

Transmission electron microscopy (TEM) and energy-dispersive X-ray spectroscopy (EDX): FEI Titan 80-300 equipped with an image-side aberration corrector, operated at 80 kV (Imaging and diffraction pattern). Thermofisher Talos 200X equipped with a SuperX EDX detector, operated at 200 kV in scanning (S) TEM mode.

Raman spectroscopy: Renishaw Raman spectrometer with a laser excitation wavelength of 532 nm.

X-ray photoelectron spectroscopy (XPS): Monochromatized Al K α exciting X-radiation using a PHI Quantera SXM system. The binding energies were calibrated based on C1s (284.8 eV).

Inductively coupled plasma atomic emission spectrometry (ICP-AES): Perkin Elmer Plasma 400 spectrometer. All samples were dissolved in 1 M aqueous H₂SO₄.

Electrochemical measurements: CH Instruments CHI 730E workstation in three-electrode setup (working electrode: a glassy carbon rotating disk electrode (RDE, disk surface area is 0.1256 cm²) and a rotating Pt ring-glassy carbon disk electrode (RRDE, carbon disk with the surface area of 0.1256 cm² surrounded by a Pt ring with a surface

area of 0.1884 cm²), reference electrode: Hg/HgO electrode, counter electrode: platinum mesh) in 30 ml 1 M aqueous KOH electrolyte (pH 13.7).

Polarization curves: recorded by linear sweep voltammetry (LSV) with a scan rate of 5 mV·s⁻¹. All potentials were converted to the reversible hydrogen electrode (RHE) according to the Nernst equation ($E_{RHE} = E_{Hg/HgO} + E_{Hg/HgO}^0 + 0.059 \text{ V} \times \text{pH}$).

Reaction pathway: The reaction pathway of OER was determined by detecting the formation of HO₂⁻ using an RRDE electrode. In this case, the current in ring was recorded with the potential being held constantly at 1.5 V to oxidize HO₂⁻ intermediates in Argon-saturated 1 M aqueous KOH solution. At the disk electrode, LSV was performed between 1.2-1.8 V at a scan rate of 5 mV·s⁻¹.

Faradaic efficiency: faradaic efficiency was calculated based on RRDE experiments, where a constant potential (1.55 V) was applied at the disk electrode to perform OER, while the ring electrode was held at a constant potential (0.4 V) to reduce the O₂ produced by OER. The electrolyte was saturated with Argon before the experiment. The faradaic efficiency (FE) was calculated with the following equation.

$$FE = I_{ring} / (I_{disk} \times N)$$

where I_{ring} and I_{disk} are the current of the ring and disk, respectively. N is the current collection efficiency (here: 0.15) of the RRDE.

Fabrication of working electrodes: Catalyst 1 (5 mg) and Nafion solution (5 wt%, 20 μL) were dispersed in 980 μL of ethanol solution, followed by ultrasonication for 1 h. 7.54 μL of the catalyst dispersion was deposited on the disk surface of an RDE or

RRDE electrode (loading density of $0.3 \text{ mg}\cdot\text{cm}^{-2}$) and dried naturally at room temperature.

Electrochemically Active Surface Area (ECSA): ECSAs for each material were estimated by determining the electrochemical double-layer (C_{dl}) capacitance of the catalytic surface using cyclic voltammograms (CVs) in a potential range of 0.82–0.92 V where no redox-processes occur. Before the CV data was collected, working electrodes were scanned for several potential cycles to stabilize the signals. There is a linear relationship between the current density difference (at 0.87 V) and scan rate, the slope is the C_{dl} .

Electrochemical impedance spectroscopy (EIS): EIS of the catalysts was recorded at a potential of 1.55 V vs. RHE with an AC amplitude of 5 mV by sweeping the frequency from 100 kHz to ~ 0.01 Hz. All samples were recorded under identical experimental conditions.

Chemicals and solvents:

Sodium tungstate dihydrate (Merck, CAS No. 10213-10-2), Disodiumhydrogenphosphate-7-hydrate (Acros Organics, CAS No. 7782-85-6), Nickel (II)-nitrate hexahydrate (Sigma-Aldrich, CAS No. 13478-00-7), Potassium chloride (Merck, CAS No. 7447-40-7), Cobalt dinitrate hexahydrate (Sigma-Aldrich, CAS No. 10026-22-9), Nickel dichloride (ABCR, CAS No. 7718-54-9), Iron trichloride (Sigma-Aldrich, CAS No. 7705-08-0), 2-Methylimidazole (Sigma-Aldrich, CAS No. 693-98-1), Potassium hydroxide (Merck, CAS No. 1310-58-3), Hydrochloric acid (37%, Merck, CAS No. 7647-01-0), Phosphotungstic acid (Sigma-Aldrich, CAS No. 1343-93-7), Methanol (VWR, CAS No. 67-56-1).

Analytical section

Table S1. The metal content of **Catalyst 1** quantified by ICP-OES

	Ni	W	Co	Fe
Wt. -%	16.5	46.6	33.6	3.3
Atomic ratio	1	1.1	2	0.2

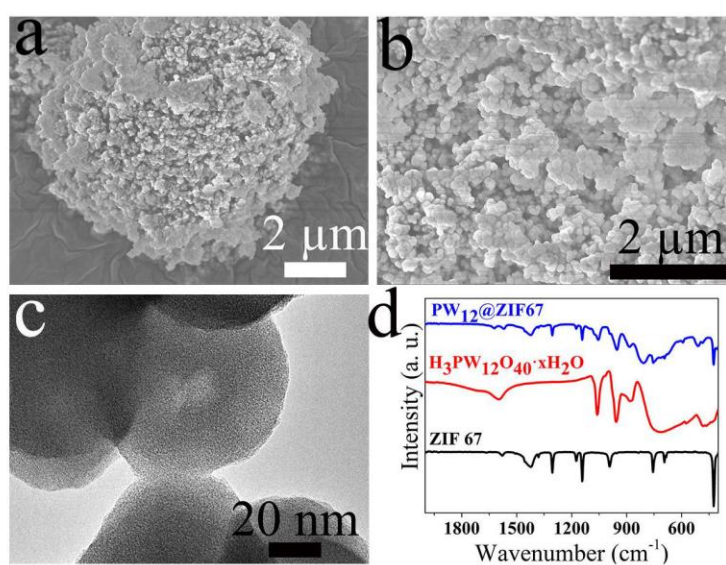


Figure S1. SEM (a and b) and TEM (c) images of $\text{PW}_{12}@am\text{ZIF}$; d) Attenuated total reflection-Fourier transform infrared (ATR-FTIR) spectrum of $\text{PW}_{12}@am\text{ZIF}$, $[\text{H}_3\text{PW}_{12}\text{O}_{40}] \cdot x\text{H}_2\text{O}$, and ZIF-67.

The TEM image suggests that $\text{PW}_{12}@am\text{ZIF}$ is amorphous. ATR-FTIR peaks of ZIF-67 and $[\text{H}_3\text{PW}_{12}\text{O}_{40}]$ can be found in $\text{PW}_{12}@am\text{ZIF}$, which indicates POM-doped ZIF-67 was successfully synthesized.

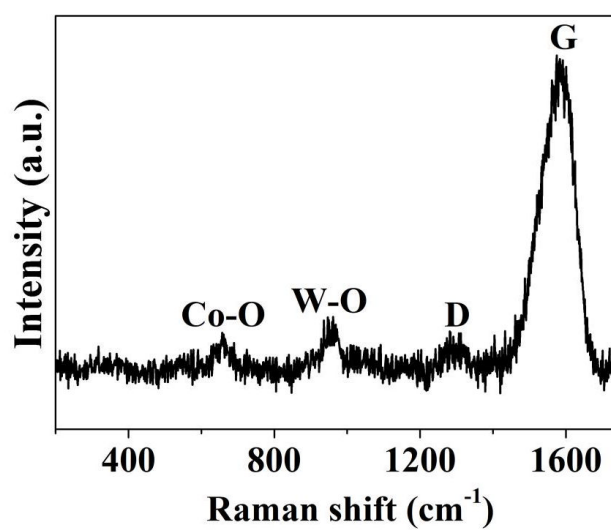


Figure S2. Raman spectrum of Catalyst 1

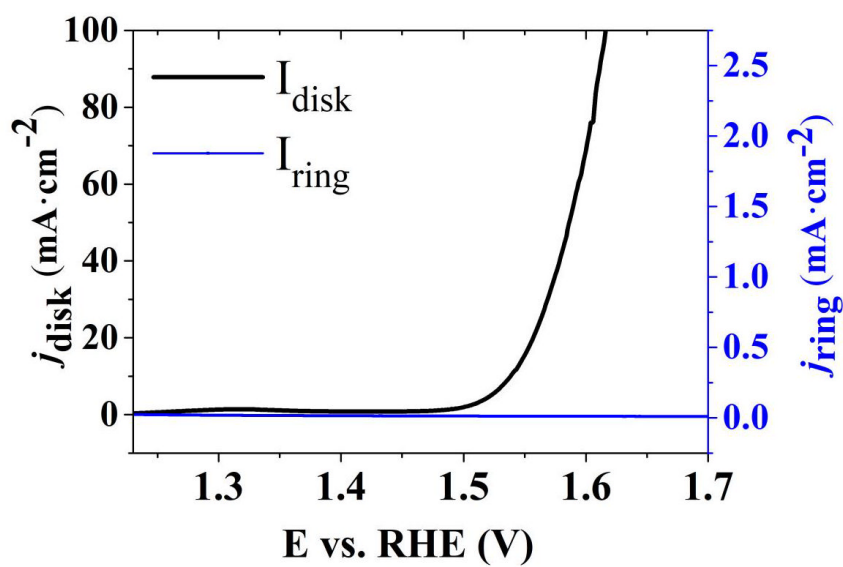


Figure S3. OER faradaic efficiency of Catalyst 1 using a RRDE as the working electrode; OER is performed at the disk electrode, while the ring electrode (at 1.5 V vs RHE) is used to detect any peroxide formation.

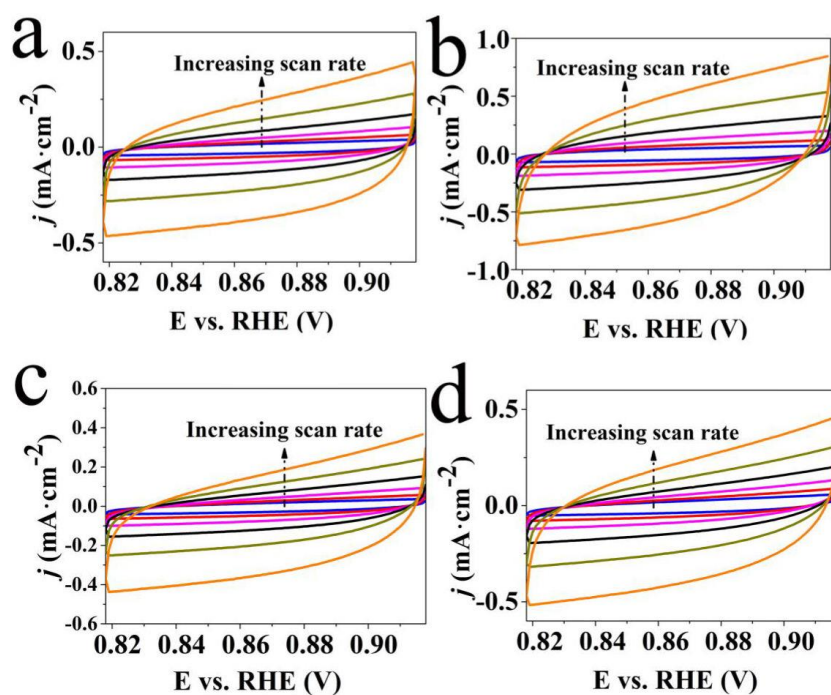


Figure S4. Double-layer capacitance measurements for determining electrochemically active surface area of different catalysts. Cyclic voltammetry of (a-d) **Catalyst 1**, **Catalyst 2**, **Catalyst 3**, and **Catalyst 4** respectively scanned from 0.82 to 0.92 V vs. RHE with the scan rates from 25 to 800 $\text{mV}\cdot\text{s}^{-1}$.

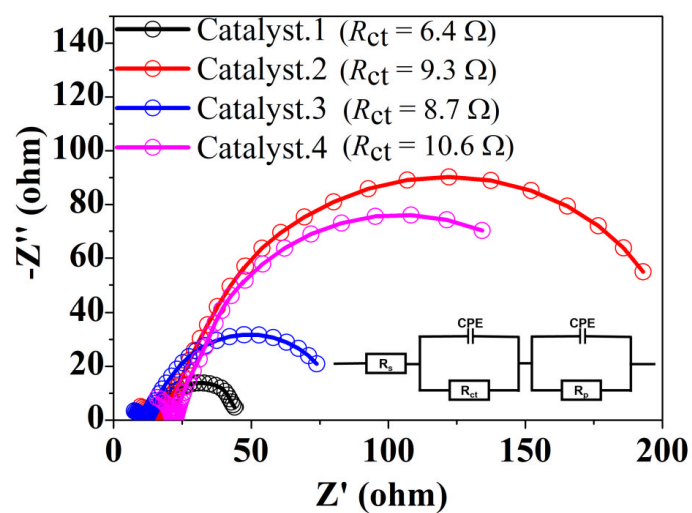


Figure S5. Electrochemical impedance spectroscopy (EIS, Nyquist plots) measured at overpotential of 320 mV, insert: equivalent circuit. The semicircles in the high-frequency range of the Nyquist plots are assigned to solution resistance (R_s) and charge transfer processes where R_{ct} is the charge transfer resistance and CPE (constant phase element) is the double layer capacitance.

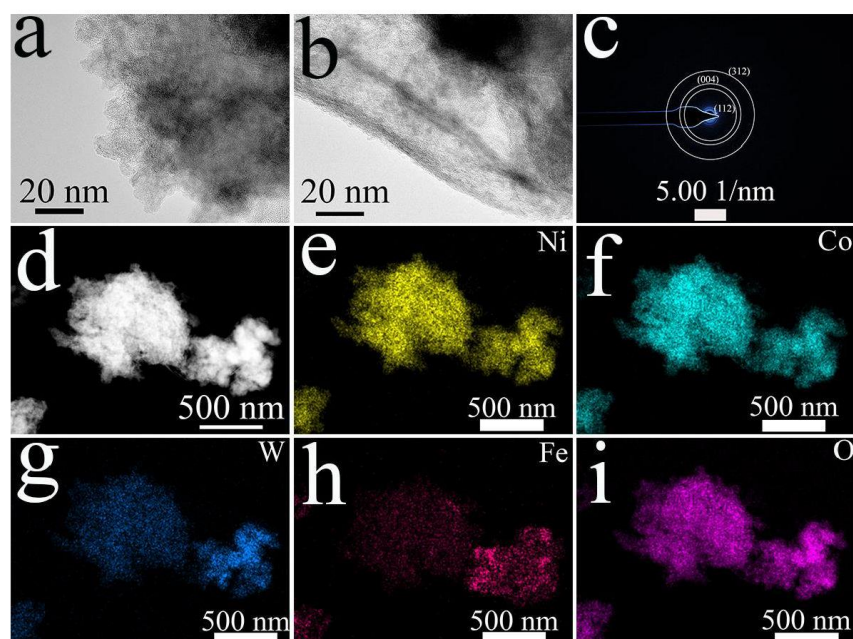


Figure S6 Post-catalysis structural compositional analysis of Catalyst 1: (a) TEM images, (b) HRTEM image, (c) SAED, and (d) Annular dark-field STEM image and corresponding elemental mappings (e-i) using EDX

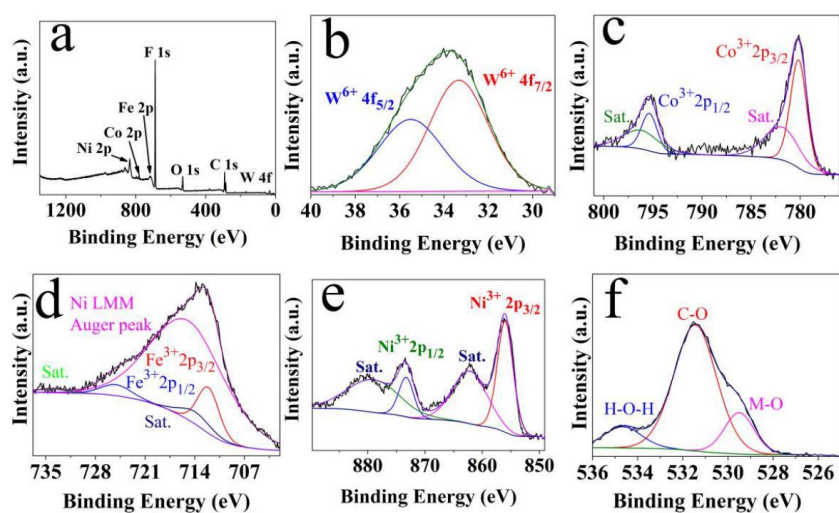


Figure S7 Post-catalytic XPS spectra of **Catalyst 1**: a) full spectra, (b-f) deconvoluted high-resolution spectra of W 4f (b), Co 2p (c), Fe 2p (d), Ni 2p (e), and (f) O 1s.

6.3 Supporting information: In situ formation of robust nanostructured Cobalt oxyhydroxide / Cobalt oxide oxygen evolution reaction electrocatalysts

In situ formation of robust nanostructured Cobalt
oxyhydroxide / Cobalt oxide oxygen evolution reaction
electrocatalysts

Yupeng Zhao, Dandan Gao, Johannes Biskupek, Ute Kaiser, Rongji Liu*, Carsten Streb*

Instrumentation and experimental section:

Powder X-ray diffraction (pXRD): Rigaku XRD-6000 diffractometer under the following conditions: 40 kV, 40 mA, CuK α radiation ($\lambda = 0.154$ nm).

Scanning electron microscopy (SEM): Hitachi 5200 SEM. Samples were measured at 10 kV acceleration voltage.

Transmission electron microscopy (TEM) and energy-dispersive X-ray spectroscopy (EDX): The samples were dispersed in ethanol and dropped casted to holey carbon support grids prior to TEM investigations. HRTEM images and diffraction patterns were acquired using a FEI Titan 80-300 equipped with an image-side aberration corrector, operated at 80 kV. A Thermo Fisher Talos 200X equipped with a SuperX EDX detector, operated at 200 kV in scanning (S) TEM mode was used for HAADF imaging and acquisition of elemental maps.

X-ray photoelectron spectroscopy (XPS): Monochromatized Al K α exciting X-radiation using a PHI Quantera SXM system. The binding energies were calibrated based on C1s (284.8 eV).

Electrochemical measurements: Ametek workstation equipped with PMC 2000A and PMC 1000 channels in three-electrode setup (working electrode: a glassy carbon rotating disk electrode (RDE, disk surface area is 0.196 cm²) and a rotating Pt ring-glassy carbon disk electrode (RRDE, carbon disk with the surface area of 0.2475 cm² surrounded by a Pt ring with a surface area of 0.1866 cm²), reference electrode: Hg/HgO electrode, counter electrode: graphite rod) in 30 ml 1 M aqueous KOH electrolyte.

Polarization curves: recorded by linear sweep voltammetry (LSV) with the scan rate of 5 mV·s⁻¹. All potentials were converted to the reversible hydrogen electrode (RHE) according to the Nernst equation ($E_{\text{RHE}} = E_{\text{Hg/HgO}} + E_{\text{Hg/HgO}}^0 + 0.059 \text{ V} \times \text{pH}$).

Electrochemical impedance spectroscopy (EIS): EIS of the catalysts was recorded at a potential of 1.55 V vs. RHE with an AC amplitude of 5 mV by sweeping the frequency from 100 kHz to ~0.01 Hz. All samples were recorded under identical experimental conditions.

In addition, *Composite 2* was prepared by the same procedures, except the reaction temperature was set at 90°C for 6 hours in the sulfidation. *Composite 3*, *Composite 4*, and *Composite 5* were also prepared with the same procedures, but without the addition of PMA (*Composite 3*), $\text{FeCl}_2 \cdot 4\text{H}_2\text{O}$ (*Composite 4*), PMA, and 40 mg of $\text{FeCl}_2 \cdot 4\text{H}_2\text{O}$ (*Composite 5*), respectively during the acid etching and ion exchange.

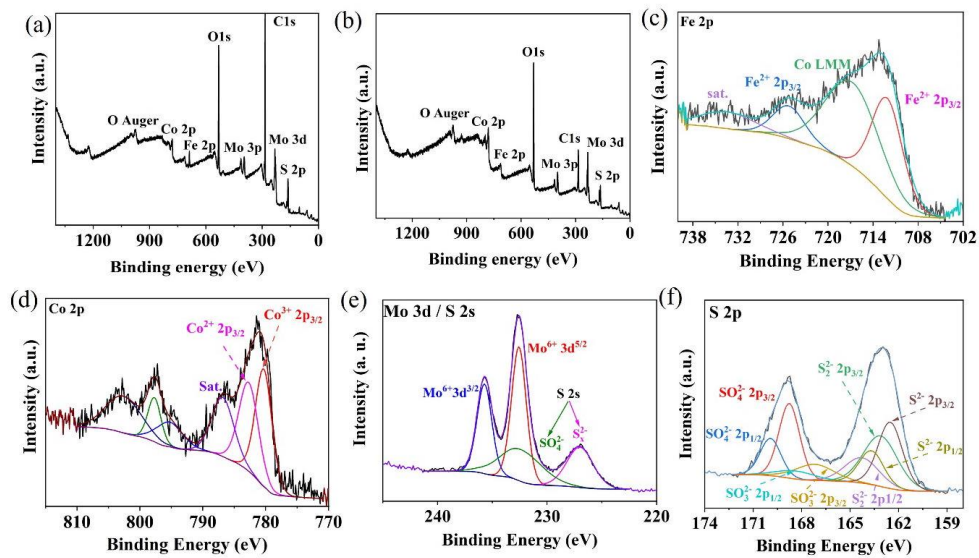


Figure S5. Overview XPS spectra of *Composite 1* (a) *Composite 2* (b), and deconvoluted high-resolution spectra of Fe 2p (c), Co 2p (d), Mo 3d (e), and S 2p (f) of *Composite 2*.

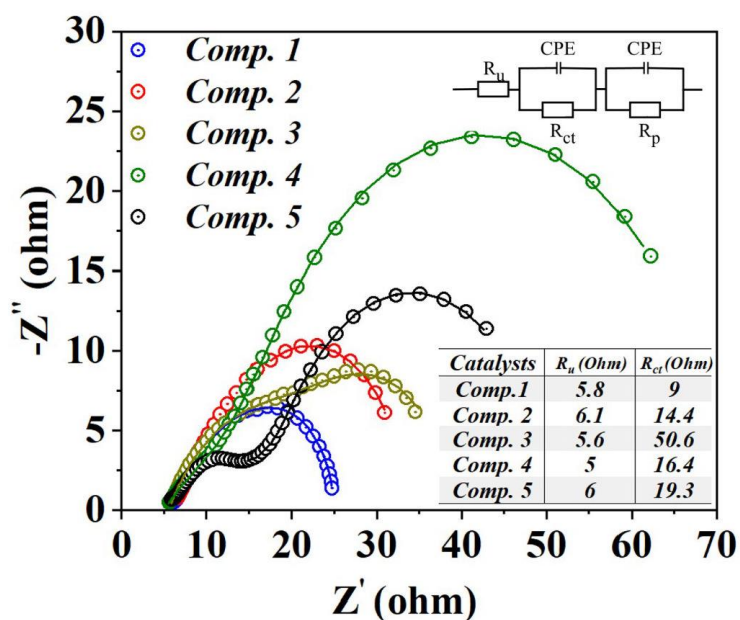


Figure S7. Electrochemical impedance spectroscopy (EIS, Nyquist plots) measured at the overpotential of 300 mV, (circles represent the experimental data, lines are the data fitting based on the equivalent circuit (insert)). The semicircles in the high-frequency range of the Nyquist plots are assigned to solution resistance (R_u) and charge transfer processes (R_{ct}). CPE (constant phase element) is the double-layer capacitance

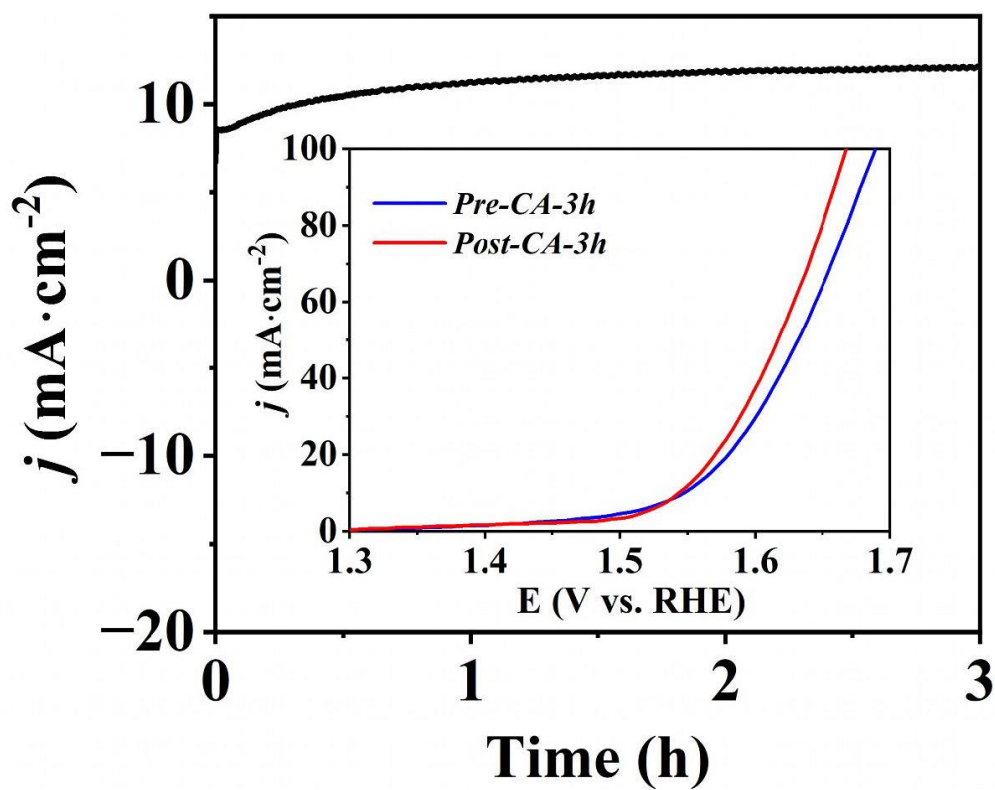


Figure S9 Chronoamperometry curves at $\eta = 330$ mV without iR compensation (insert: LSV polarization curves comparison before and after 3 h stability test).

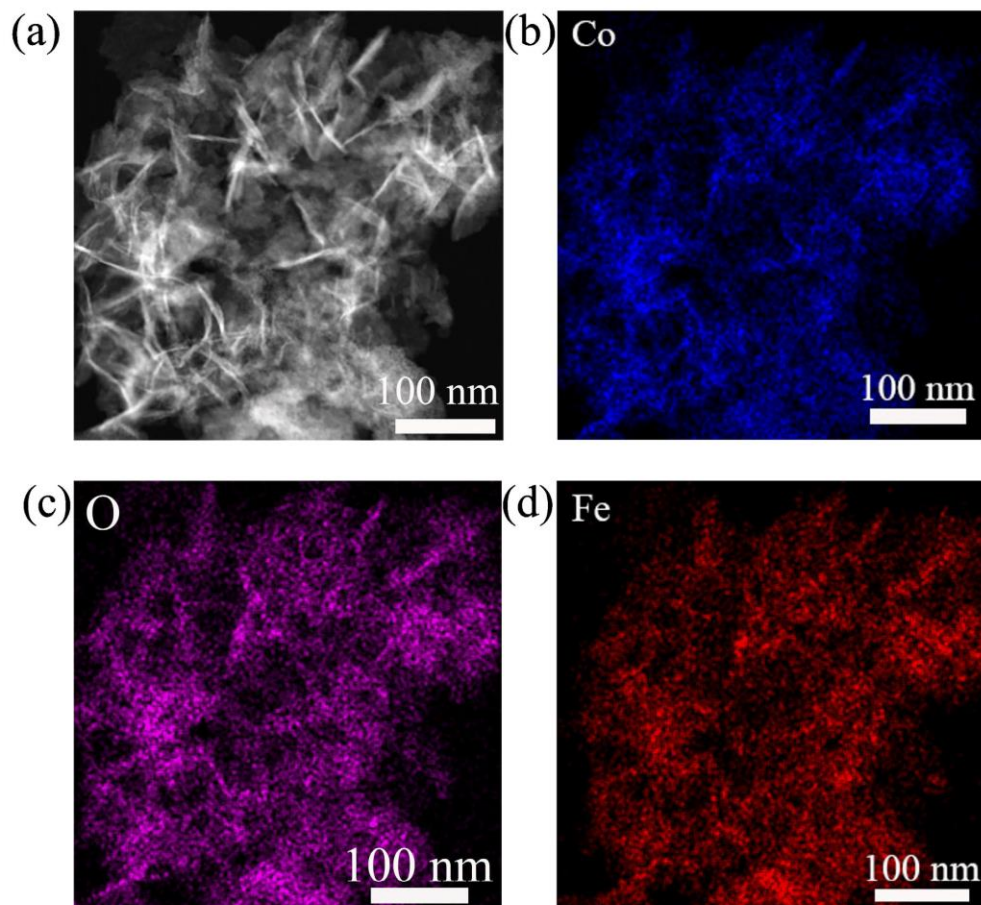


Figure S11 Compositional analysis of *Composite 1* post catalysis for 3 hours: (a) High angle annular dark-field STEM image and corresponding elemental mappings (b-d) using EDX.

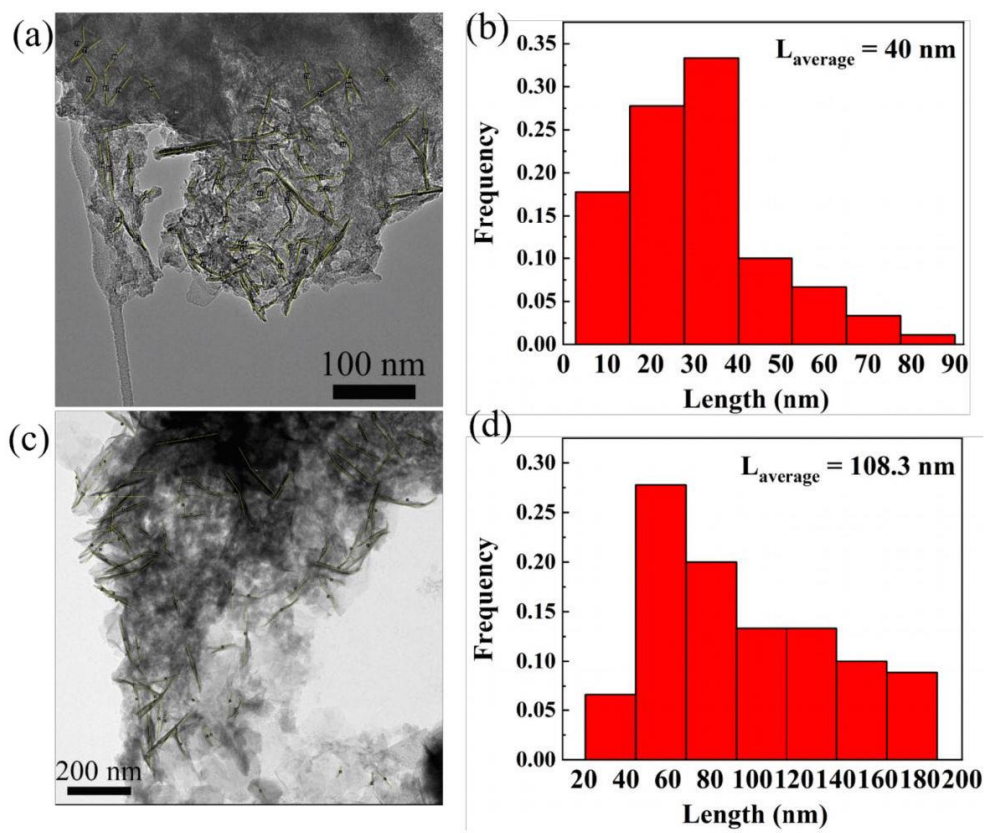


Figure S13 TEM images of *Composites 1* post electrocatalysis for 3 hours (a) and 10 hours (c), and the corresponding nanofibers length distribution (b and d)

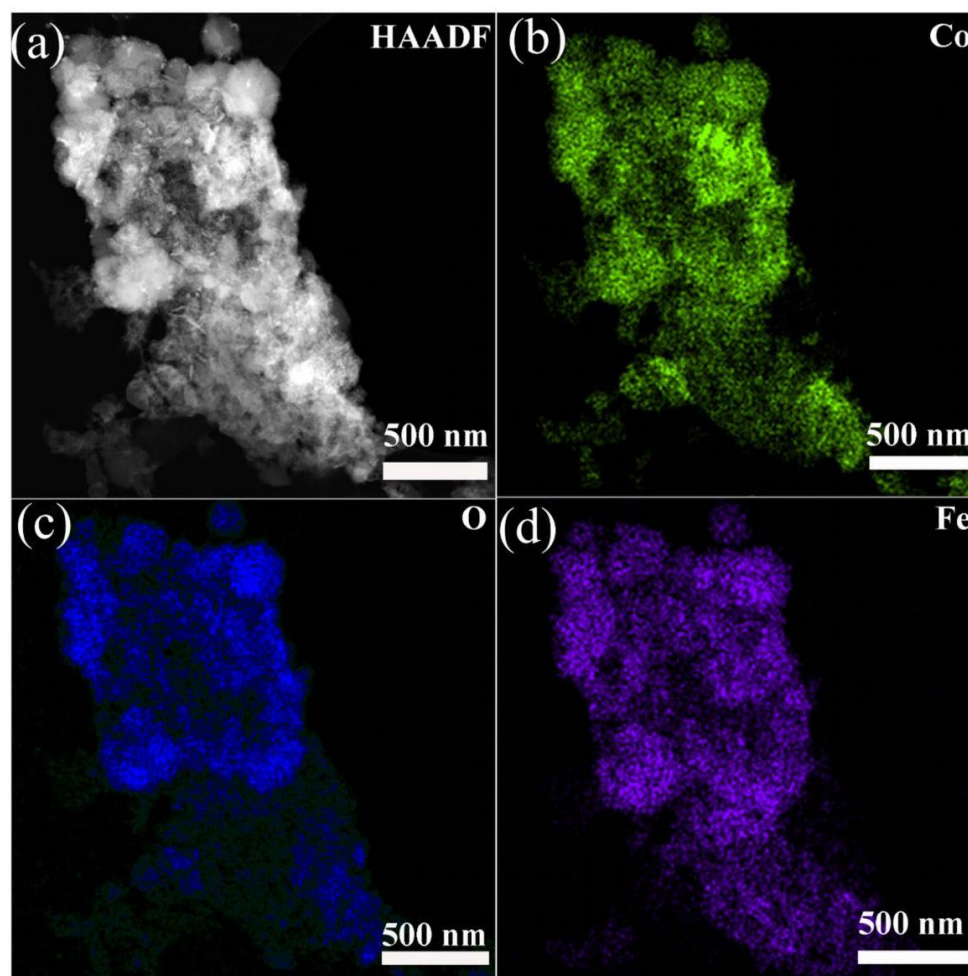


Figure S17. Post-catalysis compositional analysis of *Composite 2*: (a) High angle annular dark-field STEM image and corresponding elemental mappings (b-d) using EDX

Reference

- [1] X. Wang, L. Yu, Y. Guan, S. Song, X. Wen, D. Lou, X. Wang, L. Yu, B. Y. Guan, X. W. Lou, S. Song, *Advanced Materials* **2018**, *30*, 1801211.
- [2] Y. Guo, J. Tang, H. Qian, Z. Wang, Y. Yamauchi, *Chemistry of Materials* **2017**, *29*, 5566–5573.
- [3] F. Yousefi, S. B. Mousavi, S. Z. Heris, S. Naghash-Hamed, *Scientific Reports* **2023** *13:1* **2023**, *13*, 1–19.
- [4] M. Hashem, M. F. Al Rez, H. Fouad, T. Elsarnagawy, M. A. Elsharawy, A. Umar, M. Assery, S. G. Ansari, *Sci Adv Mater* **2017**, *9*, 938–944.

6.4 Supporting information: Atomically Engineered WO_x/MoO_x-Modified Defect-Rich Pd Metallene for Enhanced Alkaline Oxygen Reduction Electrocatalysis

Atomically Engineered WO_x/MoO_x-Modified Defect-Rich Pd Metallene for Enhanced Alkaline Oxygen Reduction Electrocatalysis

Yupeng Zhao, Zhengfan Chen, Nana Ma, Weiyi Cheng, Dong Zhang, Kecheng Cao, Fan Feng, Dandan Gao, Rongji Liu*, Shujun Li*, Carsten Streb*

Supporting Information

Table of contents

Table of contents.....	1
S1 Experimental procedures	3
S2 Characterizations	4
S3 Electrochemical measurements:	5
S4 Computational details.....	6
S5 Zn-air battery measurement.....	7
S6 Supplementary figures.....	8
S7 Reference.....	24
S8 Author contributions	24

S2

S1 Experimental procedures

Chemicals and Materials: Palladium (II) acetylacetonate ($\text{Pd}(\text{acac})_2$, 99%), 12-Molybdophosphoric acid hydrate ($\text{H}_3\text{PMo}_{12}\text{O}_{40} \cdot x\text{H}_2\text{O}$, analysis), and cyclohexane ($\geq 99.9\%$) were purchased from Merck. Tungsten hexacarbonyl ($\text{W}(\text{CO})_6$, 97%) and Nafion solution (D-520 dispersion 5% w/w aq. and 1-propanol) were purchased from Alfa Aesar. Potassium hydroxide (KOH , $\geq 85\%$), ethanol ($\text{CH}_3\text{CH}_2\text{OH}$, absolute), commercial Pt/C (20 wt%), and commercial Pd/C (10 wt%), and N, N-Dimethylformamide (DMF, 99.5%) were purchased from Fisher Scientific. Acetic acid (CH_3COOH , 99.5%) was purchased from VWR. Cetyltrimethylammonium bromide (CTAB, $\text{C}_{19}\text{H}_{42}\text{BrN}$), citric acid (CA, $\text{C}_6\text{H}_8\text{O}_7$, $\geq 99.5\%$), polyvinyl pyrrolidone (PVP, $M_w = 55\,000$) were purchased from Sigma-Aldrich. Vulcan XC-72 carbon was purchased from BC Berlin Catalysts GmbH. All chemicals were used in this experiment without further purification.

Synthesis of D-Pd M and Pd M:

The defect-rich Pd metallene (**D-Pd M**) was synthesized by a simple wet-chemical method. Typically, 42 mg of $\text{H}_3\text{PMo}_{12}\text{O}_{40} \cdot x\text{H}_2\text{O}$ was dissolved in 10 mL of DMF solution followed by deaeration with Ar for 15 min. Then the solution was irradiated under UV light (Wavelength = 254 nm) for 30 min to get solution A. In addition, 10.0 mg of $\text{Pd}(\text{acac})_2$ and 20 mg of $\text{W}(\text{CO})_6$ were added into a 25 mL bottle containing 8 mL of DMF and then sonicated for half an hour to yield a homogeneous solution (B). Afterward, solution A was added to solution B and was placed in an oil bath at 50 °C for 6 h. After cooling to room temperature, the black colloidal product was collected by centrifugation and washed six times with a mixture of ethanol and cyclohexane ($V_{\text{ethanol}}/V_{\text{cyclohexane}} = 1:1$). The final product was dispersed in cyclohexane for further use.

The hexagonal Pd metallene (Pd M) for comparison were prepared according to a previous approach with slight modifications.^[1,2] 16 mg of $\text{Pd}(\text{acac})_2$, 90 mg of CA, 60 mg of CTAB, and 30 mg of PVP were added into 10 mL of DMF and stirred for 1 h to get a homogeneous orange-red solution. The obtained solution was then transferred into a 25 mL vial and 100 mg of $\text{W}(\text{CO})_6$ was added to the vial under N_2 atmosphere. The vial was capped and heated at 80 °C for 1 h. After the reaction, Pd nanosheets were collected by centrifugation using enough acetone and then redispersed in acetone for further use.

S2 Characterizations

Powder X-ray diffraction (XRD): Bruker D2 Phaser equipment, with Cu K α radiation ($\lambda = 1.5406 \text{ \AA}$).

Transmission electron microscopy (TEM): Tecnai G2 Spirit operated at 120 kV (Imaging).

High-resolution transmission electron microscopy (HRTEM) and energy-dispersive X-ray spectroscopy (EDX): Jeol F200 equipped with a SuperX EDX detector, operated at 200 kV (Imaging and diffraction pattern).

Inductively Coupled Plasma Optical Emission Spectroscopy (ICP-OES): Agilent 5800 VDV ICP-OES (optical emission spectrometer) with the automatic sampler SPS 4.

X-ray photoelectron spectroscopy (XPS): Monochromatized Al K α exciting X-radiation using a PHI Quantera SXM system. The binding energies were calibrated based on C1s (284.8 eV).

Ultraviolet - visible spectroscopy (UV-vis): Cary 3500 UV-Vis Spectrophotometer equipped with a Xenon flash lamp (250 Hz). Measurements were performed in standard 1 cm cuvettes.

Atomic force microscopy (AFM): Bruker Dimension Icon.

X-ray absorption spectroscopy (XAS) experiment and data processing: Pd K-edge, W L₃-edge, and Mo L₃-edge X-ray absorption fine structure (XAFS) analyses were performed with Si (111) crystal monochromators at the BL14W Beam line at the Shanghai Synchrotron Radiation Facility (SSRF) (Shanghai, China). Before the analysis at the beamline, samples were placed into aluminum sample holders and sealed using Kapton tape film. The XAFS spectra were recorded at room temperature using a 4-channel Silicon Drift Detector (SDD) Bruker 5040. Pd K-edge and W L₃-edge extended X-ray absorption fine structure (EXAFS) spectra were recorded in transmission mode. Mo L₃-edge extended X-ray absorption fine structure (EXAFS) spectra were recorded in fluorescence mode. Negligible changes in the line shape and peak position of Pd K-edge, W L₃-edge, and Mo L₃-edge XANES spectra were observed between two scans taken for a specific sample. The spectra were processed and analyzed by the software code Athena.

S3 Electrochemical measurements:

The as-prepared **D-Pd M** and Pd M catalysts were loaded on carbon black (Vulcan XC-72) before electrochemical tests. Typically, the **D-Pd M** (2 mg) was mixed with carbon black (8 mg) in cyclohexane (10 mL) under ambient sonication for 1 h. After stirring for another 12 h, the product was collected by centrifugation and washed three times with ethanol. Afterward, the product was treated in pure acetic acid (10 mL) at 70 °C for 2 h to remove excess impurities and excess surfactants for further use. At the end, **D-Pd M/C** was collected by centrifugation, washed three times with ethanol, and dried at 60°C for 3 hours. Pd M/C was prepared by the same method.

To prepare the catalyst inks, the as-prepared **D-Pd M/C** (1 mg) was re-dispersed in a solution containing 15 μL DI water, 980 μL ethanol, and 5 μL Nafion solution by at least 30 min sonication in an ice-water bath to form a catalyst ink. Then the **D-Pd M/C** catalyst ink was dipped on the electrode with a controllable amount of **D-Pd M** catalyst being 10 $\mu\text{g}\cdot\text{cm}^{-2}$. Likewise, the Pd M/C was processed in the same way. The controllable amount of commercial Pd/C, and commercial Pt/C were 15 $\mu\text{g}\cdot\text{cm}^{-2}$ to reach the well-defined limited current density. The loading amount on the electrode of prepared catalysts was determined by ICP-OES.

Electrochemical tests were conducted using a three-electrode system on an Ametek electrochemical workstation (channel PMC 1000) equipped with an RRDE setup (Pine, USA). A glassy carbon rotating disk electrode (GC RDE, diameter: 5 mm, area: 0.196 cm^2), a saturated calomel electrode (SCE), and a graphite rod were used as the working electrode, reference electrode, and counter electrode, respectively. All potentials in this study were reported on a reversible hydrogen electrode (RHE) scale according to the Nernst equation ($E_{\text{RHE}} = E_{\text{SCE}} + E_{\text{SCE}}^0 + 0.059 \text{ V} \times \text{pH}$). The cyclic voltammetry (CV) curves were recorded in N_2 -saturated 0.1 M KOH at a scan rate of 50 $\text{mV}\cdot\text{s}^{-1}$. ORR linear sweep voltammetry (LSV) was recorded in O_2 -saturated 0.1 M KOH at 20 $\text{mV}\cdot\text{s}^{-1}$ and a rotating rate of 1600 rpm. It is worth noting that the ORR LSV curves have been corrected in the N_2 -saturated 0.1 M KOH to eliminate the interference of double-layer capacity. The current densities (j) were normalized regarding the geometric area of the GC RDE. Notably, all ORR LSV curves were $i\text{R}$ -corrected (95%) before applying the K-L equation: $I_k = (I_d \times I)/(I_d - I)$, where I_k , I_d , and I represent the kinetic, diffusion limiting, and measured current, respectively.

The electrochemical active surface areas (ECSAs) of all the catalysts were calculated using the underpotentially deposited H (H_{upd}) data obtained in the N_2 -saturated 0.1 M HClO_4 . The peaks

of H_{upd} were recorded by cyclic voltammetry (CV) with a scan rate of $50 \text{ mV}\cdot\text{s}^{-1}$ to calculate the ECSAs. In the calculation, we used a charge density of $210 \mu\text{C}\cdot\text{cm}^{-2}$ for one monolayer of hydrogen coverage on commercial Pt/C and Pd/C, and a charge density of $240 \mu\text{C}\cdot\text{cm}^{-2}$ (a value for the (111) surface) for one monolayer of hydrogen coverage on **D-Pd M/C** and Pd M/C.

The electron transfer number (n) and the hydrogen peroxide yield ($H_2O_2\%$) were tested by a rotating Pt ring - GC disk electrode (RRDE) device (Pine, USA), where the surface area of the GC disk and Pt ring are 0.2475 cm^2 and 0.1866 cm^2 , respectively. The disk electrode was conducted LSV scan, and the ring electrode potential was set to 1.4 V vs. RHE. The $H_2O_2\%$ and n were calculated by the following equations:

$$H_2O_2\% = 200 \times \frac{\frac{I_r}{N}}{\frac{I_r}{N} + I_d}$$

$$n = 4 \times \frac{I_d}{\frac{I_r}{N} + I_d}$$

where I_d is the disk current, I_r is the ring current, and N is the ring collection efficiency ($N=0.37$). In addition, the electron transfer number during the ORR process of **D-Pd M** was also determined by applying different rotating rates to the Koutecky-Levich equation:

$$\frac{1}{j} = \frac{1}{j_k} + \frac{1}{j_L} = \frac{1}{B\omega^{1/2}} + \frac{1}{j_L}$$

$$B = 0.2nFC_0D_0^{2/3}\nu^{-1/6}$$

where j , j_k , and j_L represent measured current density, the kinetic and limiting current densities the kinetic, respectively. F is the Faraday constant (96485 C mol^{-1}), C_0 is the bulk concentration of O_2 ($1.26 \times 10^{-6} \text{ mol}\cdot\text{cm}^{-3}$), D_0 is the diffusion coefficient of O_2 in 0.1 M KOH ($1.93 \times 10^{-5} \text{ cm}^2\cdot\text{s}^{-1}$), and ν is the kinetic viscosity ($0.01 \text{ cm}^2\cdot\text{s}^{-1}$). The rotation speed is expressed in rpm.

Accelerated durability tests (ADTs) were conducted by cycling between 0.6 V and 1.0 V vs. RHE at 200 mV/s for 5,000 cycles and 10,000 cycles in 0.1 M O_2 -saturated KOH solution at 1600 rpm.

S4 Computational details

All DFT calculations in the present work were performed using the Vienna Ab initio Simulation Package (VASP)^[3,4] with the Perdew-Burke-Ernzerhof (PBE)^[3] functional. The ion-electron

interactions were modeled using the projector-augmented wave (PAW) method^[5]. The plane wave cutoff energy was set to 400 eV in all calculations. The convergence criteria were set to be 10⁻⁵ eV and 0.01 eV/Å for wavefunction and geometry optimization, respectively. A Γ -centred Monkhorst–Pack k-point mesh with a size of 3×3×1 was applied for all supercells. The vacuum region was set to 15 Å. The DFT-D3 scheme of dispersion correction was employed to describe van der Waals interactions^[6]. The electronic density of the structure was processed using VASPKIT^[7].

S5 Zn-air battery measurement

The zinc-air battery was measured in a labmade battery mode, consisting of an anode and a cathode. The anode is a polished Zn foil (with a thickness of 0.5 mm), the air cathode is the catalyst-loaded carbon paper (ThermoFisher Scientific), and the electrolyte is a 6 M KOH solution containing 0.2 M Zn(CH₃COO)₂. The catalyst inks were prepared with the same method we mentioned above but at a concentration of 10 mg·mL⁻¹. The catalyst-loaded carbon paper was prepared by spreading as-prepared catalyst ink onto carbon paper and drying at room temperature. The mass loading of 20% **D-Pd M/C** and 20% Pt/C catalysts is 130 μg·cm⁻², and the mass loading of Pd/Pt is 26 μg·cm⁻². The polarization curves were performed at the CHI 760E electrochemistry station. Galvanostatic cycling tests were collected at the **LAND CT2003A** multi-channel battery testing system. When testing the specific capacity of zinc-air potential, the discharge current was set at 15 mA and the cut-off voltage was 0.5 V. The charge and discharge current density was set at 15 mA, the discharge cut-off voltage was set to 0.2 V, and the charge cut-off voltage was set to 1.85 V.

S6 Supplementary figures



Figure S1. The optical photographs of PMo₁₂ in DMF solution before (a) and after (b) reduction, and corresponding UV-visible spectra after being diluted to 1/10 of original concentration.

The color changes from bright yellow to dark blue and newly appeared broad in reduced solution indicate the reduction of PMo₁₂ clusters to heteropoly blue. Approximately 5.2% of PMo₁₂ underwent reduction to form heteropoly blue,^[8,9] according to the Beer-Lambert law: $A = \epsilon bc$; A is absorbance, ϵ is molar absorptivity (here: $2600 \text{ M}^{-1}\cdot\text{cm}^{-1}$), b is length of light path (here: 1 cm), and c is concentration, respectively.

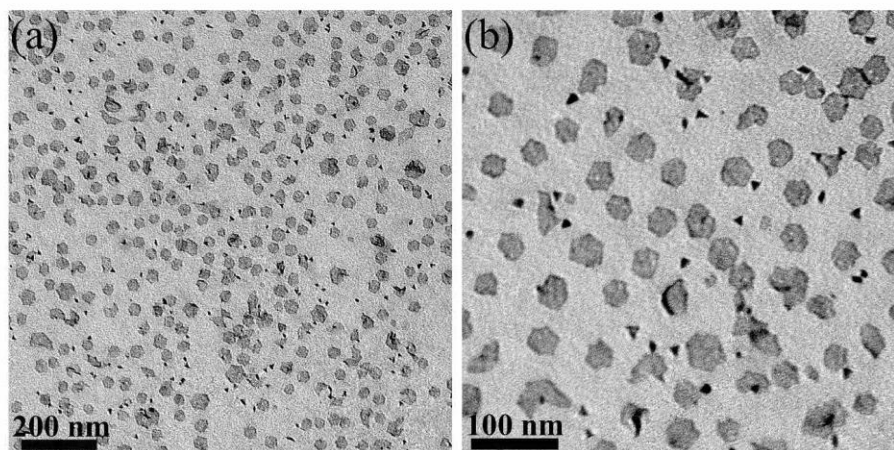


Figure S2. TEM images of Pd M at low (a) and (high) magnification.

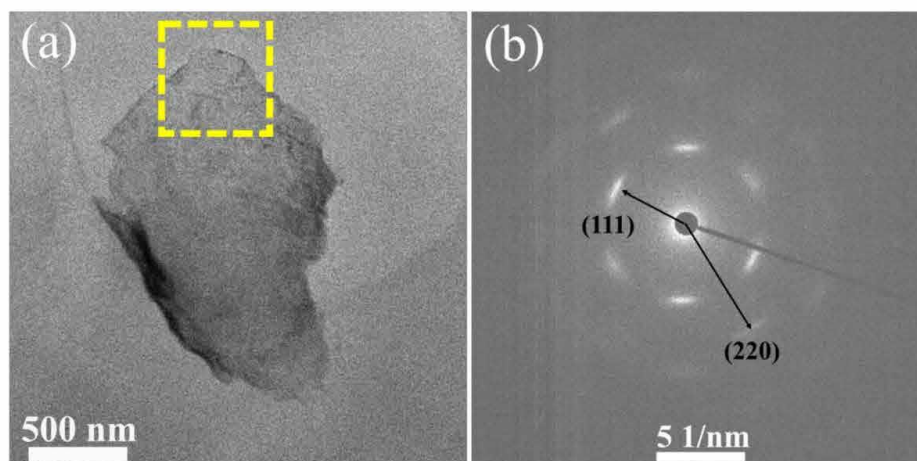


Figure S3. (a) TEM image and (b) the corresponding SAED pattern in selected area in (a) of D-Pd M.

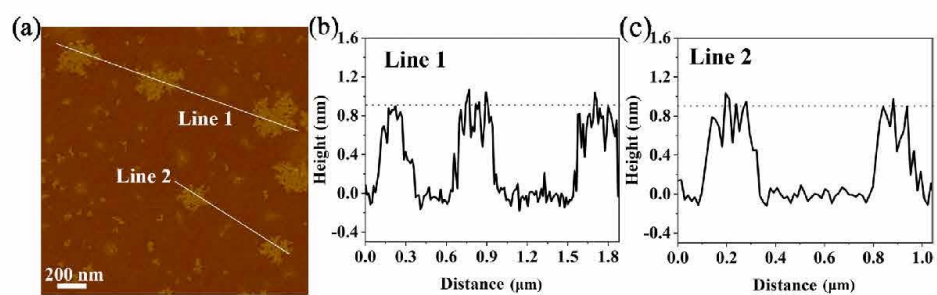


Figure S4. AFM image (a) and corresponding height profiles (b and c) of D-Pd M.

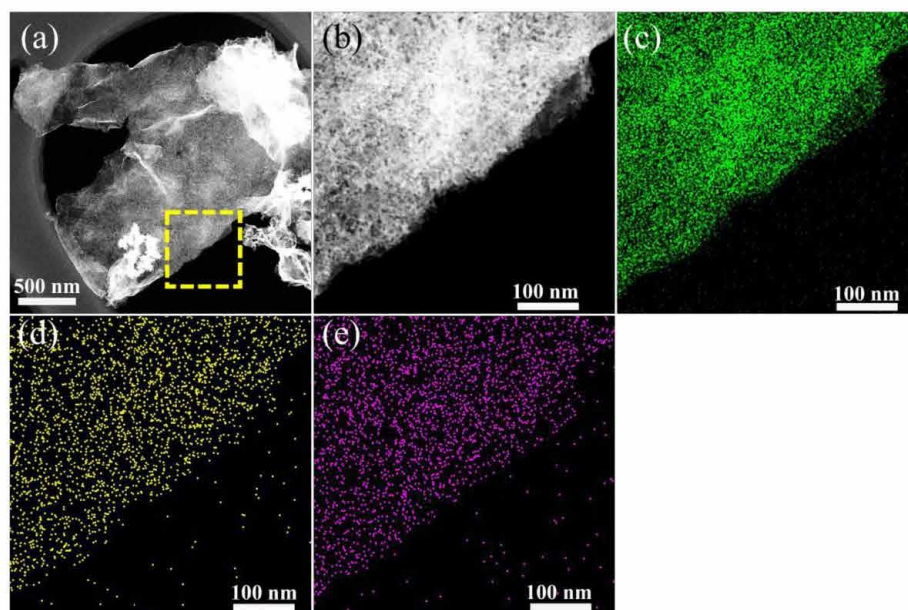


Figure S5. (a) HAADF-STEM image, (b) the magnification of selected area (in a, yellow square), (c-d) and the corresponding elemental mapping of Pd, Mo, and W elements of the **D-Pd M**.

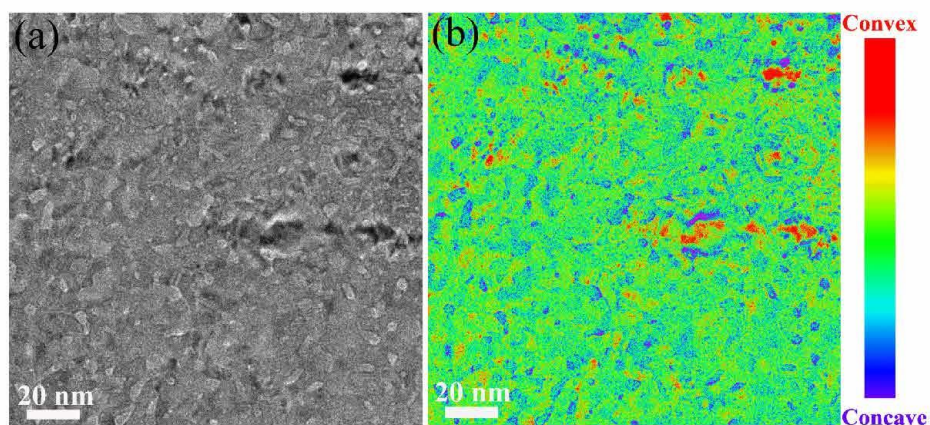


Figure S6. (a) TEM images and (b) corresponding false color mode of **D-Pd M**.

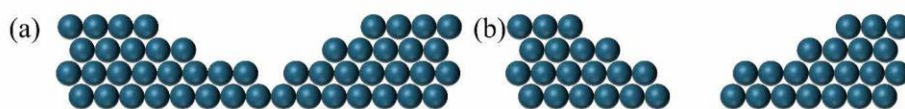


Figure S7. Schematic of pores (a) and concave (b) defects from side view.

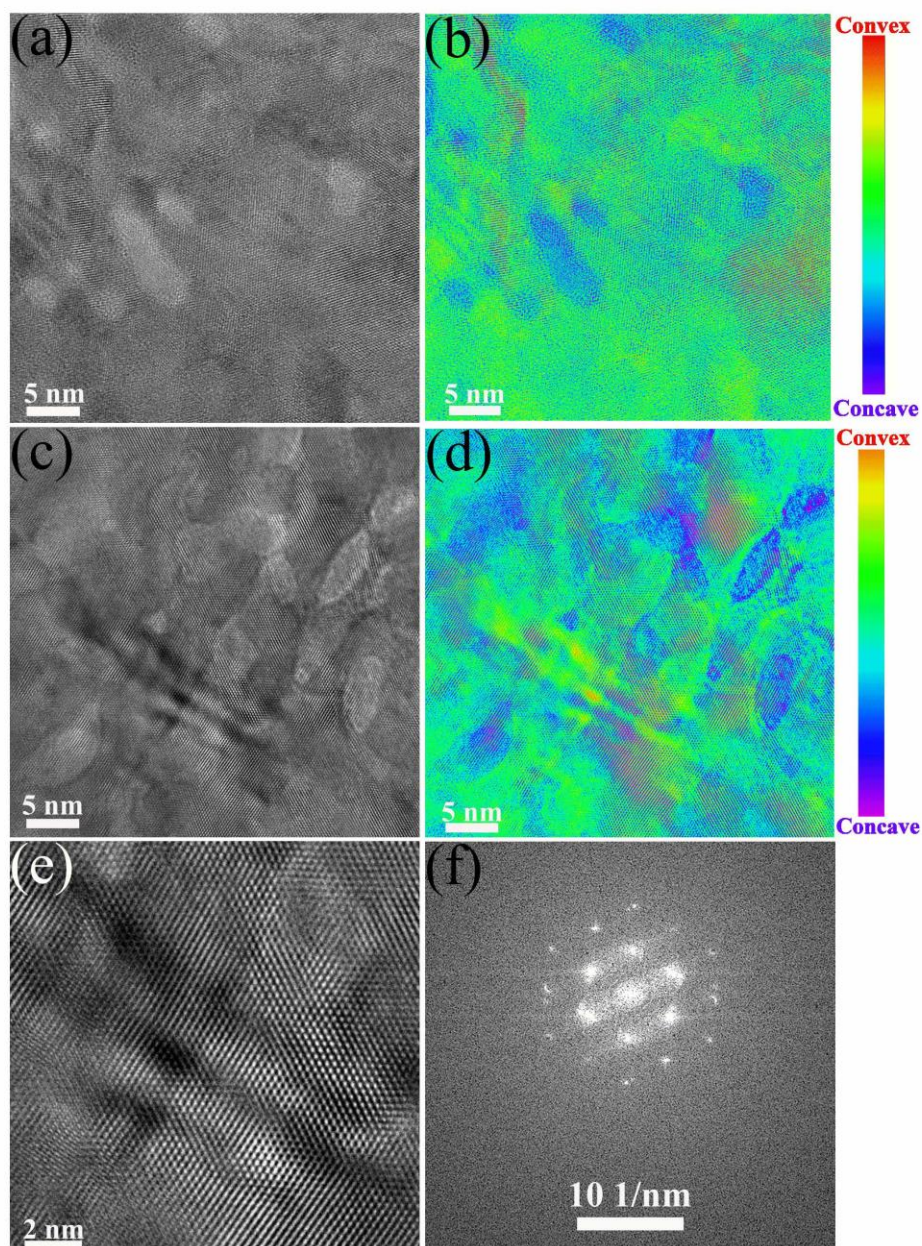


Figure S8. HRTEM images of **D-Pd M**. (a, c, and e) crude images, (b and d) temperature mode of corresponding images, in which dark blue represents concave sites and bright orange represents convex sites. (f) fast Fourier transform pattern of (e).

Table S1. EXAFS fitting parameters at the Mo&Pd *K*-edge and W *L*₃-edge for **D-Pd M**.

Sample	Shell	CN ^a	R(Å) ^b	σ ² (Å ²) ^c	ΔE ₀ (eV) ^d	R factor
Pd						
Pd foil	Pd-Pd	12*	2.737±0.002	0.0055±0.0002	3.4±0.2	0.0020
PdO	Pd-O	4.0±0.2	2.017±0.001	0.0023±0.0006	7.9±0.3	0.0042
	Pd-Pd	3.7±0.8	3.018±0.001	0.0089±0.0017	1.5±0.9	
	Pd-Pd	7.7±0.8	3.388±0.001	0.0124±0.0001	2.3±0.7	
D-Pd M	Pd-Pd/Mo/W	10.7±1.0	2.738±0.005	0.0060±0.0006	6.0±0.7	0.0062
W						
W-foil	W-W	8*	2.734±0.006	0.0037±0.0007	5.3±1.0	0.0049
	W-W	6*	3.160±0.012	0.0043±0.0010	8.4±1.7	
WO ₂	W-O	4.0±0.7	2.013±0.001	0.0015±0.0021	11.4±1.0	0.0081
D-Pd M	W-O	1.4±0.3	1.779±0.001	0.0070±0.0014	-7.9±1.0	0.0062
	W-O	2.8±0.4	2.111±0.001			
	W-Pd	6.3±0.8	2.605±0.001	0.0189±0.0011	2.0±0.6	
	W-O	15.9±1.8	3.499±0.001			
Mo						
Mo foil	Mo-Mo	8*	2.724±0.003	0.0041±0.0003	4.9±0.5	0.0040
	Mo-Mo	6*	3.150±0.005	0.0040±0.0004	7.5±1.0	
MoO ₂	Mo-O	6.0±0.3	1.999±0.001	0.0033±0.0006	2.8±0.3	0.0035
	Mo-Mo	3.1±0.6	2.569±0.001	0.0105±0.0017	8.8±0.8	
	Mo-Mo	1.9±0.2	3.087±0.001	0.0040±0.0001	-11.1±0.5	
	Mo-Mo	6.2±0.3	3.642±0.001			
	Mo-Mo	7.4±1.6	4.058±0.001	0.0130±0.0001	0.8±0.1	
MoO ₃	Mo-O	2.0±0.2	1.685±0.001	0.0037±0.0006	4.5±0.9	0.0080
	Mo-O	2.7±0.3	1.975±0.001		14.0±0.1	
	Mo-O	3.1±0.4	2.286±0.001	0.0095±0.0001	-	
	Mo-Mo	6.3±1.1	3.430±0.001			
	Mo-Mo	15.4±1.9	3.625±0.001	0.0086±0.0006	12.0±0.4	
D-Pd M	Mo-O	1.4±0.2	1.745±0.001	0.0023±0.0009	8.5±0.8	0.0070
	Mo-O	0.4±0.2	2.044±0.001			
	Mo-O	0.5±0.2	2.429±0.001	0.0046±0.0014	-3.0±1.2	
	Mo-Pd	0.9±0.2	2.681±0.001			

^aCN, coordination number; ^bR, the distance to the neighboring atom; ^cσ², Debye-Waller factor, the Mean Square Relative Displacement (MSRD); ^dΔE₀, inner potential correction; R factor indicates the goodness of the fit. S₀² was fixed to 0.992, 0.812, and 0.958, according to the experimental EXAFS fit of Mo foil, Pd foil, and W foil by fixing CN as the known crystallographic value. * This value was fixed during EXAFS fitting, based on the known structure of Mo, Pd, and W. Fitting range: 3.0 ≤ k (Å⁻¹) ≤ 14.0 and 1.0 ≤ R (Å) ≤ 3.3 (Mo foil); 3.0 ≤ k (Å⁻¹) ≤ 12.0 and 1.1 ≤ R (Å) ≤ 3.9 (MoO₂); 3.0 ≤ k (Å⁻¹) ≤ 13.0 and 1.0 ≤ R (Å) ≤ 4.1 (MoO₃); 3.0 ≤ k (Å⁻¹) ≤ 13.0 and 1.0 ≤ R (Å) ≤ 3.0 (D-Pd M_Mo); 3.0 ≤ k (Å⁻¹) ≤ 13.0 and 1.0 ≤ R (Å) ≤ 2.9 (Pd foil); 3.0 ≤ k (Å⁻¹) ≤ 12.0 and 1.0 ≤ R (Å) ≤ 3.6 (PdO); 3.0 ≤ k (Å⁻¹) ≤ 13.0 and 1.9 ≤ R (Å) ≤ 3.0 (D-Pd M_Pd); 3.0 ≤ k (Å⁻¹) ≤ 12.0 and 1.0 ≤ R (Å) ≤ 3.5 (W foil); 3.0 ≤ k (Å⁻¹) ≤ 11.0 and 1.2 ≤ R (Å) ≤ 2.0 (WO₂); 3.0 ≤ k (Å⁻¹) ≤ 10.0 and 1.0 ≤ R (Å) ≤ 3.8 (D-Pd M_W). A reasonable range of EXAFS fitting parameters: 0.700 < S₀² < 1.000; CN > 0; σ² > 0 Å²; |ΔE₀| < 15 eV; R factor < 0.02.

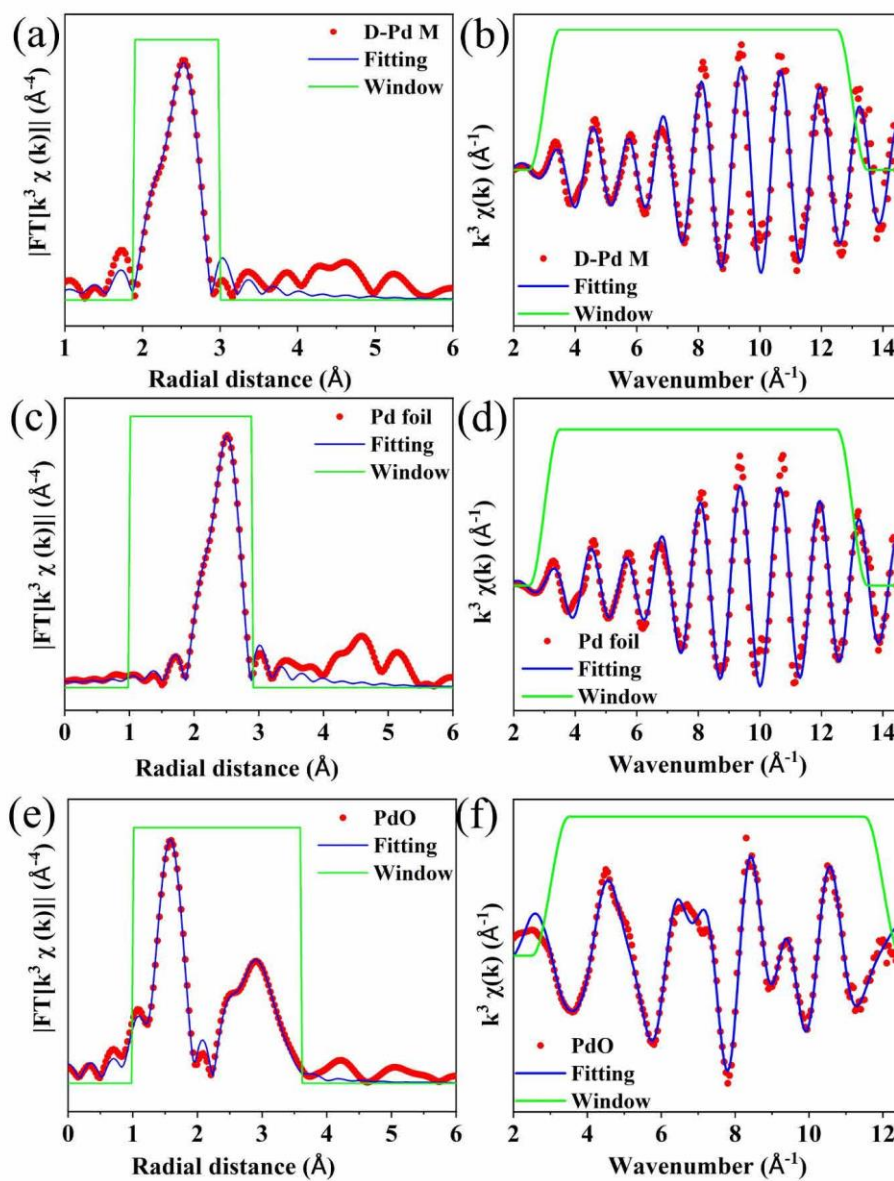


Fig. S9. R space and k space fitting results of Pd K-edge. (a and b) **D-Pd M**, (c and d) Pd foil, and (e and f) PdO. The dots or lines in red, blue, and green represent raw data, fitting results and FT fitting range windows.

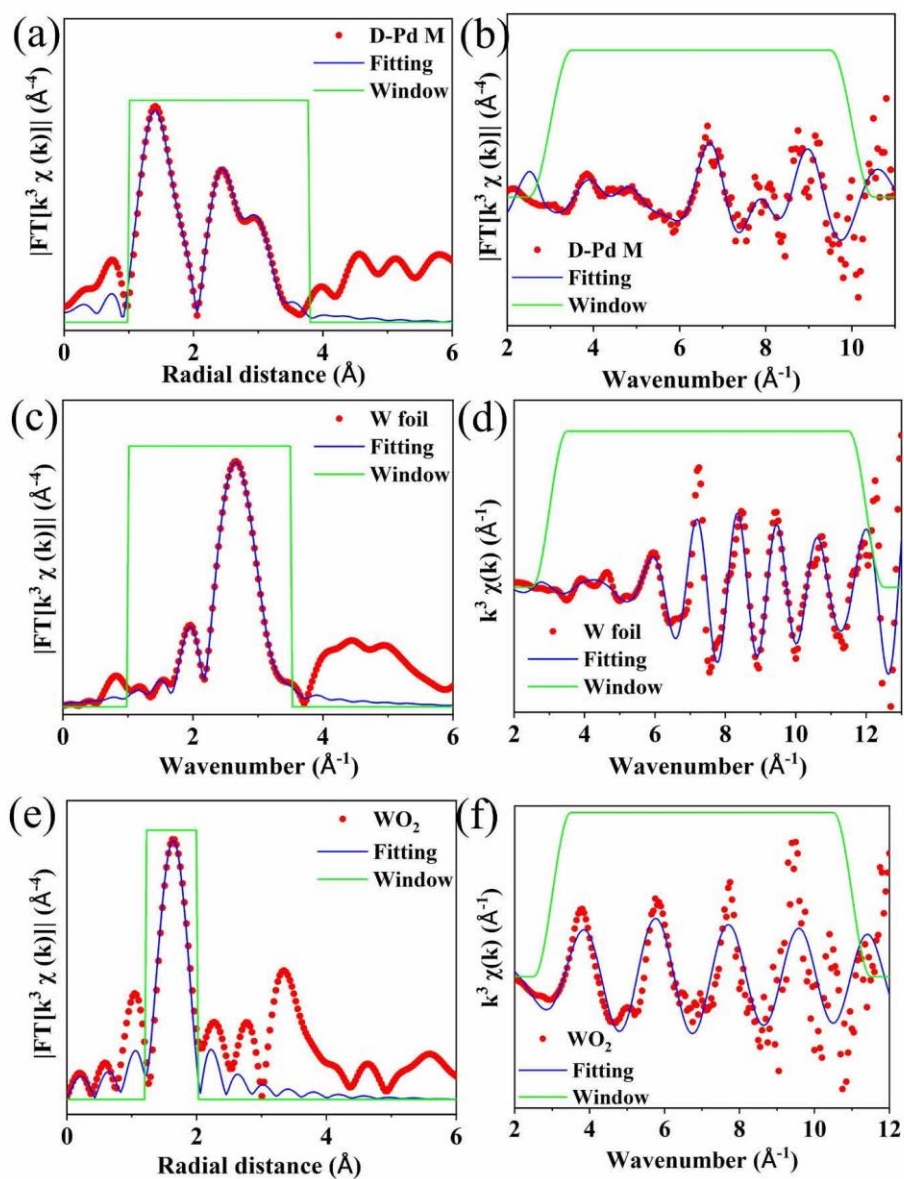


Fig. S10. R space and k space fitting results of W L-edge. (a and b) **D-Pd M**, (c and d) W foil, and (e and f) WO₂. The dots or lines in red, blue, and green represent raw data, fitting results and FT fitting range windows.

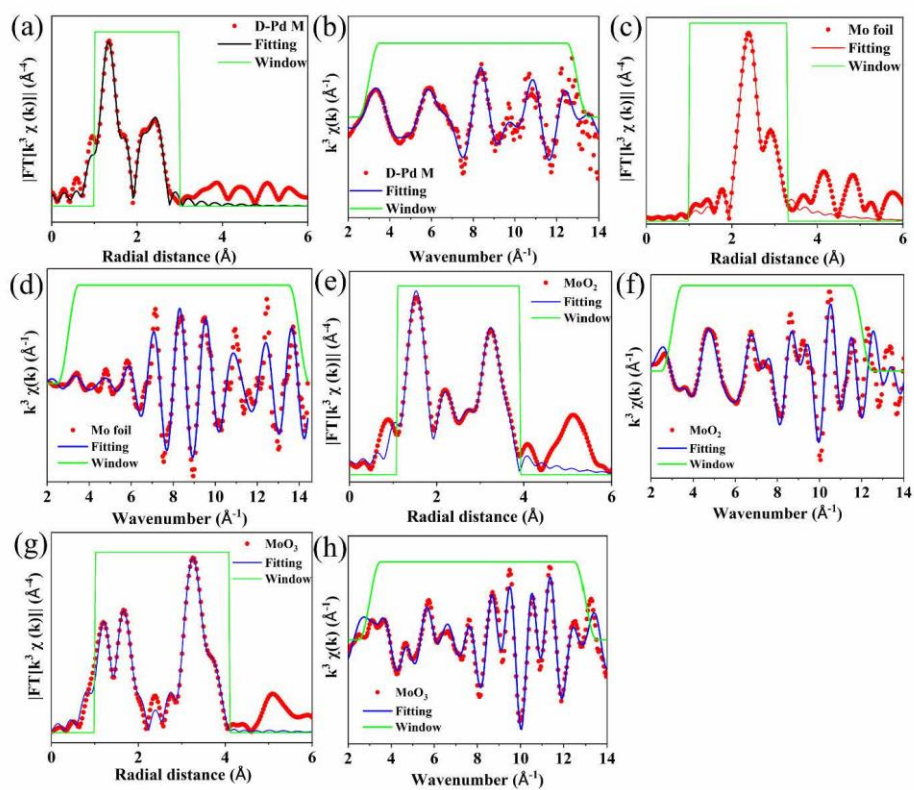


Fig. S11. R space and k space fitting results of Mo K-edge. (a and b) **D-Pd M**, (c and d) Mo foil, (e and f) MoO₂, and (g and h) MoO₃. The dots or lines in red, blue, and green represent raw data, fitting results and FT fitting range windows.

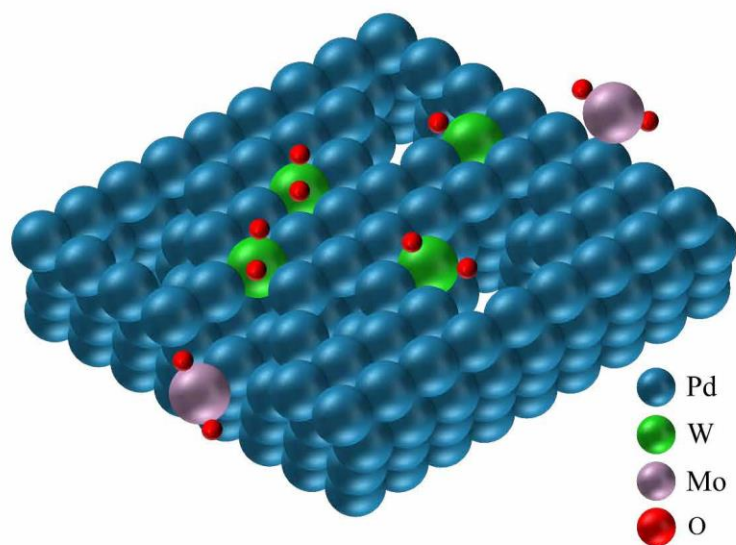


Figure S12. Schematic of MoO_x and WO_x doping. W atoms substitute the position of Pd, but Mo just dispersed on the edge of Pd.

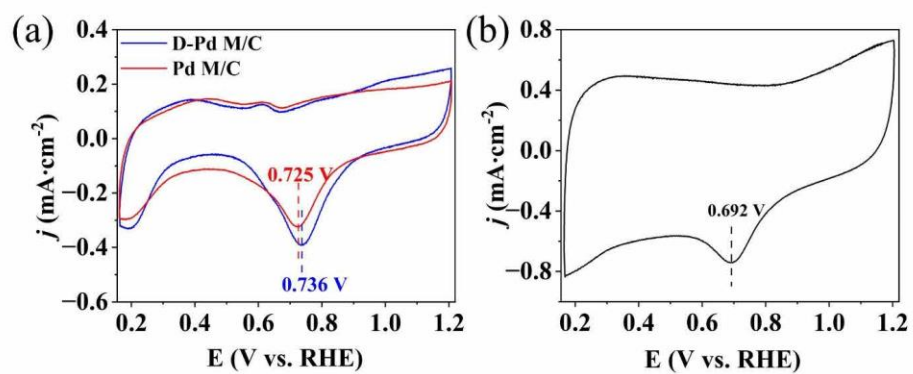


Figure S13. CV curves of (a) **D-Pd M/C**, Pd M/C, and (b) Pd/C in N_2 -saturated 0.1 M KOH solution at a scan rate of $50 \text{ mV}\cdot\text{s}^{-1}$.

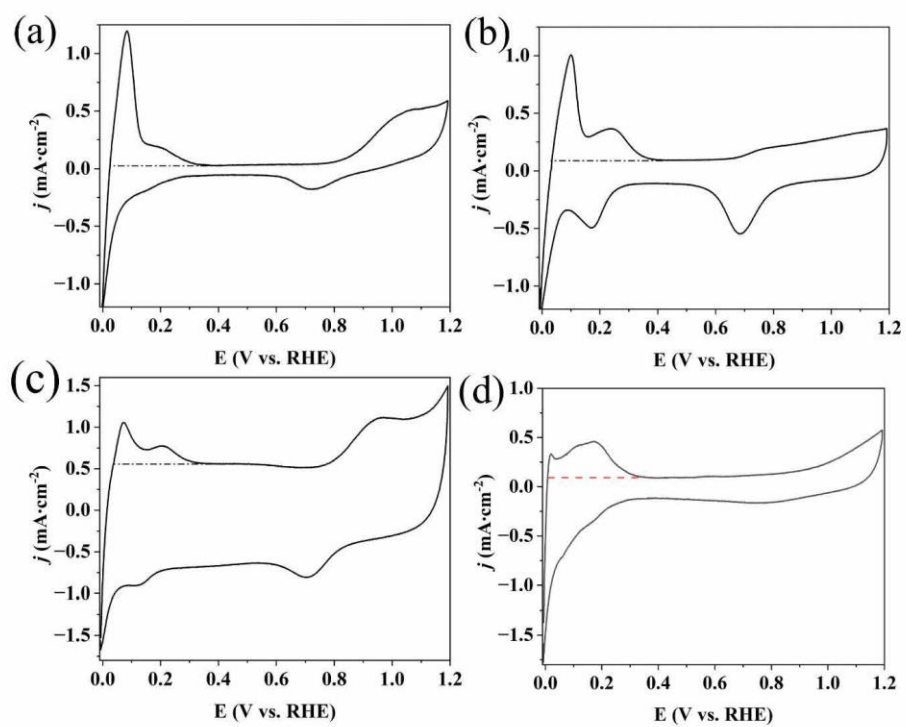


Figure S14. CVs of (a) **D-Pd M/C**, (b) **Pd M/C**, (c) **Pd/C**, and (d) **Pt/C** in N_2 -saturated 0.1 M HClO_4 at a scan rate of $50 \text{ mV}\cdot\text{s}^{-1}$

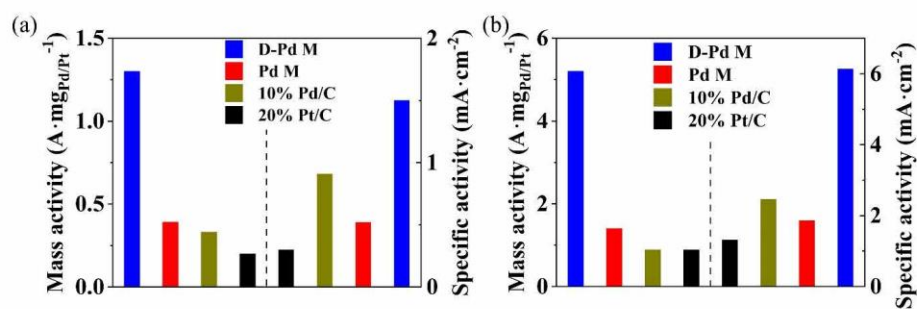


Figure S15. MAs and SAs of **D-Pd M/C**, Pd M/C, Pd/C, and Pt/C at (a) 0.9 V vs. RHE and (b) 0.85 V vs. RHE.

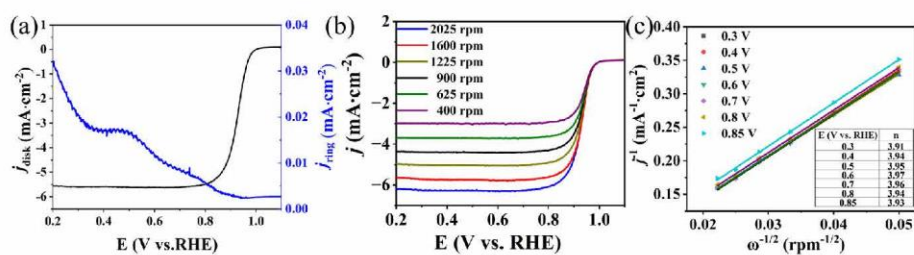


Figure S16. (a) Ring and disk current density of **D-Pd M** in O_2 -saturated 0.1 M KOH solution, potential applied on ring was set 1.4 V vs. RHE, (b) LSV curves of **D-Pd M/C** at different scan rates and (c) corresponding K-L plot and electron transfer numbers (insert).

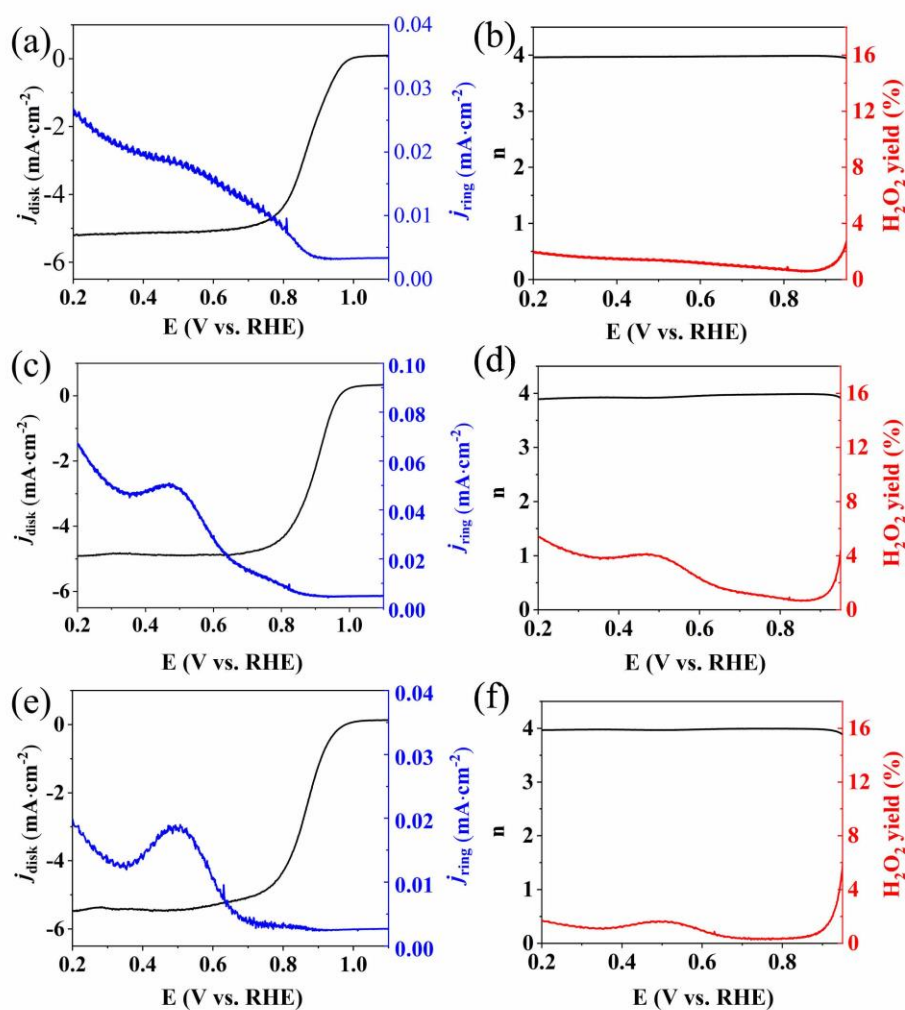


Figure S17. Ring and disk current density of (a) Pd M/C, (c) Pd/C, and (e) Pt/C in O_2 -saturated 0.1 M KOH solution, potential applied on ring was set 1.4 V vs. RHE. The electron transfer number and H_2O_2 yield of (b) Pd M/C, (d) Pd/C, and (f) Pt/C.

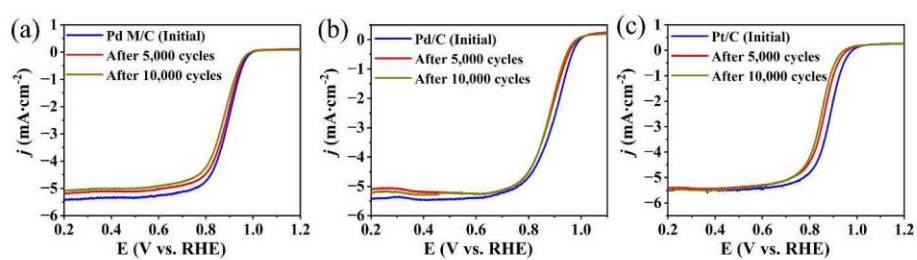


Figure S18. LSVs of (a) Pd M/C, (c) Pd/C, and (e) Pt/C in O₂-saturated 0.1 M KOH solution before and after 5,000 and 10,000 CV scans.

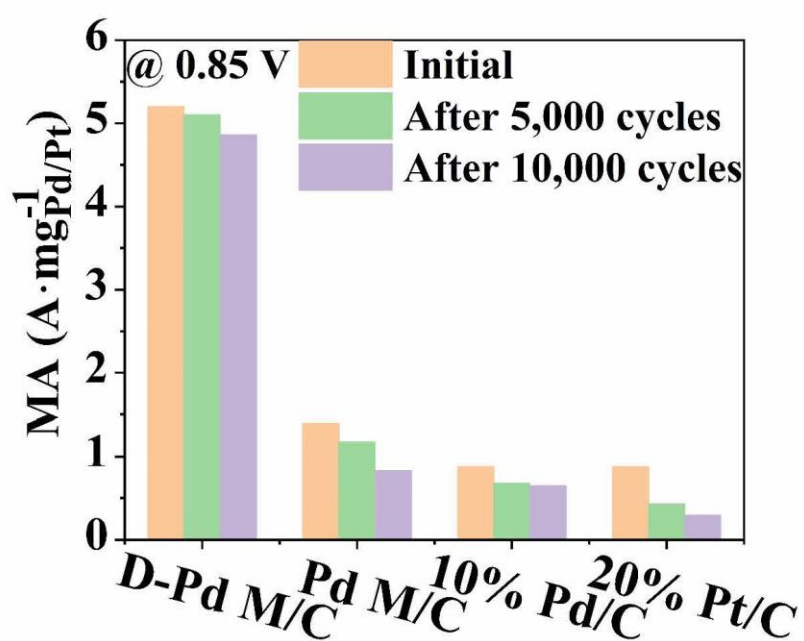


Figure S19. MAs of D-Pd M/C, Pd M/C, Pd/C, and Pt/C at 0.85 V vs. RHE before and after 5,000 and 10,000 cycles

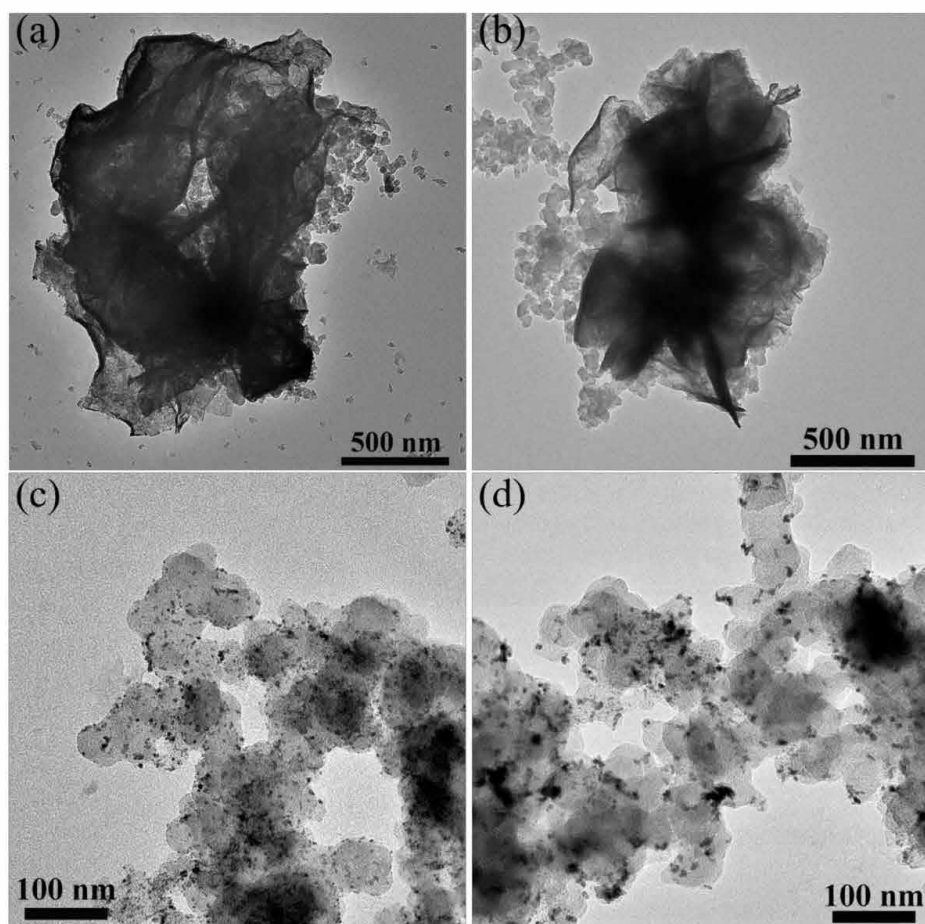


Figure S20. The morphologies of D-Pd M (a, b) and Pt/C (c, d) before and after ADT test.

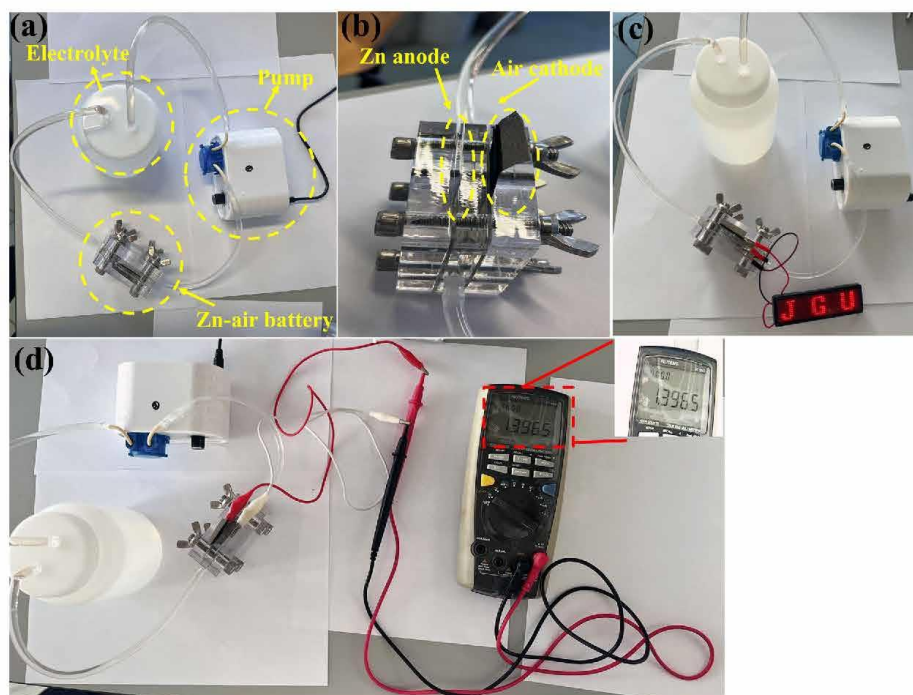


Figure S21. Photographs of the whole Zn-air battery system (a) and Zn-air battery (b), (c) red LED (the operating voltage only > 1 V) powered by **D-Pd M** based Zn-air battery, and (c) an open-circuit voltage of 1.397 V obtained with **D-Pd M** based Zn-air battery.

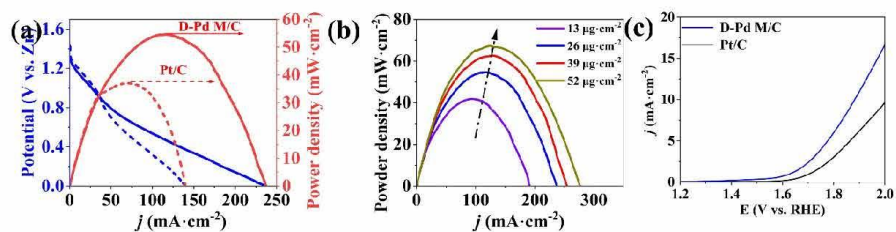


Figure S22. (a) Polarization and corresponding power density curves of **D-Pd M/C** (line) and Pt/C (dashes), (b) power density curves of **D-Pd M/C** at different loading, (c) OER polarization curves of **D-Pd M/C** and Pt/C in O_2 -saturated 0.1 M KOH at a scan rate of $5 \text{ mV}\cdot\text{s}^{-1}$.

S7 Reference

- [1] W. Zhu, L. Zhang, P. Yang, C. Hu, Z. Luo, X. Chang, Z.-J. Zhao, J. Gong,]W Zhu,] L Zhang,] P Yang, C. Hu, Z. Luo, X. Chang, Z. Zhao, J. Gong, *Angewandte Chemie International Edition* **2018**, *57*, 11544–11548.
- [2] Y. Li, Y. Yan, Y. Li, H. Zhang, D. Li, D. Yang, *CrystEngComm* **2015**, *17*, 1833–1838.
- [3] G. Kresse, J. Furthmüller, *Comput Mater Sci* **1996**, *6*, 15–50.
- [4] G. Kresse, J. Hafner, *Phys Rev B* **1994**, *49*, 14251.
- [5] G. Kresse, D. Joubert, *Phys Rev B* **1999**, *59*, 1758.
- [6] K. Lee, É. D. Murray, L. Kong, B. I. Lundqvist, D. C. Langreth, *Phys Rev B Condens Matter Mater Phys* **2010**, *82*, 081101.
- [7] V. Wang, N. Xu, J. C. Liu, G. Tang, W. T. Geng, *Comput Phys Commun* **2021**, *267*, 108033.
- [8] E. A. Nagul, I. D. McKelvie, P. Worsfold, S. D. Kolev, *Anal Chim Acta* **2015**, *890*, 60–82.
- [9] H. Zhou, Z. Ma, G. Yang, X. Jiang, S. Duan, Y. Wu, M. Wang, L. Ni, L. Feng, G. Diao, *Batter Supercaps* **2024**, e202300563.

S8 Author contributions

Y.Z., R.L., S. Li, and C.S. conceived the project. R.L., S. Li, and C.S. supervised the project. Y.Z. carried out the material fabrication. Y.Z., F. F. D. G, and R.L. designed and performed electrocatalytic studies. R.L. Y.Z., and C.S. performed data analysis. S. Li. and Y. Z. performed XAS analyses. Z.C. and Y. Z. performed battery tests. K.C. and D.Z. performed (S)TEM analyses. N. M. and W. C. performed computational calculations. All authors co-wrote the manuscript.

6.5 Supporting information: Hydrogenation Catalysis by Hydrogen Spillover on Platinum-Functionalized Heterogeneous Boronic Acid-Polyoxometalates



Supporting Information

Hydrogenation Catalysis by Hydrogen Spillover on Platinum-Functionalized Heterogeneous Boronic Acid-Polyoxometalates

S. Li, Y. Ma, Y. Zhao, R. Liu, Y. Zhao, X. Dai, N. Ma, C. Streb*, X. Chen**

Supporting Information

Table of Contents

Table of Contents	1
S1 Experimental procedures	2
S2 X-ray crystallography.....	3
S3 Structure representations	5
S4 Characterization of the title POMs	6
S5 Characterization of Pt/Ce-POM	7
S6 Catalytic Hydrogenation of Olefins and Nitrobenzene derivates	11
S7 NMR data and NMR spectra of the catalytic products.....	15
S8 References	53
S9 Author contributions	54

S1 Experimental procedures

1.1 Materials and Instruments

The precursor $K_8H[P_2W_{15}(NbO_2)_3O_{59}] \cdot 12H_2O$ was synthesized according to the procedure described in the literature.^[1] All other reagents were obtained commercially and used without further purification. Pt Nanoparticles was purchased from Macklin (Particle size: 10 nm).

FT-IR analysis in ATR mode was performed by a Perkin Elmer Spectrum 400 FT-IR/FT-FIR Spectrometer equipped with ATR module in the range of 400–4000 cm^{-1} at room temperature.

Powder X-ray diffraction (pXRD) measurements were performed on a Panalytical X'Pert3 Powder diffractometer with graphite monochromatized Cu $K\alpha$ radiation at 298 K.

Elemental analyses for B, Na, P, Nb and W were determined with a PLASMASPEC (I) ICP atomic emission spectrometer. Elemental analyses for C and N were performed on a Perkin-Elmer 2400 elemental analyzer.

Thermal analyses were performed on a Netzsch 449C thermal analyzer. The sample was heated to 1000 °C with a heating rate of 5 °C/min, under an N_2 atmosphere.

In situ X-ray photoelectron spectra (in situ XPS) were recorded using an ESCALAB 250Xi spectrometer (Thermo Scientific) with a monochromatic Al anode $K\alpha$ radiation (1486.6 eV), and the charging effects were corrected by setting the C1s binding energy of the adventitious carbon to 284.8 eV. Prior to the measurement, the sample of **Pt/Ce-POM** was kept in a pretreatment chamber in high purity hydrogen at room temperature for 15 min. Then the sample was directly moved to the analysis chamber without being exposed to the environment.

Dynamic light scattering (DLS) measurements were conducted with a Malvern Zetasizer Nano ZS90 system at room temperature.

Scanning electron microscope (SEM) analysis was conducted on a Zeiss MERLIN Compact scanning electron microscope.

High-resolution transmission electron microscopy (HRTEM) analysis was conducted on a FEI Titan G260-300 transmission electron microscope equipped with a super energy-dispersive spectrometer (EDS). TEM samples were prepared by casting several drops of a sample solution onto copper-mesh TEM grid mounted with a holey carbon film.

Small-angle X-ray scattering (SAXS) measurement was performed on an Anton Paar SAXSACE system (Anton Paar, Graz, Austria) equipped with a Microsource x-ray source (Cu $K\alpha$ radiation, wavelength 0.15418 nm).

Nuclear Magnetic Resonance (NMR) spectra were recorded on a Bruker Advance 600 MHz spectrometer. A quartz NMR tube was used to avoid the background ^{11}B NMR signal from regular glass tube.

1.2 Synthesis of the four title compounds

Synthesis of $H_{27}[(4PyBOH)_3(O)_2][La_2(H_2O)_{12}(P_2W_{15}Nb_3O_{62})_4(4PyBOH)_4] \cdot 38H_2O$ (**La-POM**)

A sample of $K_8H[P_2W_{15}(NbO_2)_3O_{59}] \cdot 12H_2O$ (0.20 g, 0.04 mmol) was dissolved in 20 mL of deionized water at 80 °C. Solid $NaHSO_3$ (0.04 g, 0.38 mmol) was added with stirring until the yellow solution became colorless. Then, solid $LaCl_3 \cdot 6H_2O$ (0.025 g, 0.071 mmol) and 4-pyridinylboronic acid (0.01g, 0.081 mmol) were added respectively. The pH of the resulting solution was adjusted to 1.0-1.5 with hydrochloric acid (1 M), and further stirred at 80 °C for 40 min. After cooled to room temperature the reaction solution was filtrated and left for evaporation. Light yellow rectangular crystal products were obtained within two weeks. Yield: 0.11 g (60.8% based on $K_8Na_4[P_2W_{15}O_{59}(NbO_2)_3] \cdot 12H_2O$). Anal. Calcd (%): B 0.42, C 2.33, N 0.54, P 1.37, La 1.54, Nb 6.17, W 61.02; found B 0.43, C 2.35, N 0.55, P 1.39, La 1.52, Nb 6.16, W 61.00. IR (KBr disks): 1614 (w), 1084 (s), 945 (s), 893 (s), 714 (vs), 594 (m), 559 (m), 515 (m) 466 (m) cm^{-1} .

Synthesis of $H_{27}[(4PyBOH)_3(O)_2][Ce_2(H_2O)_{12}(P_2W_{15}Nb_3O_{62})_4(4PyBOH)_4] \cdot 38H_2O$ (**Ce-POM**)

A sample of $K_8H[P_2W_{15}(NbO_2)_3O_{59}] \cdot 12H_2O$ (0.20 g, 0.04 mmol) was dissolved in 20 mL of deionized water at 80 °C. Solid $NaHSO_3$ (0.04 g, 0.38 mmol) was added with stirring until the yellow solution became colorless. Then, solid $CeCl_3 \cdot 6H_2O$ (0.025 g, 0.071 mmol) and 4-pyridinylboronic acid (0.01 g, 0.081 mmol) were added respectively. The pH of the resulting solution was adjusted to 1.0-1.5 with hydrochloric acid (1 M), and further stirred at 80 °C for 40 min. After cooled to room temperature the reaction solution was filtrated and left for evaporation. Light yellow rectangular crystal products were obtained within two weeks. Yield: 0.12 g (67.4% based on $K_8Na_4[P_2W_{15}O_{59}(NbO_2)_3] \cdot 12H_2O$). Anal. Calcd (%): B 0.42, C 2.36, N 0.55, P 1.40, Ce 1.57, Nb 6.26, W 61.95; found B 0.43, C 2.34, N 0.56, P 1.39, Ce 1.57, Nb 6.25, W 61.96. IR (KBr disks): 1620 (w), 1085 (s), 951 (s), 900 (s), 752 (vs), 596 (m), 563 (m), 523 (m) 465 (m) cm^{-1} .

Synthesis of $H_{27}[(4\text{PyBOH})_3(\text{O})_2][\text{Pr}_2(\text{H}_2\text{O})_{12}(\text{P}_2\text{W}_{15}\text{Nb}_3\text{O}_{62})_4(4\text{PyBOH})_4] \cdot 42\text{H}_2\text{O}$ (**Pr-POM**)

A sample of $\text{K}_5\text{H}[\text{P}_2\text{W}_{15}(\text{NbO}_2)_3\text{O}_{59}] \cdot 12\text{H}_2\text{O}$ (0.20 g, 0.04 mmol) was dissolved in 20 mL of deionized water at 80 °C. Solid NaHSO_3 (0.04 g, 0.38 mmol) was added with stirring until the yellow solution became colorless. Then, solid $\text{PrCl}_3 \cdot 6\text{H}_2\text{O}$ (0.025 g, 0.07 mmol) and 4-pyridinylboronic acid (0.01 g, 0.081 mmol) were added respectively. The pH of the resulting solution was adjusted to 1.0-1.5 with hydrochloric acid (1 M), and further stirred at 80 °C for 40 min. After cooled to room temperature the reaction solution was filtrated and left for evaporation. Light green rectangular crystal products were obtained within two weeks. Yield: 0.13 g (73.7% based on $\text{K}_5\text{Na}_4[\text{P}_2\text{W}_{15}\text{O}_{59}(\text{NbO}_2)_3] \cdot 12\text{H}_2\text{O}$). Anal. Calcd (%): B 0.43, C 2.38, N 0.56, P 1.41, Pr 1.60, Nb 6.32, W 62.56; found B 0.43, C 2.37, N 0.55, P 1.42, Pr 1.60, Nb 6.32, W 62.56. IR (KBr disks): 1614 (w), 1085 (s), 945 (s), 893 (s), 719 (vs), 596 (m), 561 (m), 517 (m) 469 (m) cm^{-1} .

Synthesis of $H_{27}[(4\text{PyBOH})_3(\text{O})_2][\text{Eu}_2(\text{H}_2\text{O})_{12}(\text{P}_2\text{W}_{15}\text{Nb}_3\text{O}_{62})_4(4\text{PyBOH})_4] \cdot 52\text{H}_2\text{O} \cdot (\text{C}_5\text{NH}_4)_2$ (**Eu-POM**)

A sample of $\text{K}_5\text{H}[\text{P}_2\text{W}_{15}(\text{NbO}_2)_3\text{O}_{59}] \cdot 12\text{H}_2\text{O}$ (0.20 g, 0.04 mmol) was dissolved in 20 mL of deionized water at 80 °C. Solid NaHSO_3 (0.04 g, 0.38 mmol) was added with stirring until the yellow solution became colorless. Then, solid $\text{EuCl}_3 \cdot 6\text{H}_2\text{O}$ (0.025 g, 0.068 mmol) and 4-pyridinylboronic acid (0.01 g, 0.081 mmol) were added respectively. The pH of the resulting solution was adjusted to 1.0-1.5 with hydrochloric acid (1 M), and further stirred at 80 °C for 40 min. After cooled to room temperature the reaction solution was filtrated and left for evaporation. Light yellow rectangular crystal products were obtained within two weeks. Yield: 0.13 g (72.7% based on $\text{K}_5\text{Na}_4[\text{P}_2\text{W}_{15}\text{O}_{59}(\text{NbO}_2)_3] \cdot 12\text{H}_2\text{O}$). Anal. Calcd (%): B 0.42, C 3.02, N 0.71, P 1.39, Eu 1.7, Nb 6.24, W 61.70; found B 0.43, C 3.03, N 0.72, P 1.39, Eu 1.68, Nb 6.25, W 61.96. IR (KBr disks): 1612 (w), 1084 (s), 945 (s), 891 (s), 702 (vs), 592 (m), 561 (m), 515 (m) 463 (m) cm^{-1} .

Preparation of **Pt/Ce-POM**

A crystalline sample of **Ce-POM** (0.1 g) was ground and added to a vial containing 100 mL of anhydrous acetonitrile. The mixture was treated by ultrasonication in a 400 W ultrasonicator under controlled temperature at 25 °C for 6 h (the mixture can also be treated by ultrasonication for 2 h and then continuously stirred at 800 rpm at room temperature for more than 6 h). The resulting colloidal suspension was centrifuged at 1000 rpm for 10 min to remove large particles, giving a colloidal suspension of **Ce-POM**. Samples of **Ce-POM** colloids for PXRD and IR measurement were isolated by centrifugation at 10000 rpm for 10 min.

For Pt-deposition, the colloidal **Ce-POM** suspension was transferred into a photochemical reactor, to which 150 mL of anhydrous ethanol and 3 mL of 10 mM chloroplatinic acid in ethanol were added. The reactor was flushed with nitrogen. The mixture was illuminated for 1 h with a 175 W medium-pressure Hg light-source resulting in a suspension, from which pale-yellow **Pt/Ce-POM** was obtained by centrifugation. The material was washed with anhydrous ethanol and dried under vacuum. The Pt loading in **Pt/Ce-POM** was 5.6 wt% as determined by ICP-AES.

Note that the colloidal suspension of **Ce-POM** cannot be prepared in non-polar or weakly polar organic solvents (toluene, benzene, cyclohexane, DCM) but can be prepared in ethanol under the same conditions as described above. DLS measurements indicate that the average size of the colloidal suspension in ethanol is larger (108 nm, Figure S6) compared with acetonitrile. The suspension in ethanol is not stable for prolonged periods, and precipitation of particles is observed after storage for one month.

S2 X-ray crystallography

Single crystal XRD analysis of the four compounds was recorded on an Agilent SuperNova Dual diffractometer using graphite-monochromated Cu K α radiation, $\lambda = 1.54184 \text{ \AA}$. The linear absorption coefficients, scattering factors for the atoms, and anomalous dispersion corrections were taken from the International Tables for X-Ray Crystallography. Empirical absorption corrections were applied. Structures were solved using direct methods (SHELXT)^[2] and refined by full-matrix least-squares (SHELXL) interfaced with the program OLEX2^[3]. Anisotropic thermal parameters were used to refine all non-hydrogen atoms, with the exception for a few oxygen atoms. Those hydrogen atoms attached to lattice water molecules were not located. The lattice water molecules were estimated by thermogravimetry and only partial oxygen atoms of water molecules were observed by X-ray structure analysis. The crystal data and structure refinement results of the four compounds are summarized in Table S1. Further details on the crystal structure investigation scan be obtained free of charge from The Cambridge Crystallographic Data Centre via www.ccdc.cam.ac.uk/data_request/cif on quoting the depository number CCDC-2144085 (**La-POM**), CCDC-2144084 (**Ce-POM**), CCDC-2144086 (**Pr-POM**), CCDC-1849595 (**Eu-POM**).

6. Appendix

Table S1. Crystal data and structural refinements.^[a]

Compounds	La-POM	Ce-POM	Pr-POM	Eu-POM
Formula	C ₃₅ H ₃₅ B ₇ La ₂ N ₇ Nb ₁₂ O ₂₈₉ P ₃ W ₆₀	C ₃₅ H ₃₅ B ₇ Ce ₂ N ₇ Nb ₁₂ O ₂₈₉ P ₃ W ₆₀	C ₃₅ H ₃₅ B ₇ Pr ₂ N ₇ Nb ₁₂ O ₂₇₁ P ₃ W ₆₀	C ₄₅ H ₃₅ B ₇ Eu ₂ N ₉ Nb ₁₂ O ₂₇₅ P ₃ W ₆₀
Formula weight (g mol ⁻¹)	9038.91	8922.13	8816.91	8939.06
T (K)	150.00(10)	169.99(10)	150.00(10)	99.99(14)
Wavelength Cu-K (Å)	1.54184	1.54184	1.54184	1.54184
Crystal system	monoclinic	monoclinic	monoclinic	monoclinic
Space group	C2/c	C2/c	C2/c	C2/c
a (Å)	46.2391(5)	46.2429(7)	46.8714(11)	45.8935(7)
b (Å)	32.9546(4)	32.7978(7)	30.8127(8)	32.9588(6)
c (Å)	25.0473(4)	25.1038(5)	24.8607(11)	25.4069(5)
α (°)	90	90	90	90
β (°)	92.7370(10)	92.5950(16)	92.395(3)	92.672(2)
γ (°)	90	90	90	90
V (Å ³)	38123.3(9)	38035.1(13)	35873(2)	38388.6(12)
Z	8	8	8	8
D _{calc} (mg m ⁻³)	3.15	3.108	3.265	3.083
μ (mm ⁻¹)	38.116	38.261	40.655	38.409
F (000)	31520	30968	30640	31136
Crystal size (mm)	0.1 × 0.05 × 0.05	0.12 × 0.08 × 0.08	0.1 × 0.05 × 0.05	0.1 × 0.05 × 0.05
Goodness-of-fit on F ²	1.346	1.028	1.029	1.079
Final R indexes	R ₁ = 0.1147	R ₁ = 0.0830	R ₁ = 0.0812	R ₁ = 0.0885
[I ≥ 2σ(I)] ^[a]	wR ₂ = 0.3248	wR ₂ = 0.1998	wR ₂ = 0.2003	wR ₂ = 0.2550
R indexes ^[a]	R ₁ = 0.1299	R ₁ = 0.1259	R ₁ = 0.1281	R ₁ = 0.1394
(all data)	wR ₂ = 0.3554	wR ₂ = 0.2332	wR ₂ = 0.2398	wR ₂ = 0.2922

^[a] R₁ = Σ||F_o - |F_c|| / Σ|F_o|; wR₂ = [Σ[w(F_o² - F_c²)²] / Σ[w(F_o²)³]^{1/2}

S3 Structural representations

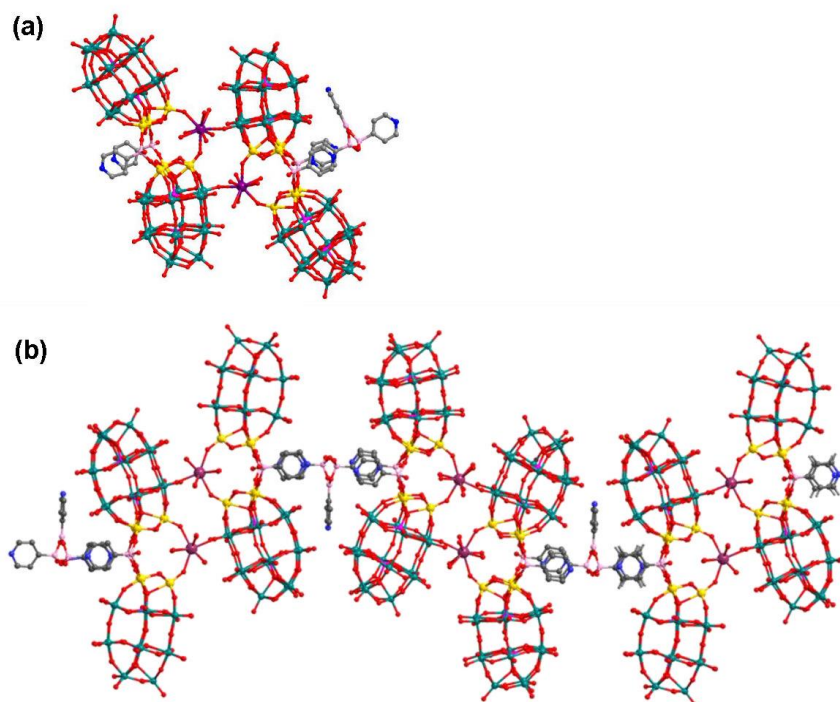
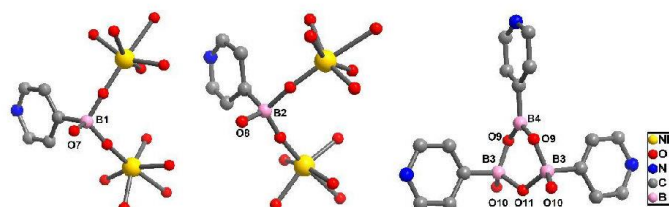


Figure S1. (a) The ball-and-stick representation of $[\text{Ce}(\text{H}_2\text{O})_6]_2[\text{P}_2\text{W}_{15}\text{Nb}_3\text{O}_{62}]_4[4\text{PyB}(\text{OH})_4]_4^{26-}$ and the stacking model in the 1D supramolecular assembly (b) (side view).

Table S2. Bond valence calculations of select O atoms.



Atom	Bond	Distance / Å	Bond Valence
O7	O7-B1	1.400	0.725
O8	O8-B2	1.500	0.706
O10	O10-B3	1.459	0.788
O11	O11-B3	1.542	1.260
	O11-B3	1.542	
O9	O9-B3	1.451	1.817
	O9-B4	1.376	

S4 Characterization of the title compounds

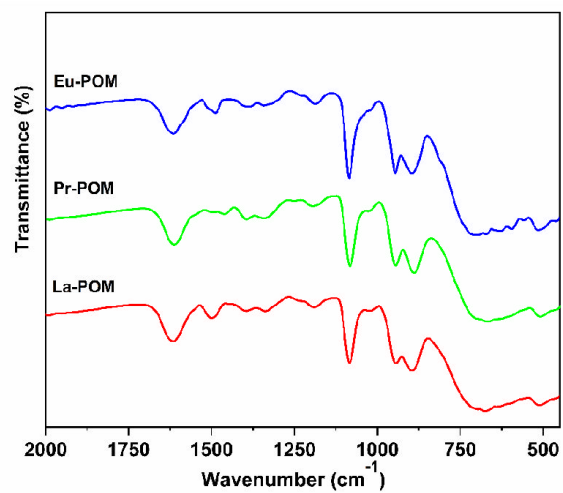
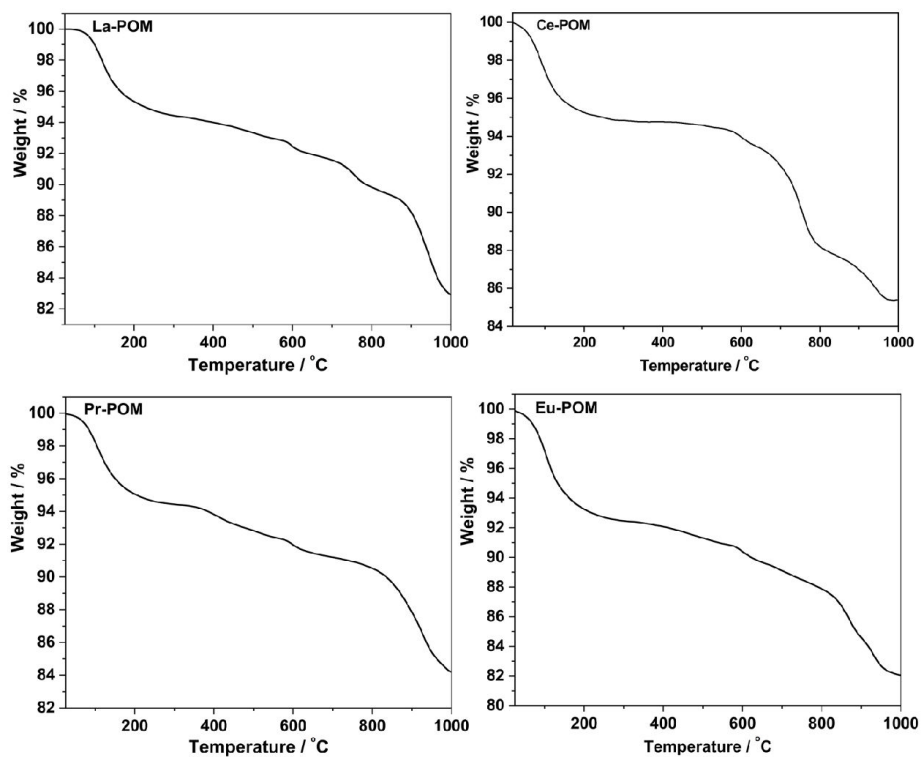


Figure S2. IR spectra of La-POM, Pr-POM and Eu-POM.

Figure S3. The TGA curves of the four compounds measured in N₂ from 25 °C to 1000 °C.

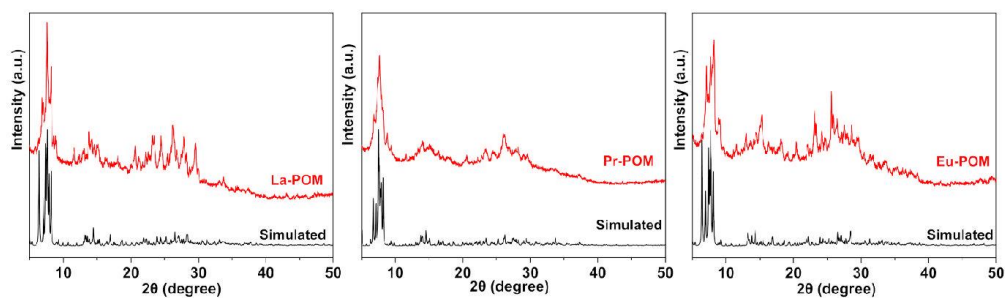


Figure S4. Simulated (black) and experimental (red) PXRD patterns of La-POM, Pr-POM and Eu-POM.

S5 Characterization of Pt/Ce-POM



Figure S5. Photograph of the Tyndall effect observed for the colloidal suspension of Ce-POM in acetonitrile after storage for one year.

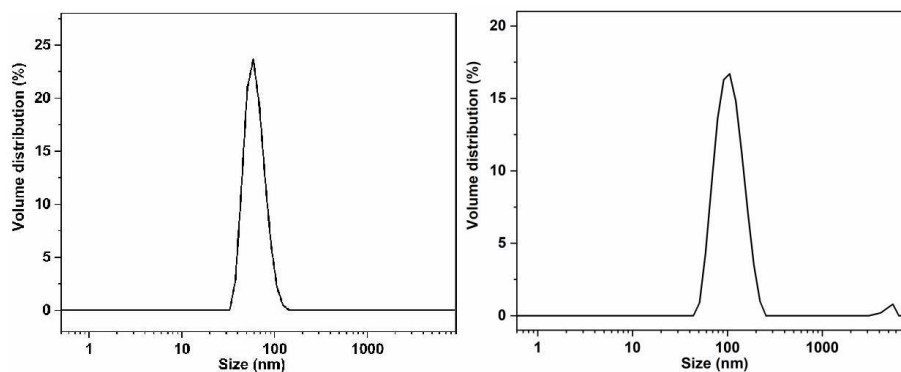


Figure S6. Dynamic light scattering (DLS) curve of the colloidal suspension of Ce-POM dispersed in acetonitrile (left) and ethanol (right).

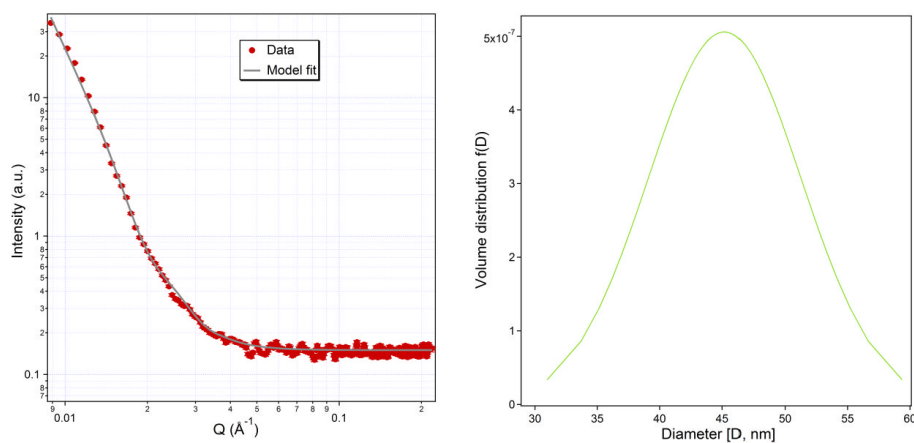


Figure S7. SAXS curve and the corresponding particle size distribution of the colloidal suspension of **Ce-POM** dispersed in acetonitrile.

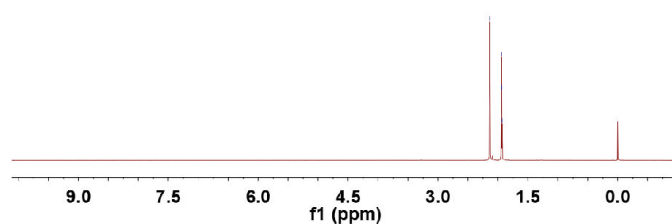


Figure S8. ^1H NMR spectrum of supramolecular assemblies of **Ce-POM** in CD_3CN . Only the signal of acetonitrile can be observed.

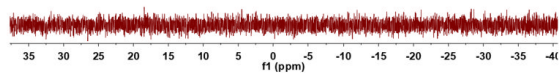


Figure S9. ^{31}P NMR spectrum of supramolecular assemblies of **Ce-POM** in CD_3CN .

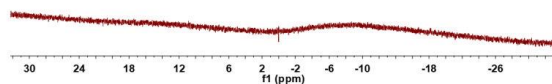


Figure S10. ^{11}B NMR spectrum of supramolecular assemblies of Ce-POM in CD_3CN .

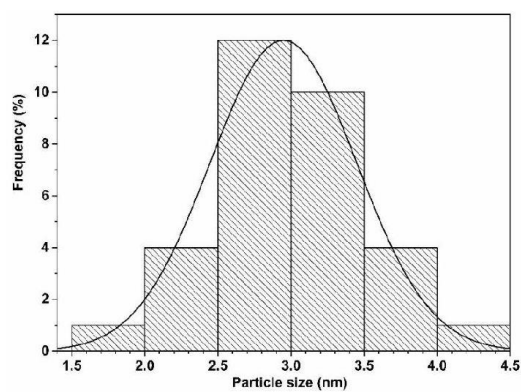


Figure S11. Particle size distribution of Pt nanoparticles for Pt/Ce-POM based on SEM image analysis.

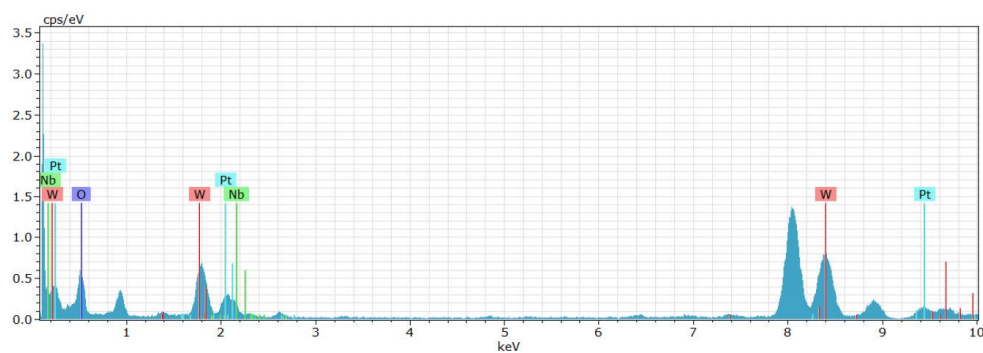


Figure S12. EDX spectra of Pt, W and Nb for Pt/Ce-POM.

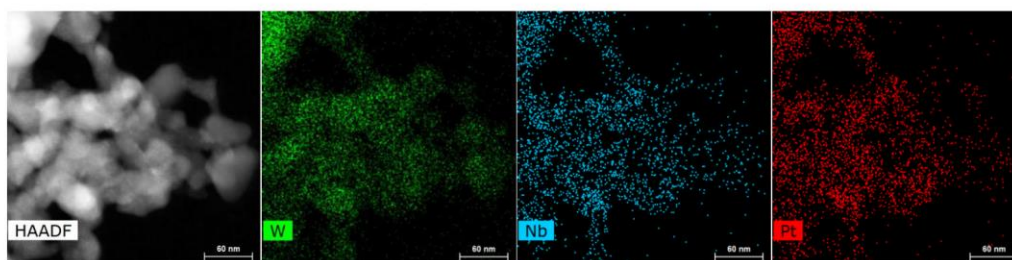


Figure S13. TEM / elemental mapping for **Pt/Ce-POM**.

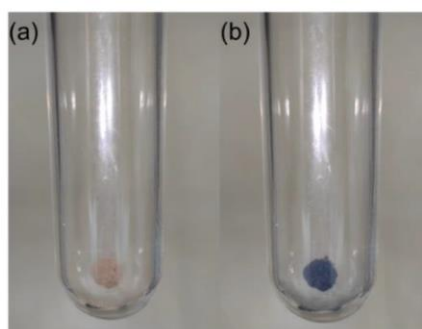


Figure S14. Color changes of **Pt/Ce-POM** before H₂ exposure (a) and when exposed to H₂ (b).

Table S3. Binding energy and percentage of various components for **Pt/Ce-POM** before and after exposure to H₂ as determined by XPS analysis.

Sample	Binding Energy (eV)	Relative Content (%) ^a
Before H ₂ exposure		
W ⁶⁺	35.95 (4f _{7/2}), 38.05 (4f _{5/2})	100
After H ₂ exposure		
W ⁶⁺	35.99 (4f _{7/2}), 38.09 (4f _{5/2})	84.1
W ⁵⁺	34.86 (4f _{7/2}), 36.90 (4f _{5/2})	15.9
Before H ₂ exposure		
Pt ⁰	71.72 (4f _{7/2}), 74.92 (4f _{5/2})	45.19
Pt ²⁺	73.26 (4f _{7/2}), 76.46 (4f _{5/2})	54.81
After H ₂ exposure		
Pt ⁰	71.69 (4f _{7/2}), 74.89 (4f _{5/2})	52.64
Pt ²⁺	73.10 (4f _{7/2}), 76.04 (4f _{5/2})	47.36
Before H ₂ exposure		
-OH	531.93 (1S)	16.71
-OH ₂	533.39 (1S)	10.17
O _{latt}	530.79 (1S)	73.12
After H ₂ exposure		
-OH	531.40 (1S)	24.27
-OH ₂	532.36 (1S)	15.15
O _{latt}	530.63 (1S)	59.22

^a Estimated based on the area of each pair of peaks

S6 Catalytic Hydrogenation of Olefins and Nitrobenzene derivatives

Hydrogenation of Olefins: Catalysts were introduced in a reaction tube with a stirrer bar and sealed with a silicone septum. After replacing the air with Hydrogen, the substrate (0.5 mmol) and solvent (2 mL) were introduced in the tube. The reaction was performed at room temperature (r.t.) under H₂ (1 bar). Yields were determined by GC-MS. Solid reaction products were recovered by centrifugation and filtering to remove the catalyst, followed by rotary evaporation to remove the solvent.

Table S4. Optimization of the conditions for hydrogenation of styrene^a.

Entry	Cat.	Solvent	Time (min)	Yield (%) ^b
1	1 mol% Pt/Ce-POM	Ethanol	15	> 99
2	1 mol% Pt/Ce-POM	Dichloromethane	15	trace
3	1 mol% Pt/Ce-POM	Toluene	15	25.7
4	1 mol% Pt/Ce-POM	Acetone	15	63.5
5	1 mol% Pt/Ce-POM	Acetonitrile	15	80.3
6	1 mol% Pt/Ce-POM	Tetrahydrofuran	15	92.6
7	0.5 mol% Pt/Ce-POM	Ethanol	15	> 99
8	0.25 mol% Pt/Ce-POM	Ethanol	15	31.5
9 ^c	0.5 mol% Pt/Ce-POM	Ethanol	15	-
10 ^d	-	Ethanol	15	-

^aReaction conditions: styrene (0.5 mmol), solvent (2 mL), r.t., H₂ (1 bar); ^byields were determined by GC-MS. ^cwithout H₂,

^dwithout catalyst.

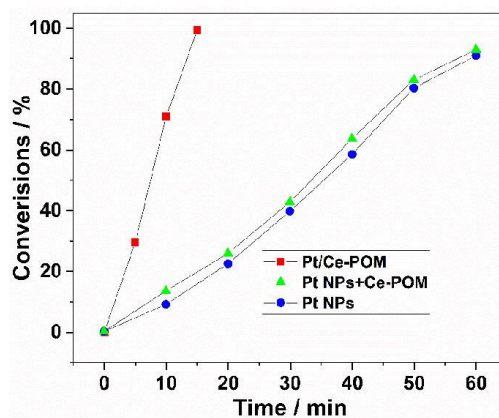


Figure S15. Styrene hydrogenation conversion over time for Pt/Ce-POM, commercial Pt NP references and the physical mixture of Pt NPs and Ce-POM. Reaction conditions: styrene (0.5 mmol), catalyst (0.5 mol% based on Pt), ethanol (2 mL), r.t., H₂ (1 bar).

6. Appendix

To gain insights into the role of **Ce-POM** in H₂ spillover and hydrogenation, we performed the following experiments. 150 mg **Pt/Ce-POM** and an equivalent amount (8.4 mg) of **Pt NPs** is dispersed in 2 mL ethanol in separate reaction vessels (A and B). The reaction vessels are sealed with silicone septums. Hydrogen was introduced and kept for 30 minutes, during which time the colloid in tube A turned deep blue, while tube B showed no color change. After replacing the excess hydrogen in the tubes with argon, 0.1 mmol styrene was injected into each reaction system. The dark blue colloid in A showed a decolorization (**Figure S16**), while tube B showed no color change. The catalysts were separated by centrifugation, the ethanol was removed under reduced pressure. The recovered products were then dissolved in deuterated chloroform for NMR measurements. ¹H NMR spectra indicated that about 10% styrene converted to phenylethylene in tube A, while no phenylethylene was observed in tube B (**Figure 3d** in the main text). These phenomena suggest that protons and electrons (formed by hydrogen spillover from the Pt to the **Ce-POM**) can directly lead to the reduction of styrene.

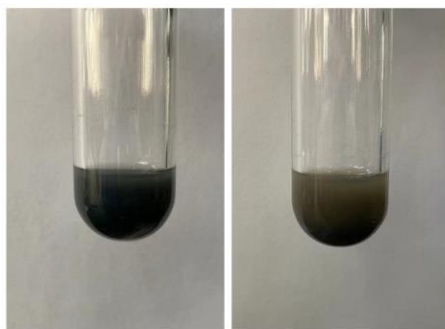


Figure S16. Color changes of **Pt/Ce-POM** (after hydrogen exposure) in ethanol before (left) and after (right) the injection of styrene.

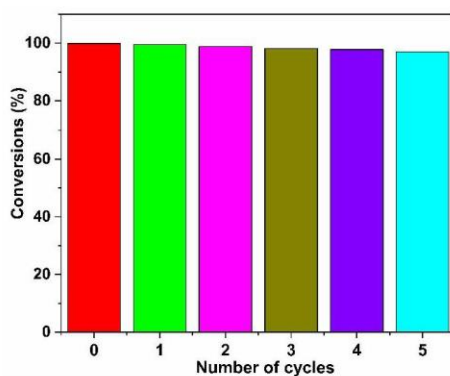


Figure S17. Recyclability of **Pt/Ce-POM** for the hydrogenation of styrene.

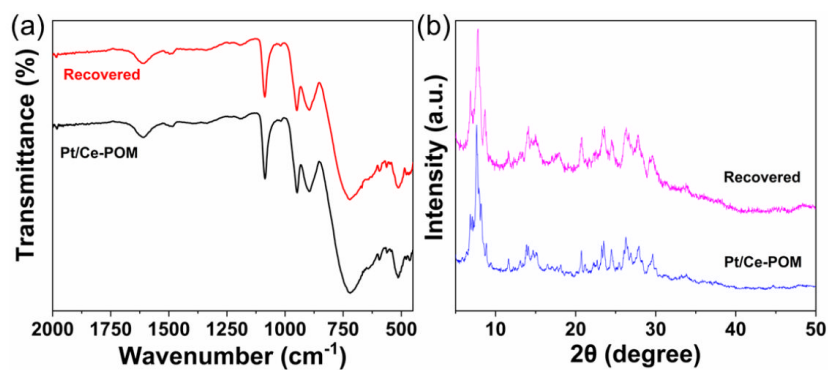


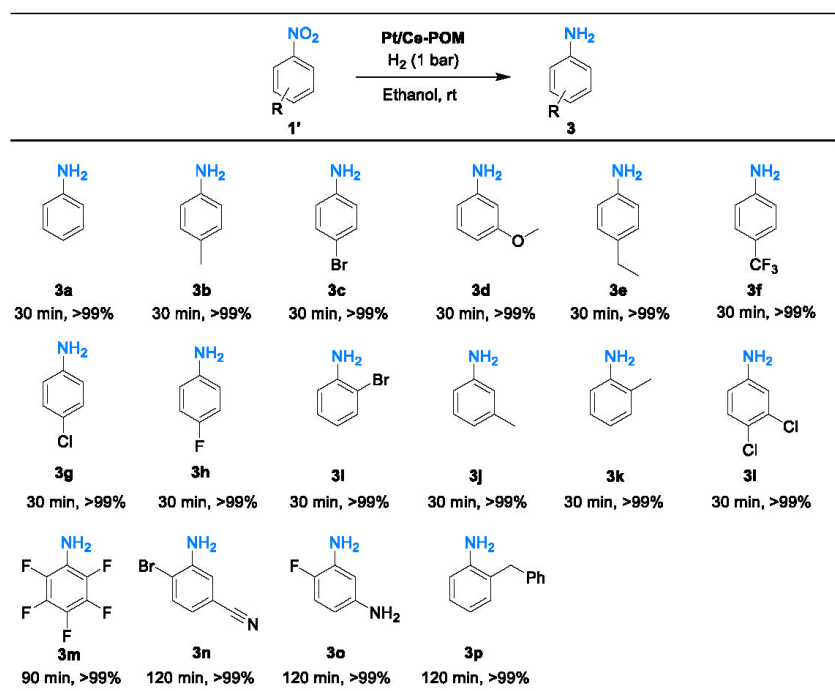
Figure S18. The IR spectra (a) and Powder XRD patterns (b) of Pt/Ce-POM before and after catalysis.

Table S5. Comparison of the catalytic activity of Pt/Ce-POM with other Pt-containing catalysts for the hydrogenation of styrene.

Catalyst	Reductant	T (°C)	t (h)	Conversion (%)	Reference
CNM/Pt	H ₂ (30 bar)	60	5	98	[4]
(Pd/bpy/Pt/bpy) ₅	H ₂ (1.2 bar)	34	0.6	99	[5]
KCC-1-PEI/Pt	H ₂ (10 bar)	r.t.	8	100	[6]
Pt@TNT	N ₂ H ₄ ·H ₂ O	90	0.75	99	[7]
Pt/15TS	H ₂ (40 bar)	60	1	100	[8]
Pt@Cu-MOC	H ₂ (1 bar)	40	2	98.8	[9]
Pd@Pt NPs	N ₂ H ₄ ·H ₂ O	60	0.5	95	[10]
Pt NPs	H ₂ (5 bar)	r.t.	2	90	[11]
Pt/Ce-POM	H ₂ (1 bar)	r.t.	0.25	99	This work

6. Appendix

Table S6. Hydrogenation of nitrobenzene derivatives ^a.

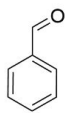
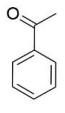
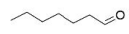


^a Reaction conditions: substrate (0.5 mmol), Pt/Ce-POM (1 mol%), ethanol (2 mL), r.t., H₂ (1 bar). Yields were determined by GC-MS.

Table S7. Comparison of the catalytic activity of Pt/Ce-POM with other Pt-containing catalysts for the hydrogenation of nitrobenzene.

Catalyst	Reductant	T (°C)	t (h)	Conversion (%)	Reference
Fe ₃ O ₄ @Pt NPs	NaBH ₄	r.t.	1	94	[12]
CNM/Pt	H ₂ (30 bar)	60	6	99	[4]
Pt(Co)@MIL-101	H ₂ (1 bar)	35	1	99	[13]
(Pd/bpy/Pt/bpy) ₅	H ₂ (1.2 bar)	34	2.6	99	[5]
Pt@Ir nanocomplexes	H ₂ (1 bar)	70	3	99	[14]
Pt@Y	H ₂ (20 bar)	100	6	100	[15]
MCPTH-Pt NPs	H ₂ (3.1 bar)	r.t.	0.5	97	[16]
KCC-1-PEI/Pt	H ₂ (10 bar)	r.t.	6	100	[6]
Pt/Ce-POM	H ₂ (1 bar)	r.t.	0.5	99	This work

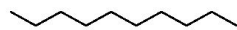
Table S8. Catalytic activity of **Pt/Ce-POM** for the hydrogenation of carbonyl derivative^a.

substrate	solvent	time	products	
			alcohol	acetals
	ethanol	10 min	- ^b	13%
	ethanol	30 min	-	36%
	ethanol	1 h	-	68%
	ethanol	2 h	6%	89%
	acetonitrile	5 h	-	-
	ethanol	10 min	-	-
	ethanol	30 min	-	-
	ethanol	1 h	12%	-
	acetonitrile	5 h	-	-
	ethanol	20 min	-	-
	ethanol	40 min	-	3%
	ethanol	1 h	-	5%
	ethanol	2 h	-	15%
	acetonitrile	5 h	-	-

^a Reaction conditions: substrate (0.5 mmol), **Pt/Ce-POM** (1 mol%), solvent (2 mL), r.t., H₂ (1 bar). Yields were determined by GC-MS. ^bNo product was detected.

S7 NMR data and NMR spectra of the catalytic products

NMR data



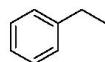
Decane (**2a**)^[17]

¹H NMR (600 MHz, CDCl₃) δ 1.38-1.19 (m, 16H), 0.89 (t, *J* = 7.1 Hz, 6H).
¹³C NMR (151 MHz, CDCl₃) δ 32.15, 29.89, 29.59, 22.90, 14.27.



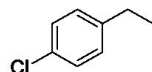
Cyclohexane (**2b**)^[18]

¹H NMR (600 MHz, CDCl₃) δ 1.43.
¹³C NMR (151 MHz, CDCl₃) δ 27.09.



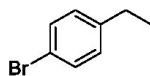
Ethylbenzene (**2c**)^[19]

¹H NMR (600 MHz, CDCl₃) δ 7.56-7.46 (m, 2H), 7.41 (dd, *J* = 18.4, 7.1 Hz, 3H), 2.88 (dd, *J* = 15.2, 7.6 Hz, 2H), 1.48 (t, *J* = 7.6 Hz, 3H).
¹³C NMR (151 MHz, CDCl₃) δ 144.35, 128.44, 127.98, 125.73, 29.04, 15.75.

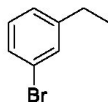


1-Chloro-4-Ethylbenzene (**2d**)^[20]

¹H NMR (600 MHz, CDCl₃) δ 7.34 (d, *J* = 8.4 Hz, 2H), 7.20 (d, *J* = 8.1 Hz, 2H), 2.71 (dd, *J* = 15.2, 7.6 Hz, 2H), 1.32 (t, *J* = 7.6 Hz, 3H).
¹³C NMR (151 MHz, CDCl₃) δ 142.68, 131.40, 129.29, 128.46, 28.36, 15.59.

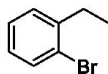
**4-Bromoethylbenzene (2e)**^[21]

¹H NMR (600 MHz, CDCl₃) δ 7.44 (d, *J* = 4.6 Hz, 2H), 7.11 (d, *J* = 3.1 Hz, 2H), 2.64 (d, *J* = 6.4 Hz, 2H), 1.33-1.20 (m, 3H).
¹³C NMR (151 MHz, CDCl₃) δ 143.25, 131.48, 129.78, 119.40, 28.45, 15.62.

**1-Bromo-3-ethylbenzene (2f)**^[22]

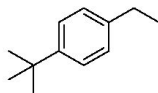
¹H NMR (600 MHz, CDCl₃) δ 7.39 (d, *J* = 0.6 Hz, 1H), 7.34 (d, *J* = 6.6 Hz, 1H), 7.22-7.11 (m, 2H), 2.72-2.58 (m, 2H), 1.26 (t, *J* = 8.9 Hz, 3H).

¹³C NMR (151 MHz, CDCl₃) δ 146.49, 130.98, 129.91, 128.76, 126.55, 122.48, 28.64, 15.41.

**2-Bromoethylbenzene (2g)**^[23]

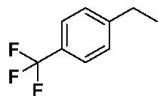
¹H NMR (600 MHz, CDCl₃) δ 7.54 (d, *J* = 8.0 Hz, 1H), 7.29-7.20 (m, 2H), 7.09-7.00 (m, 1H), 2.78 (q, *J* = 7.6 Hz, 2H), 1.25 (t, *J* = 7.6 Hz, 3H).

¹³C NMR (151 MHz, CDCl₃) δ 127.59, 127.45, 124.44, 29.50, 14.34.

**1-Tert-butyl-4-ethylbenzene (2h)**^[23]

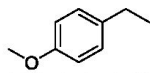
¹H NMR (600 MHz, CDCl₃) δ 7.34 (d, *J* = 8.3 Hz, 2H), 7.17 (d, *J* = 8.4 Hz, 2H), 2.65 (q, *J* = 7.6 Hz, 2H), 1.34 (s, 9H), 1.26 (t, *J* = 7.6 Hz, 3H).

¹³C NMR (151 MHz, CDCl₃) δ 148.48, 141.27, 127.62, 125.30, 34.45, 31.55, 28.38, 15.62.

**4-Ethylbenzotrifluoride (2i)**^[23]

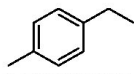
¹H NMR (600 MHz, CDCl₃) δ 7.54 (d, *J* = 8.1 Hz, 2H), 7.31 (d, *J* = 8.0 Hz, 2H), 2.71 (q, *J* = 7.6 Hz, 2H), 1.27 (t, *J* = 7.6 Hz, 3H).

¹³C NMR (151 MHz, CDCl₃) δ 148.42, 128.28, 125.34 (q, *J* = 3.8 Hz), 28.88, 15.40. ¹⁹F NMR (565 MHz, CDCl₃) δ -62.28.

**4-Ethylanisole (2j)**^[22]

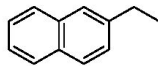
¹H NMR (600 MHz, CDCl₃) δ 7.20 (t, *J* = 8.2 Hz, 2H), 6.92 (t, *J* = 8.5 Hz, 2H), 3.89-3.82 (m, 3H), 2.68 (dd, *J* = 15.4, 7.7 Hz, 2H), 1.38-1.23 (m, 3H).

¹³C NMR (151 MHz, CDCl₃) δ 157.76, 136.34, 128.73, 113.78, 55.12, 28.05, 15.95.

**4-Ethyltoluene (2k)**^[22]

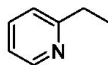
¹H NMR (600 MHz, CDCl₃) δ 7.20 (dd, *J* = 5.2, 3.5 Hz, 4H), 2.71 (dd, *J* = 5.3, 2.3 Hz, 2H), 2.42 (dd, *J* = 5.2, 3.7 Hz, 3H), 1.33 (dd, *J* = 7.6, 4.5 Hz, 3H).

¹³C NMR (151 MHz, CDCl₃) δ 141.28, 135.03, 129.12, 127.85, 28.59, 21.04, 15.90.

**2-Ethyl-naphthalene (2l)**^[22]

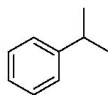
¹H NMR (600 MHz, CDCl₃) δ 7.82-7.72 (m, 3H), 7.62 (s, 1H), 7.47-7.37 (m, 2H), 7.34 (dd, *J* = 8.4, 1.4 Hz, 1H), 2.81 (q, *J* = 7.6 Hz, 2H), 1.32 (t, *J* = 7.6 Hz, 3H).

¹³C NMR (151 MHz, CDCl₃) δ 141.82, 133.87, 132.10, 127.94, 127.73, 127.56, 127.17, 125.93, 125.67, 125.12, 29.16, 15.65.

**2-Ethylpyridine (2m)**^[24]

¹H NMR (600 MHz, CDCl₃) δ 8.46 (s, 1H), 7.59-7.38 (m, 1H), 7.06 (dd, *J* = 40.0, 10.0 Hz, 2H), 2.77 (dd, *J* = 15.2, 7.6 Hz, 2H), 1.50-0.98 (m, 3H).

¹³C NMR (151 MHz, CDCl₃) δ 163.35, 149.02, 136.18, 121.87, 120.72, 31.26, 13.76.

**Cumene (2n)**^[23]

¹H NMR (600 MHz, CDCl₃) δ 7.47 – 7.27 (m, 5H), 3.16 – 2.94 (m, 1H), 1.45 – 1.33 (m, 6H).

¹³C NMR (151 MHz, CDCl₃) δ 148.95, 128.46, 126.54, 125.91, 34.29, 24.16.

**Cyclooctane (2p)**^[25]

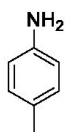
¹H NMR (600 MHz, CDCl₃) δ 1.53 (s, 16H).

¹³C NMR (151 MHz, CDCl₃) δ 26.84.

**Aniline (3a)**^[26]

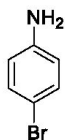
¹H NMR (600 MHz, CDCl₃) δ 7.18 (t, *J* = 6.9 Hz, 2H), 6.78 (t, *J* = 7.3 Hz, 1H), 6.70 (d, *J* = 7.8 Hz, 2H), 3.64 (s, 2H).

¹³C NMR (151 MHz, CDCl₃) δ 146.63, 129.33, 118.42, 115.14.

**p-Toluidine (3b)**^[26]

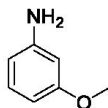
¹H NMR (600 MHz, CDCl₃) δ 6.98 (d, *J* = 7.0 Hz, 1H), 6.62 (d, *J* = 7.5 Hz, 1H), 3.51 (s, 1H), 2.26 (s, 2H).

¹³C NMR (151 MHz, CDCl₃) δ 143.83, 129.78, 127.90, 115.29, 20.48.

**4-Bromoaniline (3c)**^[26]

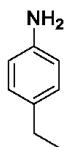
¹H NMR (600 MHz, CDCl₃) δ 7.57 (d, *J* = 8.6 Hz, 1H), 6.90 (d, *J* = 8.6 Hz, 1H), 4.00 (s, 1H).

¹³C NMR (151 MHz, CDCl₃) δ 145.55, 132.14, 116.83, 110.32.

**m-Anisidine (3d)**^[26]

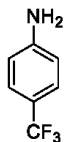
¹H NMR (600 MHz, CDCl₃) δ 7.11 (d, *J* = 8.0 Hz, 1H), 6.38 (t, *J* = 8.3 Hz, 1H), 6.32 (d, *J* = 7.9 Hz, 1H), 6.27 (s, 1H), 3.79 (s, 3H), 3.74 (s, 2H).

¹³C NMR (151 MHz, CDCl₃) δ 160.71, 148.10, 130.10, 107.90, 103.81, 100.97, 54.99.

**4-Ethylaniline (3e)**^[27]

¹H NMR (600 MHz, CDCl₃) δ 7.10 (d, *J* = 6.8 Hz, 1H), 6.71 (d, *J* = 4.4 Hz, 1H), 3.61 (s, 1H), 2.66 (dd, *J* = 14.3, 6.9 Hz, 1H), 1.39 – 1.23 (m, 2H).

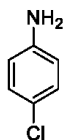
¹³C NMR (151 MHz, CDCl₃) δ 144.10, 134.29, 128.54, 115.25, 27.96, 15.95.

**4-Aminobenzotrifluoride (3f)**^[28]

¹H NMR (600 MHz, CDCl₃) δ 7.39 (d, *J* = 8.5 Hz, 2H), 6.67 (d, *J* = 8.4 Hz, 2H), 3.93 (s, 2H).

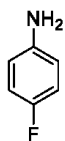
¹³C NMR (151 MHz, CDCl₃) δ 149.54, 126.80 (q, *J* = 3.8 Hz), 125.88, 124.10, 114.29.

¹⁹F NMR (565 MHz, CDCl₃) δ -61.13 (s).

**4-Chloroaniline (3g)**^[25]

¹H NMR (600 MHz, CDCl₃) δ 7.10 (d, *J* = 8.7 Hz, 2H), 6.60 (d, *J* = 8.7 Hz, 2H), 3.64 (s, 2H).

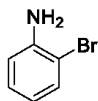
¹³C NMR (151 MHz, CDCl₃) δ 145.07, 129.23, 123.27, 116.41.

**4-Fluoroaniline (3h)**^[25]

¹H NMR (600 MHz, CDCl₃) δ 6.87 (t, *J* = 8.7 Hz, 2H), 6.61 (dd, *J* = 8.9, 4.5 Hz, 2H), 3.51 (s, 2H).

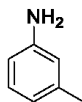
¹³C NMR (151 MHz, CDCl₃) δ 156.43 (d, *J* = 235.4 Hz), 142.53, 116.10 (d, *J* = 7.6 Hz), 115.69 (d, *J* = 22.4 Hz).

¹⁹F NMR (565 MHz, CDCl₃) δ -126.87 (s).

**2-Bromoaniline (3i)**^[29]

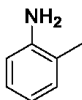
¹H NMR (600 MHz, CDCl₃) δ 7.51 – 7.36 (m, 1H), 7.13 (t, *J* = 8.9 Hz, 1H), 6.77 (d, *J* = 9.4 Hz, 1H), 6.65 (t, *J* = 9.1 Hz, 1H), 4.09 (s, 2H).

¹³C NMR (151 MHz, CDCl₃) δ 144.16, 132.63, 128.42, 119.46, 115.86, 109.36.

***m*-Toluidine (3j)**^[25]

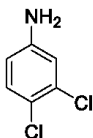
¹H NMR (600 MHz, CDCl₃) δ 7.11 (dd, *J* = 12.5, 7.6 Hz, 1H), 6.65 (d, *J* = 5.8 Hz, 1H), 6.55 (d, *J* = 12.5 Hz, 2H), 3.63 (s, 2H), 2.33 (s, 3H).

¹³C NMR (151 MHz, CDCl₃) δ 146.50, 139.14, 129.21, 119.45, 115.96, 112.29, 21.48.

**o-Toluidine (3k)**^[25]

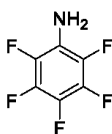
¹H NMR (600 MHz, CDCl₃) δ 7.16 (dd, *J* = 14.3, 6.4 Hz, 2H), 6.91 – 6.79 (m, 1H), 6.81 – 6.65 (m, 1H), 3.65 (s, 2H), 2.25 (s, 3H).

¹³C NMR (151 MHz, CDCl₃) δ 144.69, 130.47, 126.98, 122.32, 118.59, 114.93, 17.43.

**3,4-dichloroaniline (3l)**^[25]

¹H NMR (600 MHz, CDCl₃) δ 7.17 (d, *J* = 8.6 Hz, 1H), 6.75 (d, *J* = 2.7 Hz, 1H), 6.50 (dd, *J* = 8.6, 2.7 Hz, 1H), 3.72 (s, 2H).

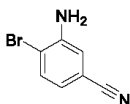
¹³C NMR (151 MHz, CDCl₃) δ 146.12, 132.80, 130.82, 121.17, 116.50, 114.71.

**2,3,4,5,6-pentafluoroaniline (3m)**^[30]

¹H NMR (600 MHz, CDCl₃) δ 3.80 (s, 2H).

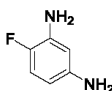
¹³C NMR (151 MHz, CDCl₃) δ 138.98 (tt, *J* = 13.7, 4.2 Hz), 138.20 – 136.79 (m), 136.55 – 135.28 (m), 134.34 (tt, *J* = 13.7, 4.1 Hz), 133.63 – 131.84 (m), 122.04 (td, *J* = 14.5, 3.2 Hz).

¹⁹F NMR (565 MHz, CDCl₃) δ -161.98 – -162.45 (m, 1F), -164.87 (t, *J* = 19.2 Hz, 2F), -172.72 – -173.55 (m, 1F).

**3-Amino-4-Bromobenzonitrile (3n)**^[31]

¹H NMR (600 MHz, CDCl₃) δ 7.37 (d, *J* = 8.7 Hz, 1H), 6.91 (d, *J* = 2.8 Hz, 1H), 6.73 (dd, *J* = 8.7, 2.8 Hz, 1H), 3.91 (s, 2H).

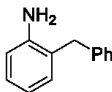
¹³C NMR (151 MHz, CDCl₃) δ 146.05, 133.79, 120.61, 119.59, 117.54, 116.02, 112.35.

**4-Fluorobenzene-1,3-Diamine (3o)**^[32]

¹H NMR (600 MHz, CDCl₃) δ 6.76 (dd, *J* = 10.8, 8.6 Hz, 1H), 6.09 (dd, *J* = 7.6, 2.7 Hz, 1H), 6.03 – 5.95 (m, 1H), 3.63 (s, 2H), 3.43 (s, 2H).

¹³C NMR (151 MHz, CDCl₃) δ 146.68, 145.17, 143.06 (d, *J* = 2.0 Hz), 134.95 (d, *J* = 14.0 Hz), 115.63 (d, *J* = 19.5 Hz), 104.45 (dd, *J* = 199.3, 4.6 Hz).

¹⁹F NMR (565 MHz, CDCl₃) δ -147.91 (s).

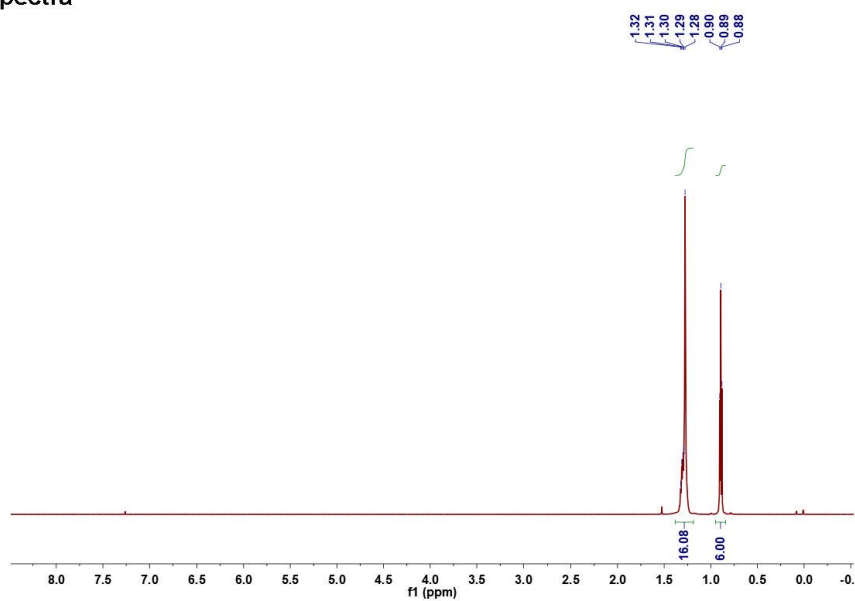
**2-Benzylaniline (3p)**^[33]

¹H NMR (600 MHz, CDCl₃) δ 7.30 (t, *J* = 7.5 Hz, 2H), 7.21 (dd, *J* = 15.6, 7.5 Hz, 3H), 7.13 – 7.04 (m, 2H), 6.78 (t, *J* = 7.4 Hz, 1H), 6.69 (d, *J* = 7.9 Hz, 1H), 3.92 (s, 2H), 3.51 (s, 2H).

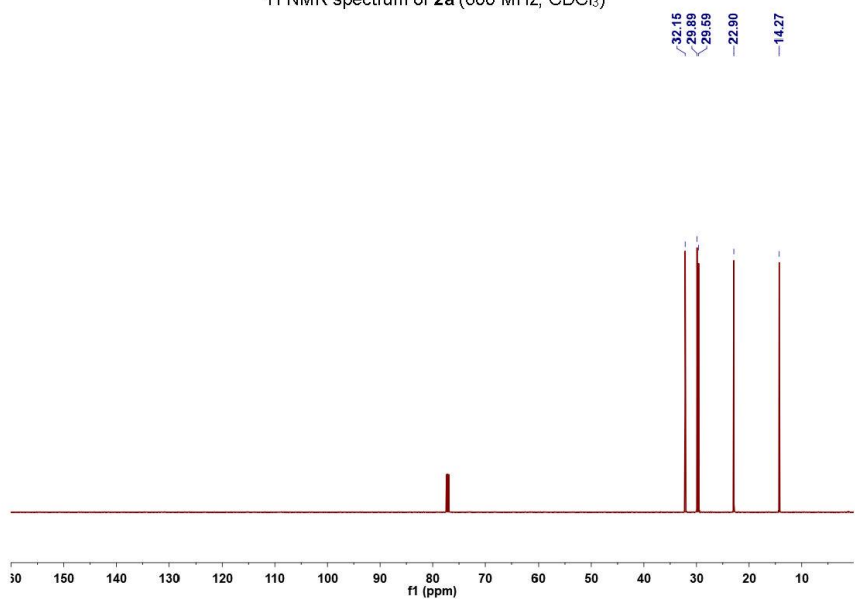
¹³C NMR (151 MHz, CDCl₃) δ 144.84, 139.52, 131.05, 128.81, 128.64, 127.82, 126.51, 125.23, 118.91, 116.06, 38.22.

6. Appendix

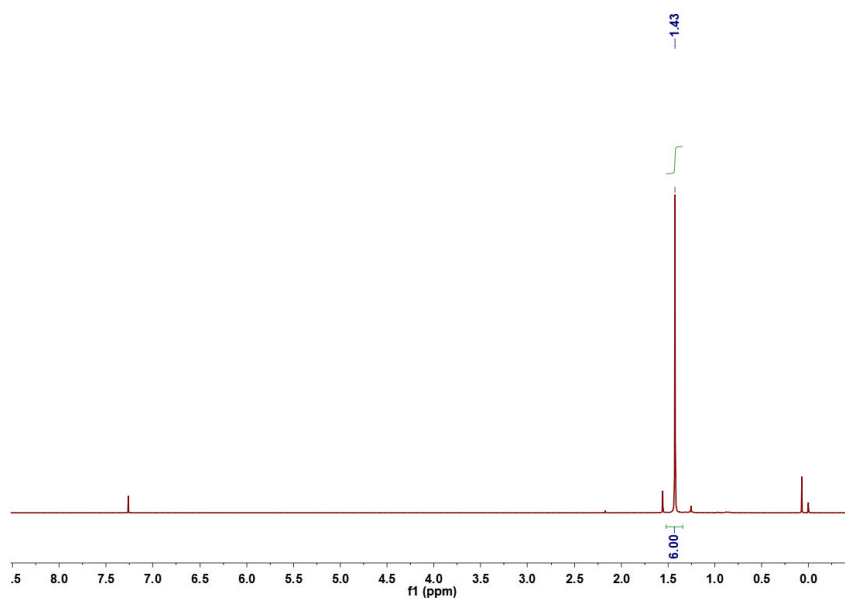
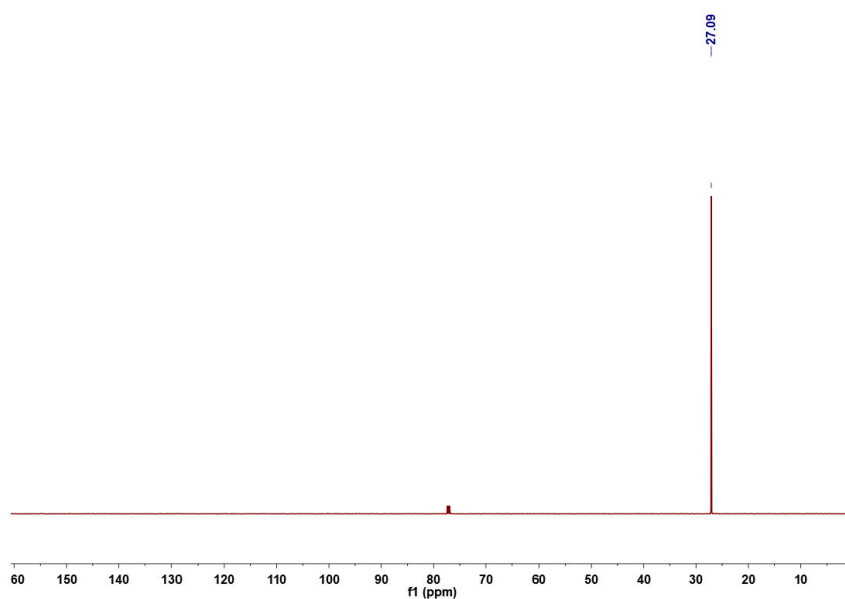
NMR spectra



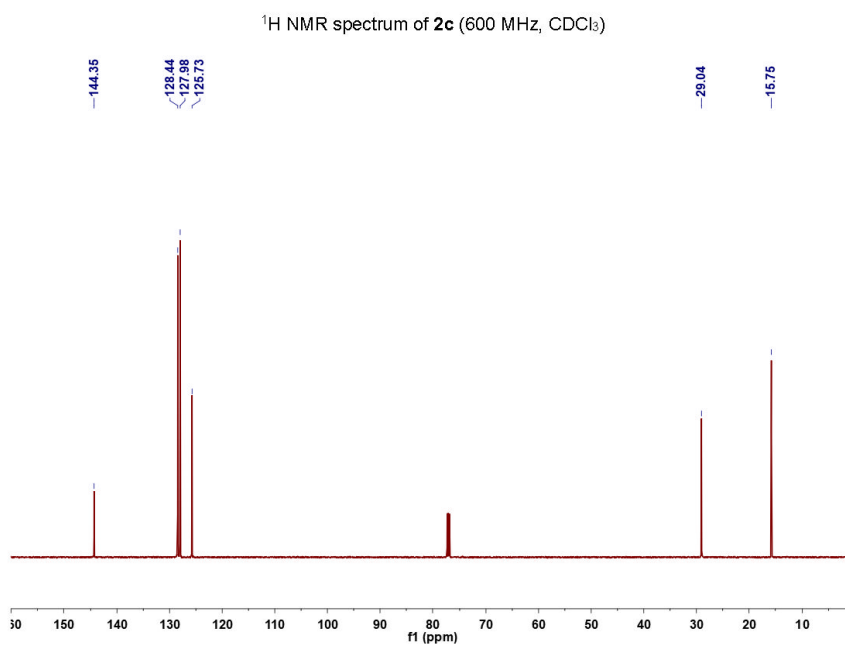
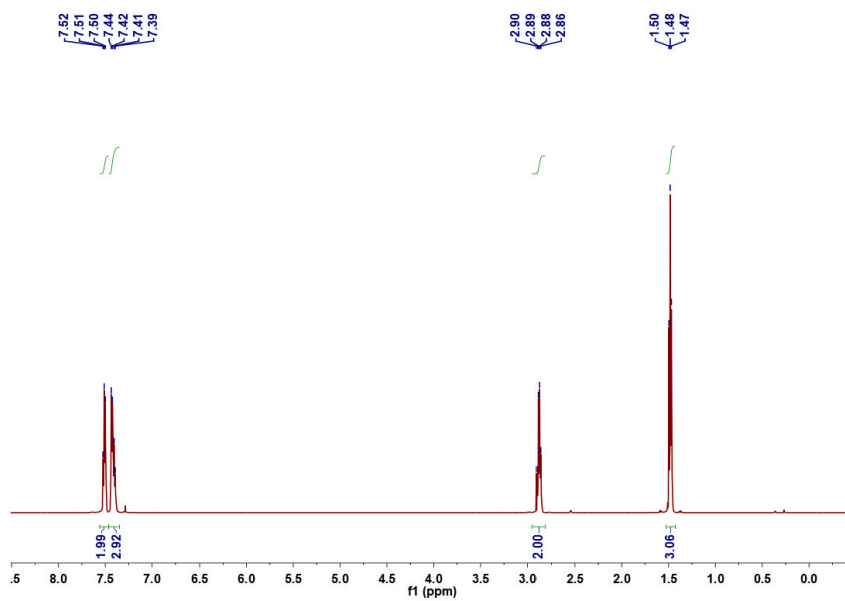
¹H NMR spectrum of 2a (600 MHz, CDCl₃)

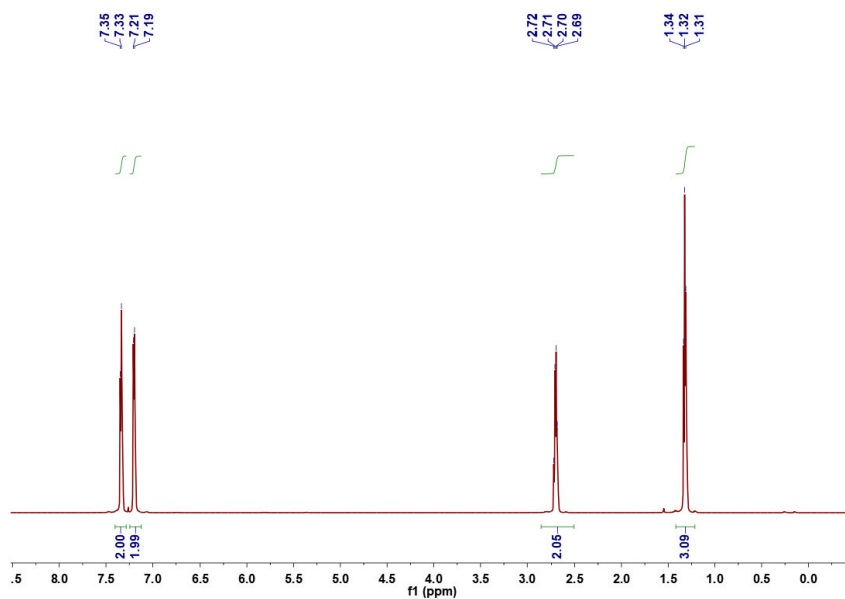
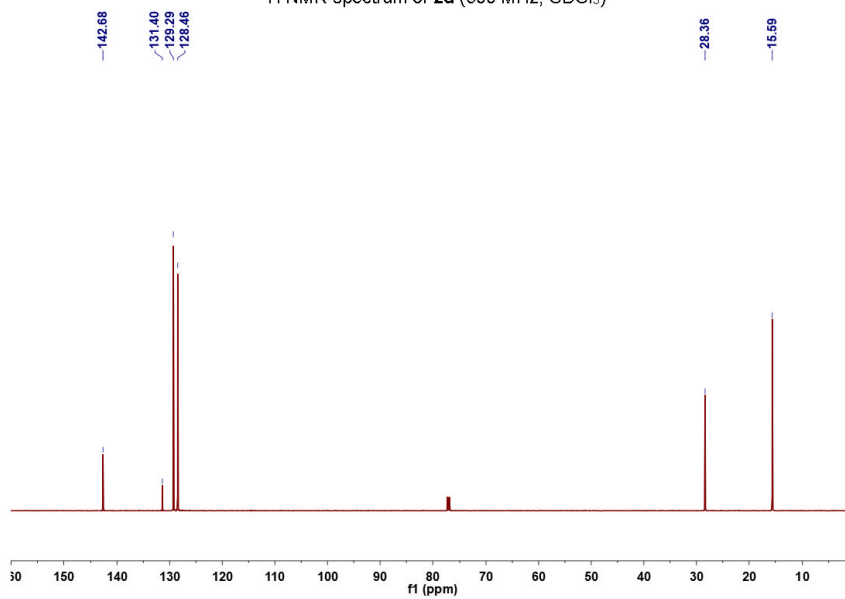


¹³C NMR spectrum of 2a (151 MHz, CDCl₃)

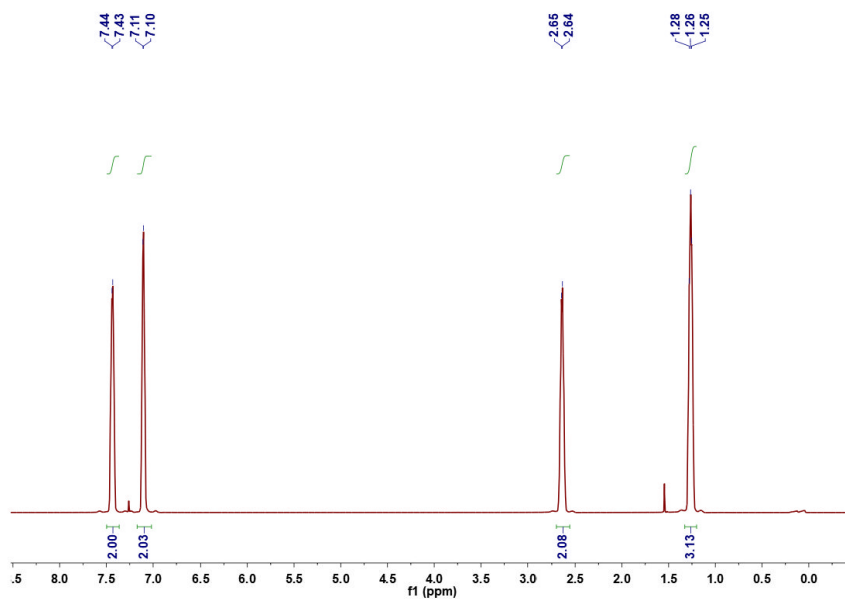
 ^1H NMR spectrum of **2b** (600 MHz, CDCl_3) ^{13}C NMR spectrum of **2b** (151 MHz, CDCl_3)

6. Appendix

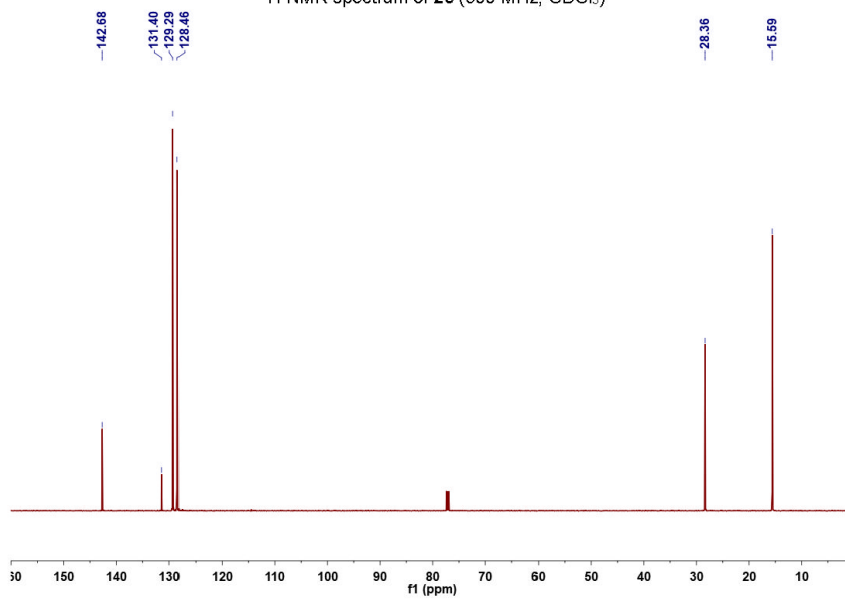


¹H NMR spectrum of 2d (600 MHz, CDCl₃)¹³C NMR spectrum of 2d (151 MHz, CDCl₃)

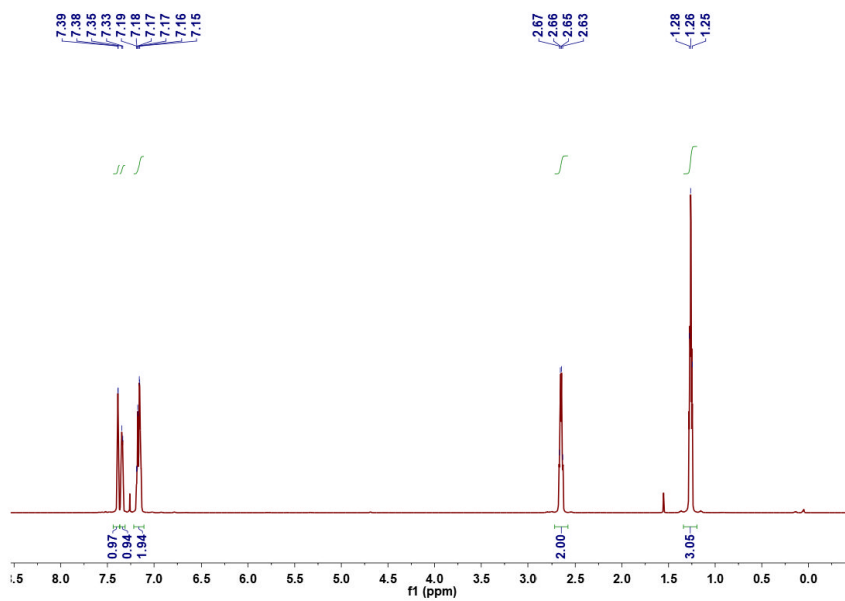
6. Appendix



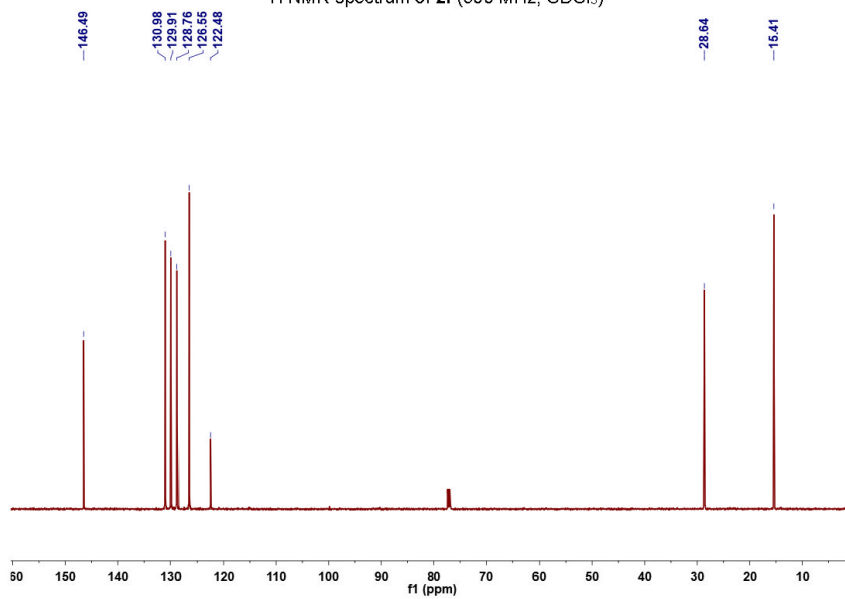
¹H NMR spectrum of 2e (600 MHz, CDCl₃)



¹³C NMR spectrum of 2e (151 MHz, CDCl₃)

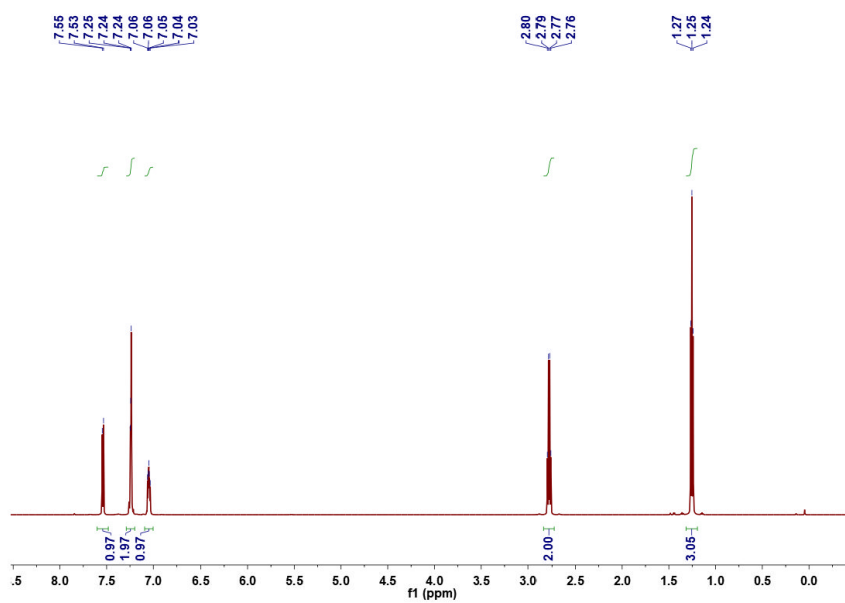


¹H NMR spectrum of 2f (600 MHz, CDCl₃)

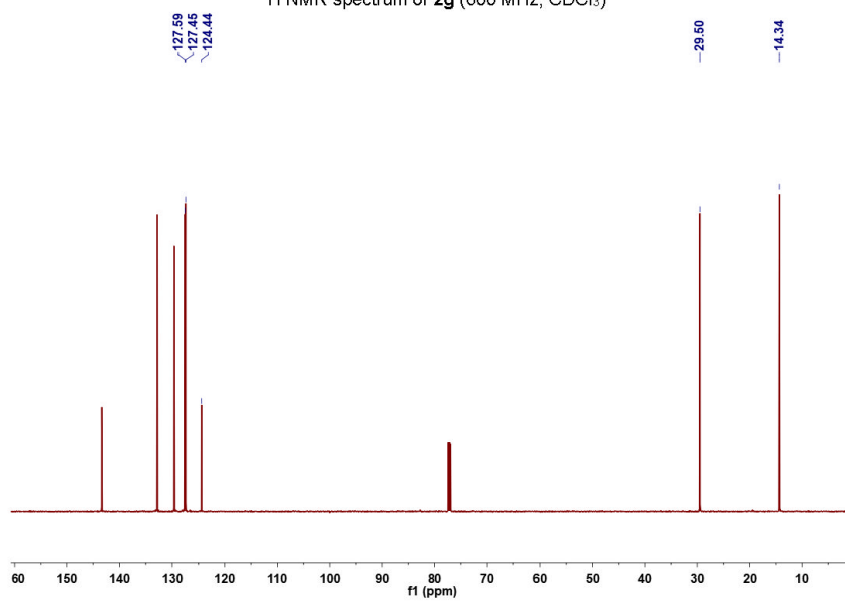


¹³C NMR spectrum of 2f (151 MHz, CDCl₃)

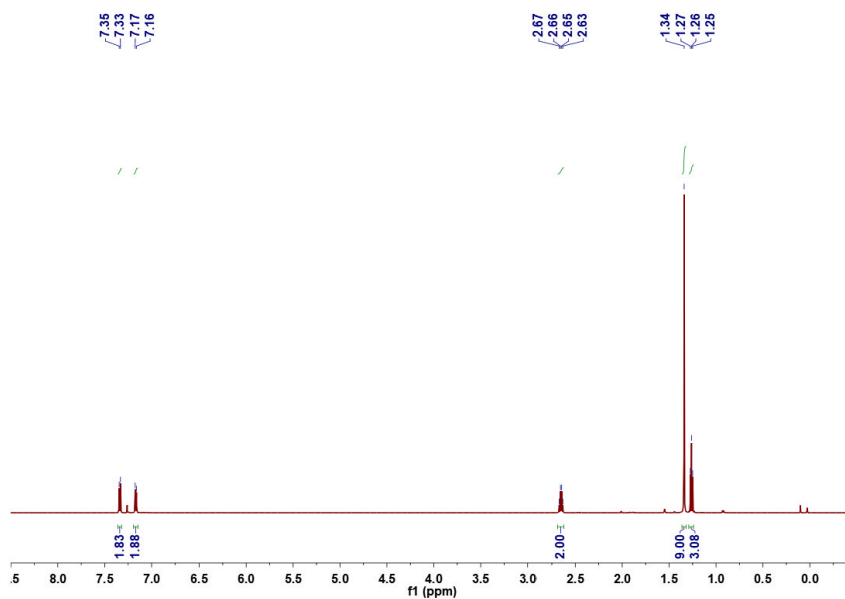
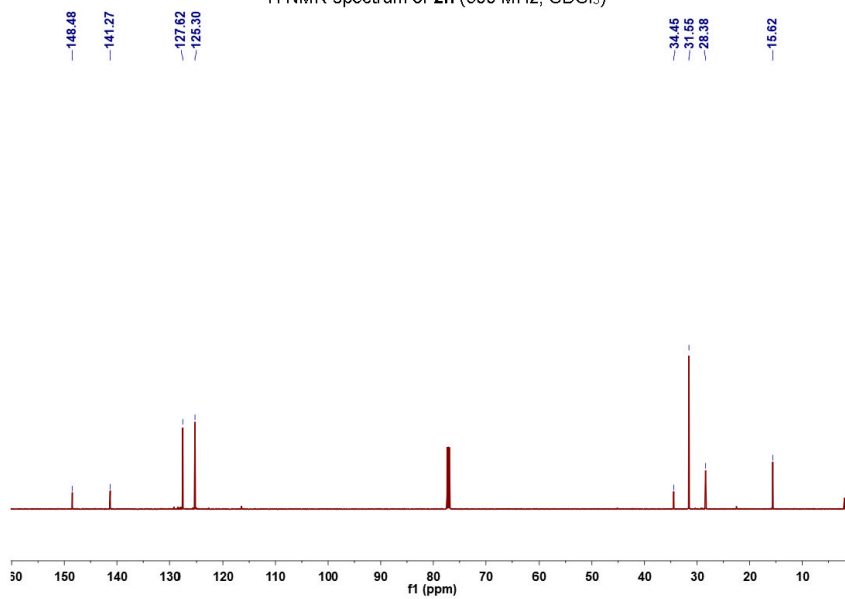
6. Appendix



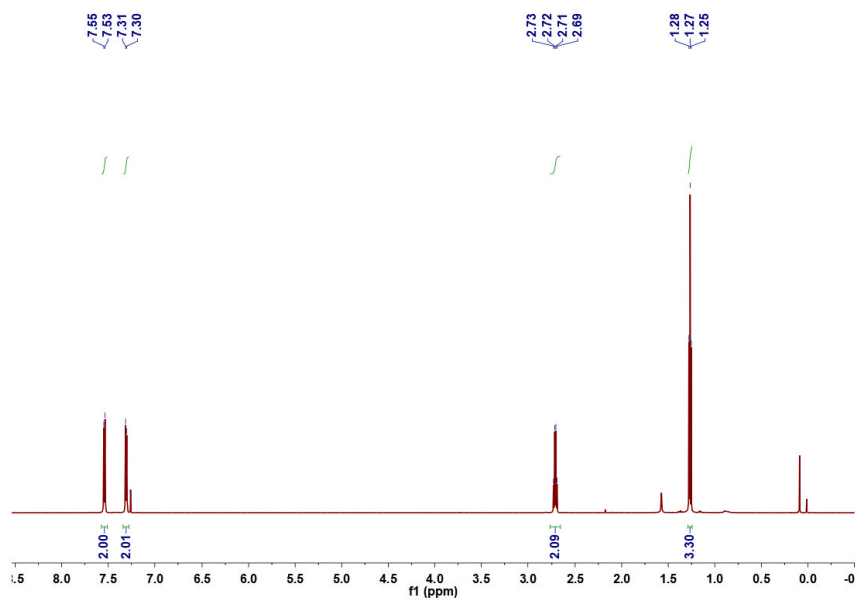
¹H NMR spectrum of 2g (600 MHz, CDCl₃)



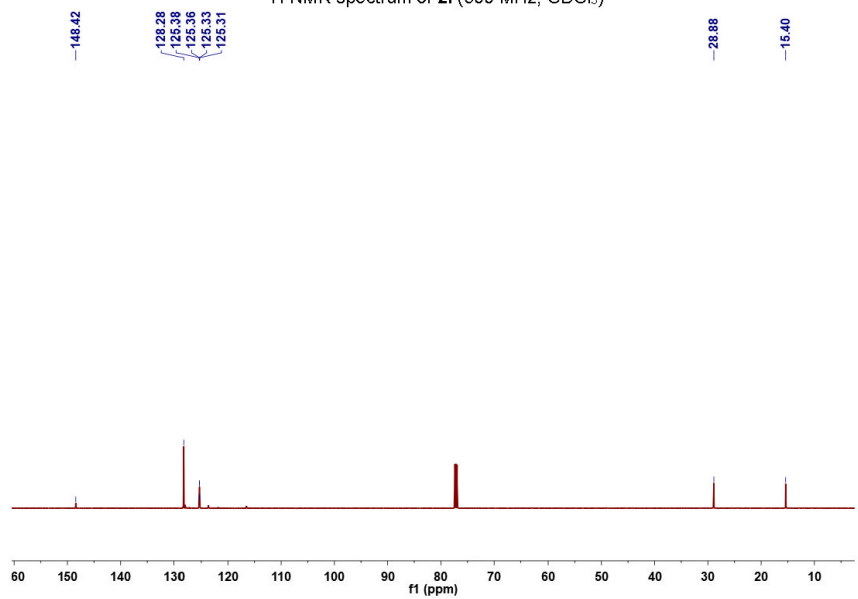
¹³C NMR spectrum of 2g (151 MHz, CDCl₃)

¹H NMR spectrum of 2h (600 MHz, CDCl₃)¹³C NMR spectrum of 2h (151 MHz, CDCl₃)

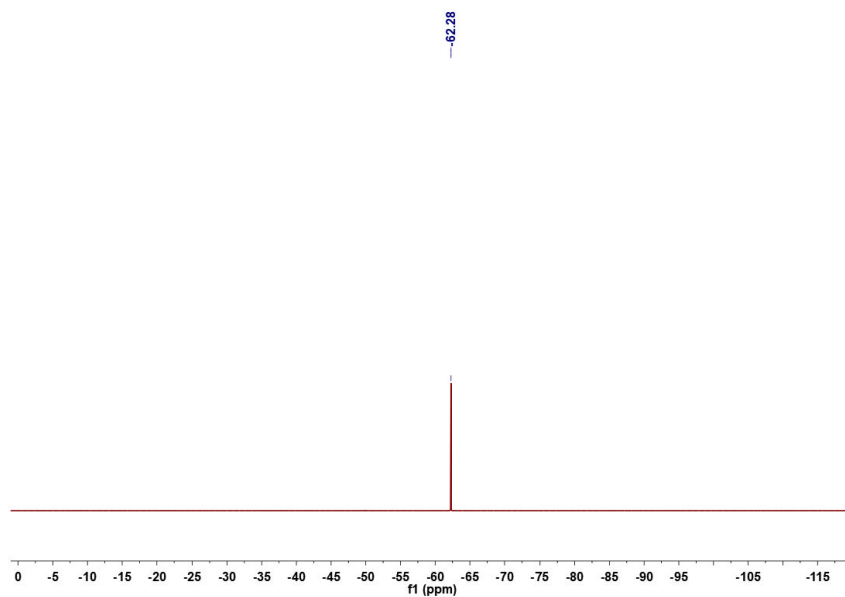
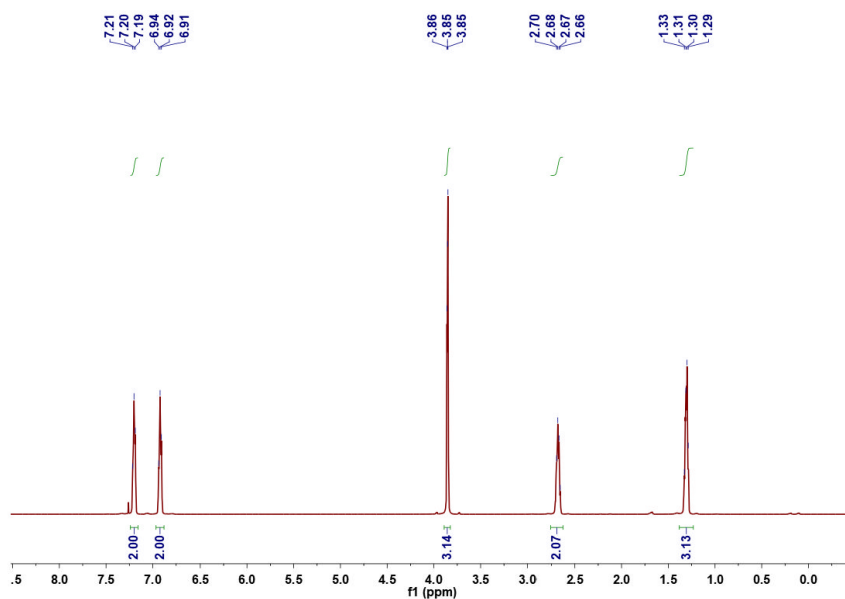
6. Appendix



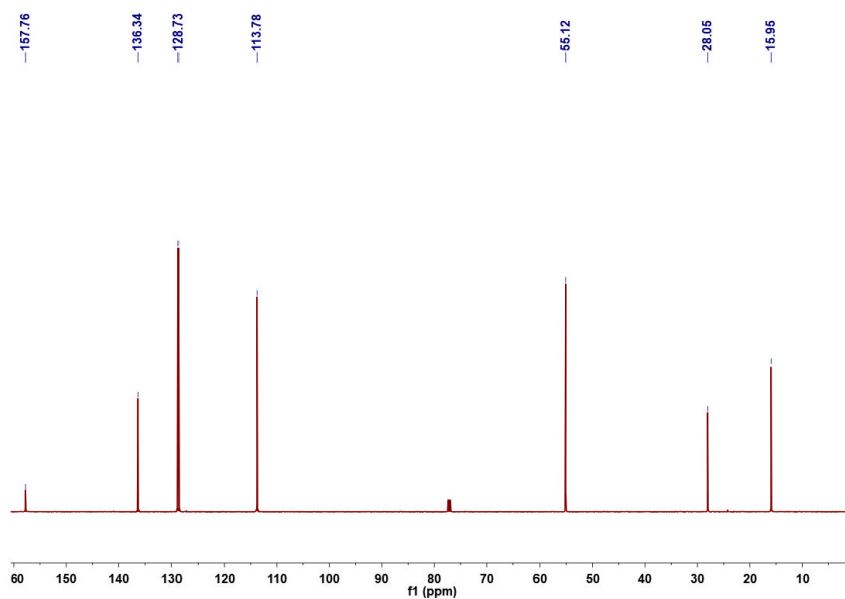
¹H NMR spectrum of 2i (600 MHz, CDCl₃)



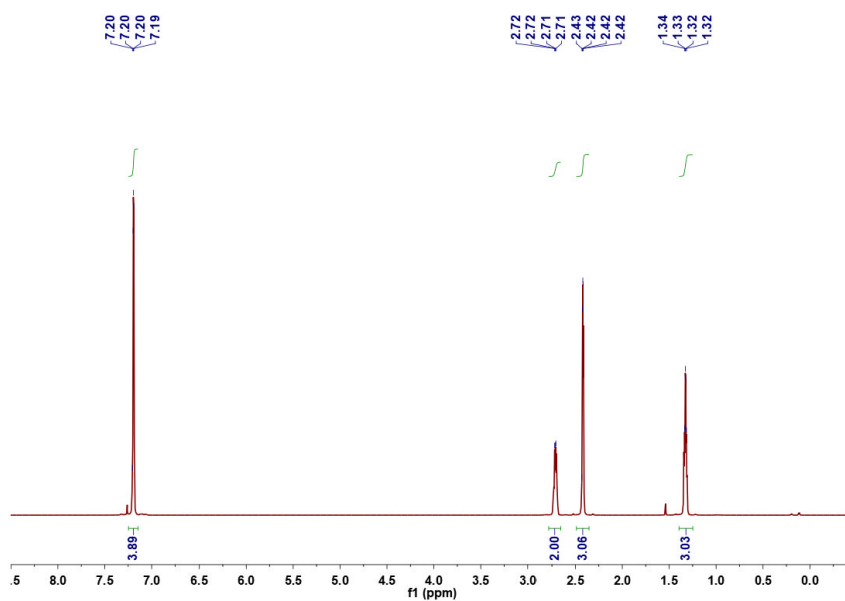
¹³C NMR spectrum of 2i (151 MHz, CDCl₃)

 ^{19}F NMR spectrum of **2i** (565 MHz, CDCl_3) ^1H NMR spectrum of **2j** (600 MHz, CDCl_3)

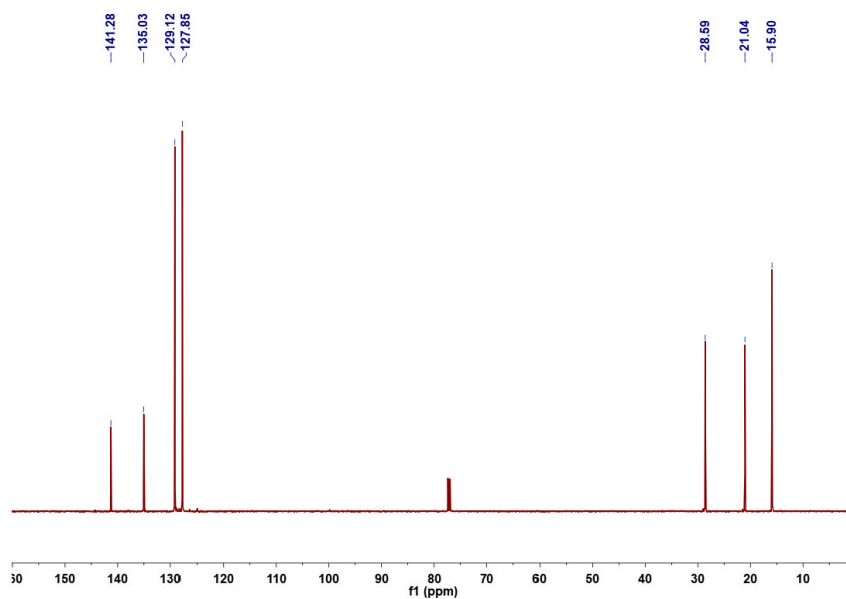
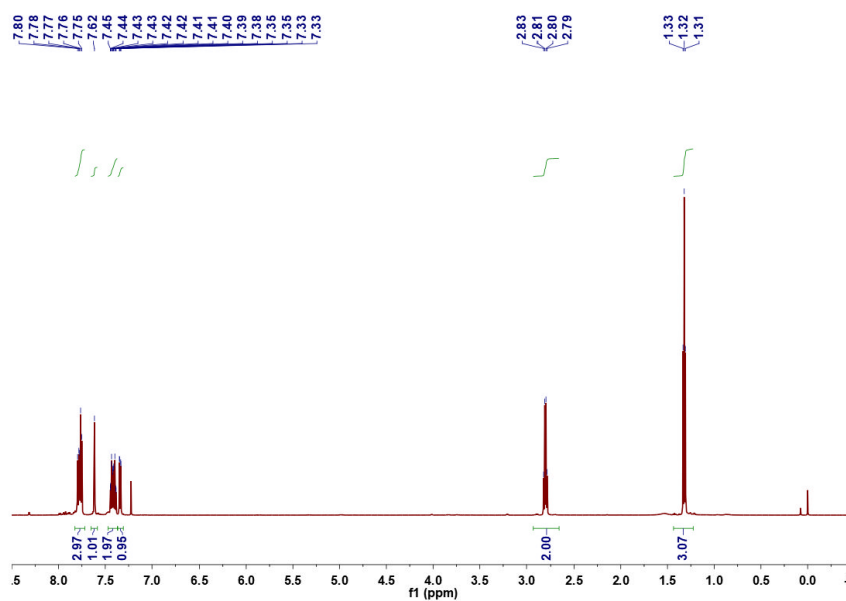
6. Appendix



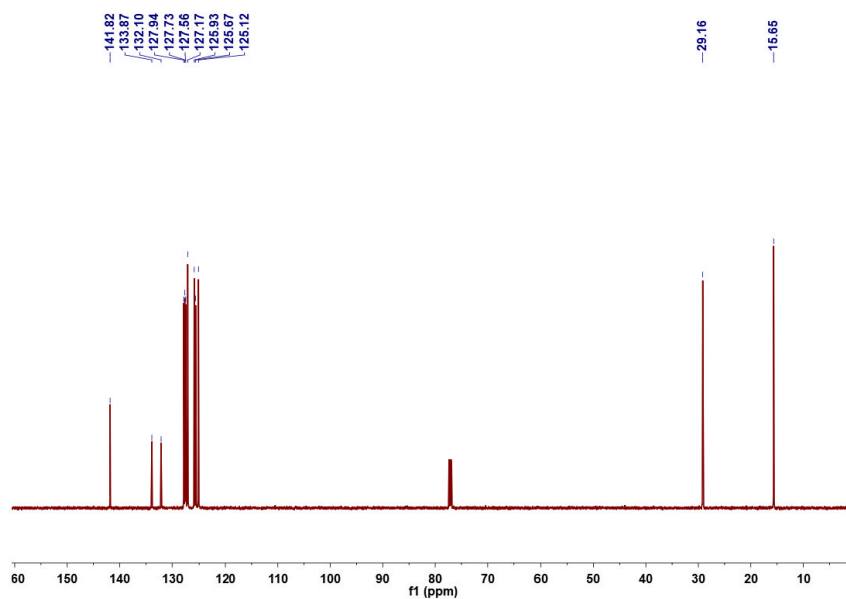
¹³C NMR spectrum of 2j (151 MHz, CDCl₃)



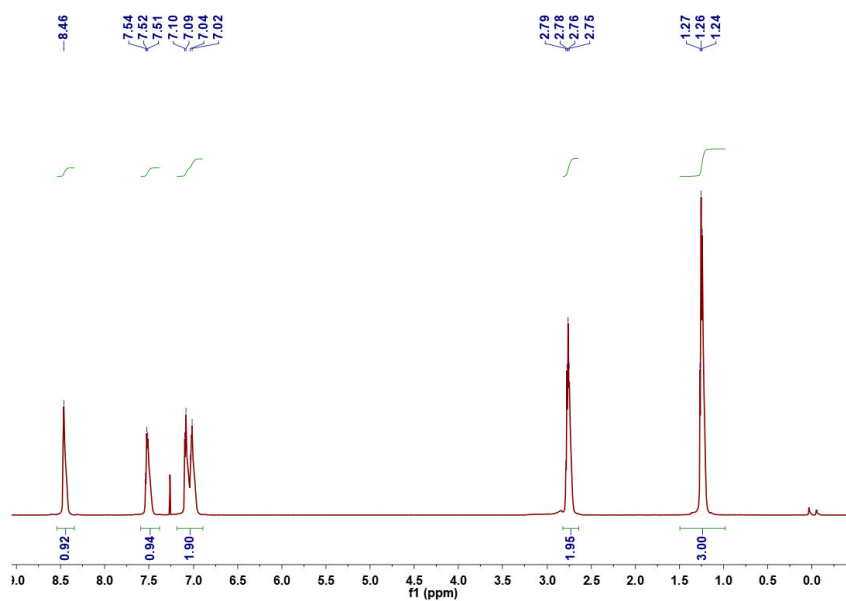
¹H NMR spectrum of 2k (600 MHz, CDCl₃)

¹³C NMR spectrum of 2k (151 MHz, CDCl₃)¹H NMR spectrum of 2l (600 MHz, CDCl₃)

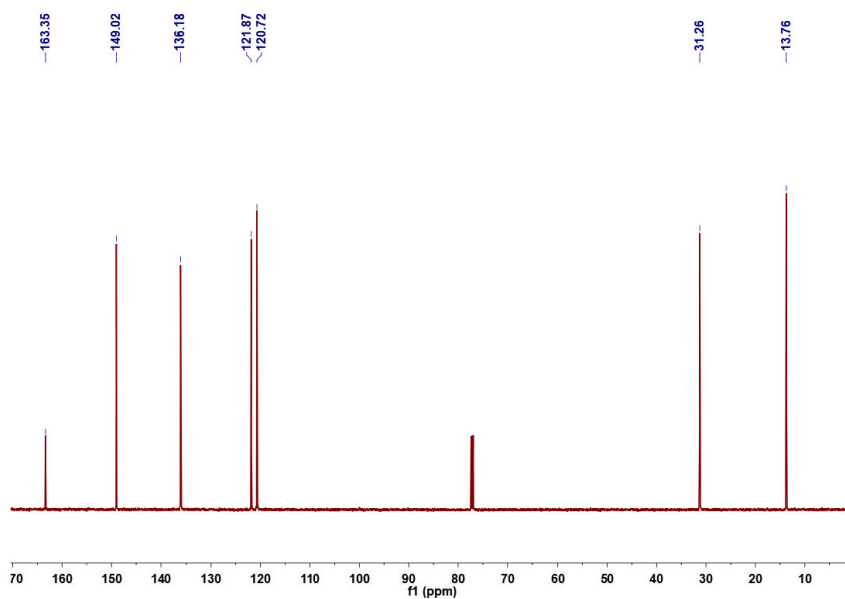
6. Appendix



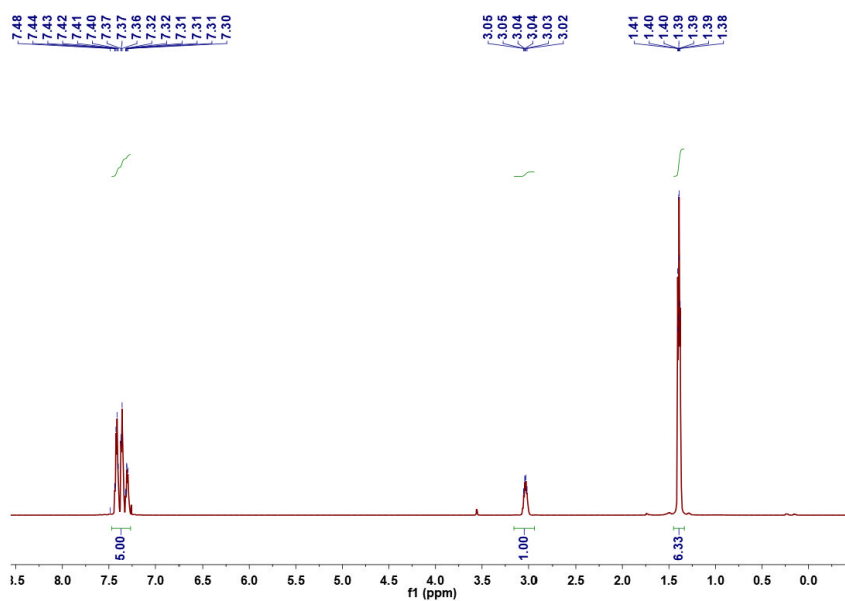
¹³C NMR spectrum of 2l (151 MHz, CDCl₃)



¹H NMR spectrum of 2m (600 MHz, CDCl₃)

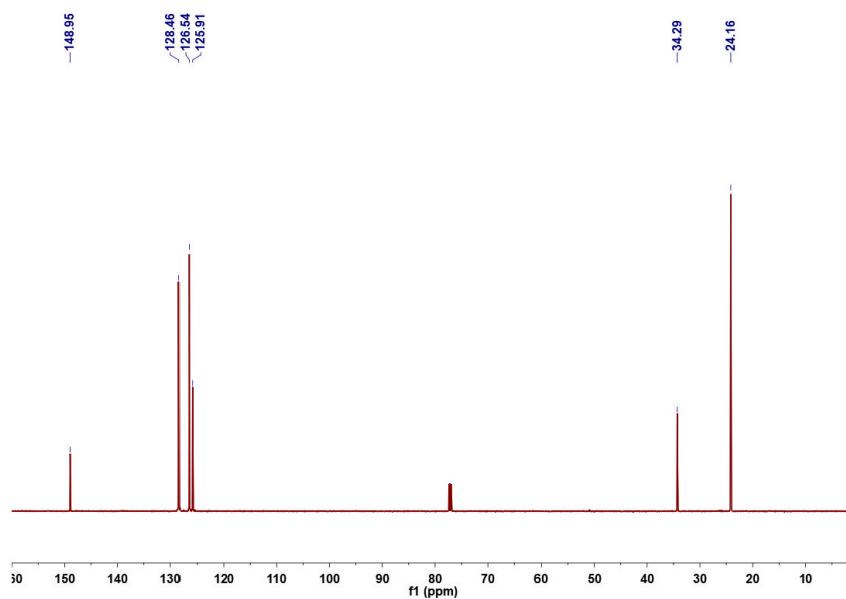


¹³C NMR spectrum of 2m (151 MHz, CDCl₃)

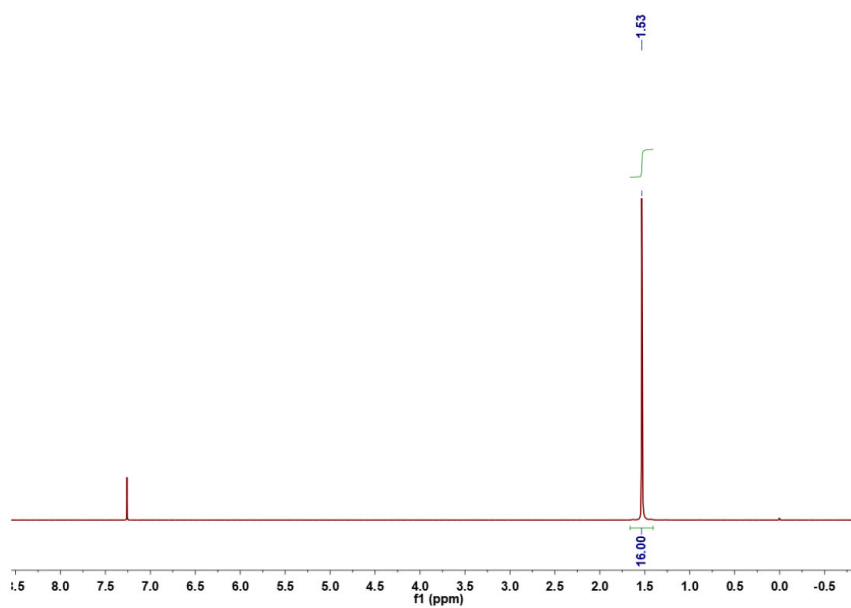


¹H NMR spectrum of 2n (600 MHz, CDCl₃)

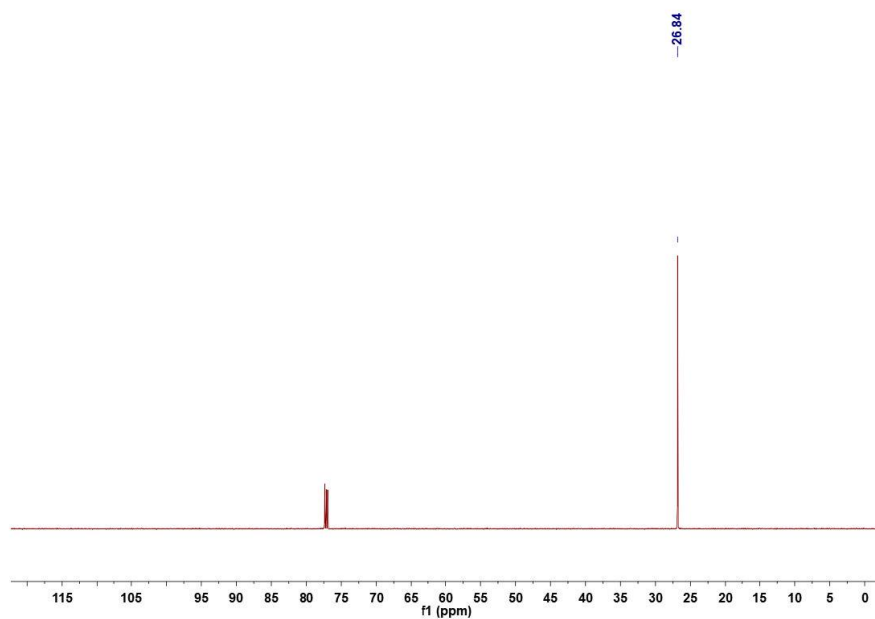
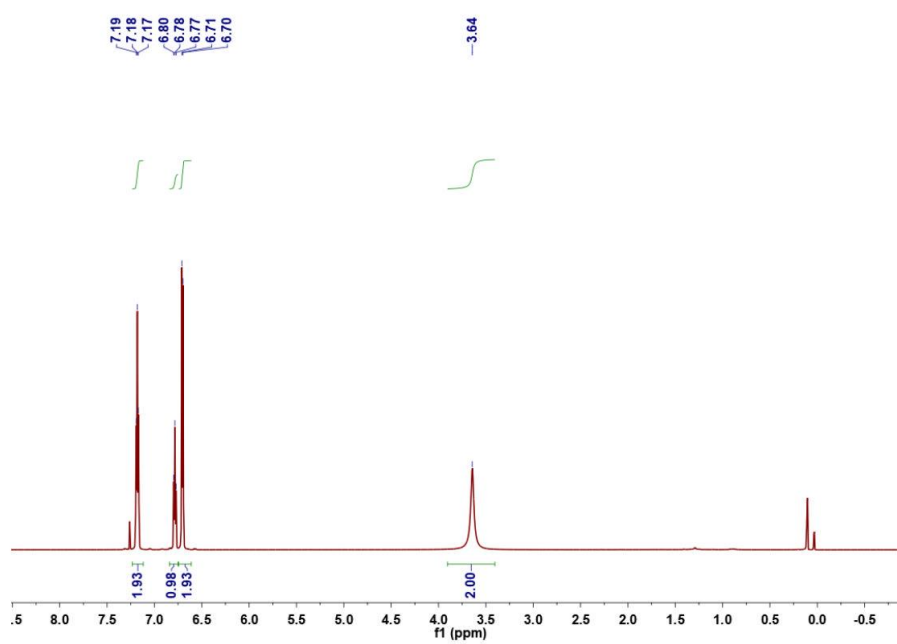
6. Appendix



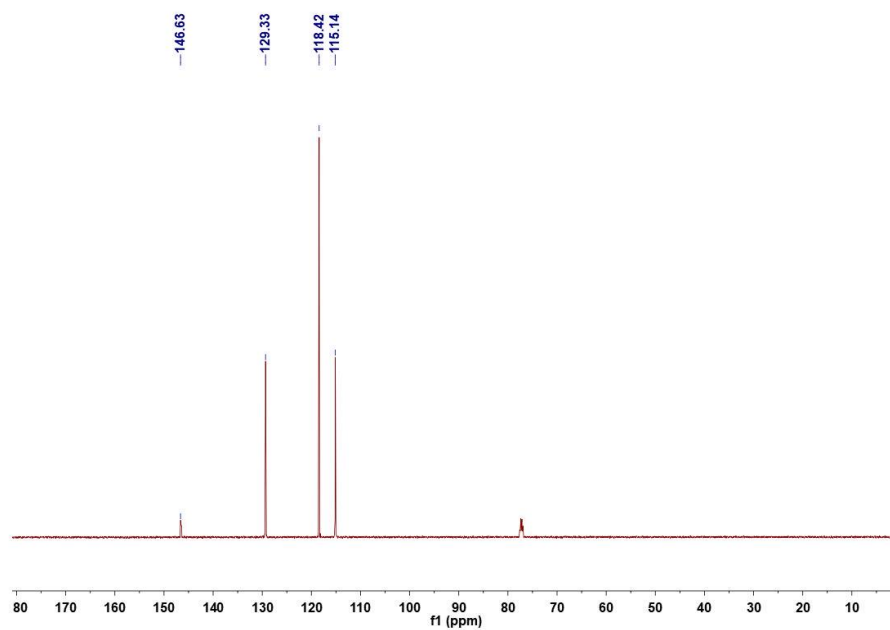
^{13}C NMR spectrum of 2n (151 MHz, CDCl_3)



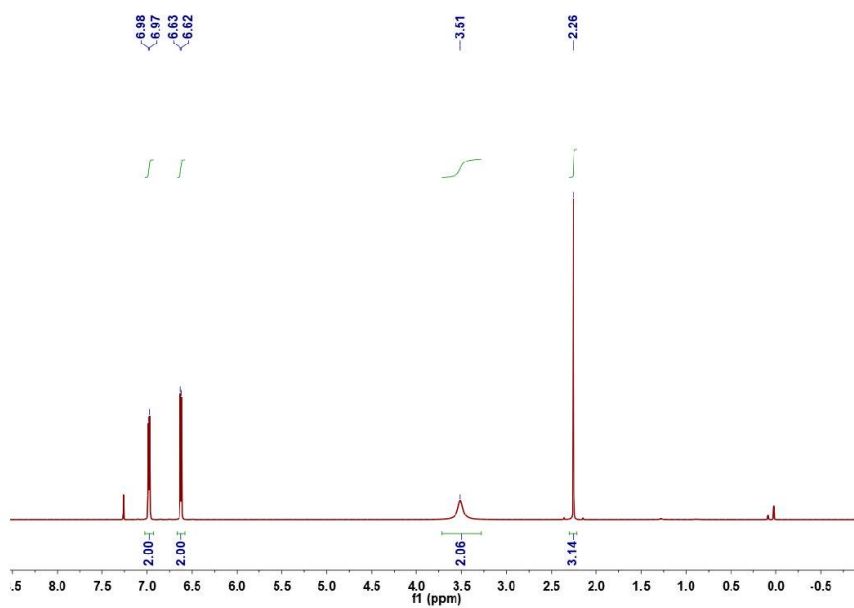
^1H NMR spectrum of 2o (600 MHz, CDCl_3)

 ^{13}C NMR spectrum of 2o (151 MHz, CDCl_3) ^1H NMR spectrum of 3a (600 MHz, CDCl_3)

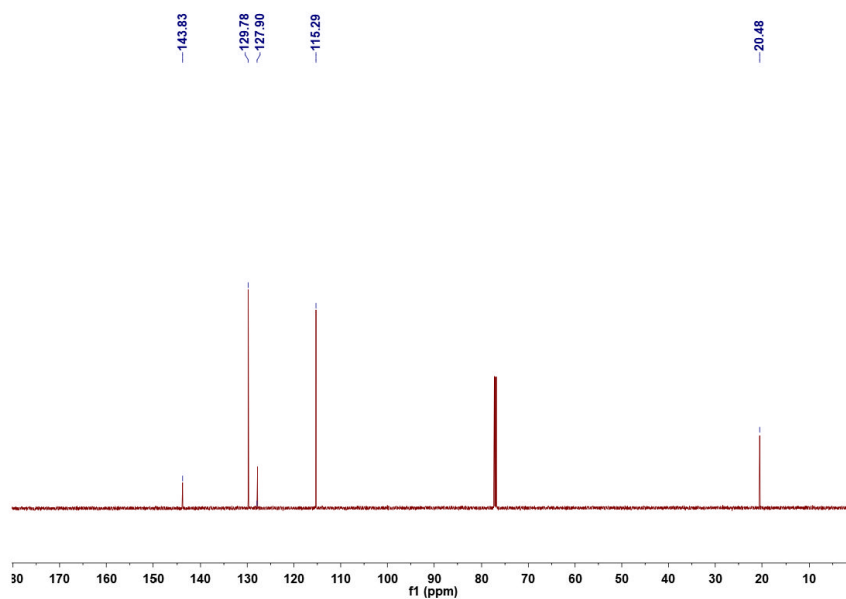
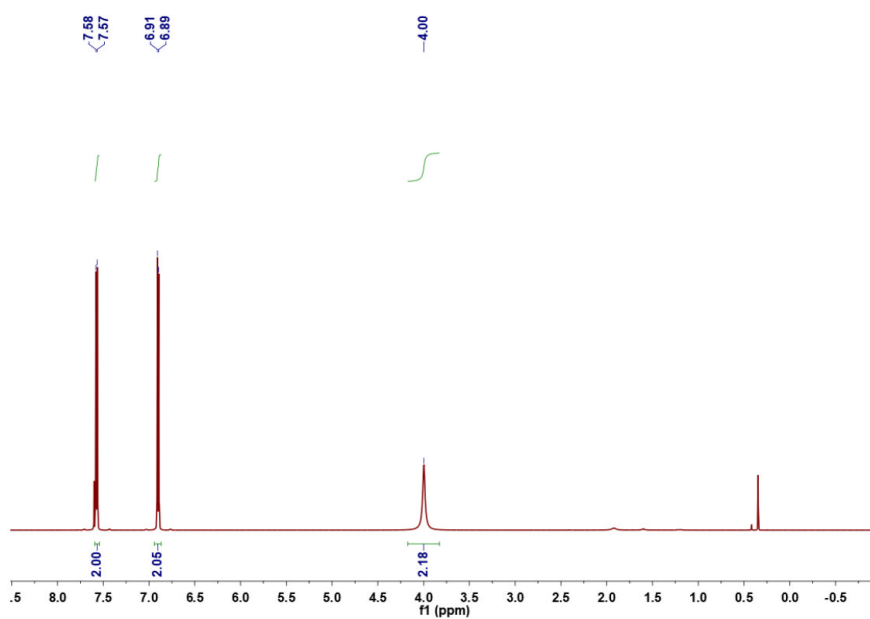
6. Appendix



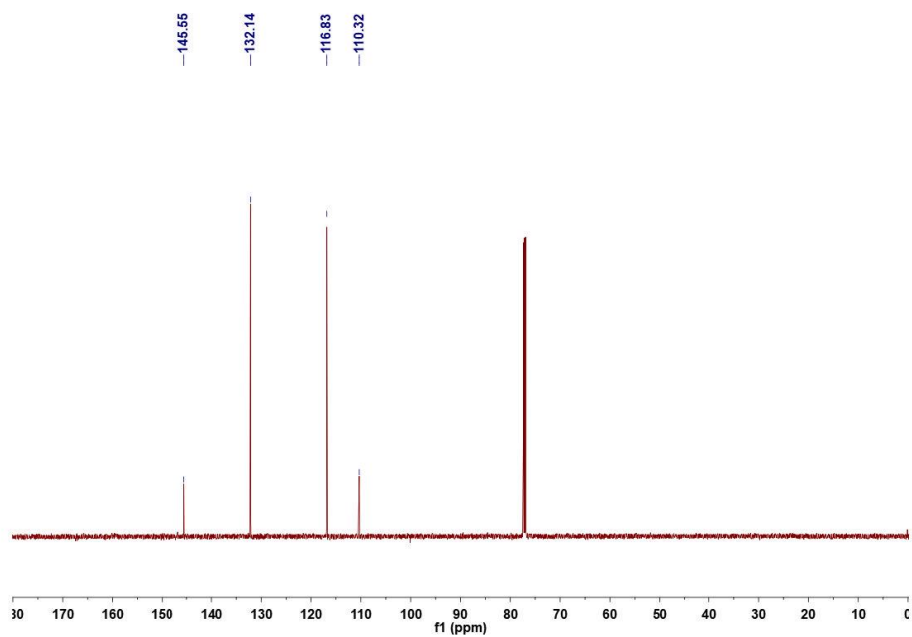
^{13}C NMR spectrum of 3a (151 MHz, CDCl_3)



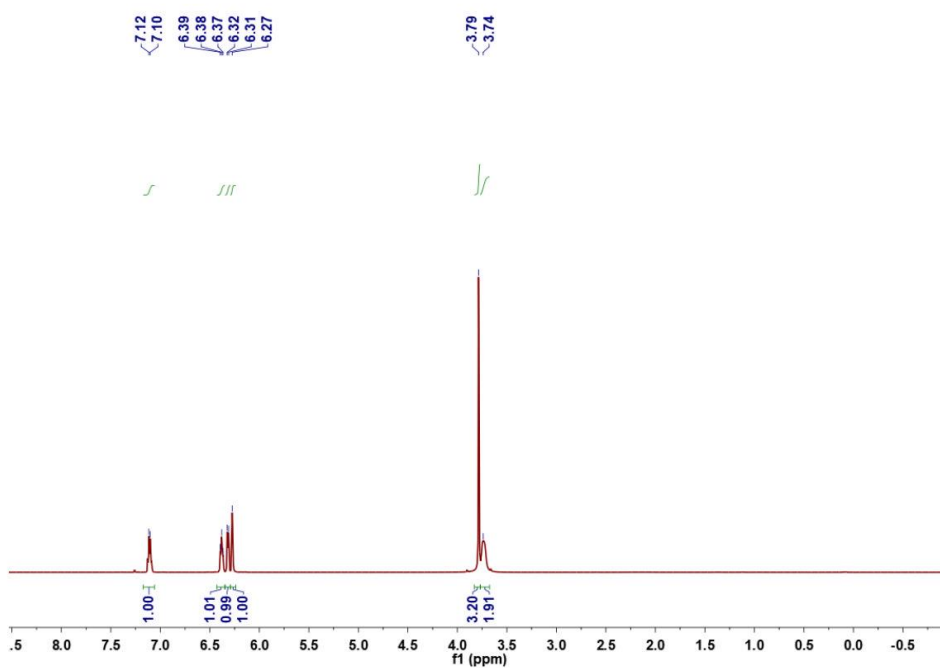
^1H NMR spectrum of 3b (600 MHz, CDCl_3)

¹³C NMR spectrum of **3b** (151 MHz, CDCl₃)¹H NMR spectrum of **3c** (600 MHz, CDCl₃)

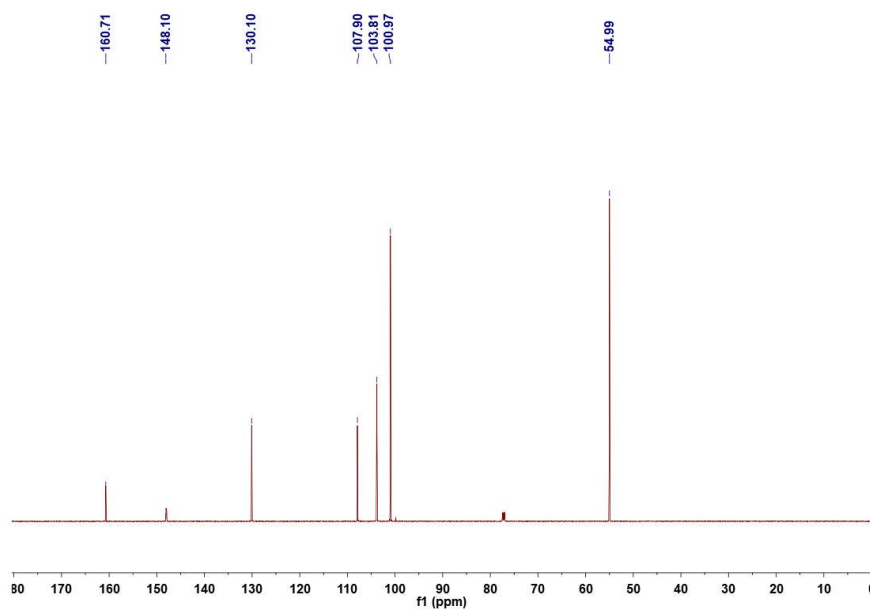
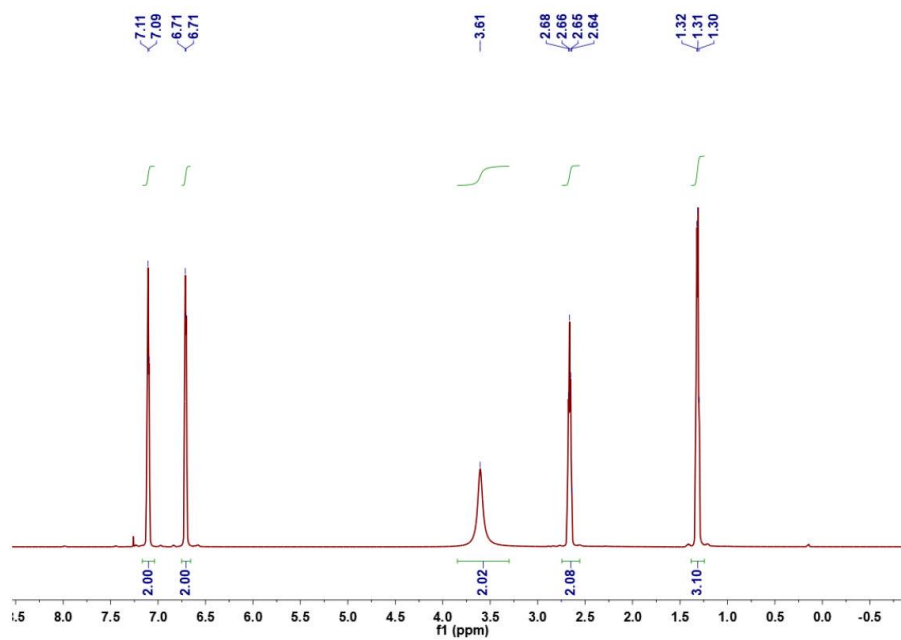
6. Appendix



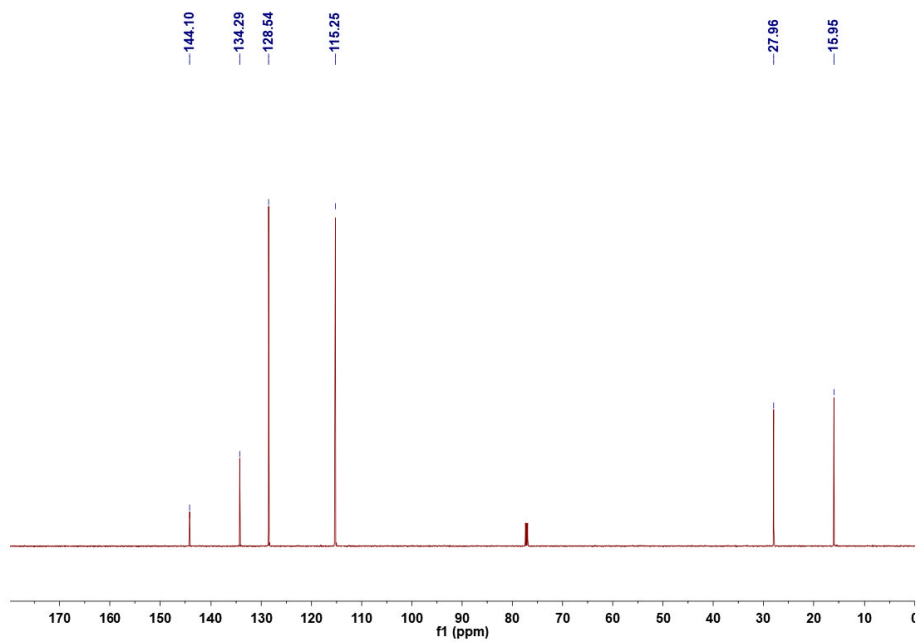
¹³C NMR spectrum of 3c (151 MHz, CDCl₃)



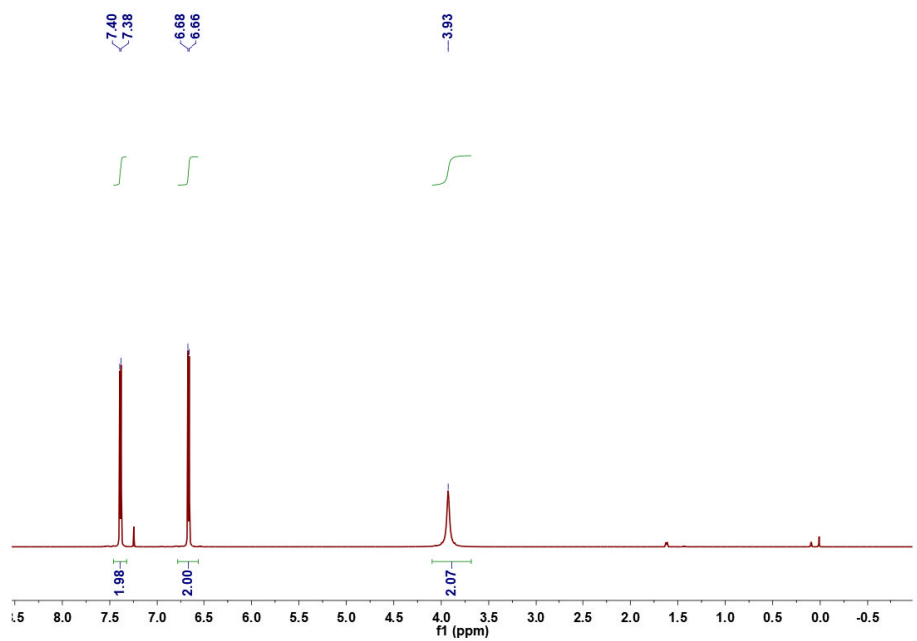
¹H NMR spectrum of 3d (600 MHz, CDCl₃)

¹³C NMR spectrum of 3d (151 MHz, CDCl₃)¹H NMR spectrum of 3e (600 MHz, CDCl₃)

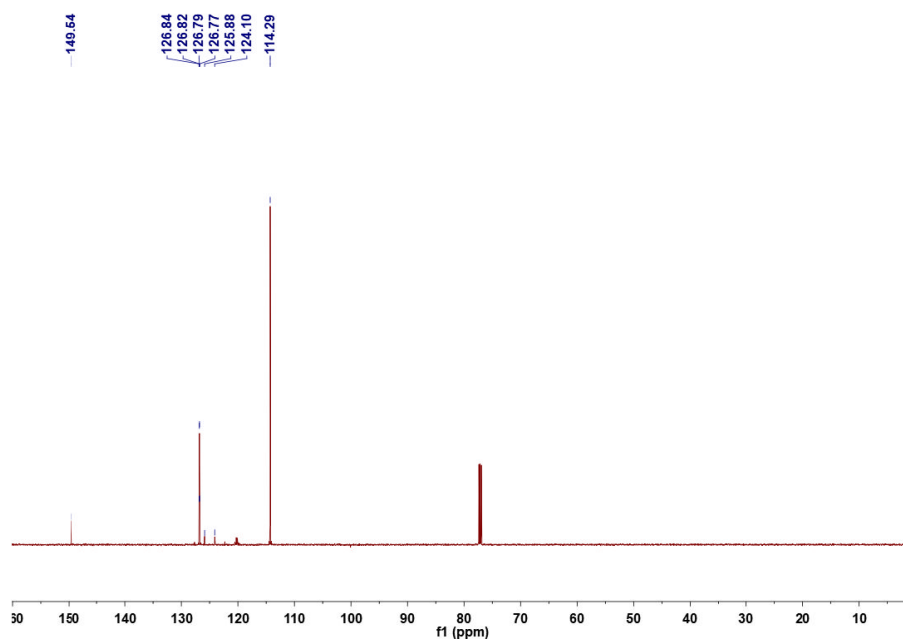
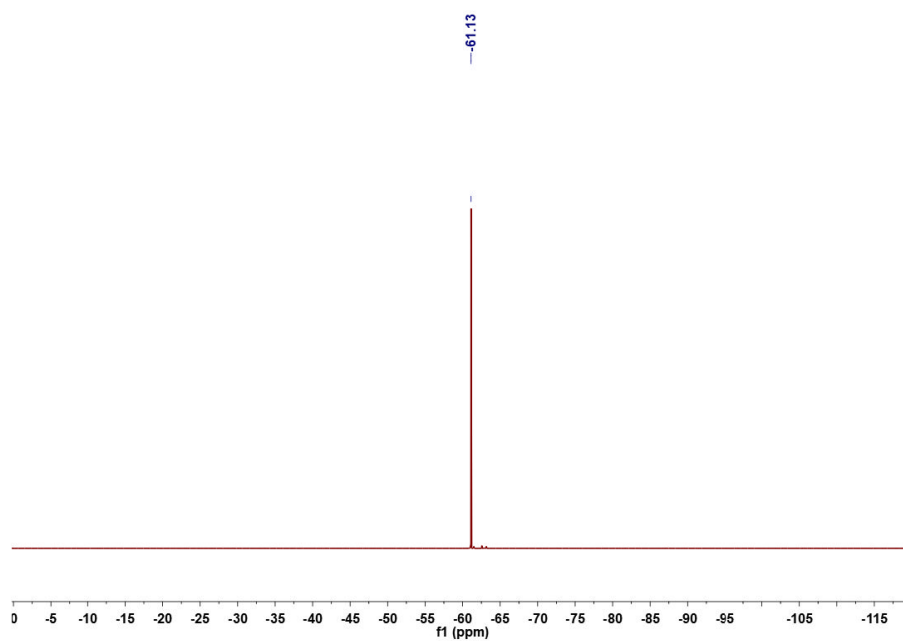
6. Appendix



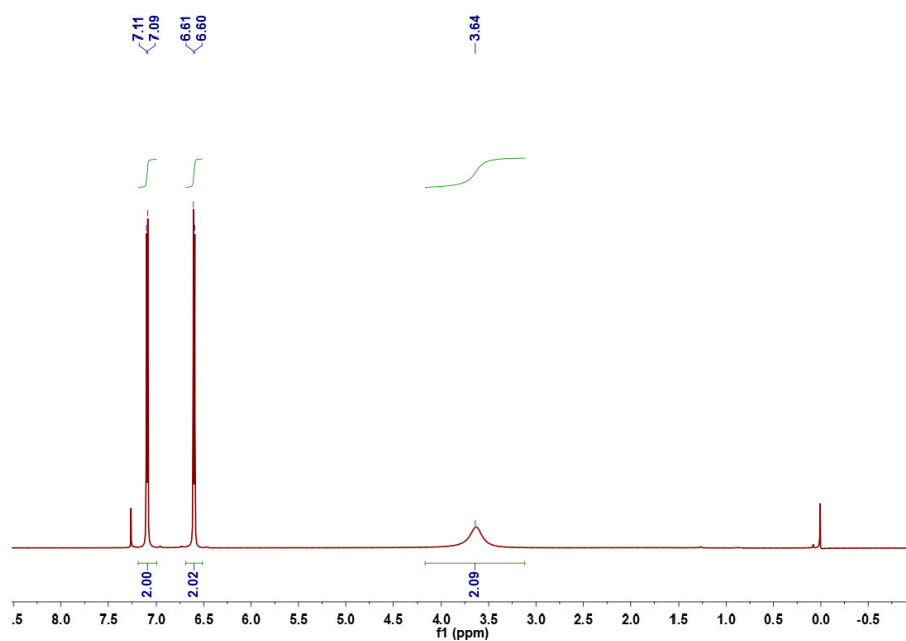
¹³C NMR spectrum of 3e (151 MHz, CDCl₃)



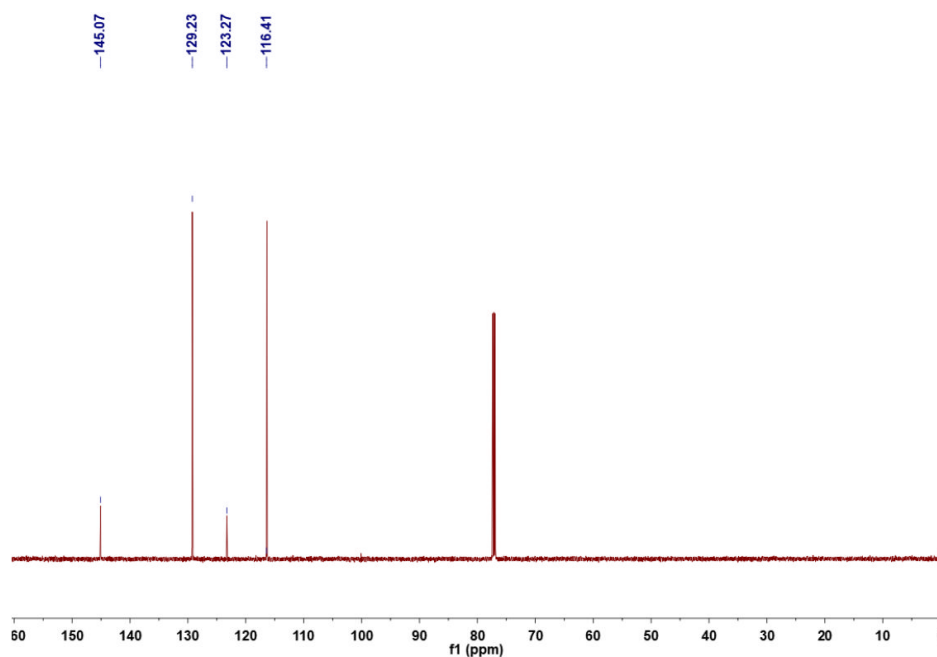
¹H NMR spectrum of 3f (600 MHz, CDCl₃)

 ^{13}C NMR spectrum of 3f (151 MHz, CDCl_3) ^{19}F NMR spectrum of 3f (565 MHz, CDCl_3)

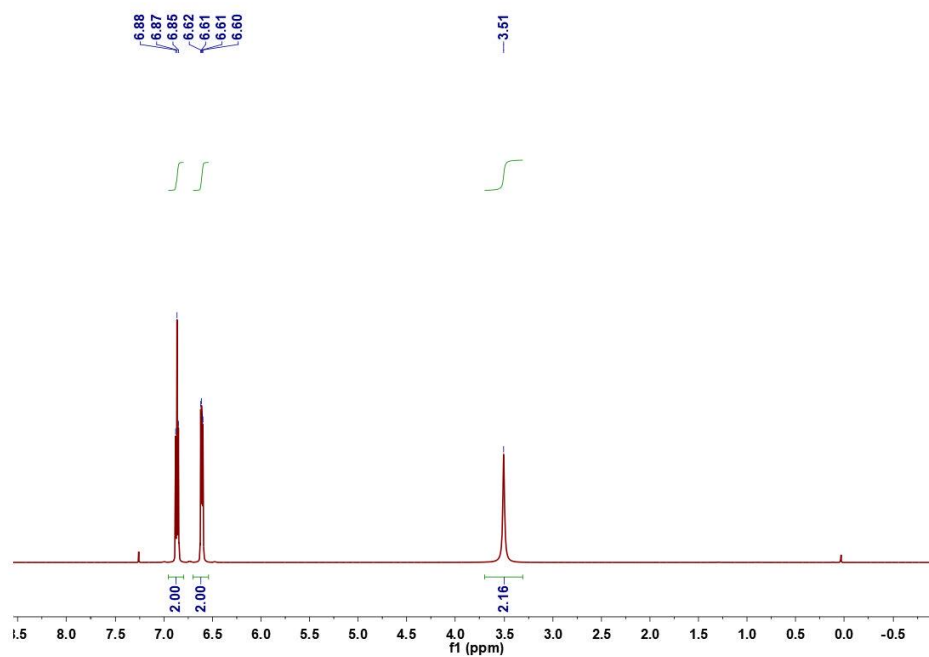
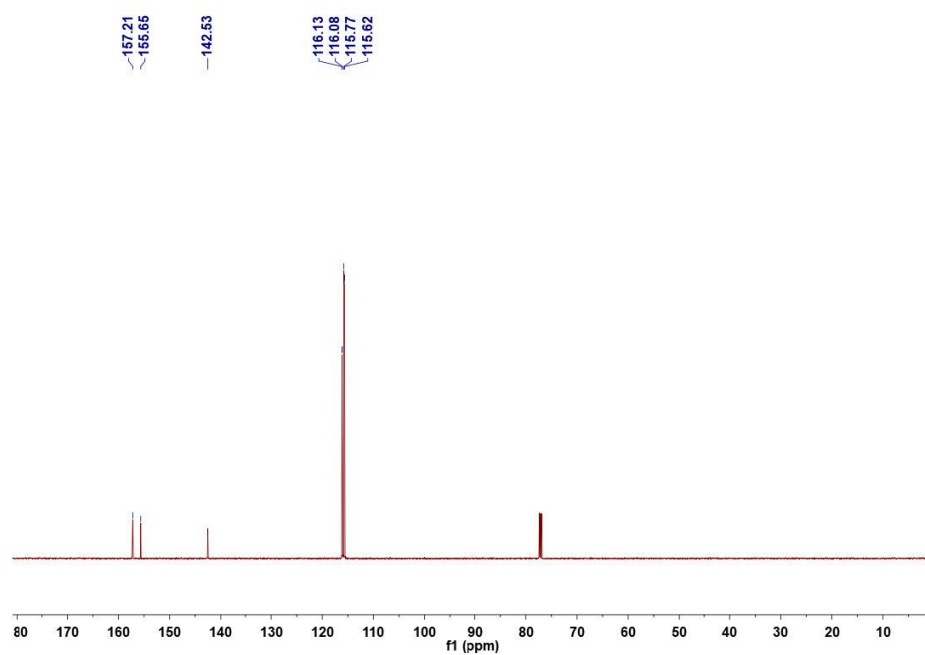
6. Appendix

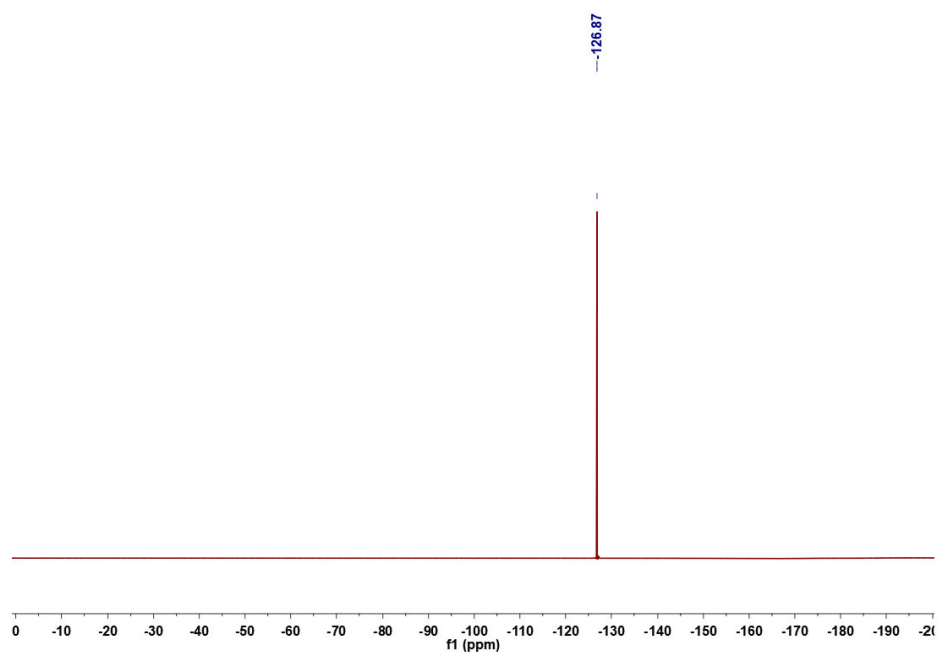
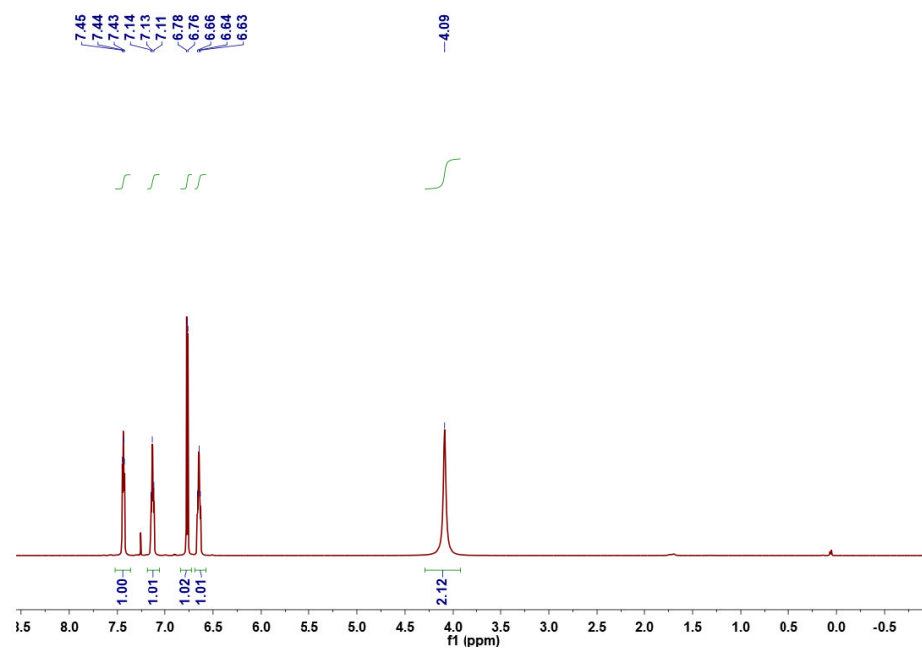


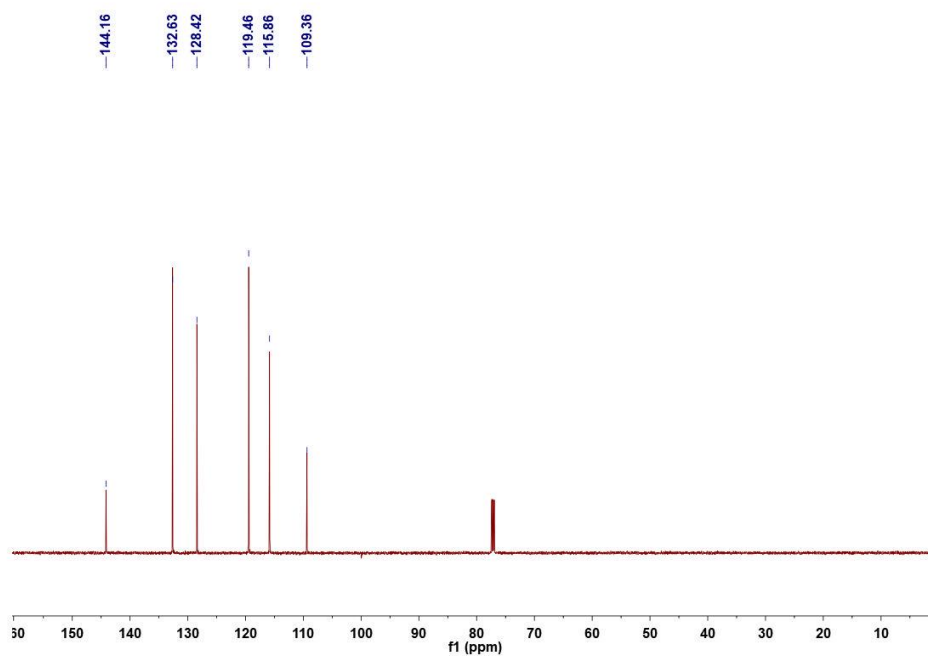
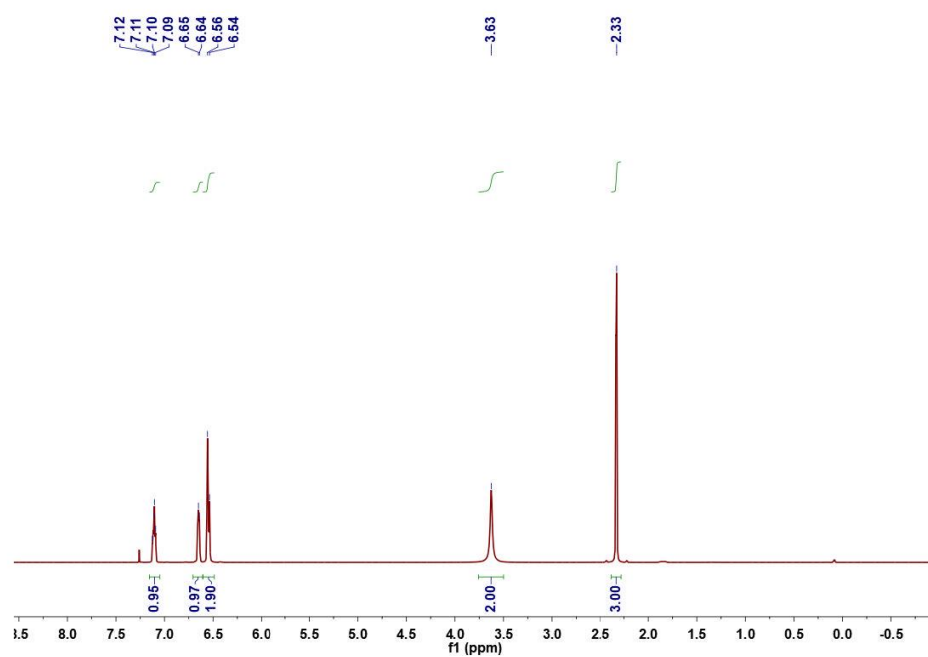
^1H NMR spectrum of 3g (600 MHz, CDCl_3)



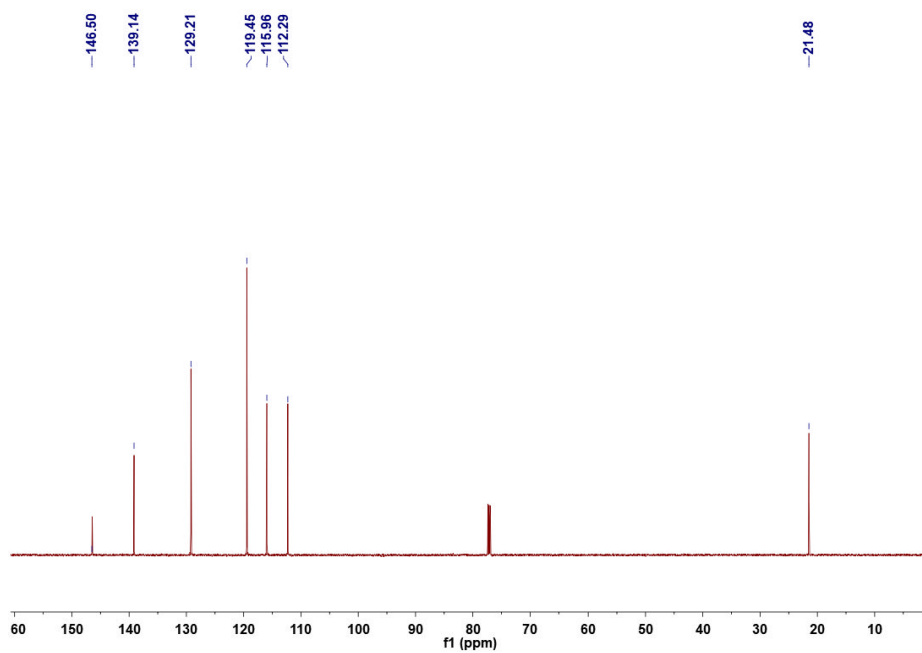
^{13}C NMR spectrum of 3g (151 MHz, CDCl_3)

¹H NMR spectrum of 3h (600 MHz, CDCl₃)¹³C NMR spectrum of 3h (151 MHz, CDCl₃)

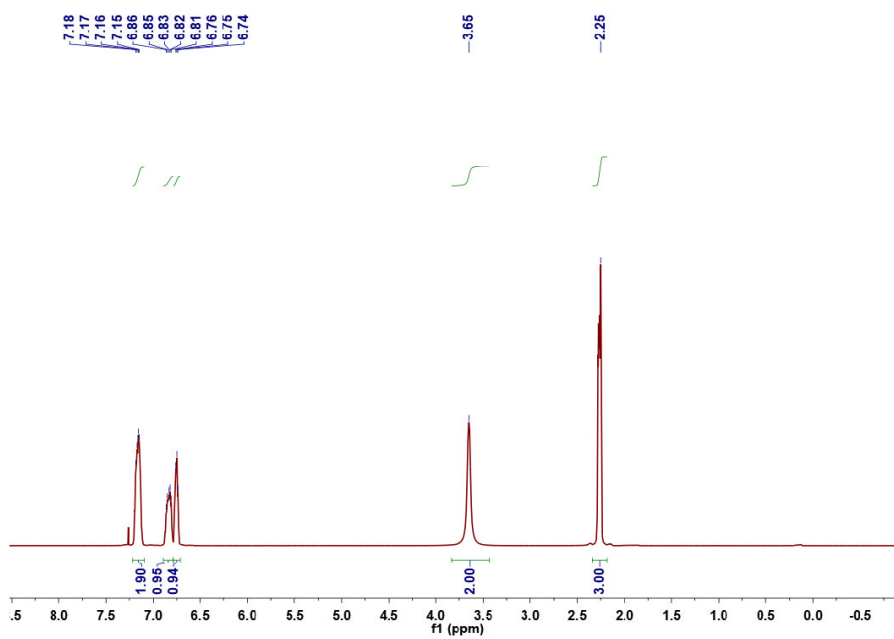
 ^{19}F NMR spectrum of 3h (565 MHz, CDCl_3) ^1H NMR spectrum of 3i (600 MHz, CDCl_3)

¹³C NMR spectrum of 3i (151 MHz, CDCl₃)¹H NMR spectrum of 3j (600 MHz, CDCl₃)

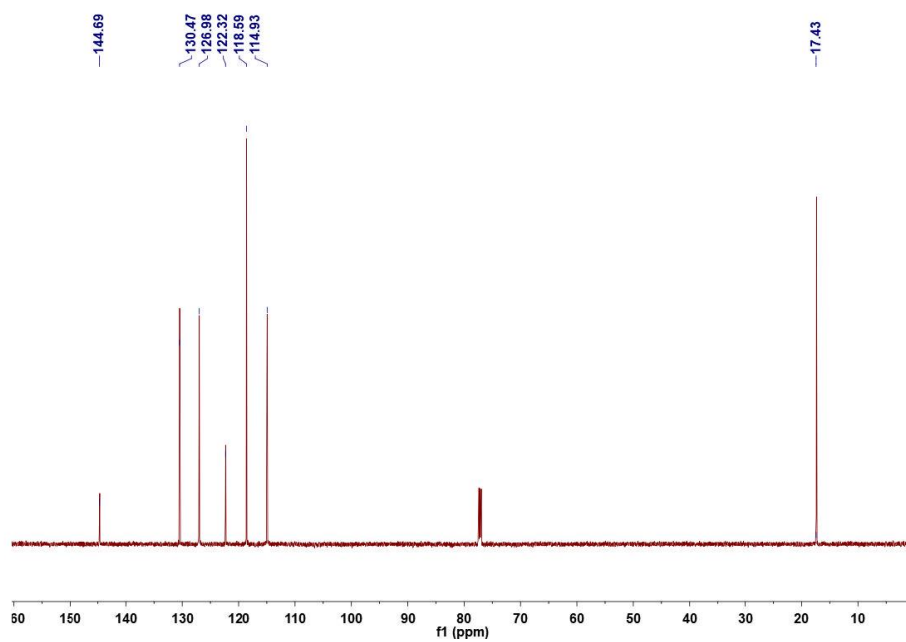
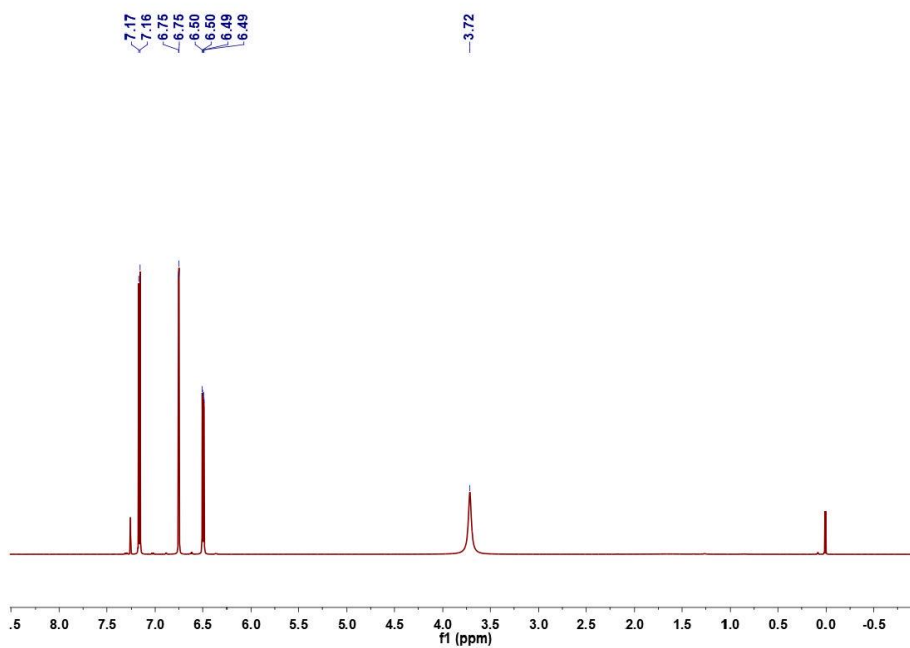
6. Appendix



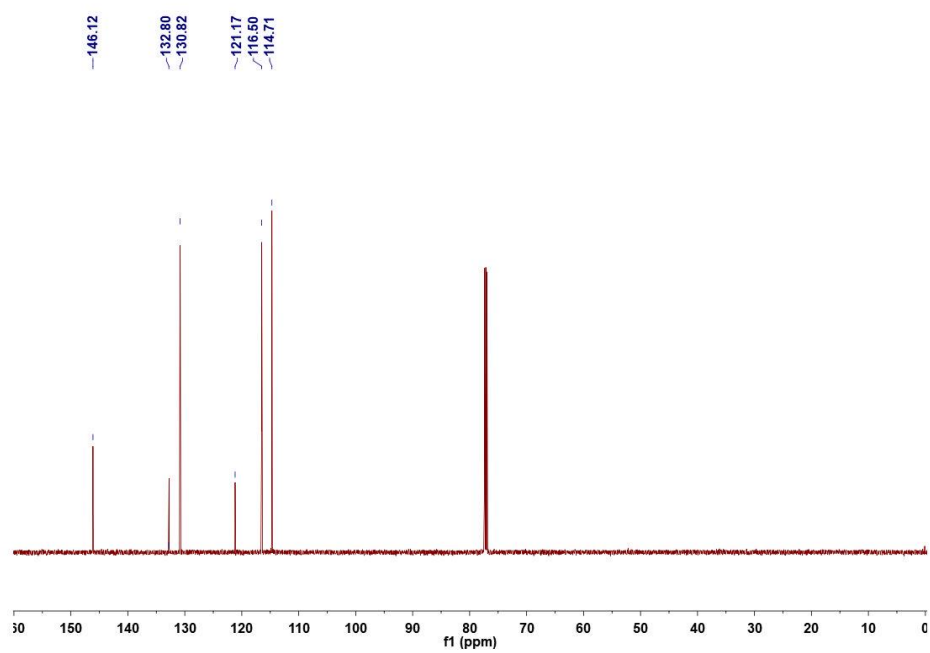
¹³C NMR spectrum of 3j (151 MHz, CDCl₃)



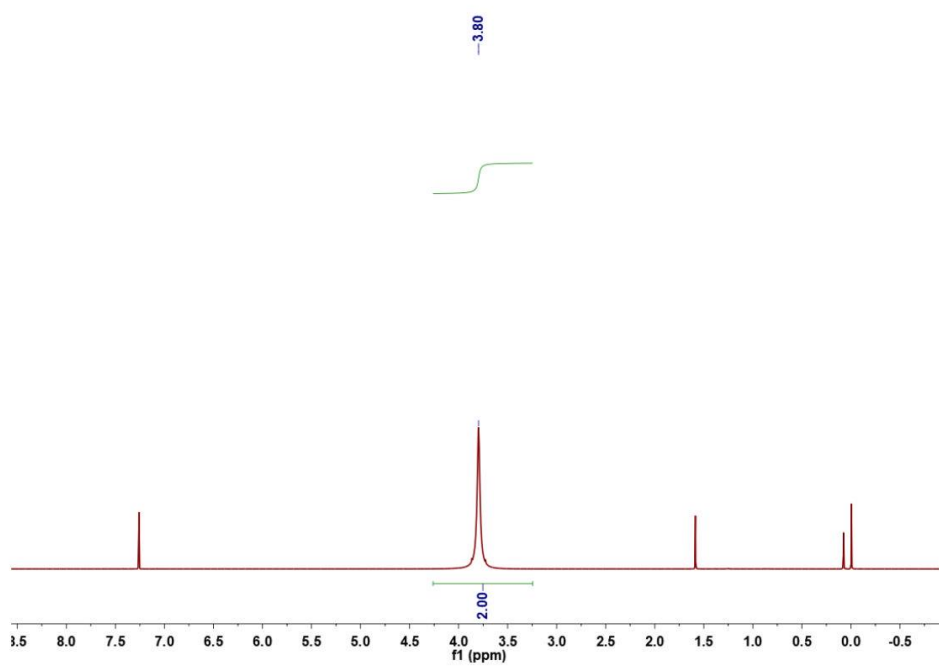
¹H NMR spectrum of 3k (600 MHz, CDCl₃)

¹³C NMR spectrum of 3k (151 MHz, CDCl₃)¹H NMR spectrum of 3l (600 MHz, CDCl₃)

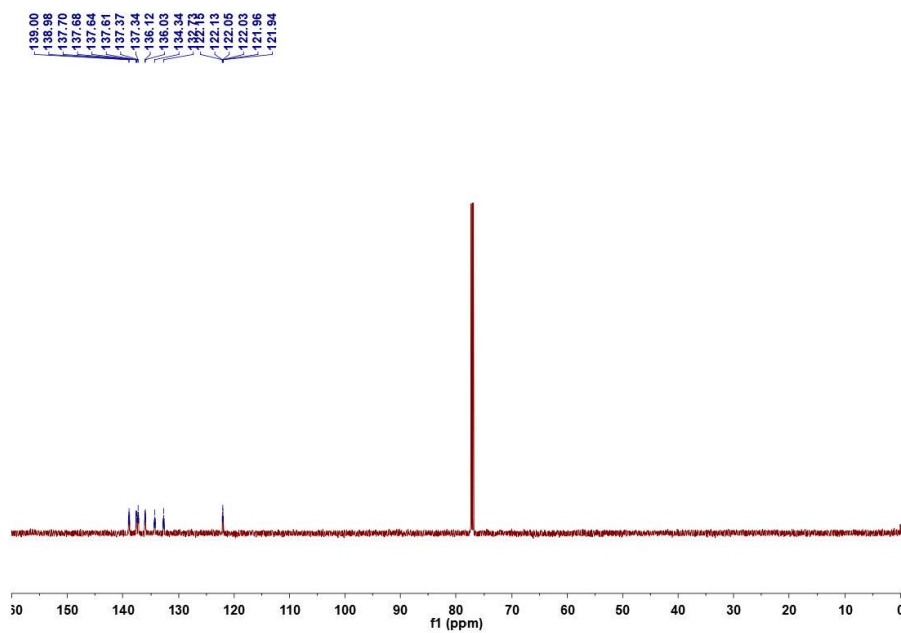
6. Appendix



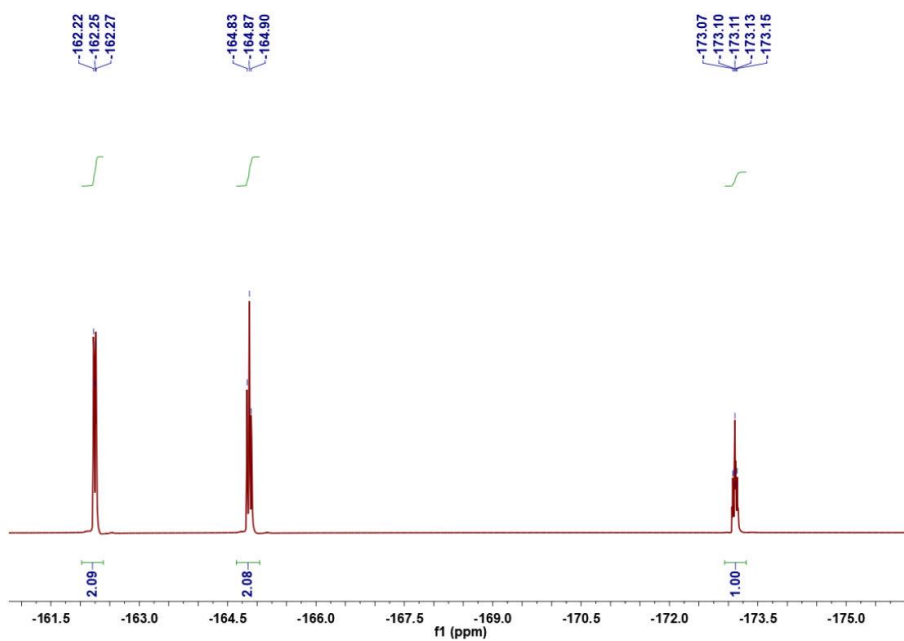
¹³C NMR spectrum of 3I (151 MHz, CDCl₃)



¹H NMR spectrum of 3m (600 MHz, CDCl₃)

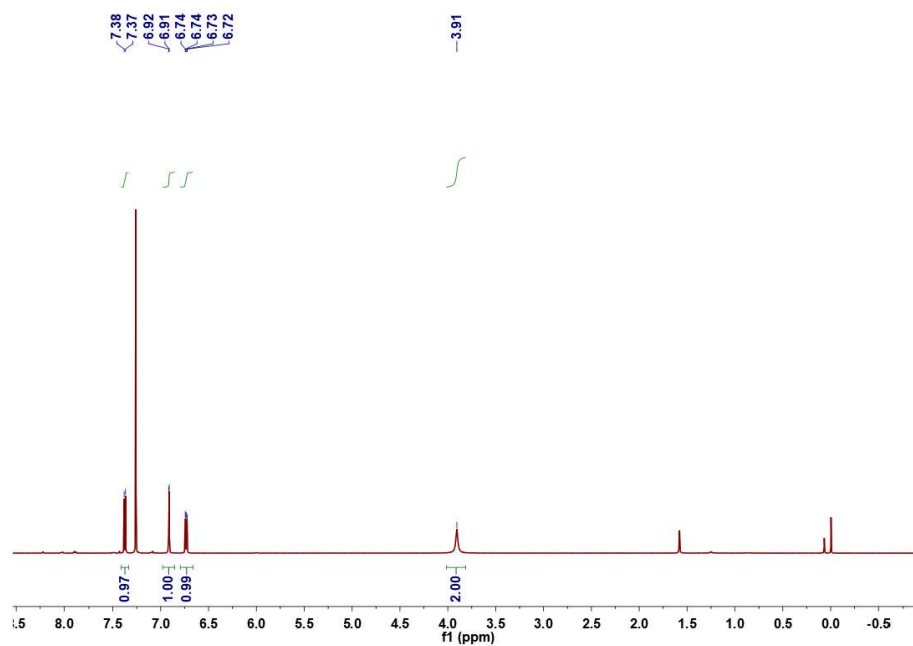


^{13}C NMR spectrum of **3m** (151 MHz, CDCl_3)

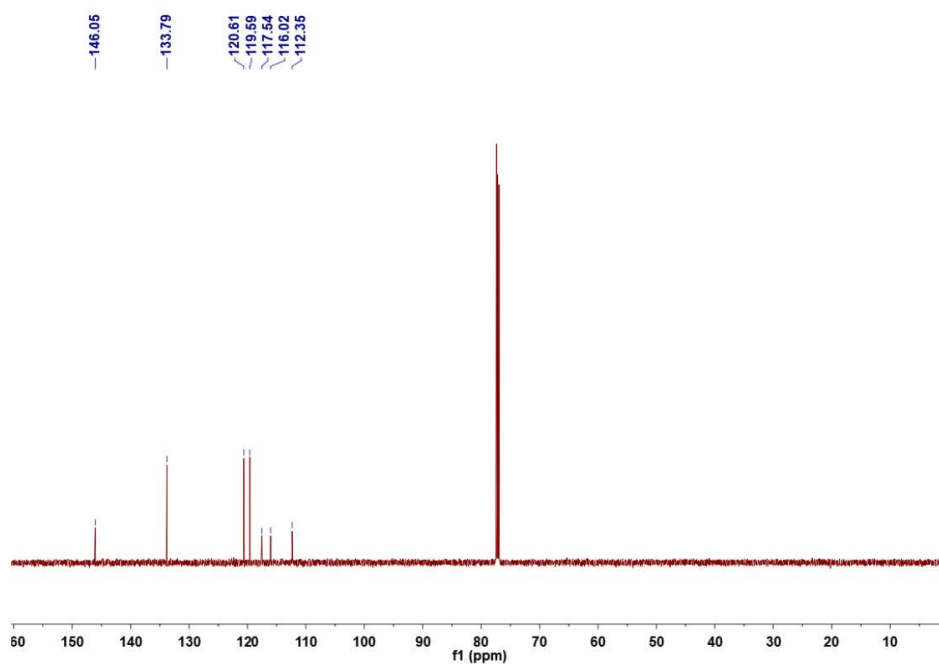


^{19}F NMR spectrum of **3m** (565 MHz, CDCl_3)

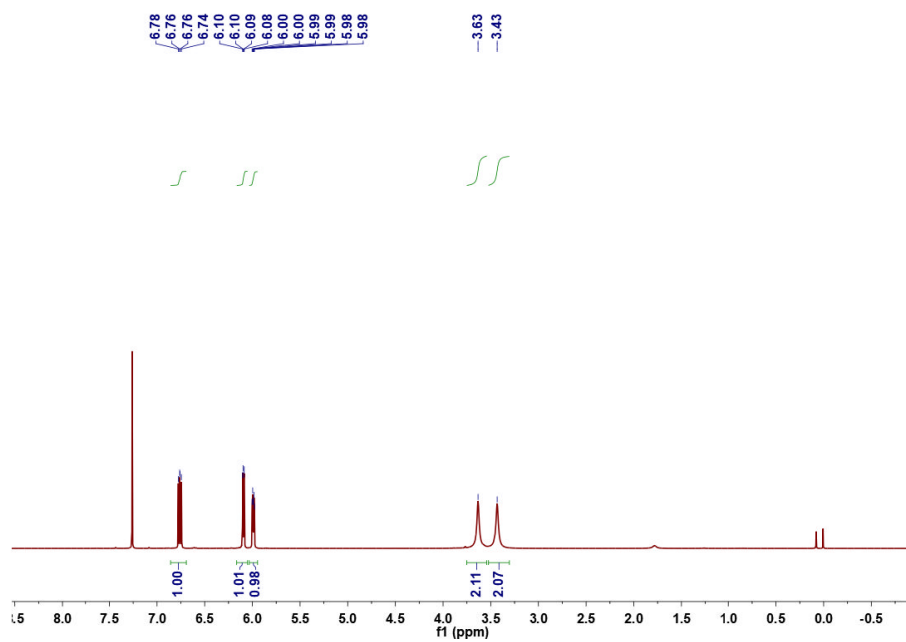
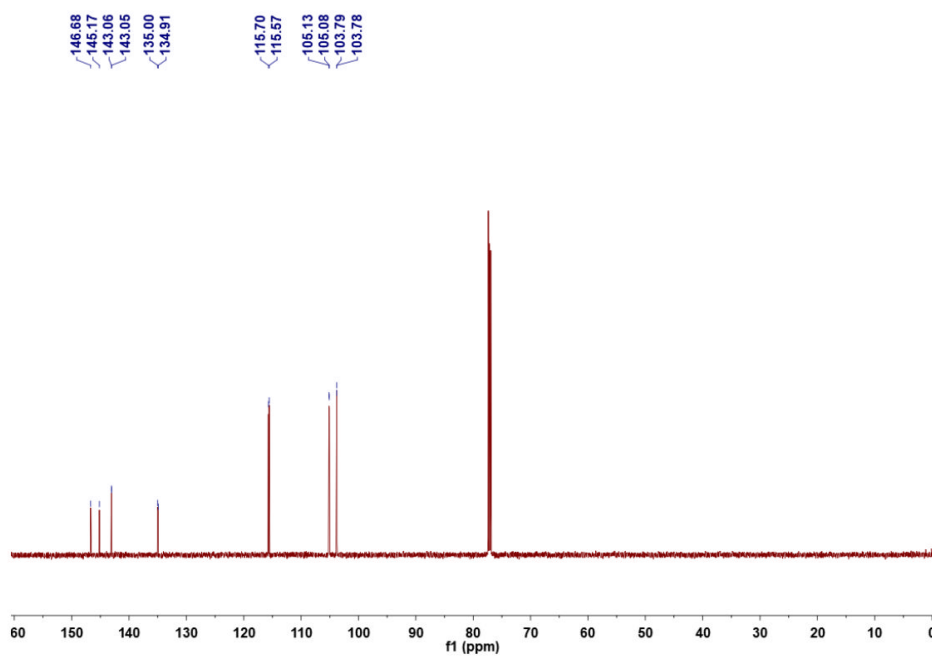
6. Appendix

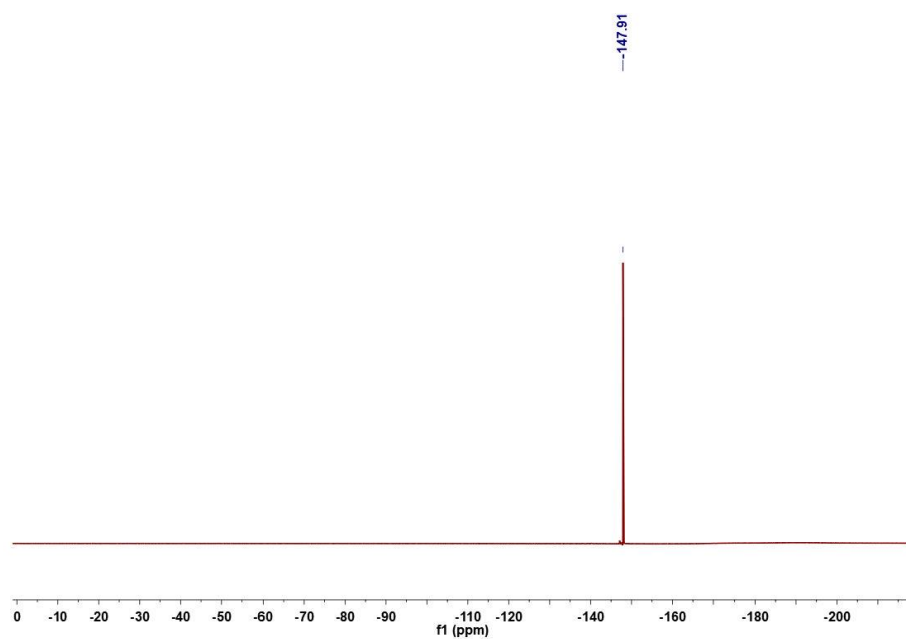
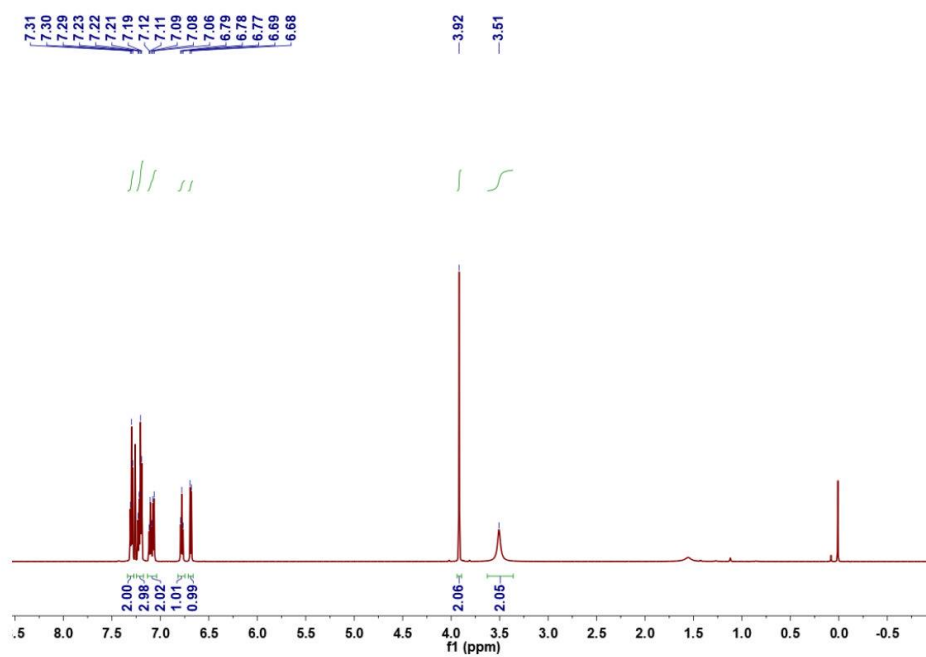


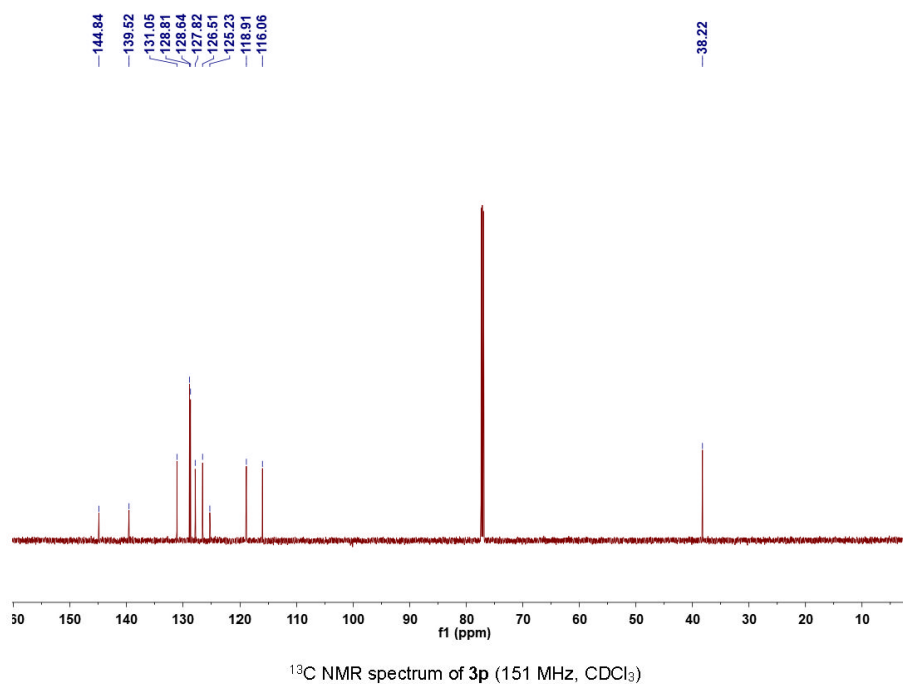
¹H NMR spectrum of 3n (600 MHz, CDCl₃)



¹³C NMR spectrum of 3n (151 MHz, CDCl₃)

¹H NMR spectrum of 3o (600 MHz, CDCl₃)¹³C NMR spectrum of 3o (151 MHz, CDCl₃)

 ^{19}F NMR spectrum of 3o (565 MHz, CDCl_3) ^1H NMR spectrum of 3p (600 MHz, CDCl_3)



S8 References

- [1] G. Jian, C. Yaguang, Q. Lunyu, L. Qin, *Polyhedron* **1996**, *15*, 2273-2277.
- [2] G. Sheldrick, *Acta Crystallogr., Sect. A* **2008**, *64*, 112-122.
- [3] O. V. Dolomanov, L. J. Bourhis, R. J. Gildea, J. A. K. Howard, H. Puschmann, *J. Appl. Crystallogr.* **2009**, *42*, 339-341.
- [4] X. Pei, H. Jiao, H. Fu, X. Yin, D. Luo, S. Long, W. Gong, L. Zhang, *ACS Appl. Mater. Interfaces* **2020**, *12*, 51459-51467.
- [5] S. Gao, W. Li, R. Cao, *Inorg. Chem. Front.* **2015**, *2*, 713-719.
- [6] M. Dhiman, V. Polshettiwar, *J. Mater. Chem. A* **2016**, *4*, 12416-12424.
- [7] A. V. C. A. Goswami, H. Sopha, D. Nandan, M. B. Gawande, K. Cepe, S. Ng, R. Zboril, J. M. Macak, *Appl. Mater. Today* **2018**, *10*, 86-92.
- [8] X. Li, W. Zheng, H. Pan, Y. Yu, L. Chen, P. Wu, *J. Catal.* **2013**, *300*, 9-19.
- [9] S.-L. Hou, J. Dong, Z.-H. Zhu, L.-C. Geng, Y. Ma, B. Zhao, *Chem. Mater.* **2020**, *32*, 7063-7069.
- [10] K. J. Datta, K. K. R. Datta, M. B. Gawande, V. Ranc, K. C epe, V. Malgras, Y. Yamauchi, R. S. Varma, R. Zboril, *Chem. Eur. J.* **2016**, *22*, 1577-1581.
- [11] E. A. Baquero, S. Tricard, J. C. Flores, E. de Jes us, B. Chaudret, *Angew. Chem. Int. Ed.* **2014**, *53*, 13220-13224.
- [12] B. Qi, C. Wu, Y. Liu, J. Liu, H. Zhang, *ACS Appl. Nano Mater.* **2019**, *2*, 4377-4385.
- [13] Q. Wang, X.-S. Wang, C.-H. Chen, X. Yang, Y.-B. Huang, R. Cao, *Chem. Commun.* **2018**, *54*, 8822-8825.
- [14] J. Wang, D. Ge, X. Cao, M. Tang, Y. Pan, H. Gu, *Chem. Commun.* **2015**, *51*, 9216-9219.
- [15] X. Deng, B. Qin, R. Liu, X. Qin, W. Dai, G. Wu, N. Guan, D. Ma, L. Li, *J. Am. Chem. Soc.* **2021**, *143*, 20898-20906.
- [16] A. Kongor, M. Panchal, M. Athar, V. Mehta, K. Bhatt, P. C. Jha, V. Jain, *Appl. Surf. Sci.* **2018**, *437*, 195-201.
- [17] Y. Imada, H. Iida, T. Naota, *J. Am. Chem. Soc.* **2005**, *127*, 14544-14545.
- [18] N. J. R. van Eikema Hommes, T. Clark, *J. Mol. Model.* **2005**, *11*, 175-185.
- [19] F. S. Tschernuth, T. Thorwart, L. Greb, F. Hanusch, S. Inoue, *Angew. Chem. Int. Ed.* **2021**, *60*, 25799-25803.
- [20] Y. Monguchi, T. Marumoto, T. Ichikawa, Y. Miyake, Y. Nagae, M. Yoshida, Y. Oumi, Y. Sawama, H. Sajiki, *ChemCatChem* **2015**, *7*, 2155-2160.
- [21] Y. Wang, Z. Huang, X. Leng, H. Zhu, G. Liu, Z. Huang, *J. Am. Chem. Soc.* **2018**, *140*, 4417-4429.
- [22] R. C. Betori, C. M. May, K. A. Scheidt, *Angew. Chem. Int. Ed.* **2019**, *58*, 16490-16494.
- [23] Y. Wang, X. Cao, L. Zhao, C. Pi, J. Ji, X. Cui, Y. Wu, *Adv. Synth. Catal.* **2020**, *362*, 4119-4129.

- [24] Z. Wei, Y. Wang, Y. Li, R. Ferraccioli, Q. Liu, *Organometallics* **2020**, *39*, 3082-3087.
- [25] N. G. Léonard, P. J. Chirik, *ACS Catal.* **2018**, *8*, 342-348.
- [26] H. Zhao, D. Leonori, *Angew. Chem. Int. Ed.* **2021**, *60*, 7669-7674.
- [27] Y. Zhang, J. Wang, Z. Yang, Z. Zhang, X. He, G. Chen, G. Huang, X. Lu, *J. Org. Chem.* **2021**, *86*, 17696-17709.
- [28] M. Jang, T. Lim, B. Y. Park, M. S. Han, *J. Org. Chem.* **2022**, *87*, 910-919.
- [29] H. Lu, Z. Geng, J. Li, D. Zou, Y. Wu, Y. Wu, *Org. Lett.* **2016**, *18*, 2774-2776.
- [30] V. Goyal, N. Sarki, M. K. Poddar, A. Narani, D. Tripathi, A. Ray, K. Natte, *New J. Chem.* **2021**, *45*, 14687-14694.
- [31] C.-Y. Long, S.-F. Ni, M.-H. Su, X.-Q. Wang, W. Tan, *ACS Catal.* **2020**, *10*, 13641-13649.
- [32] E. Dimitriou, R. H. Jones, R. G. Pritchard, G. J. Miller, M. O'Brien, *Tetrahedron* **2018**, *74*, 6795-6803.
- [33] A. Modvig, T. L. Andersen, R. H. Taaning, A. T. Lindhardt, T. Skrydstrup, *J. Org. Chem.* **2014**, *79*, 5861-5868.

S9 Author contributions

S. Li, C. Streb and X. Chen conceived the idea, supervised the project. S. Li, Y. Zhao and N. Ma designed the experiments. Y. Zhao and Y. Ma co-worked on the synthesis and characterizations of the title compounds. Y. Zhao, Y. Ma and S. Li collected the structural data and provided detailed refinements on the crystal structures. C. Streb provided structure and mechanism analysis. Y. Zhao, Y. Ma, R. Liu, Y. Zhao and X. Dai co-worked on the preparation and characterization of **Pt/Ce-POM**. Y. Ma carried out catalytic experiments. Y. Ma, R. Liu, Y. Zhao and X. Dai carried out the measurement and data analysis of the electron microscopy and XPS. All authors discussed and co-wrote the manuscript.

7 Acknowledgements

[Redacted content]

7. Acknowledgements

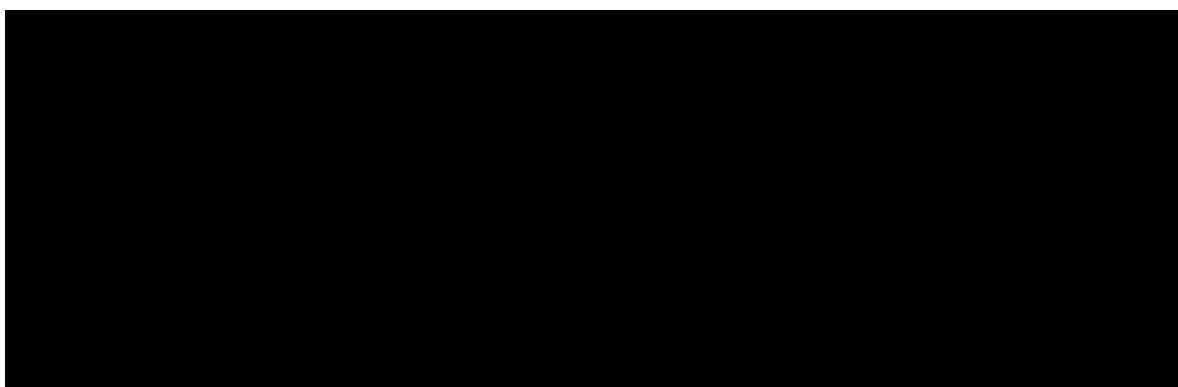
[Redacted content]

8 Curriculum Vitae

Personal Information

Date of Birth: Nov. 05. 1994
Gender: Male
Nationality: Chinese
Place of Birth: Shandong Province, P.R. China

Education



Publications

1. **Yupeng Zhao**, Dandan Gao, Johannes Biskupek, Ute Kaiser, Rongji Liu*, Carsten Streb*, Polyoxometalate-assisted synthesis of amorphous zeolitic imidazolate for efficient electrocatalytic oxygen evolution, *Results in Chemistry*, Volume 4, 2022, 100568.
2. **Yupeng Zhao**, Si Liu, Dandan Gao, Johannes Biskupek, Ute Kaiser, Rongji Liu*, Carsten Streb*, POM@ZIF derived mixed metal oxide catalysts for sustained electrocatalytic oxygen evolution, *Chemistry—A European Journal*, 2023,29, e2022032.
3. Shujun Li,* Yubin Ma, Yue Zhao, Rongji Liu, **Yupeng Zhao**, Xusheng Dai, Carsten Streb*, Xuenian Chen,* Hydrogenation Catalysis by Hydrogen Spillover on Platinum - Functionalized Heterogeneous Boronic Acid -Polyoxometalates, *Angew. Chem.Int. Ed.* 2023,62, e2023149.
4. **Yupeng Zhao**, Dandan Gao, Rongji Liu*, Carsten Streb*. In situ formation of robust nanostructured Cobalt oxyhydroxide / Cobalt oxide oxygen evolution reaction electrocatalysts. Submitted to
5. **Yupeng Zhao**, Zhengfan Chen, Nana Ma, Weiyi Cheng, Kecheng Cao, Dong Zhang, Fan Feng, Dandan Gao, Rongji Liu*, Shujun Li*, Carsten Streb*, Atomic WOx/MoOx modified defect-rich Pd metallene for Enhanced Alkaline Oxygen Reduction Electrocatalysis and Zn air batteries. Submitted to
6. Si Liu,# **Yupeng Zhao**,# Dandan Gao, Fan Feng, Joachim Bansmann, Johannes Biskupek, Ute Kaiser, Rongji Liu* and Carsten Streb*, Electroless Plating of NiCu Alloy on 3D Printed Polymer for Efficient Electrochemical Ammonia Production and Electricity Generation with Zn–Nitrate Batteries. Submitted to *ChemElectroChem*.

